FUNDAMENTAL MODELLING OF FRICTION DURING THE HOT ROLLING OF STEEL

by

Simon Peter Jupp

Thesis submitted for the degree of
Doctor of Philosophy

Department of Engineering Materials
University of Sheffield

February 2005

Abstract

Friction is one of the most significant physical phenomena influencing metal forming, yet in comparison with metallurgy, heat transfer and mechanics it remains the least understood. The goal of this project was to develop, on as fundamental a level as possible, a friction model based upon the physics of the process to be applied to the hot rolling of steel.

A fundamental friction model was developed based upon the simplified approach to the adhesion theory by Straffelini (Wear, 249, 79-85, 2001), which is an extension of Bowden and Tabor's original adhesion theory. In this work, the simplified approach's dependence on the thermodynamic work of adhesion was exploited to apply it over a wide range of temperatures. The thermodynamic work of adhesion describes the work required to form a new surface and is a function of the surface energy of the contacting materials was estimated using two approaches: Rabinowicz's and the geometric mean rule. Since high temperature surface energy data is not generally available the relative change in Young's modulus with temperature was used to estimate a material's surface energy at a desired temperature. Reciprocating friction experiments, which provided a controlled environment in which to investigate friction, were conducted to verify the application of this theory to high temperature conditions and metal-oxide contacting materials.

The fundamental model describing friction was applied to the hot rolling of steel via a friction algorithm using the commercial finite element (FE) code MARC. Simply described the friction algorithm calculated a friction coefficient using material properties, defined by the user, and contact temperatures, taken from the rolling model. This resulted in the friction coefficient predicted throughout the roll bite, compared to an average friction coefficient typically employed in rolling models. The combined friction algorithm-rolling model was validated against laboratory rolling experiments.

One of the assumptions of the finite element rolling model is the presence of a thin, continuous and adherent scale layer. To achieve this in the laboratory a two pass rolling schedule was employed; the first pass to remove the furnace scale and the second pass to input the desired deformation. The success of the friction algorithm was determined by comparing the experimental torques and loads to the predictions of the finite element model. The FE model with the friction algorithm predicted the friction coefficient to vary in the roll gap between approximately 0.25 and 0.35 and was able to predict the measured rolling torque with an average error of 15%, which was considered acceptable and the accuracy was increased after the bearing torque was considered. The error in the load predictions compared to the measured loads was 13.5% on average, which was also acceptable.

This work has been conducted in collaboration with Corus IJTC and, as such, has benefited through the access of equipment and input from an industrial viewpoint.

Table of Contents

Chapter

Appendix

List of Tables

List of Figures

List of Symbols

α	Constant
α'	Constant
α_c	Thermal expansion coefficient
α_n	Roll bite angle
β	Constant
B	Constant
γ	Scale Index
γ_{ad}	Energy of adhesion
γ_s	Surface energy
γ_T	Surface energy at a given temperature
γ_0	Surface energy at room temperature
$\bar{\dot{\varepsilon}}$	Effective strain rate
η	Efficiency term
θ	Roughness angle
λ	Neutral point as a fraction of the contact length
μ	Friction coefficient
μ_{Me}	Chemical potential of metal
ν	Poisson's ratio
ρ	Density
σ	Stress
$\bar{\sigma}_0$	Mean yield stress
σ_1	Applied tensile stress
σ_f	Flow stress
σ_d	Deformation resistance function
σ_y	Yield stress
τ	Shear stress
τ_1	Maximum shear stress
τ_m	Mean shear strength
τ_y	Shear strength
$\phi(x,y)$	Stress function
ϕ_w	Work hardening function
ϕ_r	Rate hardening function
ϕ_s	Crack angle with respect to the surface
Φ	Molar volume ratio
ψ	Airy stress function

ω	Fourier transform variable
ω_r	Radial velocity
φ	Neutral plane angle
a	Half-contact length
a_m	Moment arm
A	Area
A_c	Adhesive or cohesive effect
A_g	Area of groove that is created during sliding
A_p	Amplitude
A_r	Real area of contact
b	Strip width
c	Constant
c_m	Compatibility parameter
c_n	Compatibility parameter
C	Constant
C_1	Constant
C_2	Constant
C_3	Constant
C_4	Constant
C_V	Specific heat capacity at a constant volume
Cp	Specific heat capacity at a constant pressure
$\bar{D}$	Effective diffusion coefficient
E	Young's modulus
E_T	Young's modulus at a given temperature
E_0	Young's modulus at room temperature
E'	System stiffness
F_{ad}	Force of adhesion
F_{AD}	Total force of adhesion
F_f	Friction force
F_N	Normal force
F_R	Roll force
F'_R	Specific roll force
F_T	Tensile force
FW	Formula weight
G	Fourier transform of ψ
G_c	Effective work of adhesion
G_s	Elastic shear modulus
ΔG	Gibb's free energy of formation
h	Heat transfer coefficient
h_0	Initial strip thickness

h_1	Final strip thickness
Δh	Reduction or draught
$\bar{h}$	Mean thickness between roll bite entry and exit
k	Thermal conductivity
k_e	Constant reaction rate constant
k_p	Parabolic rate constant
k_l	Linear rate constant
$\bar{k}$	Effective rate constant
K	Probability of producing a wear particle
K_I	Stress intensity factor for Type I crack
K_{II}	Stress intensity factor for Type II crack
K_σ	Stress intensity factor for combined crack
l	Unit cell length
l_2	Post-roll stand distance
l_r	Pre-roll stand distance
Δl	Travel of the driving head
L_p	Contact length
m	Friction factor
m_{scale}	Mass of scale
M	Torque
M_T	Roll torque
M'_T	Specific roll torque
N	Number of contacting asperities
p_{O_2}	Partial pressure of oxygen
$p(y)$	Normal pressure as a function of y
p_Y	Yield pressure
P	Power
$P(\omega)$	Fourier transform of normal pressure
P_P	Hardness
P_R	Roll pressure
$q(y)$	Shear stress as a function of y
Q_e	Activation energy
$\dot{Q}$	Rate of heat generation due to plastic deformation
$Q(\omega)$	Fourier transform of shear stress
r	Average junction radius
R	Gas constant
R''	Relative radius of curvature
R_d	Interatomic distance
R_r	Work roll radius
R'_r	Deformed roll radius

s	Shear strength
S_f	Forward slip
S_b	Backward slip
t	Time
t_s	Interval between the stroke end and when slip occurs
T	Temperature
T_d	Adiabatic heat generation due to plastic deformation
T_c	Period for one cycle
$\bar{T}$	Normalised temperature
$\bar{T}_p$	Normalised phase transition temperature
U_p	Work of plastic deformation per unit volume
v_r	Relative sliding velocity
V	Volume
V_2	Strip exit velocity
V_r	Roll velocity
V_m	Mid-stroke sliding velocity
$w0$	Initial strip width
$\bar{w}_1$	Average strip width
W	Temperature compensated time parameter
W_{ab}	Thermodynamic work of adhesion
W_{coh}	Thermodynamic work of cohesion
W_{r_th}	Theoretical wear rate thickness
Δx	Scale layer thickness
Z	Ionic charge
Z_{cell}	Unit cell content

Matrices and Vectors

$[t]$	Traction force per unit area matrix
$[\partial u]$	Displacement field matrix
$[f]$	Force per unit volume matrix
$[\sigma]$	True stress (or Cauchy stress) matrix
$[x]$	Direction matrix
$\{\dot{T}\}$	Rate of temperature change vector
$\{T\}$	Temperature vector
$[K_C]$	Heat conduction matrix
$[C_P]$	Heat capacity matrix
$\{Q\}$	Heat flux vector

Acknowledgements

First and foremost I would like to express my gratitude to Professor John H. Beynon for the opportunity to study at the University of Sheffield and his continuous guidance and suggestions.

I would like to gratefully acknowledge Corus plc for their financial support and thank Jaap van der Lugt from Corus IJTC for his patience and guidance throughout the course of my studies, Henk Bolt for fruitful discussions and Theo Maalman for his assistance with the experimental apparatus in IJmuiden.

The entire membership of IMMPETUS has been helpful and supportive in this endeavour. Special thanks go to Dr. Jesus Talamantes-Silva for his invaluable assistance and instruction on the finer points of finite element modelling, Dr. Mike Frolish for his practical suggestions, Mr. Lucian Tipi for his careful nurturing of my computing resources and my PhD colleagues for maintaining a sane working environment.

Mr. Ian Watts, Mr. Stuart Bater and Mr. Dean Haylock in the Quarrell Laboratory deserve special mention for their assistance in conducting the rolling experiments and their healthy respect for Murphy's Laws.

Last, but not least, I would like to express my gratitude to Sabine, Tim and Alex for reminding me there is more to life than studying.

For Sabine

Chapter 1 - Introduction

1.1. Why is Steel Rolling Important?

The importance of the steel industry is often overlooked or taken for granted, especially compared to other metals such as aluminium or titanium. To give an idea of the relative size of the steel industry the crude steel production in the USA in 2002 was 92.2 million tonnes [1] compared with North American aluminium production of 5.4 million tonnes [2] and US titanium ingot production of 86,700 tonnes [3]. Thus if the US steel industry grows by 0.1% it will be greater than the entire titanium ingot production. In Europe, at the end of 2003 the European Union (EU) had approximately 269,000 people employed in the steel industry [1] and in 2002 the EU produced 145,992 tonnes of hot rolled steel products [1] in addition to hot rolled long products or hot rolled flat products.

Within the overall framework of steel production rolled products are a significant proportion, as demonstrated by the world steel exports for rolled products, given in Table 1.1.

Table 1.1 – World steel exports analysed by selected products, excluding stainless steels (in millions of tonnes) [1].

Product	1998	1999	2000	2001	2002
Hot-rolled strip	2.6	2.7	3.1	3.4	3.4
Hot-rolled sheets and coils	44.1	45.8	49.1	43.7	48.8
Cold-rolled strip	2.9	3.0	3.5	3.2	3.4
Cold-rolled sheets and coils	25.9	26.9	29.1	26.9	28.6
Plates	17.0	15.8	17.0	17.7	18.2
Galvanised sheet	17.9	19.1	21.9	20.5	23.0
Total	243.8	253.4	276.4	270.0	279.4

The products listed in Table 1.1, all of which are processed via the hot rolling production route, represent approximately 45% of the world steel exports and growing.

1.2. Why Model Friction?

As important as the rolled steel market is, the margins for bulk products are small, as demonstrated by Table 1.2.

Table 1.2 – Estimated hot rolled coil prices and production costs for carbon steel [4].

Year	Price (US\$ tonne^{-1})	Cost (US\$ tonne^{-1})
1995	434	295
1996	335	291
1997	330	288
1998	278	281
1999	242	262
2000	320	261
2001	213	245
2002	264	246
2003	305	267
2004	490*	325*
2005	416*	326*
2006	318*	319*
2007	320*	311*
2008	376*	296*

* forecast

Thus, in times of recession, the hot rolling of steel can become a money-losing business. This can, in part, be prevented by reducing production costs or producing products for value-added markets such as the automobile industry. Either choice requires detailed knowledge of the rolling process; the former to minimise downtime and maximise output and the latter to economically meet the necessary specifications for surface quality and shape.

The rolling process is a complex event involving inter-related and inter-dependent variables and the ability to accurately predict the final properties, thereby foregoing expensive mill trials, requires knowledge of what these variables are and how they interact. Internally, models predicting bulk properties, such as yield strength, give sufficiently accurate results, largely due to pioneering work by Sellars and Tegart [5] in the 1960s. Externally, the knowledge of the mechanisms of load transfer between contacting materials at the high temperatures and pressures of steel hot rolling is limited. This is important as, more recently, emphasis has been placed on predicting material properties in their entirety, recognising the importance of strain path and how it influences many properties [6]. In rolling it is the alternating shear at the strip surface as a result of the friction conditions that causes a complicated strain path, limiting our ability to predict the properties of the material near the surface. Furthermore, it is the friction conditions that play a large role in dictating the wear and failure of the work rolls, both of which impact on the financial aspects of rolling in terms of down time and roll replacement, as well as strip surface quality as the work roll surface deteriorates. On a larger scale, the friction level affects the roll torque, which in turn determines, along with the roll speed, the mill power requirements. Therefore modelling friction has the potential benefits of:

- Identifying the contact conditions between the work roll and the strip.
- Increasing strip surface quality and reduce wear rates by avoiding process windows that result in undesirable friction conditions.
- More accurately predicting the maximum friction conditions, giving more accurate roll torque values resulting in more accurate power requirement predictions, which may enable the mill operating window to be increased.

1.3. Objectives

Typically friction during the hot rolling of steel has been empirically modelled using laboratory rolling results [7], which is able to indicate the effect of changing a given variable on the friction condition in the industrial case but cannot be directly applied to industrial rolling. The aspiration to develop a generic friction model that may be applied to both laboratory and industrial conditions led to the project objectives, given by:

- Investigate friction from a fundamental viewpoint.
- Develop a friction model based upon the physics of the process.
- Apply the friction model to the hot rolling of steel.

The desire for a model based on fundamental physics, rather than empirical correlations, demanded that there be a close link between the theoretical development of the model and experimental validation. With these objectives in mind, the thesis is structured in the following way:

- Chapter 2 is a brief historical perspective on friction studies. Included in this overview are: examples of the application of friction from ancient civilisations, the earliest scientific studies on friction by da Vinci, the contributions by the French School of thought on friction of whom Amontons is the most recognisable member, the little known adhesion experiments by Desaguliers, the kinetic friction studies of Coulomb and, lastly, the contributions by Bowden and Tabor.
- Chapter 3 is a review of the relevant literature examining the effect of friction on the strip (e.g. surface shearing), the effect of friction on the work roll (e.g. contact fatigue), the overall effect of friction on the rolling mill (e.g. power and torque), friction determination by both direct and indirect methods and the oxidation characteristics of steel.
- Chapter 4 is a summary of material properties, among these properties are the stress-strain relationships with strain rate and temperature considerations, Young's modulus with temperature, Poisson's ratio, specific heat capacity, thermal conductivity, thermal expansion and density. The surface energy estimates are also considered in some detail, which are critical to the developed adhesion theory, as seen in Chapter 5.
- Chapter 5 covers the theoretical aspects of the project. The bulk of this chapter is dedicated to the derivation of the expanded adhesion theory of friction. Also included is the development of the finite element model with the friction algorithm based on the expanded theory incorporated. Contact mechanics for simple contact situations and more complicated layered contacts are outlined.
- Chapter 6 reports on the experiments conducted. The three experiments that were conducted during this study were: modified ring compression testing, reciprocating friction testing and laboratory rolling.
- Chapter 7 is a discussion of the model and its implications. Central to this chapter is the comparison of the developed mathematical model with the laboratory rolling experiments. Consideration is also given to the appropriateness of the chosen experiments in terms of the developed theory and validation. Other topics discussed include: a sensitivity analysis of the developed theory, the effect of the roughness angle, criticisms of the adhesion model and their rebuttals, derivation of the theory in terms of a friction factor and, lastly, material pairings to reduce the friction coefficient are speculated on.

- Chapter 8 summarises the principal observations, draws some conclusions from this work and suggests some areas for further investigation.

1.4. References

1. Internation Iron and Steel Institute, http://www.worldsteel.org/media/ssy/iisi_ssy_2004.pdf, accessed 30/08/2004
2. International Aluminium Institute, http://www.world-aluminium.org/iai/stats/index.asp, accessed 16/11/2004
3. US Geological Survey, http://minerals.usgs.gov/minerals/pubs/commodity/titanium/titanmyb02.pdf, accessed 16/11/2004
4. J.F. King, Consultant associated with steelonthenet.com, http://www.steelonthenet.com/frameTRE.html, accessed 16/11/2004
5. C. M. Sellars and W.J. MCG. Tegart "La relation entre la resistance et la structure dans la deformation a chaud", Mem. Sci. Rev. Metall., 1966, 63, 731-746
6. Q. Zhu and C. M. Sellars "Microstructural evolution of aluminium-magnesium alloys during thermomechanical processing", Materials Science Forum, 2000, 331-337, 409-420
7. J. G. Lenard and L. Barbulovic-Nad "The coefficient of friction during hot rolling of low carbon steel strips", Journal of Tribology, 2003, 124, 840-845

Chapter 2 - A Brief History of Friction

2.1. Introduction

The phenomenon of friction has been acknowledged, if not identified, since the beginning of civilisation. The development of the understanding of friction has mirrored the development of civilisation, although the causal relationship between the knowledge of friction and the increased complexity of society could be debated. Examples of increased understanding of friction come from the ancient civilisations of the Sumerians and Egyptians, through the height of the Greek and Roman civilisations, encompassing the medieval period and finally through the Renaissance, which essentially brings us to today's society. More exhaustive studies have been published regarding the historical studies of friction and tribology and some of the individuals who have studied friction [1-6]; the purpose of this chapter is to give a historical perspective with regards to the important steps that have been made.

2.2. Pre-Renaissance Civilisation

The ancient civilisations are not generally associated with technology and machinery as we know it. However, the civilisations of the Sumerians and Egyptians did take advantage of the friction phenomenon in applications to create time saving devices and other mechanical constructions. A prime archaeological example of an application based on friction is the potter's wheel. The oldest surviving example of a potter's wheel was found in 1930 at Ur, dated c. 3250 BC ([1], p.23). The fragment showed a thick clay disk with a pivot hole smoothed with bitumen, which indicates the probable use of lubricants to reduce friction.

Other early examples (c. 2500 BC) that show perhaps not the knowledge of friction but certainly cognizance of the effects of friction are wheels studded with copper nails or bound with metal hoops ([1], p.26) and the application of lubricants for reducing the rolling resistance. The first recorded example of a known lubricant being applied is shown in a tomb built at Saqqara, Egypt c. 2400 BC ([1], p.36).

Further development in wear reduction devices and lubricants could be considered evolutionary, rather than revolutionary; for example: the use of iron nails to reduce the wear of Roman caligae (a.k.a. sandals) or the embedding of stones in wooden ploughs in medieval times and the use of vegetable oils and animal fats for lubricants. Certainly in the medieval times there was a loss of knowledge gained by the Romans through the fragmentation of the Roman Empire, hence the lack of sophistication in the wear reduction techniques. An excellent example of the loss of knowledge as a result of the collapse of the Roman Empire pertinent to friction is the recognition of friction as a force, although the term "force" was not in use until Newton, by the Greek philosopher and mathematician Aristotle, c. 330 BC ([1], p.66). Unfortunately the Greeks typically applied their advanced knowledge of mechanics to construct elaborate toys rather than develop more practical applications.

2.3. Leonardo da Vinci

Perhaps the most inventive and talented person of all time was Leonardo da Vinci and while he is best known for his art, his studies of the natural world show his undisputed genius. In light of his wide-ranging studies it should not be too surprising that he studied tribology, representing the first scientific investigation of friction ([1], p.97). Most of da Vinci's work relating to friction and tribology are found in *Codex Atlanticus*, *Codex Madrid I* and *II* and a volume known as *Arundel* MSS.263 [1-3].

It is tragedy that da Vinci's notes had remained undisclosed for such a long period as many of the experiments that were performed by da Vinci were repeated, more often than not hundreds of years later. For example, da Vinci's experimental approach was similar to that of Coulomb. Some sketches from da Vinci's notebooks are shown in Figure 2.1. The similarities in approaches can be seen by comparing Figure 2.1 and Figure 2.5.

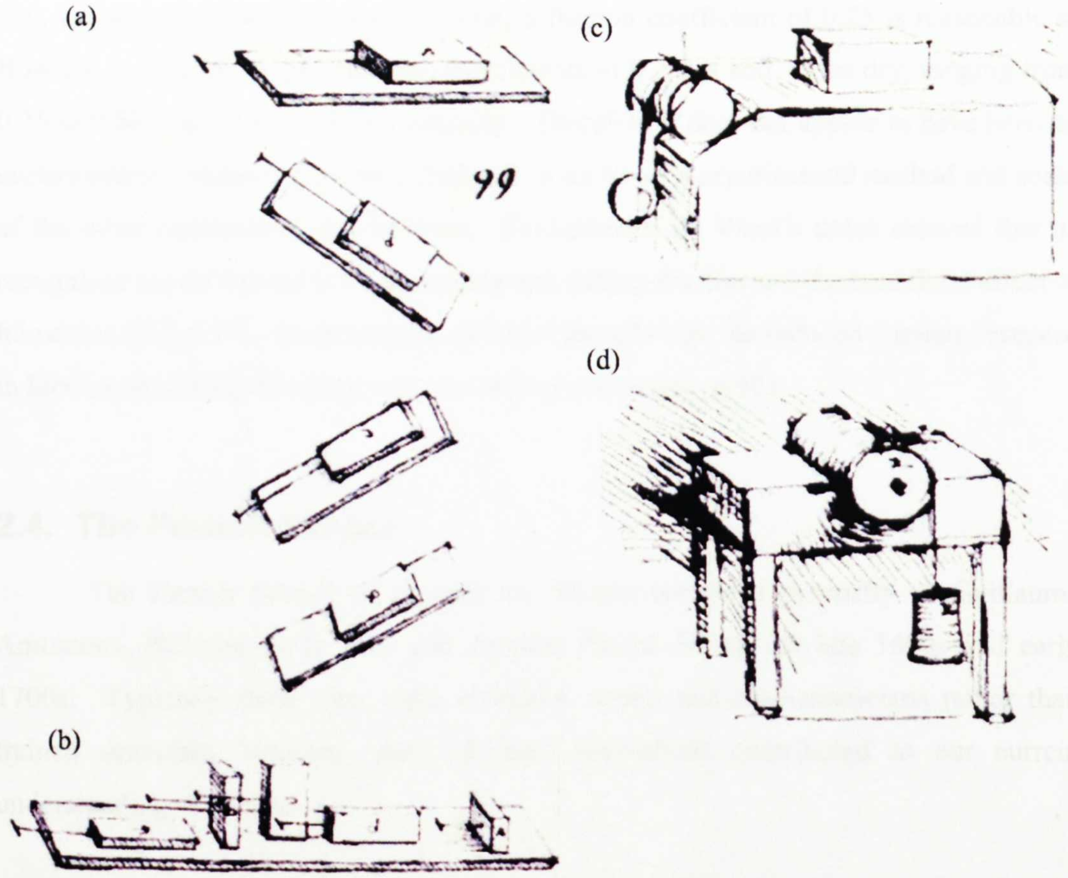

Figure 2.1 – Sketches from the *Codex Atlanticus* and the *Codex Arundel* showing experiments to determine: (a) the variation of friction force between horizontal and inclined planes; (b) the influence of apparent contact area on the force of friction; (c) the force of friction on a horizontal plane by means of a pulley; (d) the friction torque on a roller and half bearing ([1], p.98).

A summary of the more important conclusions reached by da Vinci, with respect to friction, are ([1], p.99):

- The effect of weight was directly proportional to the friction, independent of the contact area.
- The frictional resistance depended upon the nature of the surfaces in contact with smoother surfaces having smaller friction.
- For "polished and smooth" surfaces "every frictional body has a resistance of friction equal to ¼ of its weight".

This last conclusion requires further discussion. Although this has since been shown to be inaccurate, it is similar to a conclusion reached by Amontons [7] who concluded that resistance due to friction is proportional to ⅓ of the normal load. For materials of the day, i.e. wood-on-wood or wood-on-iron, a friction coefficient of 0.25 is reasonable as Bowden and Tabor [6] give friction coefficients of 0.2 wet and, when dry, ranging from 0.25 to 0.50 and 0.20 to 0.60 respectively. Therefore it does not appear to have been an unreasonable conclusion, lending credence to da Vinci's experimental method and some of the other conclusions that he drew. Furthermore, da Vinci's notes showed that he recognised the difference between sliding and rolling friction and the beneficial effect of lubricants ([1], p.97). Interestingly, da Vinci thought that the reduced friction observed in lubricated sliding was the result of a rolling action ([1], p.98).

2.4. The French School

The French School of thought on friction consisted primarily of Guillaume Amontons, Philippe de la Hire and Antoine Parent during the late 1600s and early 1700s. Typically these men were inventors, artists and mathematicians rather than trained scientists; however, each of these individuals contributed to our current understanding of friction.

Although trained as an architect, Amontons was an inventor who developed instruments for civil engineering, navigational and mechanical purposes but is best remembered for his work on static friction. The apparatuses used by Amontons [7] for his friction experiments were quite creative, consisting of test specimens loaded with springs, while the force required to overcome friction and initiate sliding was measured on a spring balance, shown in Figure 2.2. Specimens tested included copper, iron, lead and wood in various combinations with each surface coated with old pork fat. His main findings were ([1], p.154):

- That the resistance caused by rubbing only increases or diminishes in proportion to greater or lesser load and not according to the greater or lesser extent of the surfaces.
- That the resistance caused by rubbing is more or less the same for iron, lead, copper and wood in any combination if the surfaces are coated with pork fat.
- That this resistance is more or less equal to ⅓ of the load.

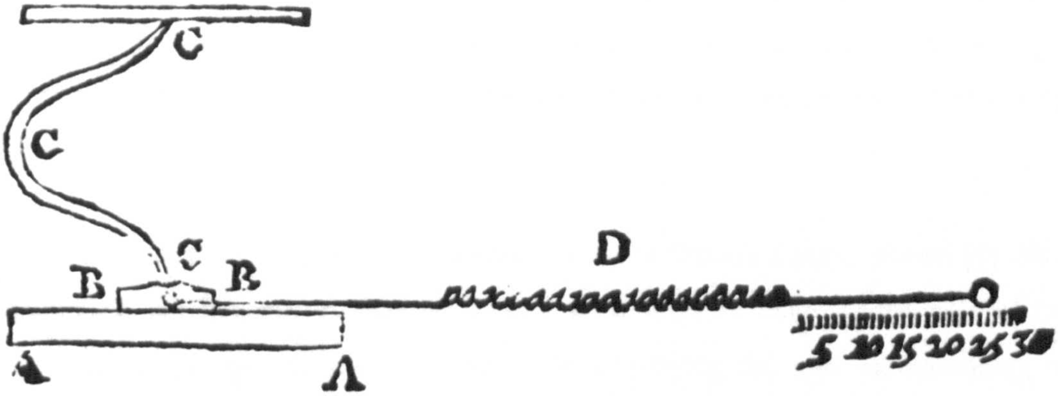

Figure 2.2 – The test apparatus used by Amontons showing the applied normal load via spring (C-C-C) to the test materials (A-A and B-B) with the resulting friction force measured with a spring balance (D) [7].

Amontons thought of the fundamental cause of friction in terms of surface roughness and the force required to lift interlocking asperities over each other in sliding motion ([1], p.156). The representations of elastic asperities are shown in Figure 2.3. Another finding of Amontons' was the independence of friction on contact area, which coincides with his concept of lifting interlocking asperities.

Figure 2.3 – Amontons representation of elastic asperities by springs [7].

The independence of friction on contact area prompted Philippe de al Hire to test and confirm this conclusion with sliding experiments involving wood-on-wood and marble-on-marble. According to de la Hire [8], the resistance arose from the texture of the surfaces which, if flexible, had to bend or lie flat or, if hard, had to disengage themselves and might become detached. This concept was able to explain the independence of friction on contact area since the possibility of detachment introduced the concept of permanent surface deformation and shearing, which implies that resistance would depend upon the number of asperities and hence the size of the surfaces ([1], p.158). In the case of elastic asperities the deflection was seen to be inversely proportional to their number (i.e. the more asperities the more difficult to cause each individual asperity to deflect), while the total reaction remained constant, giving a resistance independent of area. In the case of rigid asperities the resistance arose from the force required to lift the surface ridges over each other, thus yielding a direct relationship with load but no dependence on the apparent contact area ([1], p.157).

This leads to Antoine Parent's contribution to friction theory. Parent [9] drew attention to the fact that in drawing a body up a slope of angle θ, the ratio of the tangential to the normal force was tan θ, thus applying the new understanding of friction, demonstrated by Amontons and de la Hire, to statics and equilibrium ([1], p.158).

2.5. John Theophilus Desaguliers

John Theophilus Desaguliers is often more remembered for his friendship with Sir Isaac Newton and his work with electricity; however he made important observations which had largely gone unremarked until the early 1950s with Bowden and Tabor's [5] adhesion theory. He introduced the notion of cohesive forces and thought the action of these forces contributed to the overall frictional resistance experienced by sliding bodies. The reason for the dismissal of this theory was the inability to reconcile the necessary dependence of contact area required by the cohesive/adhesive concept with the experimentally observed independence of contact area.

The procedure used by Desaguliers [10] involved the use of lead spheres that were pressed together with a slight twist. The cohesive force was then measured by the force necessary to separate the spheres. The original apparatus was a handheld device that used a tray with a known weight to separate the spheres, shown in Figure 2.4a. Unfortunately given the small diameter of the lead balls the contact patch was difficult to measure accurately, thus a second device was built that enabled a greater weight to be applied, enabling larger lead balls to be tested with a corresponding increase in contacting area, shown in Figure 2.4b.

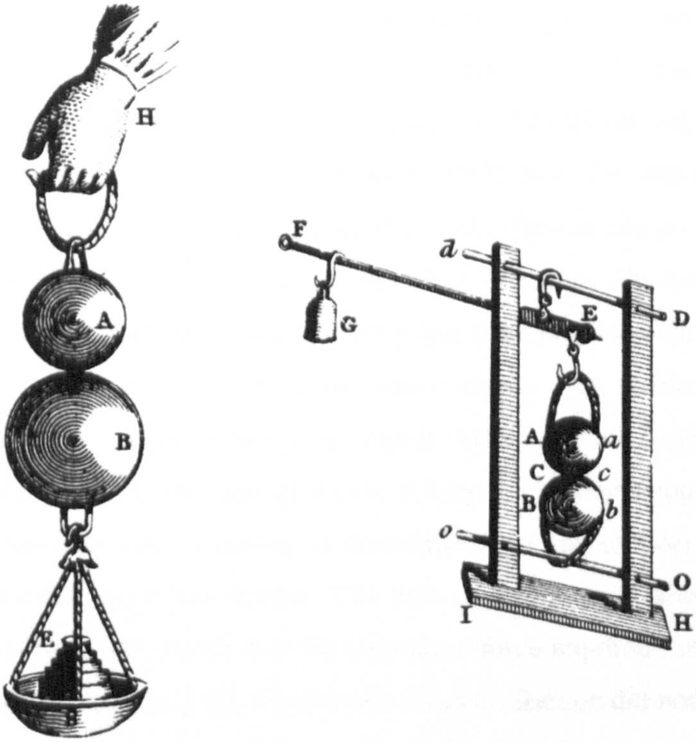

(a) (b)

Figure 2.4 – Depictions of two devices employed by Desaguliers to measure the cohesive forces between lead spheres [10].

With regards to friction, Desaguliers believed that the influence of cohesion is introduced when the role of surface finish is considered ([1], p.161). Thus, Desaguliers noted that when the sliding surfaces are highly polished the force of friction may actually rise due to the fact that the attraction of cohesion becomes sensible when the surfaces are brought nearer and nearer to contact ([1], p.161). It has since been shown that in highly polished samples there is an increase in real contact area [5,6], thereby demonstrating the accuracy of Desaguliers' hypothesis. Given the unrepeatable nature of the experiments it is remarkable that Desaguliers was able to suggest an explanation that has since been shown to be correct, to the best of our current understanding. Practically speaking, it could be said that Desaguliers demonstrated the first friction weld.

2.6. Charles Augustin Coulomb

Along with Amontons, Charles Augustin Coulomb's name is synonymous with the study of friction although Coulomb's interests were far-ranging and the study of friction played a minor role relatively late in his life. Since Coulomb was in the employ of the French army his primary interests lay in the field of civil engineering, i.e. fort reinforcements and retaining walls. In an essay entitled "Essai sur une application des règles de maximus & minimus à quelques problemes de statique, relatifs à l'architecture", Coulomb [11] writes that friction and cohesion are passive forces and can be measured by the limits of their strength. For this essay Coulomb refers to the works of Amontons [7] and others while writing that there can be some variation in the friction strength in proportion to the compressive force. For architectural purposes Coulomb [11] describes cohesion as the resistance that solid bodies offer to the simple separation of their parts. In the case of solids, if they are homogeneous, they have the same strength, and the total cohesion is proportional to the number of parts to be broken, and hence the area of the rupture. The tests conducted by Coulomb focussed on the fracture of solid objects, rather than the separation force required for two bodies in a manner similar to Desaguliers [10]. Coulomb's focus on friction did not take place until 1779 at his military posting at Rochefort ([4], p.197) where his experiments on friction won the *Académie* prize for 1781 but were not published until 1785 [12].

There are two principal differences between the studies of Amontons and Coulomb: Amontons' studies were lubricated static friction experiments while Coulomb's experiments were typically unlubricated sliding friction. Coulomb initially investigated the influence of four main factors on friction ([1], p.217):

- The nature of the materials in contact and their surface coatings.
- The extent of the surface area.
- The normal pressure (or load).
- The length of time that the surfaces remained in contact (time of repose).

The experimental apparatus used by Coulomb for studying sliding friction, shown in Figure 2.5, bears a striking resemblance to the apparatus of da Vinci, shown in Figure 2.1. From these experiments Coulomb observed the dependence of friction on the materials and coatings involved as well as the load. Although, with respect to load he noted that the direct proportionality was not strictly observed by all materials. He also observed the independence of friction on contact area. His temporal studies led to the concept of static and kinetic friction.

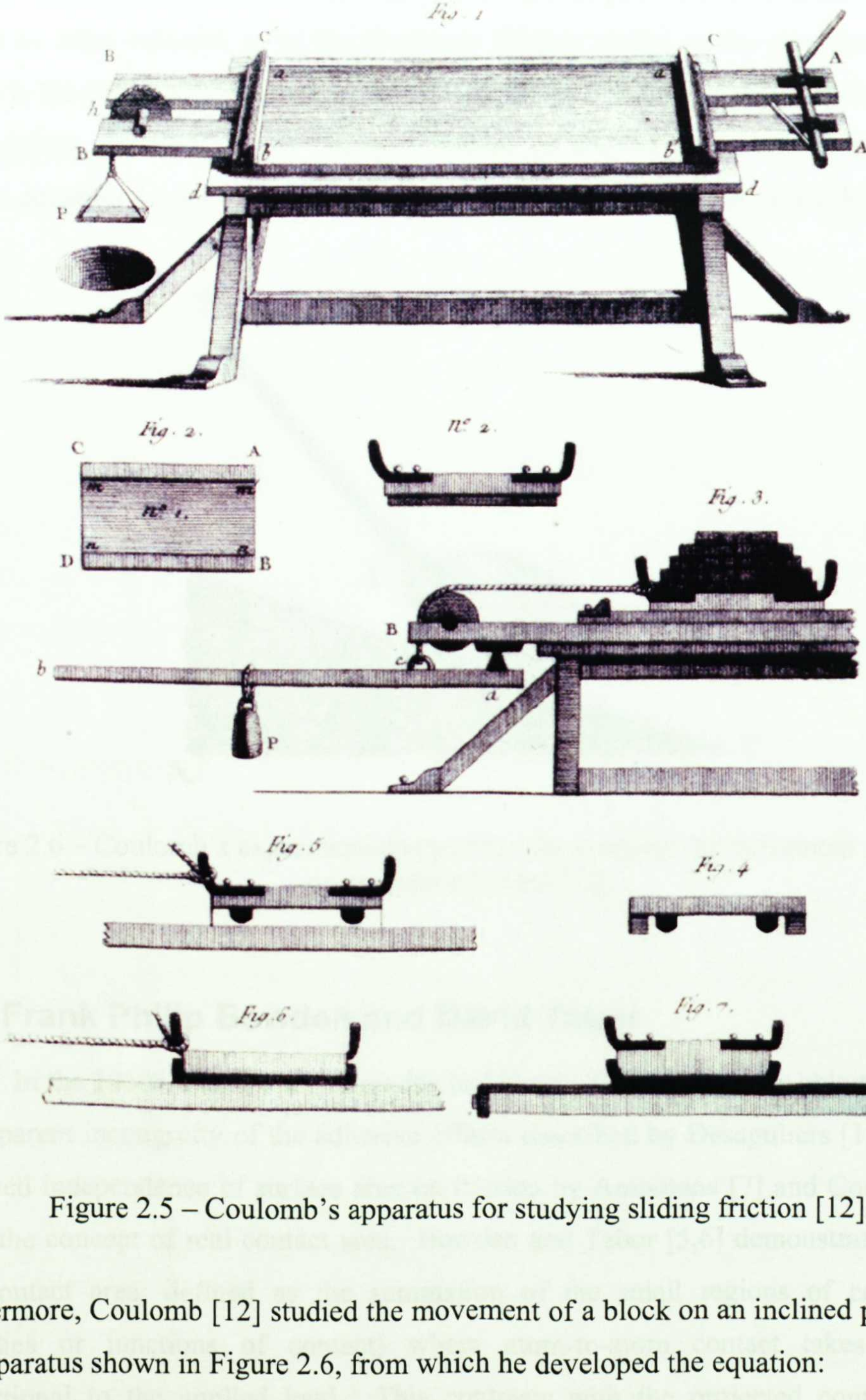

Figure 2.5 – Coulomb's apparatus for studying sliding friction [12].

Furthermore, Coulomb [12] studied the movement of a block on an inclined plane using the apparatus shown in Figure 2.6, from which he developed the equation:

$$F_f = F_T = A_c + \mu F_N \tag{2.1}$$

where F_f and F_T are the friction and tensile forces, A_c is the adhesive or cohesive effect, F_N is the normal force and μ is the coefficient of friction. The term μF_N is attributed to deformation or ploughing. From these experiments Coulomb concluded that cohesion had a very small influence upon friction, however he was the first person to use a two-term expression for friction. This is the formulation that is often used to describe friction when more accurate modelling of friction is required; however, the formulation that is as often referred to as the Coulomb friction model or the Amontons friction model is the proportionality between normal force and friction force. Another fact that demonstrates the relevance of Coulomb's work on friction is the importance of the *A* term in equation 2.1 for the tribology of micro-electromechanical systems (MEMS).

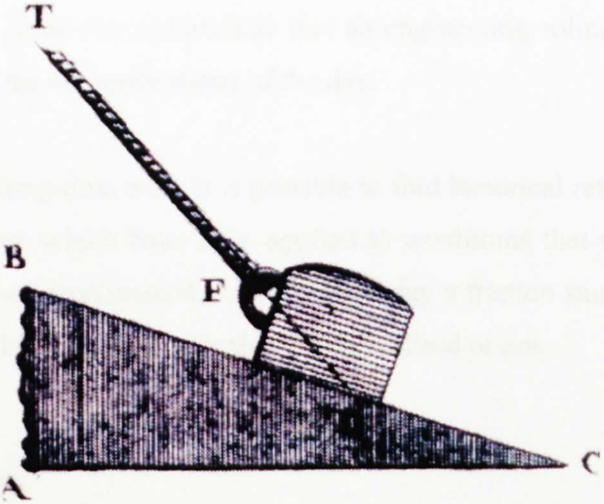

Figure 2.6 – Coulomb's experimental apparatus for studying the movement of a block on an inclined plane [12].

2.7. Frank Philip Bowden and David Tabor

In the 1950s, Frank Philip Bowden and David Tabor [5,6] were able to reconcile the apparent incongruity of the adhesive effects described by Desaguliers [10] with the observed independence of surface area on friction by Amontons [7] and Coulomb [12] using the concept of real contact area. Bowden and Tabor [5,6] demonstrated that the real contact area, defined as the summation of the small regions of contact (i.e. asperities or junctions of contact) where atom-to-atom contact takes place, is proportional to the applied load. This contrasts with the projected contacted area previously assumed. However, if fully plastic flow during a sliding process is assumed, friction is found to change linearly with the applied load, as demonstrated previously. As this theory is relevant to the current study a more complete description is included in Chapter 5.

2.8. Conclusions

It is interesting to note that despite the extended time frame from the initial studies of friction by da Vinci to the middle of the 20th century very little variation in the friction formulation arose. The loss of da Vinci's pioneering studies should be taken into consideration over the slow development of friction theory, but that only slightly changes the time scale. The consistency of the results between independent tests, within experimental error, leads one to conclude that an engineering solution had been found that was acceptable for the applications of the day.

Despite the long time scale it is possible to find historical references to even the most current theories, which have been applied to conditions that were undreamed of when the theories were first penned. Ultimately, today's friction studies borrow heavily from these historical descriptions, whether this is realised or not.

2.9. References

1. D. Dowson "History of tribology", 1st ed., Longman Group Limited, London, 1979, 0-582-44766-4
2. L. Reti "Die wiedergefundenen Leonardo-Manuskripte der Biblioteca Nacional in Madrid", Technikgeschichte, 1967, 24, 193-225
3. L. Reti "The Leonardo da Vinci codices in the Biblioteca Nacional of Madrid", Technology and Culture, 1967, 8, 437-445
4. J. Heyman "Coulomb's memoir on statics: An essay in the history of civil engineering", 1st ed., Imperial College Press, London, 1997, 1-86094-057-9
5. F.P. Bowden and D. Tabor "Friction and lubrication", 1st ed., Methuen and Co. Ltd., London, 1956
6. F.P. Bowden and D. Tabor "Friction and lubrication", 2nd ed., Methuen and Co. Ltd., London, 1967, 0416406300
7. G. Amontons "De la resistance caus'ee dans les machines", Memoires de l'Academie Royale, 1699, vol A, (Chez Gerard Kuyper, Amsterdam, 1706), 257-282
8. P. de la Hire "Sur les frottements des machines", Histoire de l'Academie Royale, 1699, vol A, (Chez Gerard Kuyper, Amsterdam, 1706), 128-134
9. A. Parent "Nouvelle Statique Avec Frotemens et Sons Frotemens ou Regles pour calculer les Frotemens des machines dans l'etal de l'equilibre", Memoires de l'Academie Royale, 1704, vol A, (Chez Gerard Kuyper, Amsterdam, 1708), 235-254
10. J.T. Desaguliers "Some experiments concerning the cohesion of lead", Phil.Trans. R. Soc. Lond., 1725, 33, 345-347
11. C.A. Coulomb "Essai sur une application des règles de maximus & minimus à quelques problèmes de statique, relatifs à l'architecture", Memoires de

Mathematique et de Physique, presentes a l'Academie Royale des Sciences par divers Savans, & lus dan ses Assemblees, 1773, 7, 343-383

12. C.A. Coulomb "Theorie des machines simples, en egant egard au frottement de leurs partres, et a la roideur des cordages", Memoires de Mathematique et de Physique l'Academie Royale des Sciences, 1785, X, 161-342

Chapter 3 - Literature Review

3.1. Introduction

Friction is one of the most significant physical phenomena influencing the forming of metal, yet in comparison with metallurgy, heat transfer and mechanics remains the least understood [1]. The reason for this is that friction is not a fundamental material property and cannot be directly measured, although there exists a large number of tests that have been developed [2]. The complexity of friction is such that it can been seen as a function of many variables, among those that have been identified to be more influential are: temperature, pressure, hardness, slip, relative roughness and lubrication. To complicate matters even further these variables interact with each other to further affect friction during rolling [3].

Friction affects, or is affected by, almost everything in rolling. The most obvious effects are seen in the strip, the work roll and the power consumed by the rolling mill. This makes it necessary to assess the level of friction during rolling, which may be done directly or indirectly. Further afield, since friction is the result of two contact surfaces, it is important to be able to characterise these surfaces in terms of microstructural properties and evolution of the surfaces over time. This leads to the realisation that the alloy additions to steel can have a significant impact on the properties of the iron oxides, which vary in consequence from element to element.

3.2. Effect of Friction in the Rolling Mill

Although friction cannot be directly measured, the presence of friction has a large impact on the rolling process, the strip, the work rolls and the rolling mill itself. Friction affects the strip by changing the amount of shear applied to the strip for a given reduction, while the work rolls are affected in terms of damage resulting from excessive friction levels and friction plays a critical role in assessing the power requirements of the mill, thus determining the capital investment necessary for a rolling mill.

3.2.1. Friction and the Strip

The primary concern regarding friction levels in rolling is for the formation of suitable textures for deep drawing applications. The shear deformation that results from friction can be both good or bad depending on the materials involved; for example, the presence of shear textures is beneficial for the deep drawing performance of aluminium but is ruinous for interstitial free (IF) steels. The reason for this is that for good drawability a $\{111\}$ recrystallisation texture parallel to the sheet plane is required. Lee and Lee [4] studied the warm rolling of IF steels and found that a Goss texture, i.e. $\{110\}$<001>, forms in the surface layer and remains unchanged after annealing. To study the effect of shear strain on the final texture of the steel they rolled layered, i.e. laminated, samples at 700°C without lubrication. They found that the increased reduction, which results in increased shear strain, had no effect on the strain in the [111] slip systems but increased the strain in the (110)[$\bar{1}$11] and the (110)[1$\bar{1}$1] systems, i.e. directions 3 and 4 in Figure 3.1.

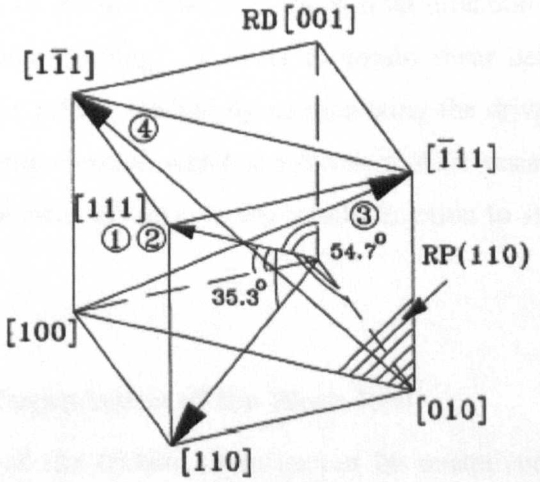

RD : Rolling direction
RP : Rolling plane

Figure 3.1 – A unit cell showing the (110)[001] texture and related slip systems [4].

The lack of change of the Goss texture, even after annealing, was explained by Lee and Lee [4] that when the [001] direction is on a $\{110\}$ plane the symmetry condition is satisfied and atoms need to undergo minimal shuffle during recrystallisation, because recrystallised grains and the deformed matrix will share the same (110) plane. As a result, the recrystallisation texture will be (110)[001], which is also the deformation texture. A study by Barrett [5] on the deep drawability of IF steel reported that the shearing action at the surface, combined with the influence of solute carbon and nitrogen results in (110) texture forming in the sheared regions, preventing the formation of (111) and (200) textures required for good drawability. Furthermore, they reported that carbon in solution has a strong influence on texture formation during ferritic hot rolling as a result of preferred nucleation sites and local crystal rotations in the vicinity of the grain boundaries, thus the absence of carbon resulting in strong (111) textures, explaining why it is necessary to use IF steels for deep drawing applications. Even the absence of carbon was not found to be sufficient to prevent the formation of shear texture; the use of excess ester oil was also required, i.e. low friction conditions.

With regards to aluminium, the situation is almost the exact opposite. Whereas in steel rolling it is desirable to minimise the amount of shear deformation for good deep drawing properties, in aluminium rolling it is necessary to maximise the amount of shear deformation as it is difficult to form the desired <111> texture. According to Sakai *et al.* [6] the <111> texture parallel to the normal direction cannot be formed in fcc metals by conventional rolling. In order to obtain shear deformation across the sample they developed a rolling method by manipulating the drive rolls, thus enabling an increase in the resulting *r* values, which is a measure of the resistance of a material to thinning, defined as the ratio of strain in the width direction to strain in the thickness direction.

3.2.2. Friction and Degradation of the Work Roll

As the source of the friction force cannot be unequivocally identified, it is assumed that the state of the work roll plays a large role in determining the level of friction that exists. There will be a large thermal fatigue component as the work roll surface heats up when contacting the strip surface only to be cooled again with spray cooling. There will also be a large mechanical fatigue component as the work roll deforms the strip followed by contacting the back-up work roll. Colas *et al.* [7] attribute accelerated oxide growth as a result of cracking within the oxide layer due to both the mechanical and thermal stress components. The thermal cycling then causes oxide loops, shown in Figure 3.2, which spall off to form pits in the oxide layer.

Figure 3.2 – An example of an oxide loop [7].

There is relatively little literature available on the study of work roll failures regarding mechanical and thermal fatigue [8-10]. Qualitative and quantitative models have been developed by Frolish and Beynon [11,12] for back-up rolls. Parallels can be drawn between back-up roll and work roll failures; therefore it would be reasonable to suppose that the work roll oxide failure could be modelled in a similar, albeit more complicated manner as a result of the additional thermal cycling. The qualitative failure model for back-up rolls is given in Figure 3.3.

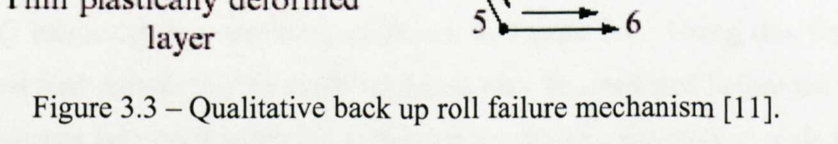

Figure 3.3 – Qualitative back up roll failure mechanism [11].

This model was validated against both laboratory scale test discs and industrial work roll/back-up roll pairings. The initial cracks typically propagated 60° from the surface before the tensile mechanism, as a result of the fluid pressure, changed the direction of the crack. In the test discs, the crack typically propagated towards the surface while in the back up rolls the crack typically propagated on a steeper trajectory downwards. The direction may be calculated by the following equation for the stress intensity factor, K [12]:

$$K_\sigma = \cos\frac{\phi}{2}\left[K_I \cos^2\frac{\phi_s}{2} - \frac{3}{2}K_{II}\sin\phi_s\right] \tag{3.1}$$

where ϕ_s is the angle of the crack with respect to the surface (in radians), $K_i = K_{iN} + K_{iT} + K_{iP}$ and $i=I, II$. The suffixes N, T, P represent normal, tangential and pressure contributions respectively. The initial direction of the mode I crack propagation predicted by equation 3.1 is determined by the crack length to half contact width ratio at the point that the mode I threshold is reached. Furthermore the role of lubricants in the crack is important in the continued propagation of surface initiated rolling contact fatigue cracks.

The work roll surface does not remain at a constant temperature but will fluctuate over time. There remains some disagreement within the literature as to what the range of temperature is experienced by the work roll. This is principally due to our inability to accurately describe the heat transfer coefficient. Fletcher [13] suggests that the surface temperature of the work roll can range between 450 and 600°C, depending upon the heat transfer coefficient. Gonzalez *et al.* [14] have used a temperature compensated time parameter, W, to determine the oxide growth during this cyclical pattern:

$$W = t \cdot \exp\left(\frac{Q_e}{R \cdot T}\right) \tag{3.2}$$

where t is the time, T is the temperature, R is the gas constant and Q_e is the apparent activation energy. The initial value of Q determined by Gonzalez *et al.* [14] was 4 kJ mol^{-1} and was shown to be relatively constant up to approximately 10 μm; beyond this point Q increased exponentially, as shown in Figure 3.4. Using this temperature compensated time parameter, the oxide thickness may be estimated before the oxidative wear mechanisms take hold, using the activation energy as a function of scale thickness. Also, if the instantaneous oxidation rate is known or calculated then the wear rate may be estimated. The increasing activation energy with oxide thickness could be a result of the wüstite lattice vacancies filling up while the lack of fit above 40 μm could indicate a transition in the oxidation mechanism.

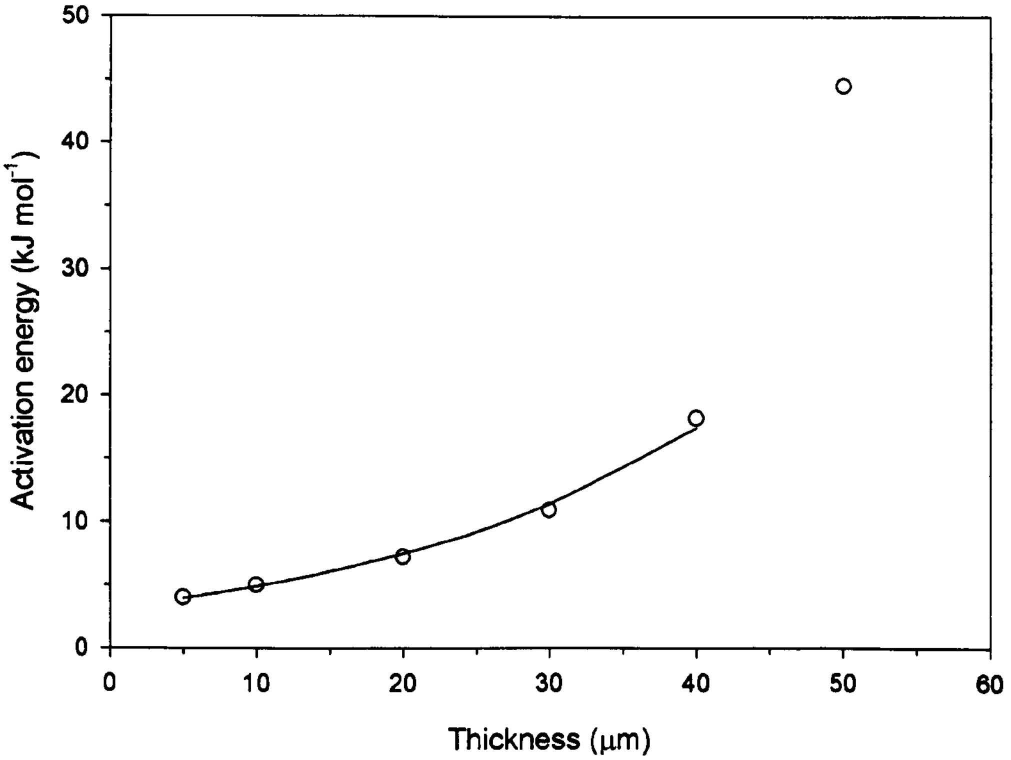

Figure 3.4 – Variation of apparent activation energy as a function of oxide thickness [14].

To investigate the roll deterioration on a laboratory scale Kato *et al.* [15] developed a disc-on-disc simulator. Using this device they determined that the temperature of the work roll strongly influences the wear patterns. When the roll temperature was 400-500°C scratches were visible on the matrix (i.e. steel) of the material and above 600°C, an oxide layer covered the simulated roll surface. The nature or source of the abrasive particle was not determined but the hardness was less than that of the carbides. Kato *et al.* [15] went on to determine that abrasion is the dominant wear mechanism in work rolls; furthermore they conclude that thermal fatigue is the one of the main surface roughening mechanisms. This is a similar conclusion to one drawn by Mercado [16] for high carbon, high chromium steel. The test, developed at the University of Sheffield, was designed to induce thermal fatigue in tool steel discs. When high speed steel was tested, the test technique did not result in any appreciable surface degradation; however, when high carbon, high chromium discs were tested thermal crack morphologies and surface defects comparable to those observed industrially were achieved. Furthermore, the test resulted in a smoothening of the surface for high speed steel discs while high carbon, high chromium steel maintained a relatively constant roughness with a sharp increase in roughness near the end of the test. It is possible that the thin black oxide observed on the high speed steel discs was responsible for the smoothening response. Thermal cracking in the high carbon, high chromium steel was observed in the early stages of the test, which propagated perpendicularly to the rolling direction. The implication of which is that the principal stress at the surface acts along the circumferential direction of the test disc. Furthermore, crack coalescence was repeatedly observed but fire cracking was not observed. Several limitations of this technique have been identified, most importantly the absence of strip surface expansion under the roll bite, no bi-directional slippage and limited contact pressure achievable at high temperature. These results quantitatively correlate with a study conducted by Beverly *et al.* [17] involving on line observation of work rolls via CCD cameras it was concluded that the formation of an oxide layer on the roll surface has a lubricating effect, while the change of appearance of the oxide layer (i.e. fire cracking, etc.) does not influence the coefficient of friction. However, an increase in the coefficient of friction was observed with the breakdown of the oxide roll surface with a maximum friction coefficient reached with the appearance of banding.

Quinn [18] related the theoretical wear rate to the real area of contact, sometimes referred to as the Archard wear law, given by:

$$W_{r\_th} = K \cdot A_r = K \cdot \frac{F_N}{P_P} \tag{3.3}$$

where W_{r_th} is the theoretical wear rate, K is the probability of producing a wear particle at each micro-contact [19], A_r is the real area of contact, F_N is the normal applied load and P_P is the hardness of the softest surface. Wear rates are typically measured in units of volume of material removed per unit sliding distance. However, Quinn [18] found that the general oxidation theory provided a better description of the pin-on-disc experiments using high-chromium ferritic steel pins and austenitic stainless steel disks. The general oxidation theory is expressed as [18]:

$$W_{r\_th} = \sum_{i=1}^{n} W_{r\_th_i} \tag{3.4}$$

where n is the number of wear mechanisms (typically n=3). Quinn [18] evaluated this relationship in a purely empirical manner and found the activation energies for mild and severe wear were very low compared to the activation energy of static oxidation of iron.

From this it can be postulated that the oxide growth rate of the high-chromium ferritic pins was not sufficient to counteract the wear rates. It is important to note that the relative hardness of the two materials in question is close.

Rainforth [20] examined the work hardening behaviour at worn surfaces using a tri-pin-on-disc apparatus. Among others, the materials investigated included: single phase fcc metals, multi-component systems (i.e. tool steel with added TiC) and oxide ceramics. The worn pins and wear tracks examined for mechanical (i.e. hardness) and microstructural features (i.e. grain size). When considering work rolls, the most important findings are:

- An exponential relationship between strain and depth below the worn surface was almost universally observed.
- The wear rate increased linearly with the depth of deformation for H21 tool steel (with TiC additions) and 316L stainless steels despite changes in wear mechanisms and material microstructures.
- Calculated flow stresses at the worn surface based on sub-grain size tends to show linear hardening, while microhardness measurements as a function of depth suggest that a saturation flow stress is achieved at the surface.
- Iron-based oxides tend to become intimately incorporated into the surface of the worn ferrous-based metals. The resulting mechanically mixed structure may have improved mechanical properties compared to the single phase material, which may result in reduced wear.
- Oxides formed by wear have ultra-fine grain sizes and no crystallographic texture.
- Tribochemical wear of a high purity alumina, tested against zirconia resulted in a thin amorphous layer containing both alumina and zirconia.

From this work some of the implications for work roll modelling are: the stress-strain behaviour of the asperities needs to be reconsidered, especially with regard to the flow stress, and mechanical mixing appears to potentially be important but the time available may not be sufficient for mixing to take place in the roll bite.

3.2.3. Friction and Torque

As noted by Duan and Sheppard [21] perhaps the most important feature when designing the pass schedule is the calculation of the energy requirement. Power and rolling torque are related through the work roll speed, or angular velocity, in the following way:

$$P = \omega_r \cdot M_T \qquad (3.5)$$

where P is the power (in Watts), ω_r is the radial velocity (in rad s^{-1}) and M_T is the torque (in Nm). The specific roll torque, defined as the torque per unit width, may be calculated using the approach taken by Sims [22] given as:

$$M'_T = 2R_r R'_r \tau_y \left(\frac{\alpha_n}{2} - \varphi \right) \qquad (3.6)$$

where M'_T is the specific roll torque (in Nm m^{-1}), R_r is the work roll radius (in m), R'_r is the deformed roll radius, $2\tau_y$ is the yield stress of the strip in plane strain compression (in N m^{-2}), α_n is the contact angle at the plane of entry (in radians) and φ is the neutral plane angle (in radians). Some of these parameters are shown schematically in Figure 3.5.

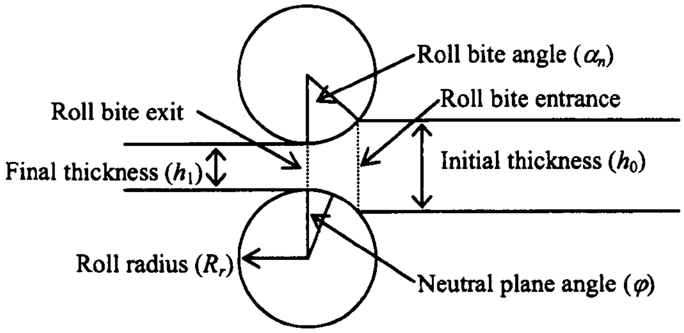

Figure 3.5 – Schematic showing selected rolling parameters.

The torque is related to the friction coefficient in terms of the neutral plane as the neutral plane angle is determined by the coefficient of friction in the absence of other parameters, such as strip tensions. The deformed roll radius may be calculated using the method devised by Hitchcock [23], given as:

$$R'_r = R_r \left(1 + \frac{cF'_R}{b \cdot \Delta h} \right) \qquad (3.7)$$

where R_r is the undeformed roll radius (in m), c is a constant (equal to 2.16×10^{-11} m^2 N^{-1} for steel rolls), F'_R is the specific roll force (in N m^{-1}), b is the width of the strip and Δh is the difference between the entry thickness and the exit thickness or draught (in m). The specific roll force may be obtained analytically from the following equation [24]:

$$F_R' = \frac{2}{\sqrt{3}}\bar{\sigma}_0\left[\frac{1}{Q}\left(e^Q - 1\right)b\sqrt{R_r \cdot \Delta h}\right] \tag{3.8}$$

where $\bar{\sigma}_0$ is the mean yield stress (in MPa) and:

$$Q = \frac{\mu \cdot L_p}{\bar{h}} \tag{3.9}$$

where μ is the friction coefficient, $\bar{h}$ is the mean thickness between entry and exit from the rolls and L_p is the contact length, given as:

$$L_p \approx \sqrt{R_r \cdot \Delta h} \tag{3.10}$$

In practice the roll force and deformed roll radius need to be iteratively calculated until the desired accuracy is obtained.

In a study to calculate the roll torque during edge rolling Lundberg [25] found that torque on each edge roll may be expressed as a function of friction in the following form:

$$M_T = 2\tau_y R_r^2\left\{\left(1-\cos\alpha_n\right)\left[h_0\left(m+1\right)-\frac{1}{2}R_r\cos\alpha_n\right]+\frac{1}{8}R_r\left(1-\cos 2\alpha_n\right)\right\} \tag{3.11}$$

where M_T is the torque (in Nm), τ_y is the shear yield stress (in N m^{-2}), α_n is the roll bite angle (in radians), h_0 is the strip initial thickness and m is the friction factor ($0<m<1$). The analysis assumes plane strain, i.e. all the deformation takes place in the draught-spread plane; thus the form of the equation may be applied to strip rolling when the reduction per pass is small.

Most studies in which the variation of torque is considered involve lubricated laboratory rolling experiments of both steel and aluminium [3,26-33], although the majority of these publications are from Lenard and colleagues, showing that the measured torque is affected by temperature, reduction and rolling speed. Not surprisingly the rolling parameter that most influences torque is the reduction while temperature and roll speed play a less significant roll. As this study is concerned with un-lubricated rolling it is only of passing interest that the choice of lubricant can strongly influence torque. In a lead analogue study, Sims [22] found that the specific torque increased with increased reduction and increased initial thickness. Also, the measured torque results compared reasonably well with predictions using equation 3.6.

With respect to calculating torque in finite element (FE) modelling, Duan and Sheppard [21] studied aluminium slab rolling and found that the ratio of initial slab thickness, *H*, to characteristic element size, *a*, will affect the calculated torque and a ratio of *H*/*a* greater than 4 was found to not improve the computing precision of the torque. An important consideration has been pointed out by Duan and Sheppard that when comparing FE torque calculations to measured torque the bearing torques must also be considered. While recognising that bearing torques will be mill specific, the industrial bearing torque reported was of the order of 0.08 MNm; thus is could be expected that other industrial mills would have bearing torques of that order of magnitude.

3.3. Determining Friction during Rolling

Historically the approach to determining the coefficient of friction can be categorized into either indirect or direct methods. Indirect methods are typically mathematical relationships based on the roll bite geometry of the industrial roll mill. Direct methods involve directly measuring parameters that are known to be affected by friction as a result of physical contact of materials, either during deformation or the normal load during sliding contact.

3.3.1. Indirect Friction Determination

Indirect methods of determining friction include the forced skidding, maximum draught and forward slip. Pavlov and Kuprin [34] proposed the method of forced skidding, whereby increasing entry tension is applied the roll slips and the neutral point is at the exit plane. The coefficient of friction is then calculated by:

$$\mu = \frac{\sigma_1 + 2P_R \tan\left(\frac{\alpha_n}{2}\right)}{2P_R - \sigma_1 \tan\left(\frac{\alpha_n}{2}\right)} \qquad (3.12)$$

where μ is the coefficient of friction, σ_1 is the applied tensile stress, P_R is the roll pressure and α_n is the roll bite angle. The maximum draught method is similar whereby the reduction is increased until the roll slips, when this happens the coefficient of friction is determined by:

$$\mu = \tan \alpha_n \tag{3.13}$$

Another is the amount of forward slip that takes place since the exit velocity of the strip is usually higher than that of the work roll thus forward slip, S_f, is defined as the difference between the two, hence:

$$S_f = \frac{V_2 - V_r}{V_r} \tag{3.14}$$

where V_2 is the exit velocity and V_r is the roll velocity. In practice the forward slip can be determined by either measuring the difference in exit strip velocity (via loopers) and work roll velocity or comparing the length of two marks before and after the roll stand, shown here:

$$S_f = \frac{l_2 - l_r}{l_r} \tag{3.15}$$

where l_2 is the post-roll stand distance and l_r is the pre-roll stand distance. The forward slip can then be related to the friction coefficient, as has been done by Wusatowski [35] and also by Li and Sellars [36]:

$$\mu = \frac{\frac{\Delta h}{R'_r}}{2\sqrt{\frac{\Delta h}{R'_r}} - 4\sqrt{\frac{2 \cdot S_f h_1}{2 \cdot R'_r - h_1}}} \tag{3.16}$$

$$\mu = \frac{\frac{\Delta h}{R'_r}}{2\sqrt{\frac{\Delta h}{R'_r}} - 4\sqrt{(1 - S_b)\frac{w_0}{\overline{w}_1}\frac{h_0}{R'_r}\cos\alpha - \frac{h_1}{R'_r}}} \tag{3.17}$$

where Δh is the reduction, h_0 is the entry thickness, h_1 is exit thickness, R' is the deformed work roll radius, S_f is the forward slip, S_b is the backward slip, w_0 is initial strip width, $\overline{w}_1$ is the average strip width after rolling and α_n is the roll bite angle. From these equations it can be seen that decreasing the coefficient of friction, reducing the work roll diameter, increasing the entry tension or decreasing the exit tension will reduce the amount of forward slip.

A method to infer the coefficient of friction, given by Hill [37], is to increase the forward strip tension such that the neutral point is located at the roll bite entrance. The coefficient of friction may then be calculated by:

$$\mu = \left[1 + \left(1 - \frac{R_r}{R'_r}\right)\left(\frac{R_r F_R \alpha_n}{2M_T} - 1\right)\right]\left(\frac{M'_T}{F'_R R_r}\right) \tag{3.18}$$

where R is the roll radius (in m), R' is the deformed roll radius (in m), F_R is the roll force (in N), α_n is the roll bite angle (in radians), M_T is the roll torque (in Nm), M'_T is the specific roll torque (in Nm m^{-1}) and F'_R is the specific roll force (in N m^{-1}).

Another approach that is often used by industry for tuning rolling models is a reverse procedure. By knowing the rolling loads and torque a mathematical model can be used to calculate a mean coefficient of friction or friction factor. The error limits are then determined by the accuracy of the material model and theoretical assumptions. An example of this is the CRM metallurgical model [17]. Often with this approach, the degree of accuracy is acceptable for design purposes but is unreliable as a research tool.

3.3.2. Direct Friction Determination

Due to the nature of rolling, the most suitable type of testing techniques should involve compression and high temperature contact. Direct methods may involve either probes or transducers embedded in the work roll to record the forces involved in rolling, used extensively by researchers such as Lenard [26,27,38] for cold rolling of steel/aluminium or hot rolling of aluminium. The embedded pin technique should not be applied to the hot rolling of steel due to the issue of scale compacting into any clearance areas [39]. Other direct techniques are off line methods involving cool, elastic tooling and hot, plastically deforming material or friction testing devices measuring the friction coefficient as a result of two contacting surfaces, such as ring compression testing and friction testing devices (i.e. reciprocating or pin-on-disc type).

3.3.2.1. Ring Compression Testing

Since the majority of metal forming processes involve compression there have been a number of compression tests developed to elucidate metal behaviour in compression. From these tests it has been found that inhomogeneous deformation is a common feature of industrial processes that is not necessarily present in the more controlled laboratory testing.

One of the tests proven to study the friction conditions in hot metal forming is the ring compression test [1]. The test was initially developed by Kunogi [40] and further developed by Male and Cockcroft [41]. The principles of the ring compression test are well understood. For given conditions of temperature, strain rate, strain and initial specimen geometry according to the ratio of outer diameter to inner diameter to height (OD:ID:H) the deformation of the inner diameter of the specimen may be calculated as a unique function of the interfacial friction coefficient. Determining the friction coefficient is done by comparing the reduction in height and the change in the inner diameter to the calibration chart for the initial ring geometry. The calibration charts are the results of mathematical analysis, examples are shown in Figure 3.6.

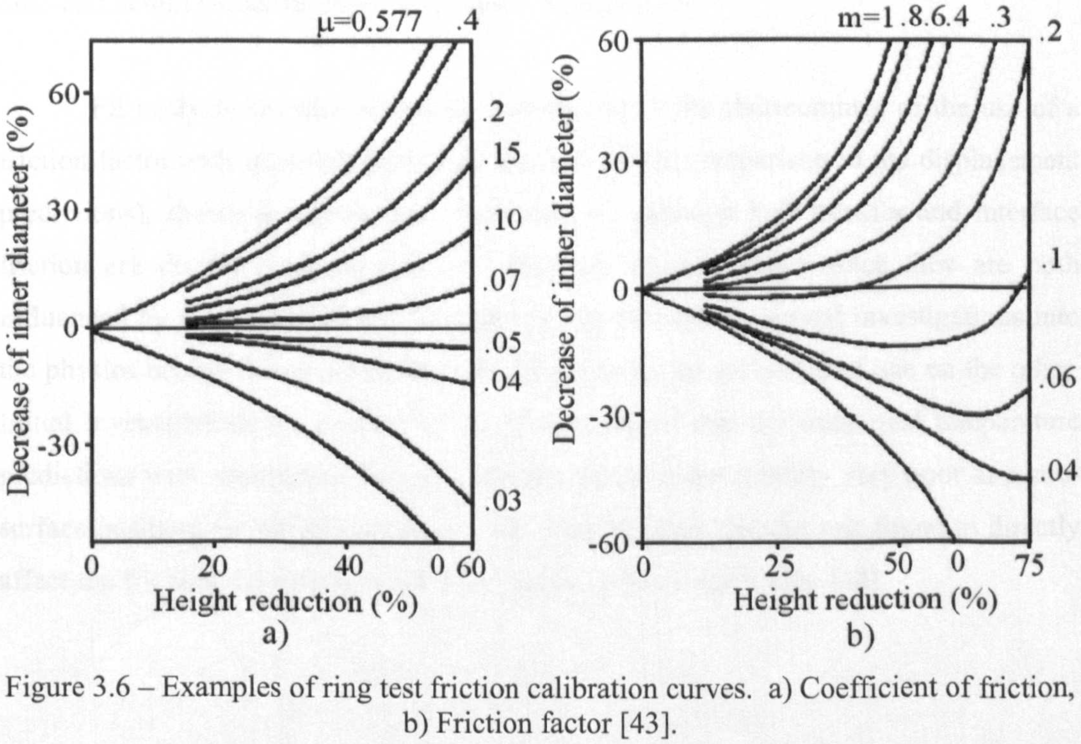

a) b)

Figure 3.6 – Examples of ring test friction calibration curves. a) Coefficient of friction, b) Friction factor [43].

Most researchers use the upper bound method and assume the existence of either a parallel velocity field or that the cylindrical surfaces barrels outwards. However, at lower values of the friction factor accounting for barrelling does not lead to significantly different values for *m* then the simple, parallel velocity field, in which the ring is assumed to retain its cylindrical shape [42]. The transition between barrelling and non-barrelling was predicted to take place between friction factors of approximately 0.45 and 0.6. The actual ring test is relatively simple, which requires a ring to be compressed between two platens. As the ring height is reduced the ring will expand in the radial direction. If the friction at the interface is zero, both the inner and outer diameters expand as if it were a solid disk. With increasing friction the inner diameter becomes smaller.

It has been found in the literature that the friction conditions are strongly affected by a large number of parameters. Conflicting experiment results regarding the influence of temperature, strain rate and lubrication have been reported [1,42,44], indicating that direct comparison of results is very difficult because of the large number of variables. The application of finite element analysis to the calibration curves has been able to improve the friction factor predictions with regards to the inner diameter ratio and height reduction [1,44-47], shown in Figure 3.7.

FE analysis has also served to identify one of the shortcomings of the use of a friction factor with relatively poor load predictions (in comparison to the displacement predictions), shown in Figure 3.8. Furthermore, although heat transfer and interface friction are disparate phenomena [48] they are closely linked since they are both influenced by the same factors. FE analysis has allowed numerical investigations into the physics behind the phenomena to shed light on to the influence of one on the other. Initial investigations by Fletcher *et al.* [44] indicated that the numerical temperature predictions were reasonable for the centreline position but initially very poor at a sub-surface position, shown in Figure 3.9. The variable heat transfer was found to directly affect the friction, deformation loads and surface plastic strain state [44].

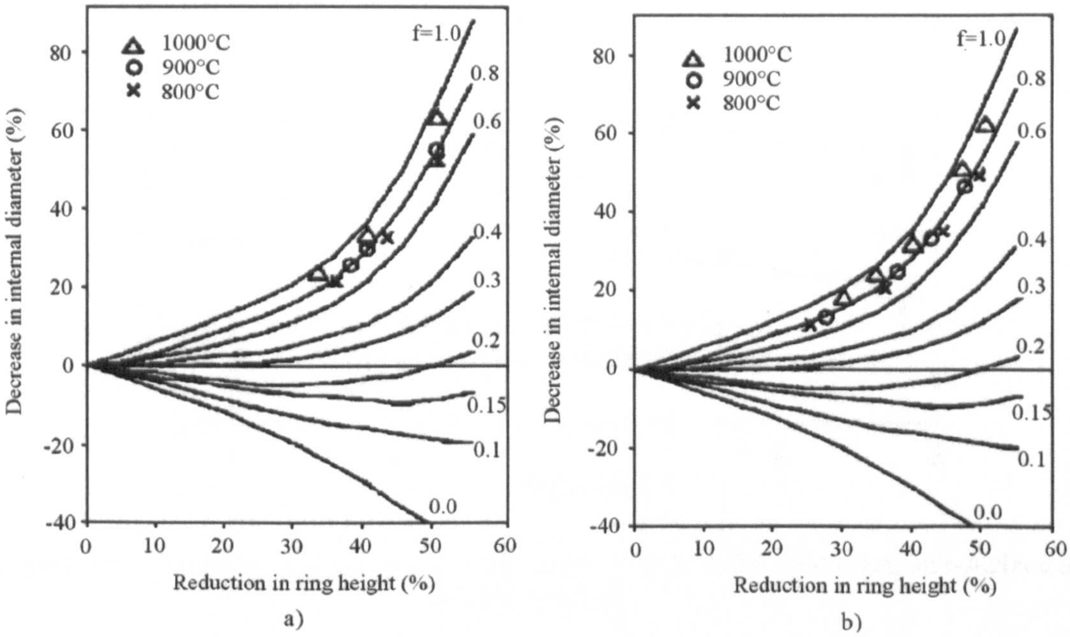

Figure 3.7 – Ring compression testing calibration curves for lead-free cutting steel. The lines are calculated friction factors and the points represent experimental data in a) and FE predictions in b) [1].

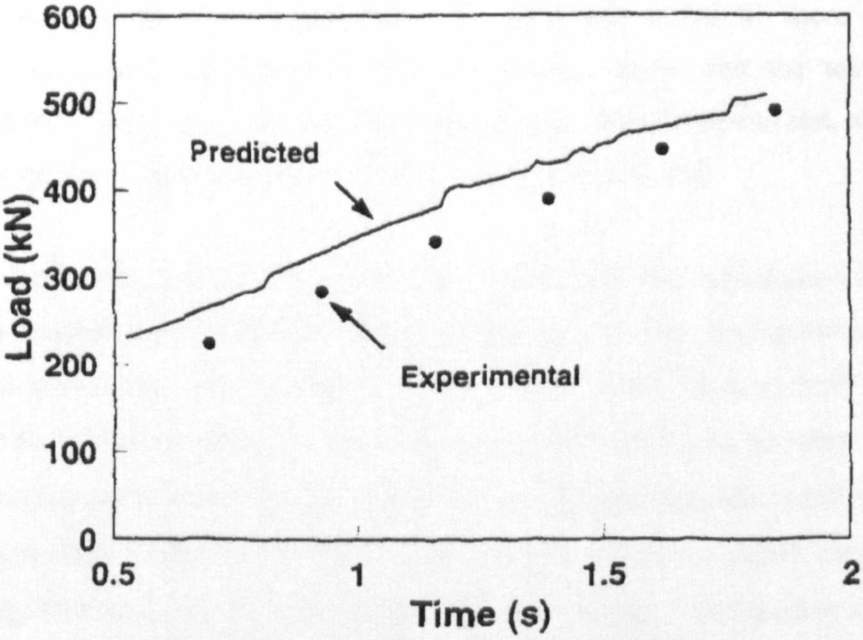

Figure 3.8 – FEM predicted and measured forging load for a total reduction of 31% and an initial scale thickness of 200 μm [44].

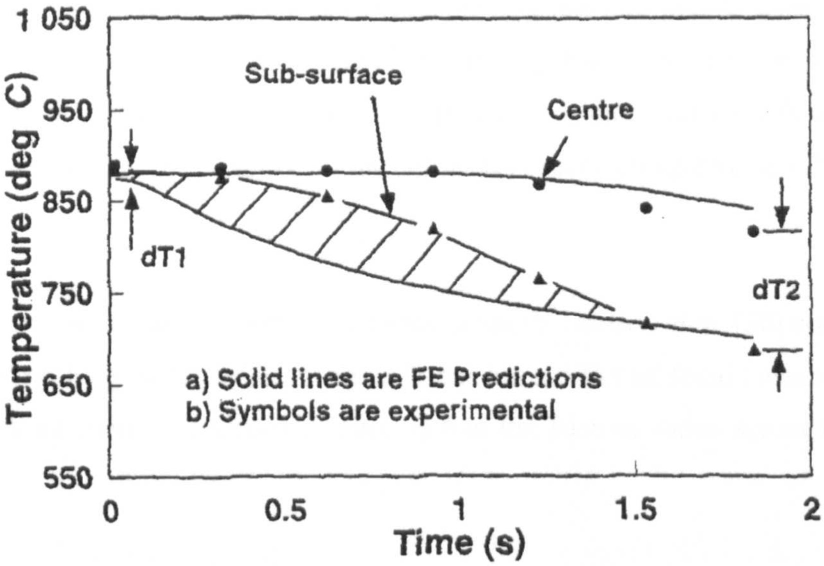

Figure 3.9 – Predicted and measured temperature change at the centre and sub-surface at mid-radius [44].

Szyndler *et al.* [47] applied an inverse analysis technique in an attempt to determine the friction factor and deformation properties of a material from one type of test, namely ring compression. Using an objective function the friction factor was fitted to a linear equation. Unfortunately, the data that was reported shows that a logarithmic function incorporating both temperature and strain rate would be more suitable. However, as a first approximation both the friction factor and the temperature dependent strain hardening curve were determined using a single type of test, albeit that numerous tests at various temperatures and strain rates are required.

Cold forming studies of aluminium by Hu and Dean [49] investigated the effect of surface roughness on the coefficient of friction using cold ring compression tests with a constant strain rate. The roughness of the samples varied between 0.167 μm and 5.212 μm *Ra*. Of primary interest is the experiment determining the lubricant retention by the various surfaces, which found that the polished surface (*Ra*=0.167 μm) had significantly better lubricant retention than the other samples (1.996 μm< *Ra* < 5.212 μm). Not surprisingly it was found that friction increased with surface roughness with the exception of the turned surface (*Ra*=2.189 μm). This may indicate that there is a directionality associated with the specimen (radially since no ovality was reported). While this study was not extended with regard to either elevated temperatures or to different materials, it does serve to show that the ring test results will be influenced by the roughness of the contacting surfaces. If this experiment were to be repeated for steel, it is possible that the lubrication retention effect is either reduced with temperature and surface material (i.e. oxides) or becomes secondary compared to other surface interactions.

Examining upset cylinders at room temperature, Devaux *et al.* [50] conclude that in localized necking under dry friction conditions has a different failure mechanism than that of sticking friction conditions, implying that the friction varies across the contact interface.

3.3.2.2. Friction Testing Devices

There are a large number of friction testing devices that are based on rubbing against a rotating disk [15,51-54]. There are also reciprocating devices available to investigate stick-slip [55]. These devices have primarily been employed to investigate either lubrication or surface deterioration (i.e. wear). Since predominantly stick-slip conditions apply in rolling a reciprocating device may more closely represent rolling conditions.

According to Plint and Plint [55] investigations of stick-slip at low velocities result in the generation of a series of random stick-slip episodes with the possibility of interaction between successive cycles. Essentially the 'stick' period is uncontrolled. In a perfectly stiff high frequency reciprocating device the velocity of the reciprocating head would be a sinusoidal curve. Since this is not possible there is some lag due to the elastic effects at the end of the stroke. The resulting stroke is demonstrated in Figure 3.10. Fortunately it is relative simple to calculate the overall stiffness of the device in the following manner:

$$\Delta l = A_p \cdot \left(1 - \cos\frac{2\pi t_s}{T_c}\right) \tag{3.19}$$

where T_c is the period for one cycle, t_s is the interval between the stroke end and when slip occurs (i.e. point 'a'), A_p is the amplitude and Δl is the travel of the driving head at point 'a' in Figure 3.10. If the corresponding change in friction force at point 'a' is ΔF_f,

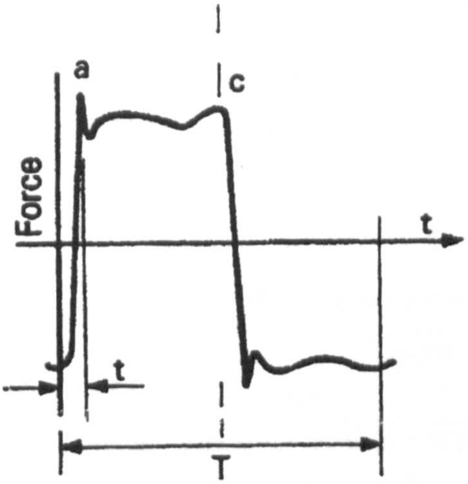

Figure 3.10 – Variation of friction force in a reciprocating contact with elasticity and stick-slip [55].

the stiffness of the system, E', is calculated by:

$$E' = \frac{\Delta F_f}{\Delta l} \tag{3.20}$$

At mid-stroke the sliding velocity, V_m, can be calculated by:

$$V_m = \frac{2\pi A_p}{T_c} \tag{3.21}$$

However, the variation of the friction coefficient is affected by the stiffness of the testing machine. The more compliant the testing machine, the more likely that relatively small frictional perturbations will be amplified by the machine and they will persist long enough to be detected by the load cells [53]. Observations by Chiou *et al.* [56] showed that it was possible to dramatically change the severity of the wear by altering the stiffness of the testing system. Furthermore, Blau [53] compared three similar devices: a friction microprobe, a laboratory-scale pin-on-flat machine and a heavy-duty Cameron-Plint TE-77 machine. He found that the different machines gave qualitative agreement as a result of the variation in machine stiffness. Thus the nominal friction coefficient consists of both a materials and system variable.

As friction coefficients from both reciprocating and pin-on-disk type friction devices are often quoted without consideration as to the source of the data it is necessary to examine the potential variation that may exist as a result of the chosen test. The UK National Physical Laboratory conducted studies designed to determine the reproducibility of friction results [57,58]. The friction and wear of 95% alumina ceramic were studied in two conditions: a) both pin and disc surfaces ground, and b) both pin and disc surfaces polished. Unfortunately only 1 of the 11 laboratories involved used a reciprocating friction device but the overall results for the study are given in Table 3.1.

Table 3.1 – Comparison of tribological results for different test configurations [58].

	Pin-on-disc	Tri-pin	Reciprocating
	Ground specimens		
Coefficient of friction	0.65 ± 0.12	0.85 ± 0.14	0.60 ± 0.01
Number of data	40	5	2
Pin scar diameter (mm)	1.38 ± 0.19	2.29 ± 0.35	1.90 ± 0.05
Number of data	42	5	2
Disc wear track width (mm)	1.27 ± 0.16	1.18 ± 0.08	1.78 ± 0.06
Number of data	25	5	2
Total linear wear (μm)	40 ± 13	81 ± 57	
Number of data	25	5	
	Polished specimens		
Coefficient of friction	0.75 ± 0.13	0.64 ± 0.10	0.61 ± 0.07
Number of data	35	5	4
Pin scar diameter (mm)	1.07 ± 0.18	1.35 ± 0.19	1.88 ± 0.42
Number of data	38	5	4
Disc wear track diameter (mm)	0.96 ± 0.17	1.35 ± 0.19	1.88 ± 0.42
Number of data	33	5	4
Total linear wear (μm)	21 ± 10	11 ± 11	
Number of data	21	5	

Referring only to the friction coefficient data, the reciprocating friction device used in this study was consistently lower than the pin-on-disc devices (both single and tri-pin configurations); however, the actual values are generally within the plus minus range. With regards to the consistency of the results, the reciprocating device was more consistent but given the relatively few number of tests conducted on the reciprocating device no conclusions should be drawn regarding the relative consistency as compared with the other devices. The reciprocating device appeared to be less sensitive to the initial surface conditions of the samples, i.e. ground versus polished, than the pin-on-disc devices. This may be due to the repetitive nature of the reciprocating test as the same patch of sample is in repeated contact over a short time scale, thus reaching an equilibrium condition earlier; it is noteworthy that the device description for the pin-on-disc devices did not indicate the frequency of contact between the pin and any given area of the disc. The humidity for the test was specified at 50% R.H. but this was not possible at the majority of the testing laboratories, which will have a considerable affect on the scatter of the data. Tanaka *et al.* [59] have shown that humidity will affect the measured friction coefficient with the effect of increasing the coefficient of friction with increasing relative humidity.

Hwang *et al.* [60] examined the friction coefficients of tribological pairings based on the compatibility parameters proposed by Rabinowicz [61] and found that the reciprocating device typically measured a lower friction coefficient than the pin-on-disc machine. However, substantial scatter in the data was reported and the reciprocating device results were within the scatter of the pin-on-disc device. In a study limited only to pin-on-disc devices using tool steel pins and Cr-Mo-Ni steel discs, Almond and Gee [62] found that for the results of five tests the variation of any given machine was relatively small varied widely between machines. It has been suggested that the variation between machines could be the result of different damping capacities and machine stiffnesses in addition to different thermal cycling experienced by the samples as a result of the differences in the cooling capacities of the various specimen holders. The end result of this comparison is that the testing conditions should be considered, including a friction device's past history, when friction coefficient values are taken from the literature.

3.4. Material Considerations

In the hot rolling of steel there are essentially four materials that must be considered in the roll gap, excluding any lubrication that may be used; these are: the steel strip, the strip oxide, the work roll steel and the work roll oxide. The materials that are actually interacting are the oxides but these are dependent upon the host materials. How the different oxides grow will affect the friction conditions in the roll gap. Essentially the strip oxide will stay the same throughout the initial stages of the finishing rolling since there is a prescribed time between secondary descaling, where the steel is considered to be nominally free of scale, to the entrance of the first rolling stand.

It is this period where the majority of the scale involved in hot rolling is developed, although the scale layer is modified in the process of rolling. This amount of time is relatively independent of process upsets, which results in a relatively constant strip thickness entering the first stand. The work rolls experience a much more complicated life cycle resulting in an evolving oxide layer over the course of a rolling campaign.

3.4.1. Physical Description of Iron Oxides

During the hot rolling of low carbon steels there are three principal oxides present: wüstite, magnetite and hæmatite. Wüstite has the chemical formula Fe_xO and is a non-protective, rapidly growing oxide that is stable above 570°C. Wüstite is the thickest oxide layer formed during production, and has a typical scale thickness of 10 μm [63]. The high ratio of wüstite to magnetite and hæmatite has been attributed to the greater mobility of defects in wüstite [63]. Wüstite can exhibit marked departures from stoichiometry, typically $Fe_{0.95}O$ but the ratio has been found to be temperature dependent and values as low as $Fe_{0.84}O$ have been reported [64,65]. The high proportion of cation vacancies leads to the rapid cation transport responsible for its growth behaviour, even though a proportion of these vacancies exist as vacancy clusters with no significant contribution to diffusion/oxidation. A description of oxide growth mechanisms is given in §3.4.2. Room temperature hardness has been reported to be 460 HV and 105 HV at 900°C [63]; however, the hardness of wüstite prepared by powder metallurgical methods has been measured as approximately 20 HV at 800°C [66]. The density and heat capacity of wüstite have been reported to be 7750 kg m^{-3} [63,67] and 725 J kg^{-1} K^{-1} respectively [67]. There is some disagreement in the literature regarding the density, which has also been reported to be 5250 kg m^{-3} [68], perhaps as a result of wüstite's ability to exist in both bcc and fcc crystal structures [69]. Furthermore, wüstite can exist in three different subphases identified as W1, W2 and W3 [70]. The W1 subphase is the most plastic and exists closest to the metal surface. W2 and W3 are less plastic and have less frequent but much larger structural defects. The oxygen to iron ratio increases from W1 to W3 at any given temperature, although beyond approximately 1180°C W1 is the only stable sub-phase [70].

The next oxide to be considered is magnetite with the chemical formula Fe_3O_4. Magnetite is moderately protective and generally exhibits growth by cation vacancy transport (p-type) but can show some cation interstitial transport and intrinsic semi-conductor behaviour [64]. Below 700°C it grows predominantly by cation transport along oxide grain boundaries [64]. Room temperature hardness has been reported to be 540 HV and 366 HV at 900°C [63]. The density and heat capacity of magnetite have been reported to be 5000 kg m^{-3} and 870 J $kg^{-1}K^{-1}$ respectively [67]. Again, there is some disagreement with the reported density but the differences are relatively small.

The third oxide of iron is hæmatite with the chemical formula of Fe_2O_3. Hæmatite is reasonably protective with similar diffusivities of iron and oxygen. No general agreement exists as to whether its dominant growth mode is by cation or anion transport [64,65]. Room temperature hardness has been reported to be 1050 HV and 516 HV at 900°C [63]. The density and heat capacity of hæmatite have been reported to be 4900 kg m^{-3} and 980 J $kg^{-1}K^{-1}$ respectively [67].

The structure of the scale layer is also of interest since the classical three-layer system is not always present. The classical three-layer system consists of wüstite, magnetite and hæmatite going from the steel surface to air, shown in Figure 3.11, as a result of the increasing oxygen content. One of the reasons for the deviation from the three-layer system is the presence of cracks or porosity. Cracks provide a path for oxygen to short-circuit the diffusion process while pores can obstruct the outwards diffusion of iron ions. The formation of pores is a common feature of oxide scales on mild steels and medium-purity iron although high-purity iron has been found to have thick, pore-free scales [71]. These pores are most often found in the wüstite layer close to or at the scale-metal interface. The Fe-O phase diagram is given in Figure 3.12.

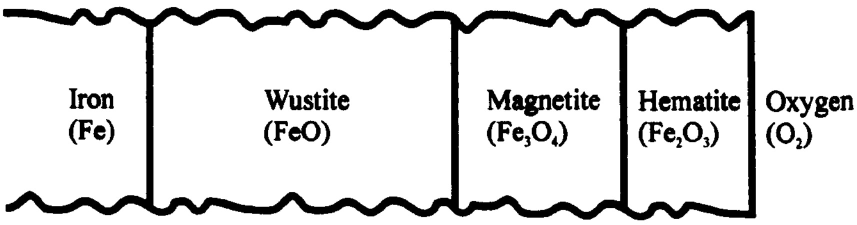

Figure 3.11 – Schematic showing the classical three-layer iron oxide system (Not to scale).

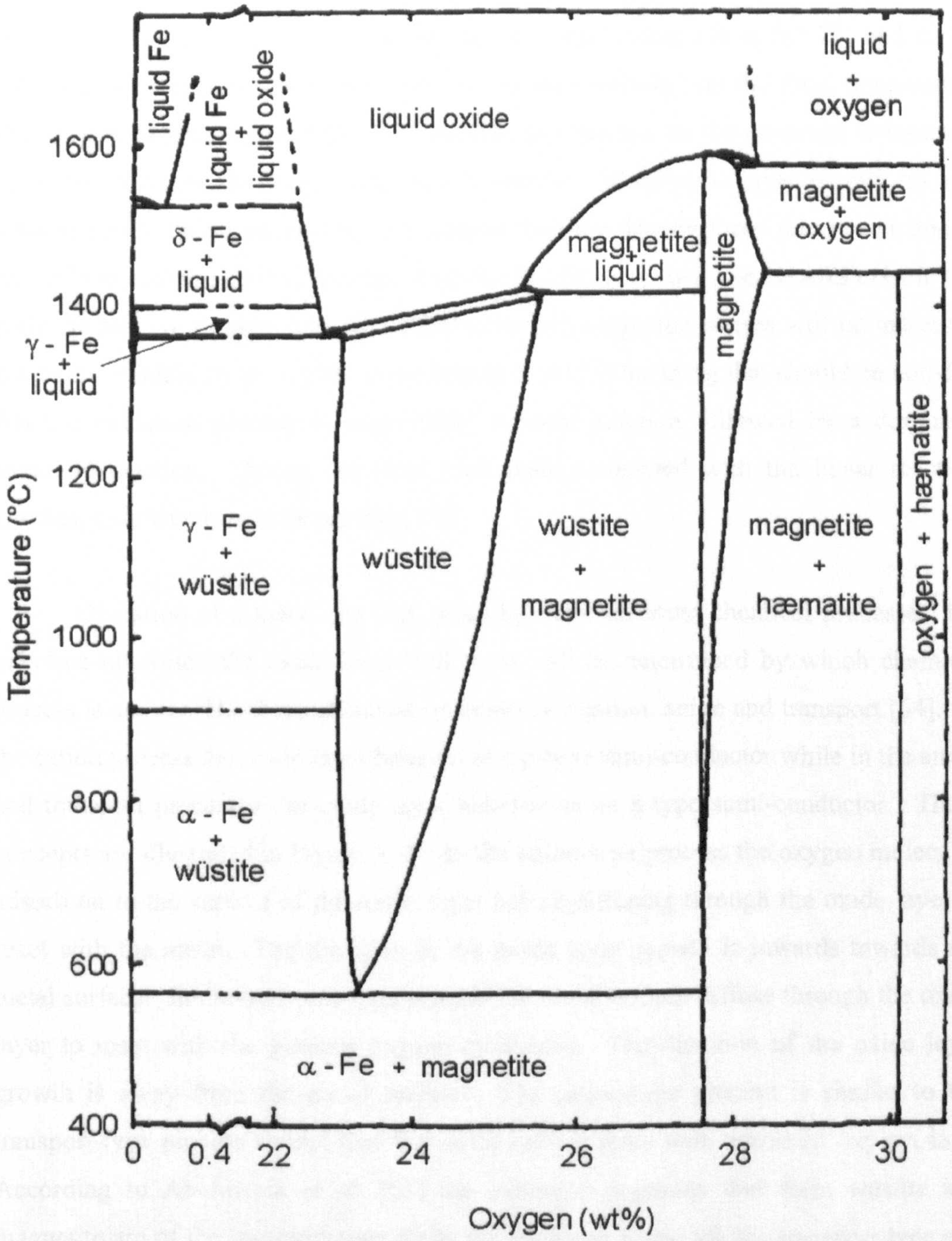

Figure 3.12 – Fe-O phase diagram at 1 atm [74].

3.4.2. Oxidation Process

There is a consensus that the wüstite to magnetite to hæmatite thickness (or volume) ratio is approximately 95:4:1 for scales formed in the 700-1100°C temperature range [63], while at around 560°C the ratio has been reported to be 90:8:2 [67]. It is recognised that this ratio is dependent upon the steel composition [63,72] and oxide growth experiments have obtained different ratios depending on the time, temperature and oxygen partial pressures [65]. A possible explanation for the observed differences could be related to the local chemical equilibrium. If the scale layer is uniform and remains intact during the course of oxidation then the driving force for the reaction is the diffusion of iron cations through the oxide layers. If porosity and cracks exist in the scale the relative growth rates of the hæmatite and magnetite phases will be increased due to the availability of oxygen at random sites [65]. One thing that should be noted is that the oxidation process is sequentially a linear reaction followed by a dominant parabolic reaction. During the short time scale associated with the linear reaction kinetics, only wüstite can be present [73].

Oxidation of a metal can take place by three different chemical processes; the interface on which the oxide layer will grow will be determined by which chemical process is active. The three chemical processes are cation, anion and transport [64]. In the cation process the oxide layer behaves as a p-type semi-conductor while in the anion and transport processes the oxide layer behaves as an n-type semi-conductor. These concepts are illustrated in Figure 3.13. In the anion-type process the oxygen molecules adsorb on to the surface of the oxide layer before diffusing through the oxide layer to react with the metal. The direction of the oxide layer growth is inwards towards the metal surface. In the transport-type process the metal cations diffuse through the oxide layer to react with the gaseous oxygen molecules. The direction of the oxide layer growth is away from the metal surface. The cation-type process is similar to the transport-type process except that the metal cations react with adsorbed oxygen ions. According to Abuluwefa *et al.* [65] the oxidation reactions that form wüstite and magnetite are of the transport-type while the hæmatite forms via the transport-type and the anion-type.

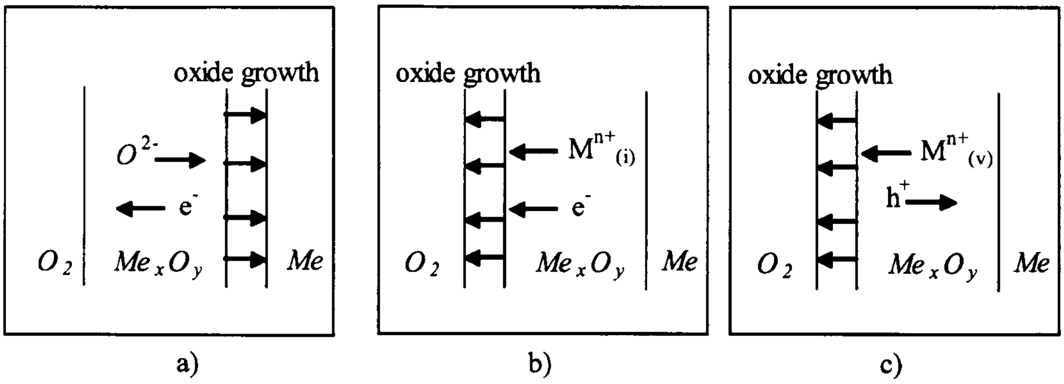

Figure 3.13 – Schematic showing the basic oxidation processes: a) anion, b) cation, c) transport. M^{n+} are the metal cations, O^{2-} are the oxygen anions, e^- are the electrons, h^+ are the electron holes, (i) indicates interstitial diffusion and (v) indicates vacancy diffusion (from [64]).

The diffusion of oxygen in oxides is slower than that of iron; hence growth requires the iron ions to diffuse to the gas-oxide interface. Since there is an abundance of oxygen at the surface the diffusivity of iron ions determines the growth rate [63]. The governing growth mechanism of the scale will be determined by the thickness; therefore the transport and cation mechanisms seen in Figure 3.13 will play a more important role as the scale layer becomes thicker. However, with a porous oxide layer it is just as likely that oxygen molecules can penetrate the scale and react with the iron ions to form new oxides, which results in a parabolic rate of reaction. Examining the distribution of iron and oxygen through the thickness of the oxide layers may provide insight into the oxidation process. The phenomenon of spatial diffusion has been examined by Banks [75], demonstrating general diffusion calculations and more specific conditions that are relevant to the problem of scale formation on steel. The primary difficulty with diffusion calculations is the lack of diffusivity data. Also, there will likely be an increased hindrance to diffusion crossing the oxide layer interface that has not yet been considered in oxide growth analyses.

3.4.3. Oxidation Modelling

Despite the complex nature of oxidation and the delicate balance between diffusion and reaction kinetics, semi-empirical modelling techniques are still sufficiently accurate for industrial purposes on the proviso that test conditions are similar. According to Munther and Lenard [63], the reaction kinetics of iron oxide formation are commonly seen as parabolic with respect to time and exponential with respect to temperature. The parabolic nature of scale formation is shown in Figure 3.14. The Scale Index, γ, used by Munther and Lenard [63] represents the mass of scale that is formed over the exposed surface area.

$$\gamma = \frac{m_{scale}}{A} = \Delta x \cdot \rho_{scale} \qquad (3.22)$$

where m_{scale} is the mass of the scale, A is the area, Δx is the scale thickness and ρ_{scale} is the density.

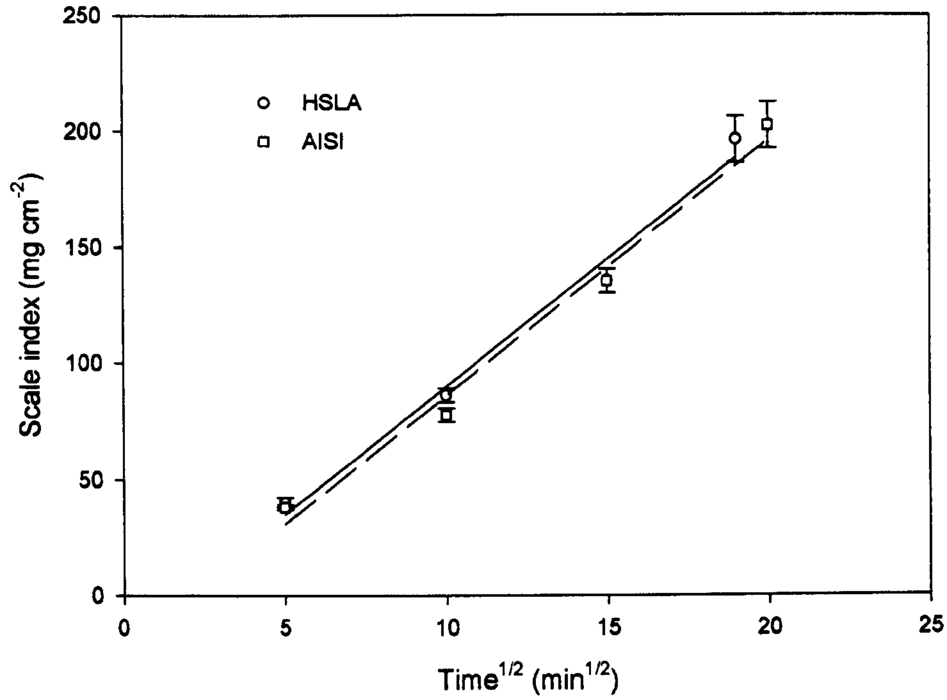

Figure 3.14 – Experimental data for HSLA and plain carbon steel at 1125°C showing the parabolic nature of the oxidation reaction [63].

In general, Schmalzried [76] states that the parabolic rate law is the most important reaction kinetic law for heterogeneous reactions. Furthermore, essentially the same reaction kinetics for solid-gas reactions exist as for diffusion controlled solid-state reactions. The most important assumption is that thermodynamic equilibrium is maintained throughout the entire process, both at the phase boundary between the metal/oxide and the oxide/oxygen interface, as well as locally within the compact, strongly adherent metal oxide product layer. A guideline has been developed regarding the morphology of the oxide layer stating the oxide layer will be porous if its molar volume is less than that of the metal consumed [76]. Unfortunately, there is not a sound basis for this guideline and the true compactness and adherence of the oxide layer can only be determined experimentally.

Schmalzried [76] has considered the general oxidation reaction of a metal, which has been applied to the oxidation of iron to wüstite. Using the assumptions stated above the average gradient in the chemical potential is inversely proportional to the product layer thickness, Δx, at any time. Therefore the instantaneous rate of increase in thickness, $d\Delta x/dt$, is proportional to the inverse of the product layer thickness, $1/\Delta x$. This relationship can be integrated to give the parabolic rate law in the form:

$$\Delta x^2 = 2 \cdot \bar{k} \cdot t \tag{3.23}$$

where Δx is the product layer thickness (in m), $\bar{k}$ is the effective rate constant (in $m^2\ s^{-1}$) and t is time (in s). In terms of the Scale Index used by Munther and Lenard [63] the parabolic reaction is given by:

$$\gamma = k_p \sqrt{t} \tag{3.24}$$

where k_p is the parabolic rate constant. However, for short time periods the linear and parabolic nature of the oxide must be considered. This is most conveniently described in the following equation [71,73,77]:

$$\frac{dm_{scale}}{dt} = \frac{k_p}{m_{scale} + \frac{k_p}{k_l}} \tag{3.25}$$

where m_{scale} is the mass of the scale (in kg) and k_l is the linear rate constant. Thus as the mass approaches zero, i.e. at the very beginning, the linear rate constant dominates while at long times the parabolic rate constant dominates. Since the short time periods are very difficult to measure experimentally they are often ignored and only the parabolic rate constant experimentally determined.

The reaction rate constant can be calculated if the standard Gibbs energy of formation for the oxide layer is known. The effective rate constant can then be calculated using:

$$\bar{k} = \overline{D}_{Fe} \frac{|\Delta G_{FeO}|}{RT} \tag{3.26}$$

where $\overline{D}_{Fe}$ is the effective diffusion coefficient (in m^2 s^{-1}), ΔG_{FeO} is the Gibbs free energy of formation for FeO (in J mol^{-1}), R is the gas constant (in J mol^{-1}K^{-1}) and T is the temperature (in K). The temperature dependence of the Gibbs free energy for the iron oxide reactions is shown in Table 3.2.

Table 3.2 – Temperature dependence of the iron oxide reactions free energy [78]

Reaction	ΔG (kJ mol^{-1})	Temperature range (K)
$Fe+\frac{1}{2}O_2 \rightarrow FeO$	$-274.033+1.291\times10^{-1}\cdot T$ $-7.812\times10^{-3}\cdot T\cdot\ln T$	1184-1600
$3FeO+\frac{1}{2}O_2 \rightarrow Fe_3O_4$	$-311.867+1.229\times10^{-1}\cdot T$	949-1272
$2Fe_3O_4+\frac{1}{2}O_2 \rightarrow 3Fe_2O_3$	$-247.053+1.417\times10^{-1}\cdot T$	967-1373

The average diffusion coefficient can be defined as:

$$\overline{D}_{Fe}=\frac{1}{\mu_{Fe}^{o}-\mu_{Fe}(O_2)}\int_{\mu_{Fe}(O_2)}^{\mu_{Fe}^{o}} D_{Fe}\,d\mu_{Fe} \qquad (3.27)$$

where μ_{Fe}^{o} is the chemical potential of the metal at the metal-oxide interface (in J mol^{-1}), $\mu_{Fe}(O_2)$ is the chemical potential of the metal at the metal oxide-gas interface (in J mol^{-1}). The chemical potential at the metal oxide-gas interface can be calculated by:

$$\mu_{Fe}=\mu_{Fe}^{o}+R\cdot T\cdot\ln\left(\frac{1}{p_{O_2}^{1/2}}\right) \qquad (3.28)$$

This enables the thickness prediction of the oxide layer to be related to both time and partial pressure of oxygen.

Experiments by Munther and Lenard [63] describe the effect of time and temperature on the scale formation using their Scale Index, shown in Figure 3.15. The parallel trend of the experimental data for the different oxidation times indicates that there exists an Arrhenius-type relationship of the form:

$$k_p=k_e\cdot\exp\left(-\frac{Q_e}{RT}\right) \qquad (3.29)$$

where k_e is a constant reaction rate (in kg $m^{-2}s^{-1/2}$) and Q_e is an activation energy (in J mol^{-1}). From Figure 3.15, Munther and Lenard [63] determined the average activation energy for the scale growth in air to be 120 kJ mol^{-1}. Munther and Lenard [63] also reported literature values of 124, 188 and 419 kJ mol^{-1} for wüstite, magnetite and hæmatite respectively. Referring to Figure 3.14, Munther and Lenard [63] determined that the rate constant, k_p, was 1.42 x 10^{-4} kg $m^{-2}s^{-1/2}$ (i.e. 11 mg $cm^{-2}min^{-1/2}$) at 1125°C. Assuming that the relationship in equation 3.29 is correct, k_e can then be solved to give 4.31 kg $m^{-2}s^{-1/2}$ (i.e. 3.34 x 10^5 mg cm^{-2} $min^{-1/2}$). Furthermore Munther and Lenard [63] were able to show that in experiments with purged nitrogen were able to reduce the rate constant from 1.42 x 10^{-4} to 7.36 x 10^{-6} kg $m^{-2}s^{-1/2}$ (i.e. 11 to 0.57 mg $cm^{-2}min^{-1/2}$). Unfortunately the relationship between the reaction rate constant and oxygen partial pressure was not further explored.

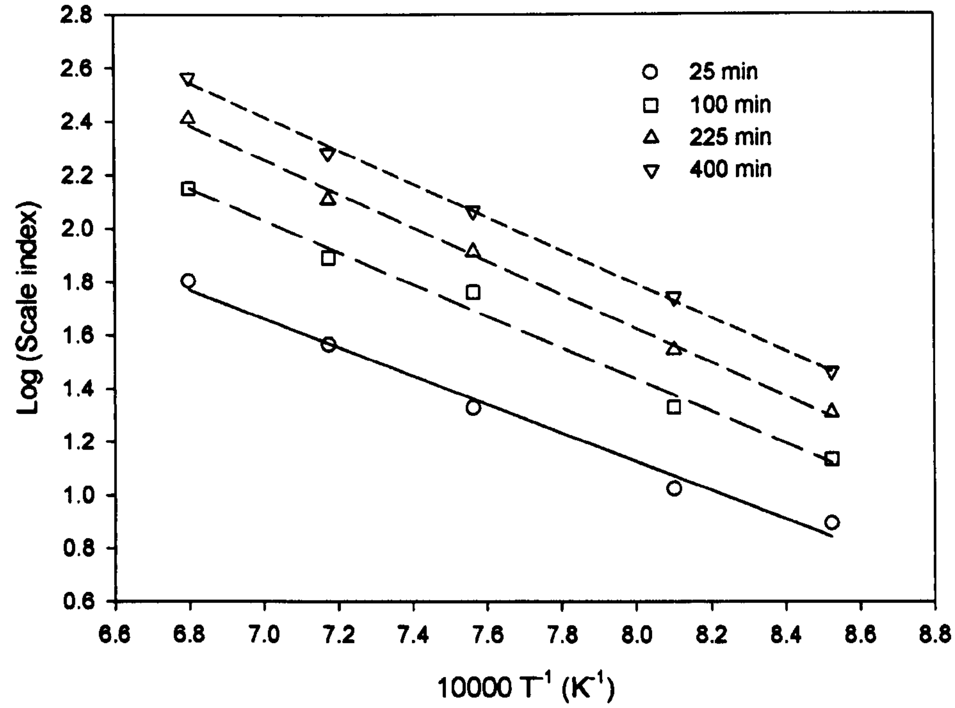

Figure 3.15 – Oxidation reaction of low carbon steel (AISI 1018) in air, using a Scale Index, as a function of time and temperature (from [63]).

3.4.4. Effect of Alloy Additions on the Oxide Layer

The diffusion of iron and oxygen ions through the oxide layers is in part influenced by the chemical composition of the steel. This in turn changes the ratio of the phases and the morphology of the oxide layer. The presence of alloying and tramp elements can have a large effect on the composition and adhesion of the scale layer to the metal surface. The effect of a given element typically falls into one of four categories: gas formation, formation of alternative compounds, surface enrichment and lattice substitution.

Very few elements will react with oxygen from the steel and scale layers to form a gas. The only element to do this on a significant level is carbon [74,77,79]. The main effect of carbon is to make the oxidation rates more erratic as carbon will diffuse to the metal-oxide interface and reacts to form carbon monoxide gas and develop a gap. In high carbon steels at high temperatures, the gas pressure in the gaps may cause cracking through the oxide layer exposing the metal surface to the atmosphere and increasing the oxidation rates. If the scale does not crack then the gap hinders the outward diffusion of iron, decreasing the oxidation rate. However, if there is a sufficient amount of carbon monoxide gas it will facilitate oxygen transport and increase the oxidation rate. The decarburization of the surface caused by the oxidation results in grain growth and a corresponding decrease in hardness. The diffusion of the carbon from the steel subsurface closely follows Fick's second law [80].

Typically the reaction of steel alloying elements at the steel-oxide interface is a spinel-type reaction; examples of this are aluminium, silicon, chromium and molybdenum. The effect of the spinel layer is to retard the diffusion of iron ions to the oxide surface, thus increasing oxidation resistance. The alloying level of the element will affect the behaviour of the scale in different ways. In alloys with aluminium, the aluminium-rich layer will vary in composition depending upon the temperature. From approximately 500-700°C the aluminium-rich layer is probably Al_2O_3 in 1 atmosphere oxygen [74]. In the same atmosphere from 700-900°C the aluminium-rich layer is $FeAl_2O_4$ spinel. In alloys with higher amounts of aluminium another oxidation resistant mechanism is to increase the temperature of the wüstite formation. For example, steel containing 1.8 wt% aluminium was found to increase the wüstite formation temperature to 798°C from approximately 570°C according to the Fe-O phase diagram. Whereas the effect of silicon is somewhat different where dilute iron-silicon alloys are subject to internal oxidation and the slower oxidation rates are probably due to the lower diffusion rate of silicon through the oxide layers and the hindered iron diffusion through the silica layer. In alloys with low silicon additions, the silica formed at the metal-oxide interface (or internally) may react with the FeO to form the spinel fayalite (Fe_2SiO_4). The spinel is less protective than silica and has a lower melting point that limits the upper temperature stability limit of dilute iron-silicon alloys to 1150°C. In dilute iron-chromium alloys there is a strong tendency for the chromium-containing scales to spall off upon cooling [74], while at higher chromium contents the spinel often forms a significant portion of the scale [73]. On stainless steels a protective chrome oxide layer is form. However, the presence of steam has a detrimental effect on the oxidation resistance and scale adhesion of alloys with a chromium level of 1% or greater [81]. In the normal range of molybdenum additions (i.e. below 1%) the oxidation rate is reduced by the spinel reaction and higher levels of molybdenum promote scale adhesion [73]. If the alloys contain less than 0.25 wt% the amount of spinel is not sufficient to form a continuous layer at the interface.

Elements that are more noble than iron tend to be rejected at the oxide-metal interface. Among these elements are: antimony, arsenic, cerium, copper, nickel, niobium, tin, titanium, yttrium and zirconium [79,82,83]. Ultimately, strong accumulation results in the retardation of the iron ion diffusion thereby reducing the oxidation rate. Some of these elements have more of an overall effect than others. For example, tin improves scale adhesion but has a very detrimental effect in the presence of copper since it aggravates the problem of hot shortness [84,85]. The presence of copper is often associated with increased scale adhesion [74,77]. The mechanism by which copper retards oxidation is by copper segregation. However the temperature will strongly influence this effect since the melting point of copper is around 1100°C. Above the melting point segregated liquid copper will penetrate into the metal along the grain boundaries, weakening the surface leading to crack formation during rolling [73]. Nickel ions do not readily diffuse to the metal surface which means the scale advances inward by preferred oxidation along grain boundaries. As a result the metal/scale interface consist of entangled nickel-rich metal and scale causing strong scale adhesion

[74,77]. Also, nickel has a beneficial effect with respect to the problem of hot shortness [86].

Manganese can substitute for iron in the wüstite and magnetite lattices; therefore it was reported to have a very slight effect alone on the oxidation of steel [73,74,77]. However, experimental data shows that mild steel (0.065 wt% C, <0.01 wt% Si and 0.29 wt% Mn) oxidised slower than relatively pure iron (0.006 wt% C) in air at 1000°C and 1100°C. The reduced oxidation rate was probably due to either the manganese content or the difference in carbon content. However, manganese together with silicon can combine with iron oxide to form pools and extended stringers of iron-manganese-silicate in the scale layer. This can accelerate the scaling rate and may contribute to the formation of 'sticky scale' [74]. 'Sticky scale' is a generic term referring to strongly adherent, highly deformable scale that is difficult to remove using conventional hydraulic descalers. Manganese was also reported to promote the formation of spinels on heat-resistant steels.

Boron, magnesium and phosphorus are elements that react to form alternative compounds within the scale. Boron has a higher oxygen affinity than iron and is oxidised at the metal-scale interface to form borate. Borate suppresses the annihilation and adsorption of vacancies from the scale growth mechanism discussed (see §3.4.2) thus enhancing void formation at the interface by vacancy condensation [79]. Magnesium forms wüstite-magnesium oxide solid solutions. Plastic deformation of these solid solutions has been observed above 600°C, although the deformability decreases with increasing magnesium content [66]. Phosphorus is one of the most important alloying elements with respect to scale adhesion [79,87]. In general phosphorus decreases scale adhesion but the mechanism by which it accomplishes this is temperature dependent. Between 800°C and 900°C phosphorus promotes scale flaking and above 900-950°C scale blistering is enhanced. To complicate matters phosphorus has been found to retard oxidation between 500°C and 900°C but the effect was found to be non-linear. To explain this behaviour it has been suggested that iron phosphate precipitates near the scale-metal interface and at oxide grain boundaries [88]. At temperatures below 900°C the diffusion of iron ions and electrons is prevented. Furthermore phosphates promote void formation by vacancy condensation. Above 950°C, iron phosphate and phosphorus oxide was found to decompose leading to a cracked, non-protective scale, thus allowing increased oxidation rates. Furthermore, the phosphorus behaviour changes again with the presence of copper or silicon. Copper acts as a catalyst for the oxidation of phosphorus, thus increasing the number of cracks within the scale while in the presence of silicon, phosphorus is rejected from the interface since silicon is more strongly enriched [89].

Sulphur is a unique element with respect to scale formation. Despite the fact that sulphur is less noble than iron there is still some sulphur enrichment at the scale-metal interface. In general sulphur is detrimental to scale adhesion, although this is accomplished via different mechanisms. The presence of sulphur promotes void formation but can also internally oxidise manganese sulphate to manganese oxide and thus form iron sulphate, which is highly plastic. However, with sufficient iron sulphate segregation a low-melting (T_M=940°C) iron sulphate-iron oxide eutectic is formed at the scale-metal interface [90]. The presence of this compound leads to rapid or catastrophic oxidation and very strong scale adherence, which may give rise to hot rolling problems [79].

3.5. Conclusions

As has been shown here, friction plays an important role in the hot rolling of steel. The level of friction will impact upon the microstructure of the strip, the working life of the work rolls and the power consumed during rolling. Friction may be assessed by indirect methods, relying heavily upon the geometry on the roll bite, and indirect methods, which vary in reliability and robustness in their application to industrial rolling. The indirect methods of determining friction need to be viewed within the context of the experimental apparatus as experiments under nominally identical conditions may record different results. A consideration that cannot be overemphasised is that friction is the result of contacting surfaces, both of which need to be characterised. To this end, the evolution of the oxide layer on the work roll over a rolling campaign deserves some attention in addition to characterising the oxide layer of the strip.

3.6. References

1. N.T. Rudkins, P. Hartley, I. Pillinger and D. Petty "Friction modelling and experimental observations in hot ring compression tests", Journal of Materials Processing Technology, 1996, 60, 349-353
2. J.A. Schey "Tribology in Metalworking: Friction, Lubrication and Wear", 1st ed., American Society for Metals, Metals Park, Ohio, 1983, 0871701553
3. J.G. Lenard "The effect of lubricant additives on the coefficient of friction in cold rolling", Journal of Materials Processing Technology, 1998, 80-81, 232-238
4. D. N. Lee and S. H. Lee "Shear rolling and recrystallization textures of interstitial-free steel sheet", Materials Science and Engineering A, 1998, 249, 84-90
5. C. J. Barrett "Influence of lubrication on through thickness texture of ferritically hot rolled interstitial free steel", Ironmaking and Steelmaking, 1999, 26, 393-397
6. T. Sakai, S. Hamada and Y. Saito "Improvement of the r-value in 5052 aluminum alloy sheets having through-thickness shear texture by 2-pass single-roll drive unidirectional shear rolling", Scripta Materialia, 2001, 44, 2569-2573
7. R. Colas, J. Ramirez, I. Sandoval, J. C. Morales and L. A. Leduc "Damage in hot rolling work rolls", Wear, 1999, 230, 56-60
8. A. Dias and H. P. Lieurade "Contribution to the Study of Thermal and Mechanical Fatigue. Experimental Procedure and Application", Bull. Cercle Etud. Metaux, 1982, 14, 1-1 to 1-15
9. M. A. De Carvalho, R. R. Xavier, C. S. P. Filho, C. Morone, M. Boccallini and A. Sinatpra "Microstructure, mechanical properties and wear resistance of high speed steel rolls for hot rolling mills", Iron and Steelmaker, 2002, 29, 27-32
10. B. M. Kapadia and K. W. Marsden "Fracture analysis of hot mill work rolls", 40th Mechanical Working and Steel Processing Conference, Pittsburgh, USA, ed. by Iron and Steel Society/AIME, 25-28 Oct. 1998, 395-405
11. M.F. Frolish and J.H. Beynon "Establishing a qualitative model for rolling contact fatigue and spalling failure of back-up rolls", Fatigue 2000, Cambridge, UK, ed. by Bache *et al.*, 10-12 April 2000, 363-370
12. M.F. Frolish, D.I. Fletcher and J.H. Beynon "A quantitative model for predicting the morphology of surface initiated rolling contact fatique cracks in back up rolls", Fatigue and Fracture of Engineering Materials and Structures, 2002, 25, 1073-1086
13. J.D. Fletcher "Process simulation of the hot rolling of thin gauge strip by finite element modelling", Ph.D., University of Sheffield, 1998
14. V. Gonzalez, P. Rodriguez, Z. Haduck and R. Colas "Modelling oxidation of hot rolling work rolls", Ironmaking and Steelmaking, 2001, 28, 470-473
15. O. Kato, H. Yamamoto, M. Ataka and K. Nakajima "Mechanisms of Surface Deterioration of Roll for Hot Strip Rolling", ISIJ International, 1992, 32, 1216-1220
16. R.D. Mercado-Solis "Simulation of thermal fatigue in work rolls", PhD, University of Sheffield, 2002
17. I. Beverly, H. Uijtdebroeks, J.J. de Roo, V. Lanteri and J.M. Phillipe "Improving the hot rolling process of surface-critical steels by improved and prolonged working life of work rolls in the finishing mill train", EUR 19871 EN, 1 July 1996 to 31 December 2000
18. T.F.J. Quinn "Computational methods applied to oxidational wear", Wear, 1996, 199, 169-180

19. J.F. Archard "Single contacts and multiple encounters", J. Appl. Phys., 1961, 32, 1420
20. W.M. Rainforth "Microstructural evolution at the worn surface: a comparison of metals and ceramics", Wear, 2000, 245, 162-177
21. X. Duan and T. Sheppard "Three dimensional thermal mechanical coupled simulation during hot rolling of aluminium alloy 3003", International Journal of Mechanical Sciences, 2002, 44, 2155-2172
22. R.B. Sims "The calculation of roll force and torque in hot rolling mills", Proc. Instn. Mech. Engrs., 1954, 168, 191-200
23. J.H. Hitchcock "Appendix I" in Roll Neck Bearing, ASME, New York, USA, 1935, 33
24. G.E. Dieter "Mechanical metallurgy", SI Metric ed., McGraw-Hill Book Company, London, 1988, 0-07-084187-X
25. S. E. Lundberg "An approximate theory for calculation of roll torque during edge rolling of steel slabs", Steel Research, 1986, 57, 325-330
26. J.G. Lenard "The effect of temperature on the coefficient of friction in flat rolling", CIRP Annales, 1991, 40, 223-226
27. J.G. Lenard "Friction and Forward Slip in Cold Strip Rolling", Tribology Transactions, 1992, 35, 423-428
28. J.G. Lenard and Z. Malinowski "Measurements of Friction During the Warm Rolling of Aluminum", Journal of Materials Processing Technology, 1993, 39, 357-371
29. J.G. Lenard and S. Zhang "A study of friction during the lubricated cold rolling of an aluminum alloy", Journal of Materials Processing Technology, 1997, 72, 293-301
30. C. McConnell and J.G. Lenard "Friction in cold rolling of a low carbon steel with lubricants", Journal of Materials Processing Technology, 2000, 99, 86-93
31. A. Said, J.G. Lenard, A.R. Ragab and M.A. Elkhier "The temperature, roll force and roll torque during hot bar rolling", Journal of Materials Processing Technology, 1999, 88, 147-153
32. M.A. Samad and R.S. Rao "Minimization of energy in the multipass rolling process", Journal of Manufacturing Science and Engineering, 2001, 123, 135-141
33. Y. Yu and J.G. Lenard "Estimating the resistance to deformation of the layer of scale during hot rolling of carbon steel strips", Journal of Materials Processing Technology, 2002, 121, 60-68
34. I.M. Pavlov and M.I. Kuprin "Technological processes of treatments of steels and alloys", Metallurgizdat, 1955, 33, 154-192
35. Z. Wusatowski "Fundamentals of rolling", 1st ed., Pergamon Press, 1969, 0080122760
36. Y.H. Li and C.M. Sellars "Development of forward slip friction measurement method of rolling", IMMPETUS, 0009, Oct. 1998
37. R. Hill "The mathematical theory of plasticity", 1st ed., Oxford University Press, Oxford, 1950
38. J.G. Lenard "Roll Deformation in Cold Strip Rolling", J. Eng. Mater. Technol., 1980, 102, 382-384
39. J.H. Beynon, Y.H. Li, M. Krzyzanowski and C.M. Sellars "Measuring, modelling and understanding friction in the hot rolling of steel", Metal Forming 2000, Krakow, Poland, ed. by Pietrzyk *et al.*, Balkema Publishers, Rotterdam, 3-7 Sept. 2000, 3-10

40. M. Kunogi "On the plastic behaviour of the hollow cylinder under axial load", J. Sci. Res. Inst., 1954, 30, 63-92
41. A.T. Male and M.G. Cockcroft "A method for the determination of the coefficient of friction of metals under conditions of bulk plastic deformation", J. Inst. Metals, 1964, 93, 38-46
42. F. Wang and J.G. Lenard "An Experimental Study of Interfacial Friction-Hot Ring Compression", J. Eng. Mater. Technol., 1992, 114, 13-18
43. S.E. Lundberg and B. Walden "Evaluation of Friction Under Hot Working Conditions in a High Temperature Test Rig", Steel Research, 1992, 63, 304-308
44. J.D. Fletcher, Y.H. Li, J.H. Beynon and C.M. Sellars "The influence of surface conditions in hot forming determined by ring upsetting: a numerical and experimental investigation", Proc Instn Mech Engrs Part J, Journal of Engineering Tribology, 1998, 212, 453-465
45. J.P. Wang "A new evaluation to friction analysis for the ring test", International Journal of Machine Tools & Manufacture, 2001, 41, 311-324
46. O.M. Ettouney and K.A. Stelson "An Approximate Model to Calculate Foldover and Strains During Cold Upsetting of Cylinders. II. Use of the Foldover Model to Estimate Friction", Journal of Engineering for Industry, 1990, 112, 267-271
47. D. Szyndler, M. Pietrzyk, J.G. Lenard and S.H. Fyke "Inverse analysis applied to the evaluation of friction and rheological parameters in hot forming of steels", Metal Forming 2000, Krakow, Poland, ed. by Pietrzyk *et al.*, Balkema Publishers, Rotterdam, 3-7 Sept. 2000, 101-106
48. J.H. Beynon "Tribology of hot metal forming", New Directions in Tribology, London, UK, ed. by Mechanical Engineering Publications Ltd., 8-12 Sept. 1997, 135-139
49. Z. M. Hu and T. A. Dean "Study of surface topography, friction and lubricants in metalforming", International Journal of Machine Tools & Manufacture, 2000, 40, 1637-1649
50. J. Devaux, J. C. Gelin, J. Oudin and Y. Ravalard "Theoretical Analysis and Experimental Applications of Barelling and Folding in Cylinder Upsetting Tests", Int. J. Mech. Sci., 1984, 26, 555-572
51. D.H. Hwang, D. E. Kim and S. J. Lee "Influence of wear particle interaction in the sliding interface on friction of metals", Wear, 1999, 225-229, 427-439
52. C. L. Chang and D. Y. Wang "Microstructure and adhesion characteristics of diamond-like carbon films deposited on steel substrates", Diamond and Related Materials, 2001, 10, 1528-1534
53. P.J. Blau "Scale effects in sliding friction: an experimental study" in Fundamentals of Friction: Macroscopic and Microscopic Processes, ed. by Singer and Pollock, Kluwer Academic Publishers, Amsterdam, 1992, 523-534
54. C. Vergne, C. Boher, C. Levaillant and R. Gras "Analysis of the friction and wear behavior of hot work tool scale: application to the hot rolling process", Wear, 2001, 250, 322-333
55. A.G. Plint and M.A. Plint "A new technique for the investigation of stick-slip", Tribology International, 1985, 18, 247-249
56. Y.C. Chiou, K. Kato and T. Kayaba "Effect of normal stiffness in loading system on wear of carbon steel - part 1: sever-mild wear transition", Journal of Tribology, 1985, 107, 491-495
57. M.G. Gee "Results from a UK interlaboratory project on dry sliding wear of alumina" in Wear Testing of Advanced Materials, ASTM STP 1167, ed. by

Divakar and Blau, American Society for Testing and Materials, Philadelphia, 1992, 129-150

58. M.G. Gee and L.A. Lay "Results of the second round robin exercise carried out by the UK wear test methods group on the sliding wear of alumina ceramic", NPL DMA(D) 751, November 1989
59. K. Tanaka, J. Ishikawa and A. Shimamoto "Elastic contact and friction between sliders and circumferentially textured disks-Part III: Experiments", Journal of Tribology, 1998, 120, 800-807
60. D. H. Hwang, I. H. Sung, D. E. Kim and S. H. Lee "Effects of material pair properties on the frictional behavior of metals", Wear, 1999, 225-229, 600-614
61. E. Rabinowicz "Friction and wear of materials", 2nd ed., John Wiley & Sons, Inc., New York, 1995, 0-471-83084-4
62. E.A. Almond and M.G. Gee "Results from a UK interlaboratory project on dry sliding wear", Wear, 1987, 120, 101-116
63. P.A. Munther and J.G. Lenard "The effect of scaling on interfacial friction in hot rolling of steels", Journal of Materials Processing Technology, 1999, 88, 105-113
64. A.A. Howe "Oxide scales on stainless hot-band at BSC stainless", Swinden Laboratories, Ph/TN/7/-/88/D, 17 June 1988
65. H.T. Abuluwefa, J.H. Root, R.I.L. Guthrie and F. Ajersch "Real-time observations of the oxidation of mild steel at high temperature by neutron diffraction", Metallurgical and Materials Transactions B, 1996, 27B, 993-997
66. F. Matsuno and S.-I. Nishikida "Mechanical properties of FeO-MnO s.s. and FeO-MgO s.s. at high temperatures", Transactions ISIJ, 1986, 26, B-251
67. M. Torres and R. Colas "A model for heat conduction through the oxide layer of steel during hot rolling", Journal of Materials Processing Technology, 2000, 105, 258-263
68. G. Garnaud and R.A. Rapp "Thickness of the oxide layers formed during the oxidation of iron", Oxidation of Metals, 1977, 11, 193-198
69. O. Kubaschewski and B.E. Hopkins "Oxidation of metals and alloys", 2nd ed., Butterworths, London, 1962
70. N.E. Moore, P.S. Oldroyd, P.J. Lewis and M. Westacott "An investigation of the formation, constitution and properties of scale formed in the reheating furnace and during the hot rolling process", ECSC, 7210.KB/809, Final Report, May 1991
71. P. Kofstad "High Temperature Corrosion", 1st ed., Elsevier Applied Science Publishers, New York, 1988, 1-85166-154-9
72. H.T. Abuluwefa, R.I.L. Guthrie and F. Ajersch "Oxidation of low carbon steel in multicomponent gases: Part I. Reaction mechanisms during isothermal oxidation", Metallurgical and Materials Transactions A, 1997, 28A, 1633-1641
73. K. Sachs and C.W. Tuck "Surface oxidation of steel in industrial furnaces", Proceedings of the Conference on Reheating for Hot Working, London, ed. by Iron and Steel Institute, 1968, 1-17
74. Y.-N. Chang and F.-I. Wei "High Temperature Oxidation of Low Alloy Steels", J. Mater. Sci., 1989, 24, 14-22
75. R.B. Banks "Growth and diffusion phenomena - mathematical frameworks and applications", 1st ed., Springer-Verlag, Berlin, 1994, 3-540-55507-2
76. H. Schmalzried "Solid state reactions", 2nd ed., Verlag Chemie GmbH, Weinheim, 1981, 3-527-25872-8

77. P.H. Bolt "The properties of oxide scales on hot rolled steels: a literature review", Corus IJTC, March 2000

78. Y.A. Chang and N. Ahmad "Thermodynamic data on metal carbonates and related oxides", 1st ed., The Metallurgical Society of the AIME, Warrendale, 1982, 0-89520-451-7

79. H. J. Grabke, V. Leroy and H. Viefhaus "Segregation on the surface of steels in heat treatment and oxidation (review)", ISIJ Int., 1995, 35, 95-113

80. J. Kucera, M. Hajduga, J. Glowacki and P. Broz "Decarburization and hardness changes of Fe-C-Cr-Mn-Si steels caused by high temperature oxidation in ambient air", Zeitschrift für Metallkunde, 1999, 90, 514-521

81. J. Slowik, G. Borchandt, C. Kohler, R. Jeschar and R. Scholz "Influence of oxide scales on heat transfer in secondary cooling zones in the continuous casting process. Part II: Determination of material properties of oxide scales under spray-water cooling conditions", Steel Research, 1990, 61, 302-311

82. D. L. Douglass, P. Kofstad, A. Rahmel and G. C. Wood "International workshop on high temperature corrosion", Oxidation of Metals, 1996, 45, 529-620

83. B. Regad, M. Viennot, D. David and S. Lecourt "Influence de elements d'addition sur les premiers stades de l'oxydation d'un acier faiblement allie, entre 600 et 800°C", Rev. Metall., Cah. Inf. Tech., 1994, 91, 1805-1813

84. N. Imai, N. Komatsubara and K. Kunishige "Effect of copper, tin and nickel on hot workability of hot-rolled mild steel", ISIJ International, 1997, 37, 217-223

85. N. Imai, N. Komatsubara and K. Kunishige "Effect of copper and nickel on hot workability of hot-rolled mild steel", ISIJ International, 1997, 37, 224-231

86. H. Ohtani, H. Suda and K. Ishida "Solid/liquid equilibria in Fe-Cu based ternary systems", ISIJ International, 1997, 37, 207-216

87. I. Svedung and N. G. Vannerberg "Influence of Small Amounts of P on the Oxidation Properties of Fe at High Temperatures", Scand. J. Metall., 1972, 1, 141-144

88. I. Svedung, R. Pompe and N. G. Vannerberg "Combined Effect of Cu and P on the Oxidation Properties of Steel", Scand. J. Metall., 1976, 5, 129-133

89. R. Pompe, I. Svedung and N. G. Vannerberg "Combined Effect of Si and P on the Oxidation of Fe and the CAMECA (Ion Analyser) Studies of the Oxide Scale", Scand. J. Metall., 1976, 5, 258-261

90. V. V. Belousov and B. S. Bokshtein "Model of the rapid stage of the catastrophic oxidation of metals", Oxidation of Metals, 1998, 50, 389-397

Chapter 4 - Material Properties

4.1. Introduction

In order to develop a model based upon fundamental material properties it is necessary to have more than a passing acquaintance with the true physical properties. Unfortunately it is often not possible to state with 100% certainty what any given property is at a given temperature, largely as a result of the difficulty in measuring parameters at high temperatures and small length scales; thus one must rely upon the extrapolation of data and the application of analogies. When using these techniques it is crucial that the results are viewed with care to ensure that they have some physical meaning, even if they are not perfect.

For the purposes of this project the required material properties have been arbitrarily differentiated between thermomechanical properties and surface energy. In this context the thermomechanical properties primarily consist of properties that are affected by temperature and have been limited to those properties needed for finite element calculations. Surface energy is a specific topic with many variations; with this in mind the discussion has been limited to the determination of surface energies for the conditions that are considered to exist under hot rolling conditions.

4.2. Thermomechanical Properties

To provide an accurate representation of any physical system that is modelled in terms of high temperature deformation it is necessary to include as many temperature dependent properties as is practical. Of the thermomechanical properties available the following properties are considered: Young's modulus, stress-strain curves, Poisson's ratio, specific heat capacity, thermal conductivity, thermal expansion and density.

4.2.1. Young's Modulus

Young's modulus is defined as the slope of the stress-strain curve in the elastic region, representing the stiffness of the material. Young's modulus for plain carbon steels and iron oxides is shown in Figure 4.1.

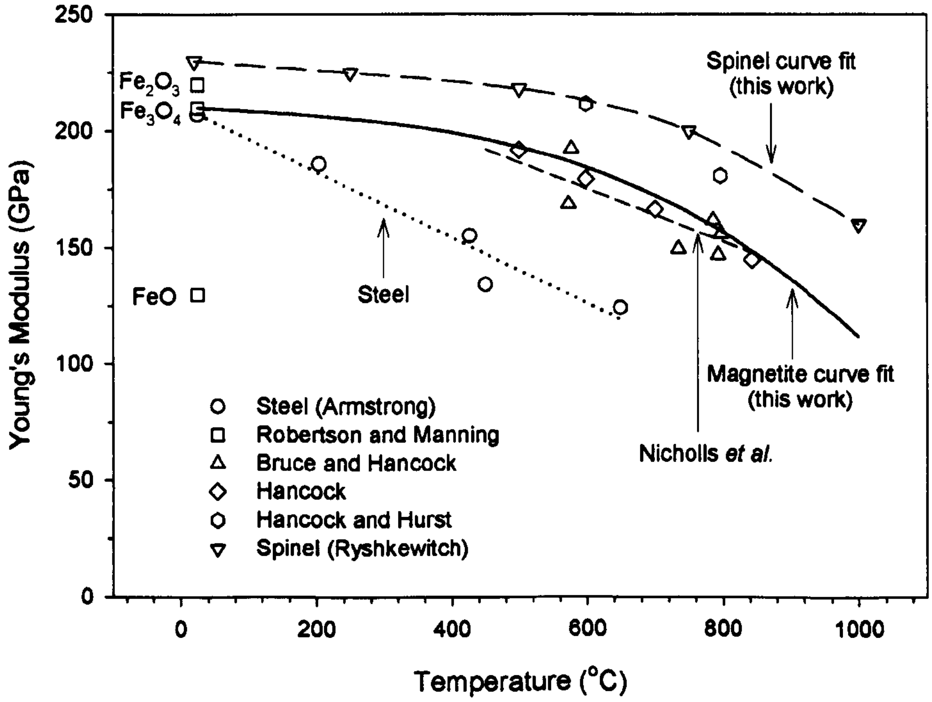

Figure 4.1 – Effect of temperature on the Young's modulus of steel [1] and iron oxides (iron oxide data compiled by Nicholls *et al.* [2], spinel data from [3]). The spinel curve fit was then used to generate the curve fit for magnetite.

The significant drop with temperature for steel is dramatic but, as a first approximation, Young's modulus may be ignored in hot working calculations. Young's modulus for steel may be estimated using the following equation:

$$E = -0.1413 \cdot T + 210.81 \tag{4.1}$$

where E is the Young's modulus (in GPa) and T is the temperature (in °C).

There is little agreement in the literature as to the effect of temperature on Young's modulus for iron oxides. The reason for this is the brittle nature of the oxide and the large effect that porosity and micro-cracks have on the test procedure. The most widely accepted values for room temperature values iron oxides are compared with steel in Table 4.1.

Table 4.1 – Young's modulus for steel [1] and single crystal iron oxides at room temperature [4].

Material	E (GPa)
Steel	207
FeO	130
Fe_3O_4	210
Fe_2O_3	220

Nicholls *et al.* [2] used high temperature data from Bruce and Hancock [5] to give the effect of temperature on iron oxide scales to be:

$$E = 240\left[1 - 4.7\times10^{-4}\cdot(T-25)\right] \tag{4.2}$$

where E is the Young's modulus (in GPa) and T is the temperature (in °C). Equation 4.2 was derived for iron oxide that was grown in air [5,6], therefore the resulting scale will be composed primarily of magnetite with some wüstite and hæmatite. In the absence of more information, it is assumed that these data are representative for magnetite. However, examining data for another spinel ($MgO{:}Al_2O_3$) shows that temperature has a non-linear effect on Young's modulus, shown in Figure 4.1, which means that equation 4.2 cannot be extrapolated beyond the 500°C to 800°C temperature range that the data covers. To estimate the effect of temperature on the Young's modulus of magnetite in the region of interest, i.e. room temperature to 450°C, a curve was developed based upon the available data and the behaviour of spinel. This relationship was estimated to be:

$$E = -1.004\times10^{-7}\cdot T^3 + 2.260\times10^{-5}\cdot T^2 - 2.102\times10^{-2}\cdot T + 210.4 \tag{4.3}$$

where E is the Young's modulus (in GPa) and T is the temperature (in °C). This equation assumes that the inverse spinel structure of magnetite will behave in a similar manner to the spinel structure. Given the large degree of scatter in the experimental data at the higher temperatures, the suggested relationship appears reasonable.

4.2.2. Stress-Strain Curves

At its most basic level a stress-strain curve defines the amount of stress in a material for a given strain, where stress is defined as the force per unit area and strain as the relative deformation. Stress-strain curves are typically generated from a tensile test, which is not a problem for elastic-plastic materials such as steel; however this technique has important implications on primarily elastic materials such as oxides at low temperatures. An elastic material usually fails in a brittle manner, the implications of which are that the stress level at fracture is strongly influenced by any defects that may exist within the structure.

4.2.2.1. Steel Strength

The flow stress of steel during hot rolling has been shown to be modelled with an acceptable accuracy and precision by the Shida equation [7,8], which is valid for the following conditions: carbon contents < 1.2 wt%, temperatures between 700°C and 1200°C, strain rates between 0.1 s^{-1} and 100 s^{-1} and strains up to 0.7. The flow stress (σ_f in kg mm^{-2}) is given as a function of carbon content (C in wt%), strain (ε), strain rate ($\dot{\varepsilon}$ in s^{-1}) and temperature (T in °C) as shown here [7]:

$$\sigma_f = \sigma_d \cdot \phi_w \cdot \phi_r \tag{4.4}$$

where σ_d is the deformation resistance function, ϕ_w is the work hardening function and ϕ_r is the rate hardening function. The manner in which the flow stress is calculated depends upon whether or not the normalised temperature, $\bar{T}$, is greater or less than a normalised phase transition temperature, $\bar{T}_p$, defined as:

$$\bar{T} = \frac{T+273}{1000} \tag{4.5}$$

$$\bar{T}_p = 0.95\left(\frac{C+0.41}{C+0.32}\right) \tag{4.6}$$

The sub-equations from equation 4.4 are defined below:

$$\sigma_d = 0.28 \cdot \exp\left(\frac{5}{\bar{T}} - \frac{0.01}{C+0.05}\right) \cdot \gamma \tag{4.7}$$

$$\phi_w = 1.3(5\varepsilon)^{0.41-0.07C} - 1.5\varepsilon \tag{4.8}$$

$$\phi_r = (0.1\dot{\varepsilon})^m \tag{4.9}$$

where, for $\bar{T} \geq \bar{T}_p$, γ=1 and:

$$m = (-0.019C + 0.126)\bar{T} + 0.076C - 0.05 \tag{4.10}$$

whereas for $\bar{T} < \bar{T}_p$:

$$\gamma = 30(C+0.9)\left[\bar{T} - 0.95\frac{C+0.49}{C+0.42}\right]^2 + \frac{C+0.06}{C+0.09} \tag{4.11}$$

$$m = (0.081 \cdot C - 0.154)\bar{T} - 0.019 \cdot C + 0.207 + \frac{0.027}{C+0.320} \tag{4.12}$$

The Shida equation, described above, was compared to plane strain compression tests (PSC) tests that were conducted by the author as part of this work at the University of Sheffield using the Thermo Mechanical Compression (TMC) machine. The PSC samples were 60 mm long, 30 mm wide and 10 mm thick with small semi-circular cavities removed from the 30 mm x 10 mm faces for manipulation by the robotic actuator. A thermocouple hole, 1.6 mm in diameter, was drilled into the centre of the deformation zone of each sample from the centre of the 60 mm x 10 mm face. The samples were machined from low carbon steel, the chemistry of which is listed in Table 4.2. The PSC experiments were conducted at 800°C at strain rates of 0.47 s^{-1}, 4.8 s^{-1} and 39.7 s^{-1}, and are shown in Figure 4.2

Table 4.2 – Steel composition used in the experiments (wt %, rem. Fe).

C	Mn	Si	S	P
0.11±0.01	0.49±0.02	<0.02	0.007±0.001	0.013±0.002

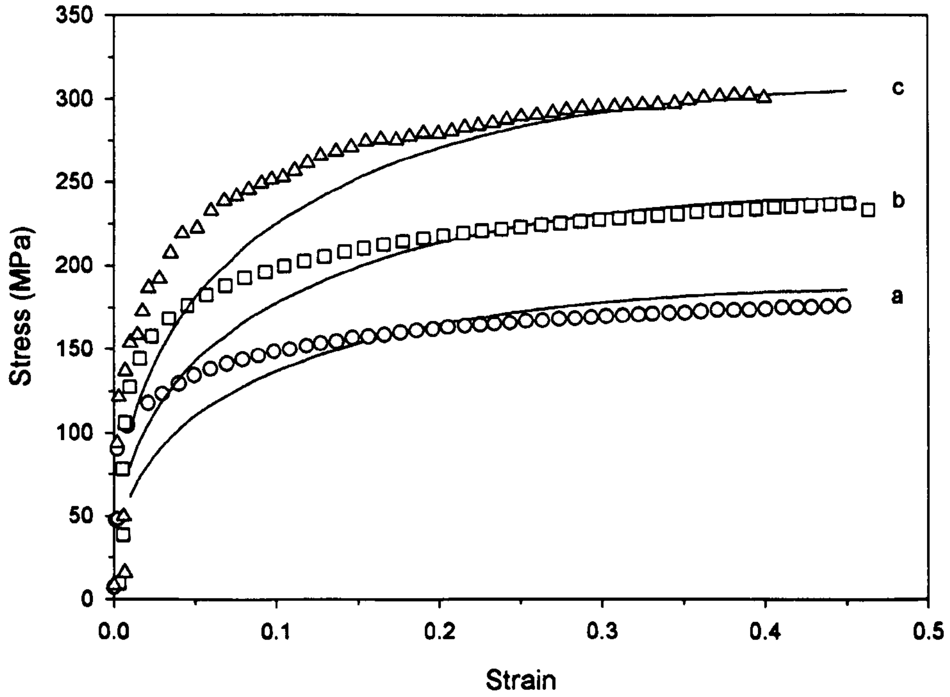

Figure 4.2 – Comparison between plane strain compression tests (symbols) conducted at 800°C at strain rates of 0.47 s^{-1}, 4.8 s^{-1} and 39.7 s^{-1} (a, b and c respectively) and Shida equation predictions (solid lines).

4.2.2.2. Iron Oxide Strength

Iron oxides are ceramics and display brittle fracture mechanisms at low temperature enabling linear elastic fracture mechanics (LEFM) theory to be applied to estimate the critical stresses at which failure takes place. Above a critical temperature the oxide behaviour becomes plastic; unfortunately there does not appear to be any agreement in the literature defining the transition temperature between elastic and plastic behaviour. For example, work by Hidaka *et al.* [9,10] shows that this temperature is around 700°C while Hancock and Nicholls [11] have applied LEFM theory to iron oxides up to 800°C, although they did recognise a change in fracture mechanism at around 600°C. There is a major difference in experimental technique in determination of these temperatures; Hidaka *et al.* used controlled gas atmospheres to create their tensile specimens of the desired composition while Hancock and Nicholls used 'real' scales (i.e. mixed wüstite/magnetite) on steel substrates. The variation in fracture stress with temperature for iron oxides, either calculated using a fracture mechanics approach from the data given by Hancock and Nicholls [11], or directly measured [9], is given in Figure 4.3. Adding to the debate, Krzyzanowski and Beynon [12] have shown that the failure mechanism of the scale is not only affected by the temperature but also the chemistry of the steel substrate. The deformation behaviour of scale can vary from raft sliding, where great swaths of oxide break off from the substrate, to brittle failure, where the oxide remains adhered to the surface but suffers substantial cracking throughout the oxide layer.

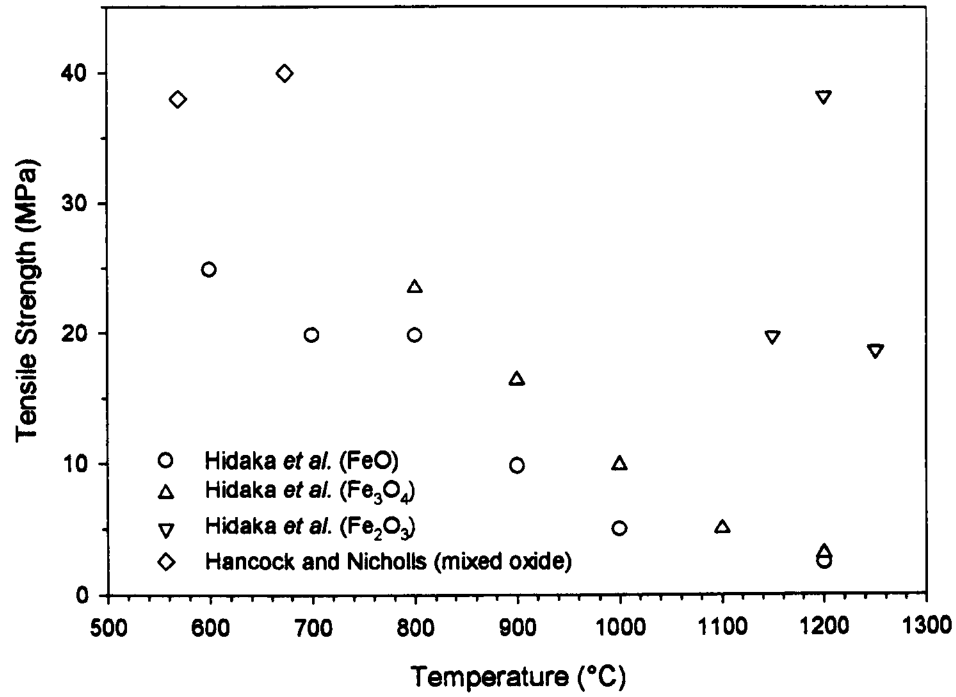

Figure 4.3 – The apparent tensile strength of iron oxide specimens. Hidaka *et al.* [9] tensile samples deformed at a strain rate of 2.0×10^{-4} s^{-1}, Hancock and Nicholls [11] estimates using an effective crack length.

In the overlapping temperature range of 600-800°C conflicting trends are indicated with Hancock and Nicholls [11] showing an increasing fracture stress (not included in Figure 4.3 are estimates for 800°C giving a fracture stress that varies between 74 and 120 MPa despite increasing crack lengths) while Hidaka *et al.* [9,10] show a decrease in fracture stress. This can be attributed to the highly porous tensile samples resulting from the oxidation of 99.99% iron; however, the effect of the pores should be increasingly negligible as the oxide behaves plastically at higher temperatures and this may be the case as necking was observed. Furthermore, the fracture may have been premature as a result of the presence of pre-existing cracks in the neck.

Hidaka *et al.* [9,10] report a change in deformation mechanisms at high temperature. They define Type I plasticity (i.e. work hardening) in wüstite and magnetite as a result of dislocation glide below 1000°C and 1200°C respectively. Above these temperatures they define Type II plasticity (steady-state deformation) as a result of dislocation climb. The difference in temperature at which steady-state deformation is achieved between wüstite and magnetite is due to the difference between diffusion coefficients. Hidaka *et al.* examined the effect of strain rate and found that at high temperatures it will directly affect the saturation stress for the dislocation climb mechanism, thus showing that strain rate will affect the deformation stress. At lower temperatures Hancock and Nicholls [11] examined the effect of strain rate on crack spacing, which indirectly affects the strength of the oxide by providing more locations for failures to initiate, and found that above a minimum strain rate crack spacing is independent of strain rate while below it is linearly dependent, although the influence of the strain rate decreases with temperature. Unfortunately the strain rates examined in these two studies were extremely low, therefore these results cannot be directly applied to hot rolling where the strain rates at the surface of the stock are many orders of magnitude greater than those employed by Hidaka *et al.* and Hancock and Nicholls.

In the context of hot rolling of steel, the oxide layer is very thin (relative to the strip) and, of interest to this work, between the hot strip and the relatively cold work roll. Thus the surface of the oxide will be much colder than the oxide at the steel-oxide interface as a result of the contact with the colder work roll and iron oxide's low thermal conductivity. This scenario implies that even within the scale layer there could be a transition between purely elastic behaviour and elastic-plastic behaviour. The end result is a very complicated scale morphology that is, for most purposes, unnecessary to model since the principal effect of the scale layer appears to act as a thermal barrier and, as such, can mathematically be accounted for using the concept of a heat transfer coefficient. Therefore, while scientifically worthwhile, knowing the detailed behaviour of the scale layer will not likely have a dramatic effect any model predictions.

4.2.3. Poisson's Ratio

Poisson's ratio is defined as the ratio of lateral strain to axial strain in an axially loaded specimen. In the elastic region Poisson's ratio, ν, is given by:

$$\nu = \frac{E}{2G_s} - 1 \qquad (4.13)$$

where E is the Young's modulus and G_s is the elastic shear modulus. In principle Poisson's ratio will be affected by temperature but in practice this temperature dependence is usually neglected as a result of the reduced elasticity at higher temperatures and the reduction of shear modulus with temperature is similar in magnitude as Young's modulus, thus there is a minimal overall effect [13]. Room temperature values for Poisson's ratio are given for steel and iron oxides in Table 4.1.

Table 4.3 – Poisson's ratio for steel and iron oxides.

Material	ν	Reference
Steel	0.3	[14]
FeO	0.36	[4]
Fe_3O_4	0.29	[4]
Fe_2O_3	0.19 (0.33)	[4] ([15])

4.2.4. Specific Heat Capacity

The conventional definition of specific heat capacity is the amount of heat required to change the temperature of a unit of mass of a substance by one Kelvin. In thermodynamics specific heat capacity is further broken down into the specific heat capacity for a constant volume, C_V, or the specific heat capacity at a constant pressure, C_P. The majority of material processing is conducted at nominally constant pressure, i.e. atmospheric pressure, thus specific heat capacity almost always refers to specific heat capacity at a constant pressure. The effect of temperature on the specific heat capacity of steel for selected carbon compositions and magnetite is shown in Figure 4.4. Both steel compositions follow an upwards trend from room temperature to approximately 700°C. At 770°C there is a drastic change in the behaviour of the heat capacity, associated with the change in magnetic properties at the Curie temperature. In general carbon does not have much effect on the heat capacity of steel as the size of the spike of the two steel examples is misleading as the specific heat capacity will be asymptotic at 770°C and the higher value for the 1.2 wt%C is mostly a result of sampling frequency. Far greater is the effect of phase since ferrite is far more temperature sensitive than austenite.

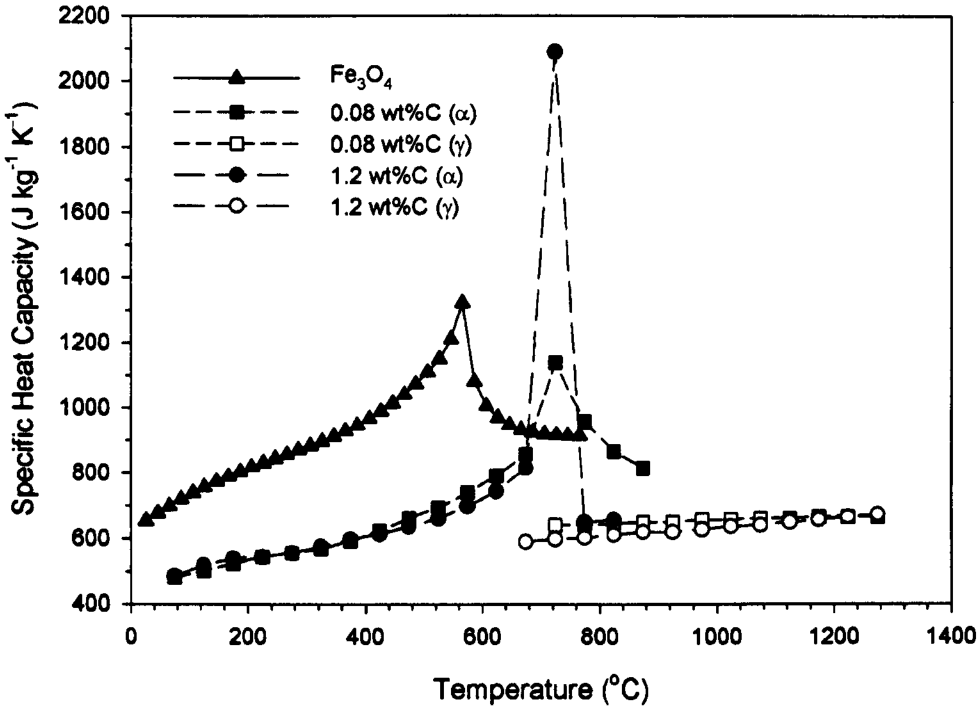

Figure 4.4 – Variation of specific heat capacity with temperature for selected carbon steels [16] and magnetite [17].

Grønvold and Sveen [17] used a synthetic magnetite and showed a similar temperature dependence as steel, with a spike at the Néel temperature, which is approximately 575°C. The Néel temperature identifies the transition from ferrimagnetic to paramagnetic. Modelling of specific heat capacity behaviour by Lynch *et al.* [18] indicates that there is little difference in heat capacity between the heat capacity of magnetite and hæmatite although the spike at the Néel temperature shown by Grønvold and Sveen was neglected.

4.2.5. Thermal Conductivity

Thermal conductivity is defined as the quantity of heat that passes in a unit of time through a unit of area of a plate, whose thickness is unity, when its opposite faces differ in temperature by one degree; practically speaking it is a measure of a material's ability to transfer heat. The thermal conductivity of selected steels and magnetite over a wide temperature range is shown in Figure 4.5.

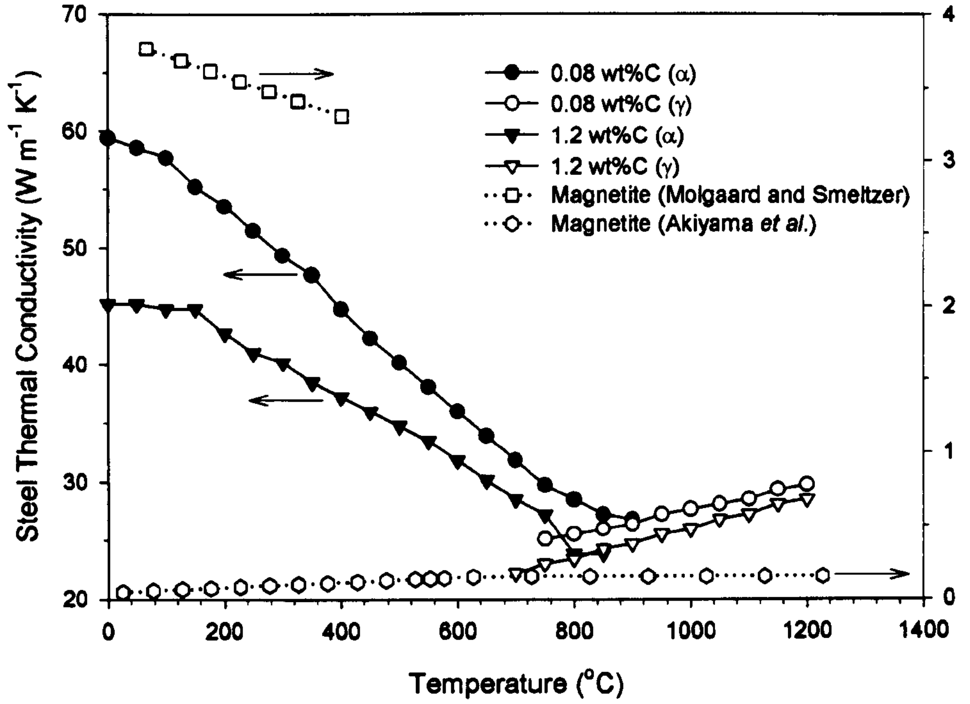

Figure 4.5 – Variation of thermal conductivity with temperature for selected steels [16] and magnetite [19-21].

The general trend of thermal conductivity in steel is to decrease with increasing temperature until the austenite transition temperature is reached, whereupon there is a small increase. Since carbon is an interstitial element its effect is to reduce thermal conductivity by increasing resistance to heat flow until the austenite region is reached, at which point the mobility of carbon within the fcc lattice reduces its ability to act as a source of thermal resistance.

There is some disagreement in the literature as to the magnitude of the thermal conductivity for iron oxides. In the temperature range of 340 K to 675 K Molgaard and Smeltzer [21] give the following relationships for magnetite and hæmatite respectively:

$$k_{Fe_3O_4} = 0.0423 - 1.37\times10^{-5}T \tag{4.14}$$

$$k_{Fe_2O_3} = 0.0839 - 6.63\times10^{-5}T \tag{4.15}$$

where k is the thermal conductivity (in W cm^{-1}K^{-1}) and T is the temperature (in K). Whereas Akiyama *et al.* [19,20] report the following relationships for the given temperature ranges:

$$k_{FeO} = \begin{array}{c} 2.335\times10^{-4}T+0.1136 \\ -1.047\times10^{-4}+0.3926 \end{array} \rightarrow \begin{array}{c} 298\leq T\leq 825 \\ 825\leq T\leq 1500 \end{array} \tag{4.16}$$

$$k_{Fe_3O_4} = \begin{array}{c} 1.693\times10^{-4}T \\ 2.967\times10^{-4}T+0.1508 \end{array} \rightarrow \begin{array}{c} 298\leq T\leq 906 \\ 906\leq T\leq 1500 \end{array} \tag{4.17}$$

$$k_{Fe_2O_3} = \begin{array}{c} 1.844\times10^{-4}T \\ 8.319\times10^{-5}T+9.243\times10^{-2} \end{array} \rightarrow \begin{array}{c} 298\leq T\leq 912 \\ 912\leq T\leq 1500 \end{array} \tag{4.18}$$

where k is the thermal conductivity (in W m^{-1}K^{-1}) and T is the temperature (in K). It is noteworthy that Molgaard and Smeltzer's [21] results are two orders of magnitude greater than Akiyama *et al.*'s [19,20], as demonstrated for magnetite in Figure 4.5. The samples used by Akiyama *et al.* were formed by Hot Isostatic Pressing (HIP) from fine materials whose average particle size was 1 μm. Although the porosity was found to be less than 0.1% the HIP process could result in an increased number of grain boundaries compared with sample wafers cut from crystals used by Mogaard and Smeltzer. Given that the electrical conductivity of magnetite is relatively high for an oxide [22], the magnitude of the thermal conductivity is more likely to be that of Molgaard and Smeltzer rather than Akiyama *et al.* Torres and Colas [23] employed constant values of 3.2, 1.5 and 1.2 for wüstite, magnetite and hæmatite respectively for modelling heat conduction through an oxide layer during hot rolling. Regardless, the thermal conductivity of iron oxides is another order of magnitude below that of steel. This, combined with the fact that the oxide layer on hot rolled steel strip is thin compared to the strip, means that the choice of thermal conductivity equation for iron oxides will not have a large impact on the overall predictions primarily because the oxide layer is modelled as a thermal barrier which is accounted for by the heat transfer coefficient.

4.2.6. Thermal Expansion Coefficient

Thermal expansion coefficient is defined as the proportionate change in length for one degree change in temperature. The variation of thermal expansion coefficient for selected steels and room temperature values for iron oxides is given in Figure 4.6.

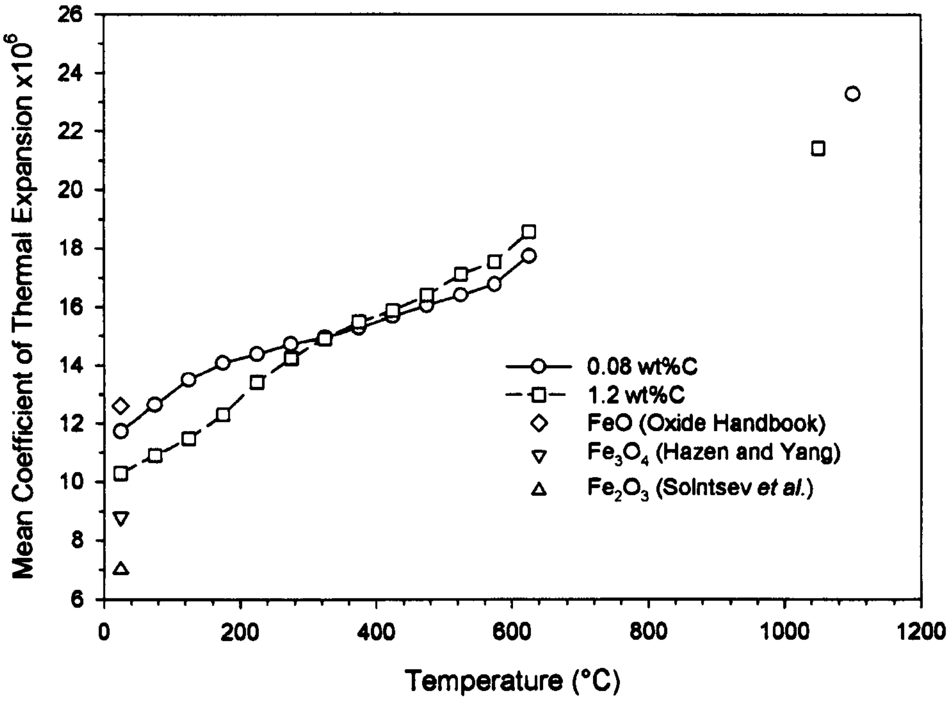

Figure 4.6 – Variation of mean thermal expansion coefficient with temperature for selected steels [16] and room temperature values for wüstite [24], magnetite [25] and hæmatite [15].

The effect of carbon on the expansion coefficient is a small reduction at lower temperatures but between approximately 300°C and 600°C it has little effect. In the austenitic region the data is skewed slightly as a result of the 0.06 wt%C and 0.08 wt%C coefficients of thermal expansion being applicable from 1000°C to 1200°C while the remaining carbon contents data points are from 900°C to 1200°. However, there is a small reduction in thermal expansion coefficients at the higher carbon contents. The thermal expansion coefficient for oxides should also increase with temperature. Unfortunately this information is currently unavailable but one would expect it to be similar, albeit slightly less, to that of steel given the similar magnitudes of their melting temperatures.

4.2.7. Density

The variation of density with temperature for selected steels and oxides is shown in Figure 4.7.

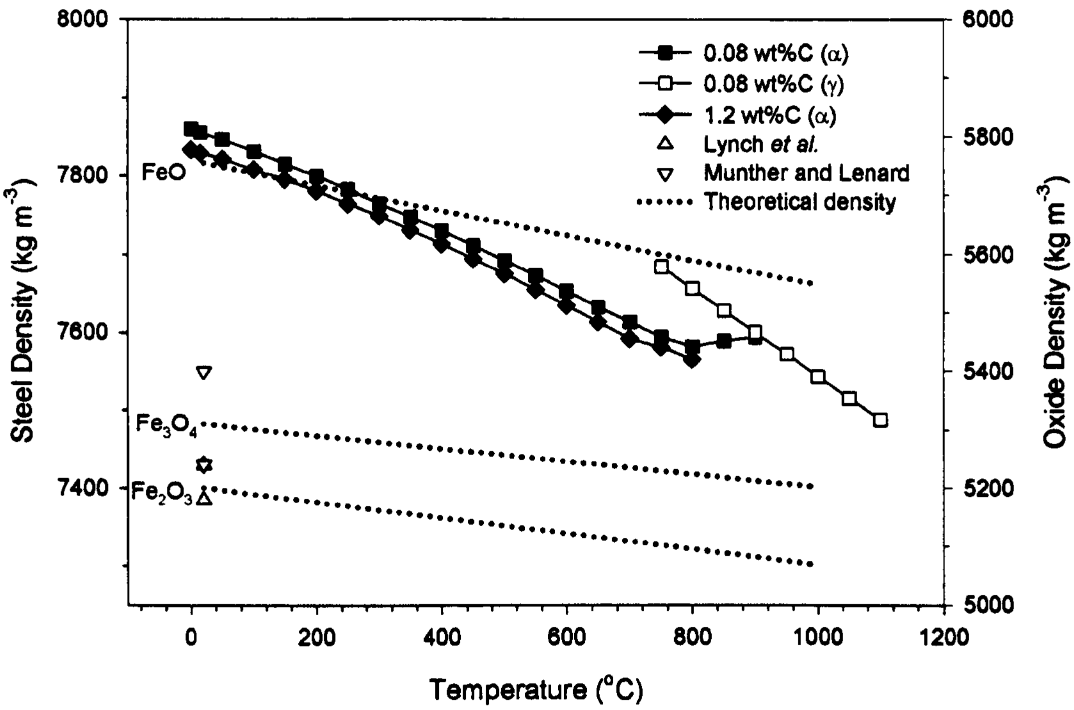

Figure 4.7 – Variation of selected steel densities and theoretical density with temperature compared to selected reported room temperature densities [18,26]. Variation of density with temperature calculated using thermal expansion coefficients of 12.6x10^{-6} [24], 8.8x10^{-6} [25] and 7x10^{-6} [15] for wüstite, magnetite and hæmatite respectively.

As shown in Figure 4.7, neither temperature nor carbon content has a substantial effect on the density of steel. The theoretical oxide density, ρ_{th}, may be calculated using the approach given by West [22]:

$$\rho_{th} = \frac{FW \cdot 1.66 \cdot Z_{cell}}{V} \qquad (4.19)$$

where FW is the formula weight, Z_{cell} is the unit cell content and V is the volume of the unit cell (in Å^3). The parameters for the iron oxides of interest for Equation 4.19 are given in Table 4.4.

Table 4.4 – Molecular properties of selected iron oxides [22].

Oxide	Unit Cell Length (Å)	*FW*	*Z*	ρ_{th} (kg m^{-3})
FeO	4.36	71.846	4	5755.9
Fe_3O_4	8.393	231.539	8	5200.8
Fe_2O_3	6.691	159.692	6	5308.9

Oxide densities reported in the literature are 7750 kg m^{-3} [23], 5250 kg m^{-3} [27] and 5460 kg m^{-3} [19] for wüstite; 5000 kg m^{-3} [23] and 5400 kg m^{-3} [26] for magnetite; and 4900 kg m^{-3} [23] and 5240 kg m^{-3} [26] for hæmatite. In all three cases the theoretical oxide densities broadly agree with the literature values. For wüstite and hæmatite the theoretical densities are slightly greater than the measured densities while the magnetite theoretical density straddles the measured densities. These differences could be accounted for by porosity.

The effect of temperature on the oxide density can be deduced using the following equation:

$$l_T = l_{20}\left[\alpha_c\left(T-20\right)+1\right] \tag{4.20}$$

where l is the unit cell length (in Å), α_c is the thermal expansion coefficient (in K^{-1}) and T is the temperature (in °C). Thus the effect of temperature on the theoretical density of iron oxides is shown in Figure 4.7. Although the effect of increasing thermal expansion with temperature is not accounted for in these estimations, the effect should be minimal, as seen for steel.

4.3. Surface Energy

Surface energy values are employed in a number of different types of calculations, most notably fracture mechanics. However, there is a difference between surface energy during fracture processes and a material's surface energy, which is not always specified. Fracture energy may be measured using notched sample techniques, from which surface energy values are often extrapolated. Alternatively, surface energy values may be estimated using sessile drop techniques. The flaw of this technique is that it inevitably involves liquids contacting solids, thus it is difficult to extrapolate the

Table 4.5 – Room temperature surface energy values for selected metals [28] and selected oxides.

Metal	γ_s (J m^{-2})	Crystal	Face	$\gamma_{s,theory}$ (J m^{-2})	Reference
Fe	1.5	Fe_3O_4	(100)	1.5	[29]
Al	0.9	Fe_3O_4	(110)	1.8	[29]
Be	1.0	Fe_3O_4	(111)	2.2	[29]
Co	1.53	FeO	(100)	0.94	[29]
Cu	1.1	FeO	(100)	1.06*	[30]
Au	1.12	Fe_2O_3	$(10\bar{1}0)$	2.24	[29]
Pb	0.45	Fe_2O_3	(0001)	2.3	[29]
Mg	0.56	Fe_2O_3	$(10\bar{1}2)$	1.95	[29]
Ni	1.7	Al_2O_3	-	0.74	[31]
Pt	1.8	Al_2O_3	$(10\bar{1}0)$	2.89	[32]
Ag	0.92	Al_2O_3	(0001)	2.97	[32]
Zn	0.79	Al_2O_3	$(10\bar{1}2)$	2.57	[32]
		MgO	(100)	1.16	[33]
		MgO	(110)	2.92	[33]
		Cr_2O_3	$(10\bar{1}0)$	2.1	[34]
		Cr_2O_3	(0001)	1.6	[34]
		Cr_2O_3	$(10\bar{1}2)$	1.7	[34]

* estimated for 0 K.

surface energy back to room temperature. A list of the surface energies for selected metals and oxides is given in Table 4.5. The surface energy for elements appears to follow a general trend along the chemical groups with a step increase in surface energy with increasing chemical period, as shown in Figure 4.8. The period of the elements is demonstrated by the relatively consistent behaviour of the elements going across the periodic table. The surface energy for periods III and up has been fitted by the author to the following regression formula:

$$\gamma_s = 10^{-0.11147(Atomic\_Number)+C} \qquad (4.21)$$

where C is a constant that depends on the period, given in Table 4.6. There does not appear to be a direct relationship between the period and the step change in the surface energy so that the surface energy values for other elements of period II cannot be estimated. Furthermore, any estimation of surface energy for additional elements in period III would be dubious given the lack of fit of the curve, particularly given the satisfactory fit in the higher periods. A reason for the decreasing reliability of the equation for the lower periods could be a result of increased quantum effects as the valence electrons become closer to the nucleus.

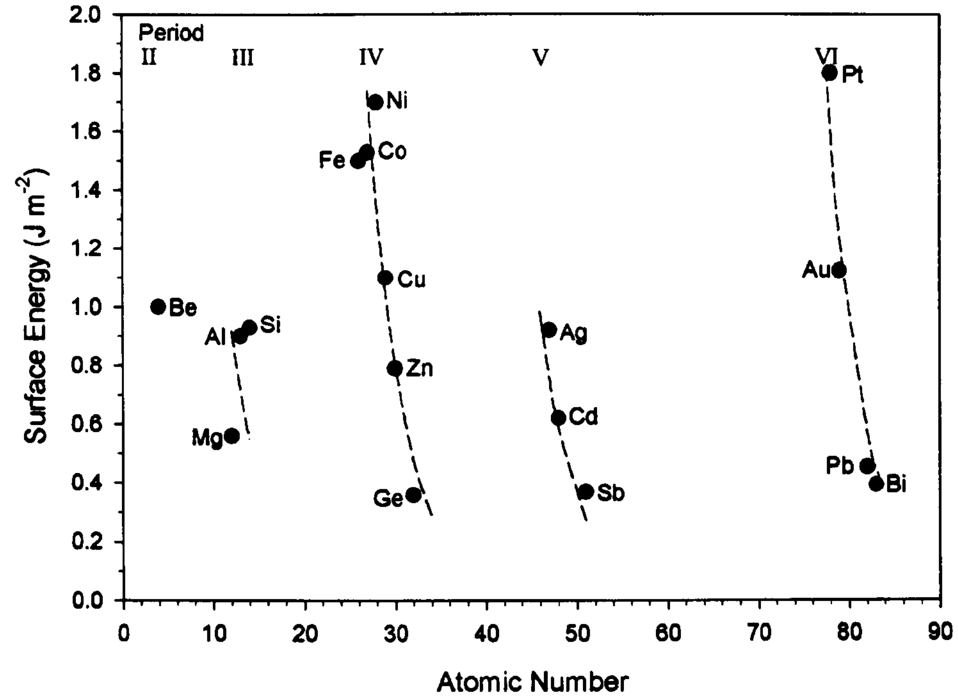

Figure 4.8 – Variation of surface energy with atomic number. Solid symbols represent surface energy data from Rabinowicz [28], dashed lines generated by equation 4.21.

Table 4.6 – C value, as determined by curve fitting techniques, for a given chemical period for equation 4.21.

Period	C
III	1.30
IV	3.25
V	5.12
VI	8.90

From

Table 4.5 it can be seen that compounds do not follow such a convenient pattern as elements since oxides have different surface energies for different cleavage planes. As a first approximation the oxides are assumed to break along the plane of lowest surface energy [4]; for example, the (100) plane for magnetite with an associated surface energy of 1.5 J m^{-2}.

There are some discrepancies in the reported literature as a result of the difficulty in measuring surface energy, which is particularly relevant to compounds. An example of this is the conflicting results for alumina surface energy; it is noted by Livey and Murray [30] that the values for alumina are probably not true reflections of the theoretical value since the surface energy value obtained will vary depending on the conditions of the measurement. If the oxide is ground to expose regular crystal faces and a measurement is made at low temperatures where the ions are immobile, then the surface energy measured will be high. If the oxide is then annealed at high temperature, a low energy surface will be formed and the measured surface energy should drop.

As many metal forming processes take place at temperatures well above room temperature, some properties of surface energy need to be considered to ascertain a relevant surface energy value. In general surface energy, γ_s, is expected to scale to the following proportions [4]:

$$\gamma_s \propto \frac{Z^2}{R_d^3} \tag{4.22}$$

where Z is the ionic charge and R_d is the interatomic distance. Young's modulus also scales according to this ratio, leading to the empirical correlation between Young's modulus and surface energy found by Mecholsky *et al.* [35] of the form:

$$\frac{\gamma}{E} = C_3 \tag{4.23}$$

where C_3 is a constant equal to 0.04 nm. Robertson and Manning [4] have shown that this correlation is closer to C_3 = 0.02 nm for surface fracture energy, in part illustrating the difference between surface fracture energy and surface energy. However, these constants were derived for polycrystals and for the fracture surface energy rather than surface energy. The difference between these values is an increase in surface energy due to the plastic component of fracture. Assuming that this ratio remains constant then it is not unreasonable to assume that surface energy has a temperature dependence, which is in agreement with results compiled by Semenchenko [36] for the surface tensions of liquids where the surface tension decreases with increasing temperature. Since the friction tests were conducted at temperatures well above room temperature, the surface energies should be reduced by the same relative difference experienced by the Young's modulus at that temperature. As a first approximation, the change of Young's modulus with temperature for carbon steel and iron oxides is given in Figure 4.1. The effect of temperature on the surface energy is given by:

$$\gamma_T = \left(1 - \frac{E_0 - E_T}{E_0}\right)\gamma_0 \qquad (4.24)$$

where γ_T is the surface energy at a given temperature, E_0 is the room temperature Young's modulus, E_T is the Young's modulus at a given temperature and γ_0 is the room temperature surface energy. This enables the surface energy for a given temperature to be estimated, assuming that both the variation of Young's modulus with temperature and the surface energy at room temperature are known.

4.4. Conclusions

The fundamental material properties necessary for this project have been defined and, where possible, described as functions of temperature. Many of the properties, particularly for steel, are well established in the literature. Where literature data does not exist, the required information has been extrapolated based either upon available data or theoretical considerations. Examples of this are the modelling of Young's modulus for magnetite and the effect of temperature on the density of oxides. Other properties have required more involved derivations, such as the experimental determination of the stress-strain behaviour with consideration of strain rate for steel and the analogies employed in estimating surface energy for a given temperature.

When extrapolations and analogies have been employed, the reasoning for the steps taken has been elucidated upon and the results tested against experimental data or, when this is not possible, observed physical phenomena. As surface energy estimates were not able to be compared experimental results they were evaluated against the phenomena of materials melting, recognising that the surface energy must reduce with temperature as the surface energy of a liquid will be lower than its solid form.

Overall, the necessary information for modelling friction has been described here. However, a model is only a reflection of reality and is only as good as the information provided to it.

4.5. References

1. P.E. Armstrong "Measurement of elastic constants" in Techniques of Metal Research, Interscience Publishers, Inc., New York, 1971
2. J. R. Nicholls, D. J. Hall and P. F. Tortorelli "Hardness and modulus measurements on oxide scales", Mater. High Temp., 1994, 12, 141-150
3. E. Ryshkewitch "Oxide ceramics: Physical chemistry and technology", 1st ed., Academic Press, New York, 1960, Library of Congress# 60-8056
4. J. Robertson and M.I. Manning "Limits to Adherence of Oxide Scales", Mater. Sci. Technol., 1990, 6, 81-91
5. D. Bruce and P. Hancock "Influence of Mechanical Properties of Surface Oxide Films on Oxidation Mechanisms. Pt. 2. Mechanical Properties and Adhesion of Surface Oxide Films on Iron and Nickel Measured During Growth", J. Inst. Metals, 1969, 97, 148-155
6. D. Bruce and P. Hancock "Influence of Mechanical Properties of Surface Oxide Films on Oxidation Mechnisms. Pt. 1. A Vibrational Technique to Study the Nature and Growth of Thermally Formed Oxide Films on Metals", J. Inst. Metals, 1969, 97, 140-148
7. A. Murthy and J. G. Lenard "Statistical Evaluation of Some Hot Rolling Theories", J. Eng. Mater. Technol., 1982, 104, 47-52
8. S. Shida "Effect of carbon content, temperature and strain rate on compressive flow-stress of carbon steels", Hitachi Research Laboratory, 1974
9. Y. Hidaka, T. Anraku and N. Ostuka "Deformation of iron oxides upon tensile tests at 600-1250°C", Oxid. Met., 2003, 59, 97-113
10. Y. Hidaka, T. Anraku and N. Otsuka "Tensile Deformation of Iron Oxides at 600-1250°C", Oxid. Met., 2002, 58, 469-485
11. P. Hancock and J. R. Nicholls "Failure of oxide scales", Mater. High Temp., 1994, 12, 209-218
12. M. Krzyzanowski and J.H. Beynon "Modelling the boundary conditions for thermo-mechanical processing - oxide scale behaviour and composition effects", Modelling Simul. Mater. Sci. Eng., 2000, 8, 927-945
13. K. Shiba, I. Ioka, J. E. Robertson, M. Suzuki and A. Hishinuma "Mechanical properties of neutron irradiated F82H", Euromat '96, Bournemouth, UK, ed. by Institute of Materials, 21-23 Oct 1996, 265-272
14. H.E. Boyer and T.L. Gall "Metals Handbook", Desk ed., ASM International, 1985, 0-87170-188-X
15. K.A. Solntsev, E.M. Shustorovich and Yu.A. Buslaev "Oxidative constructing of thin-walled ceramics (OCTC)", Doklady Chemistry, 2001, 378, 143-149

16. British Iron and Steel Association "Physical constants of some commercial steels at elevated temperatures", Butterworths Scientific Publications, 1953
17. F. Grønvold and A. Sveen "Heat capacity and thermodynamic properties of synthetic magnetite (Fe_3O_4) from 300 to 1050 K. Ferrimagnetic transition and zero-point entropy", J. Chem. Thermodynamics, 1974, 6, 859-872
18. J.F. Lynch, C.G. Ruderer and W.H. Duckworth "Engineering properties of selected ceramic materials", 1st ed., American Ceramics Society, Columbus, USA, 1966
19. T. Akiyama, G. Ogura, H. Ohota, R. Takahashi, Y. Waseda and J. Yagi "Thermal-Conductivities of Dense Iron-Oxides", Tetsu to Hagane-Journal of the Iron and Steel Institute of Japan, 1991, 77, 231-235
20. T. Akiyama, H. Ohta, R. Takahashi, Y. Waseda and J. Yagi "Measurement and Modeling of Thermal-Conductivity for Dense Iron-Oxide and Porous Iron-Ore Agglomerates in Stepwise Reduction", ISIJ International, 1992, 32, 829-837
21. J. Molgaard and W.W. Smeltzer "Thermal conductivity of magnetite and haematite", Journal of Applied Physics, 1971, 42, 3644
22. A.R. West "Basic solid state chemistry", 2nd ed., John Wiley & Sons, Chichester, 1999, 0-471-987565-5
23. M. Torres and R. Colas "A model for heat conduction through the oxide layer of steel during hot rolling", Journal of Materials Processing Technology, 2000, 105, 258-263
24. G.V. Samsonov "The oxide handbook", 1st ed., IFI/Plenum, New York, 1973,
25. R.M. Hazen and H. Yang "Effect of cation substitution and order-disorder on P-V-T equation of state of cubic spinels", American Mineralogist, 1999, 84, 1956-1960
26. P.A. Munther and J.G. Lenard "The effect of scaling on interfacial friction in hot rolling of steels", Journal of Materials Processing Technology, 1999, 88, 105-113
27. G. Garnaud and R.A. Rapp "Thickness of the oxide layers formed during the oxidation of iron", Oxidation of Metals, 1977, 11, 193-198
28. E. Rabinowicz "Friction and wear of materials", 2nd ed., John Wiley & Sons, Inc., New York, 1995, 0-471-83084-4
29. M.J. Davies and S. C. Parker, Unpublished work
30. D.T. Livey and P. Murray "Surface energies of solid oxides and carbides", J. Am. Ceram. Soc., 1956, 39, 363-372
31. E. Rabinowicz "Friction and wear of materials", 1st ed., John Wiley and Sons, Inc., New York, 1965, Library of Congress # 65-12704
32. P.W. Tasker "Surfaces of magnesia and alumina", Advances in Ceramics, 1984, 10, 176-189
33. P.W. Tasker and D.M. Duffy "The structure and properties of the stepped surfaces of MgO and NiO", Surf. Sci., 1984, 137, 91-102
34. P.J. Lawrence, S. C. Parker and P.W. Tasker "Computer simulation studies of perfect and defective surfaces in Cr_2O_3", J. Am. Ceram. Soc., 1988, 71, C389-391
35. J.J. Mecholsky, S.W. Freimam and R.W. Rice "Fracture surface analysis of ceramics", J. Mat. Sci., 1976, 11, 1310-1319
36. V.K. Semenchenko "Surface phenomena in metals and alloys", 1st ed., Pergamon Press, Oxford, 1961, Library of Congress # 60-53072

Chapter 5 - Theory

5.1. Introduction

There are many theoretical considerations involved in modelling friction; however, the following chapter deals only with the description of the present fundamental model for friction, its application to steel hot rolling and important considerations arising from the contact conditions. To this end the adhesion theory of friction is developed and expanded to account for variations in material properties as a result of the changing temperatures experienced during hot rolling. The resulting friction model is applied to the hot rolling of steel using finite element modelling via a user-defined subroutine for the interface contact boundary condition. However, as the thickness of the oxide layer is orders of magnitude smaller than the thickness of the strip (i.e. microns versus millimetres), it is not viable to model the detail of the oxide layer within the global context of the hot rolling model. Thus it is important to examine the contact conditions with both Hertzian and non-Hertzian contact mechanics.

5.2. Adhesion Theory

Adhesion theory has its roots in the 1700s with simple experiments conducted by Desaguliers [1], as discussed in Chapter 2. His hypothesis was dismissed until the 1950s with experiments conducted by Bowden and Tabor [2,3] who reconciled the apparent incongruity between the experimental independence of friction on contact area and the dependence of adhesion on the contact area in its influence of friction through the concept of real area of contact. Their new theory was expanded upon by Rabinowicz [4] before the theory was generalized to account for different material properties by Straffelini [5]. The dependence of friction on fundamental material properties is further expanded upon in addition to charting the development of the adhesion theory of friction. The majority of the theory was derived by Straffelini [5]; however, not all steps were published thus the derivation was clarified by the author and extended with regards to the method of estimated the thermodynamic work of adhesion term.

Bowden and Tabor [3,6] based their adhesion theory on the following: when surfaces are placed together they make contact over the tips of their asperities and the pressures are extremely high. Over the regions where intimate contact occurs, strong adhesion takes place and the specimens become, in effect, a continuous solid. When the surfaces slide over one another the junctions so formed must be sheared and the force to do this is approximately equal to the frictional resistance. A copper hemisphere sliding over a flat steel surface at an extremely slow speed has been given as experimental evidence for this behaviour. At one point along the wear track the copper has actually lifted a portion of the steel above its original level. Similarly to Amontons' Laws, as a first approximation the coefficient of friction may be taken as:

$$\mu = \frac{F_f}{F_N} = \frac{\tau_m}{p_Y} \tag{5.1}$$

where F_f is the tangential force (i.e. frictional force), F_N is the normal force, τ_m is a mean shear strength, and p_Y is the yield pressure. Thus the friction between clean surfaces is determined by the yield stress and the shear strength of the materials in question, although small amounts of surface contamination can drastically affect adhesion.

Unfortunately adhesion is not a directly observed phenomenon. There are primarily two reasons for this, the first being that in sliding there is more chance of breaking up surface contamination so that the junctions formed may be stronger than those formed under normal loading. The other reason is friction is always measured while the normal load is applied; to study adhesion the normal load must be removed and in the course of removal the elastic stresses will be released breaking the adhered junctions [6], as shown in Figure 5.1.

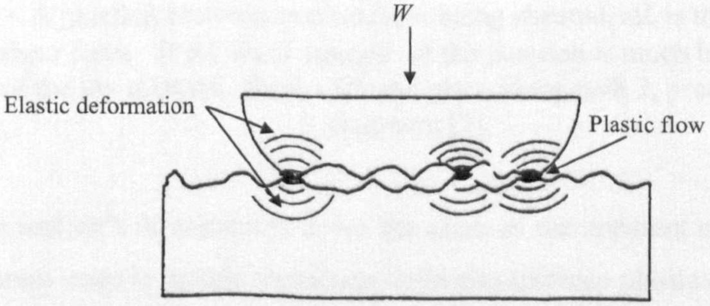

Figure 5.1 – Sketch showing plastic and elastic deformation at the points of contact, where W is the applied normal force [6].

Later Rabinowicz [4,7] considered the case where the surfaces are pressed together by a load and sliding is induced by a shear force. Assuming that when the sliding occurs the total friction force is determined by the mean shear stress multiplied by the real area of contact, i.e.:

$$F_T = \tau_m A_r \tag{5.2}$$

where F_T is a tensile force, A_r is the real contacting area and τ_m is a mean shear stress. The parameter, τ_m, appears in most friction theories but is usually only vaguely defined [5]. Bowden and Tabor [6] consider it to be the surface shear strength of the contacting junctions, which is proportional to the material yield strength, while others simply consider it to be equal to τ_y but suppose that not all junctions are active [8]. Straffelini [5] defines τ_m as the critical value of the local shear stress for the separation of the junctions to take place. From this the coefficient of friction can be derived as the ratio between the average shear stress and the applied pressure. Since the shear stress of the contacting surfaces cannot exceed the bulk shear strength of the weakest material, Rabinowicz [7] postulates that, when the applied shear stress is greater in magnitude than the shear strength, the weaker material at the junction would shear off and adhere to the surface of the stronger material, as shown in Figure 5.2.

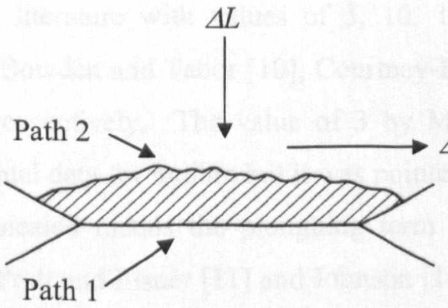

Figure 5.2 – A junction between two surfaces being sheared, ΔL is the applied force and ΔF is the shear force. If the shear strength of the junction is much bigger than the bulk strength of the top material, shear will take place along path 2, producing the shaded fragment [7].

The real area of contact is never the same as the apparent contact area (i.e. the projected area) since in metals contacting asperities undergo plastic deformation even at very low applied loads, thus the real area of contact can be expressed by [3]:

$$A_r = \frac{F_N}{p_y} \tag{5.3}$$

where F_N is the applied load (in N) and p_y is the material yield pressure (in N m^{-2}). From this it can be seen that as the load increases, the real area of contact increases, assuming that the pressure does not exceed $1/\sqrt{3}$ times the material yield stress, as a result of the von Mises yield criterion. This is due to the increased number of contacting asperities, N, which may be expressed as [2]:

$$N = \frac{A_r}{\pi r^2} = \frac{F_N}{p_y \pi r^2} \tag{5.4}$$

where r is the average junction radius (in m). However, if the contacting surfaces are sliding the junctions will be continuously breaking and reforming at other areas. The junctions will be broken when the local shear stress reaches a critical value, τ_m. The presence of a local critical shear stress implies plastic flow of each asperity, resulting in an increase in real contact area, which, following Bowden and Tabor [2], can be written as:

$$\left(\frac{F_N}{A_r}\right)^2 + \alpha\left(\frac{F_T}{A_r}\right)^2 = p_Y^2 \tag{5.5}$$

where F_N is the normal force, F_T is the friction (i.e. shear) force and α is a constant. Values for α vary in the literature with values of 3, 10, 12 and 25 suggested by McFarlane and Tabor [9], Bowden and Tabor [10], Courtney-Pratt and Eisner [11] and Tabor [12]/Ludema [13] respectively. The value of 3 by McFarlane and Tabor [9] agreed well with experimental data for indium but it was pointed out later by Tabor [12] that with soft or fully annealed metals the ploughing term is no longer negligible. Experiments by Courtney-Pratt and Eisner [11] and Johnson [14] measured the increase in contact area as a result of applied normal and tangential forces agreed well with equation 5.5 for copper wedges and platinum cones when α was 12. Tabor [12] comments that where electrical resistance measurements are used, contamination will tend to give a higher resistance and hence a lower area of contact. He concludes that a value of 12 for platinum would not seem unreasonable if some work-hardening occurs to raise the effective shear stress of the metal. The value of 25 is a result of the assumption that the uniaxial yield strength of metals is approximately 5 times their shear strength. The value of 25 is unreasonably high since this result is from measurements of yield strength and shear strength in plane stress and is unlikely to apply to the complex stress states involved in the 3-D deformation of an asperity [13]. Discounting values for α of 3 and 25 as unrealistic, the difference between 10 and 12 for α is more significant with larger values of μ; however Bowden and Tabor [10] do not justify their choice of 10 beyond a convenient approximation while also quoting Courtney-Pratt and Eisner's [11] experimental value of 12 for α. Thus, assuming a value of 12 for α, the real area of contact can then be defined in terms of the friction coefficient (i.e. $F_T = \mu F_N$) as:

$$A_r = \frac{F_N}{p_Y}\sqrt{1+12\mu^2} \tag{5.6}$$

The average asperity junction radius, r, may be estimated in the following form [4,5]:

$$r = \frac{C_1}{p_y} \tag{5.7}$$

where r is the average junction radius (in m), C_1 is a proportionality constant (in MN m^{-1}) and p_y is the yield pressure of the softer material (in MPa). Rabinowicz [4] uses C_1 equal to 0.0012 to give values for of r varying between 5 and 15 μm depending upon the materials involved. Lim and Ashby [15] note that the average asperity radius is typically between 1 and 10 μm, with the argument that it is the number of contacting asperities that change with pressure rather than the size of the junction. Straffelini [5] uses a value C_1 of 0.002 MN m^{-1} to estimate the average asperity junction radius, according to data from Chowdhury and Pollock [16].

Rabinowicz [4] modelled the adhesive interaction between a hard asperity and a soft, flat surface using an energy balance approach. If the deformation energy is not significant the force of adhesion, F_{ad}, is given by:

$$F_{ad} = 2\pi r W_{ab} \cot\theta \tag{5.8}$$

where r is the impressed radius of the impressed asperity, θ is the angle formed by conical asperity with the nominal horizontal line or roughness angle, shown in Figure 5.3, and W_{ab} is the thermodynamic work of adhesion.

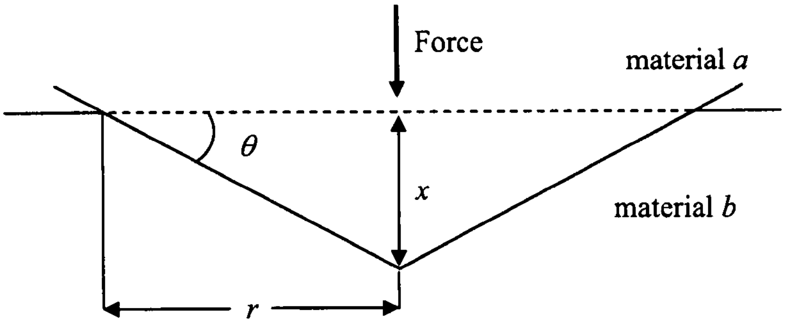

Figure 5.3 – Elucidation of the definition of asperity radius, *r*, and roughness angle, *θ*, in equation 5.8.

The assumption that the deformation energy is not significant appears to be reasonable as the expression for adhesion force is similar to the model developed by Johnson *et al.* [17], who developed their model, known as the JKR model, as a result of experimental contradictions to the Hertz [18] theory of elastic contact. The JKR model is given by:

$$F_N = -\frac{3}{2}\gamma_{ad}\pi R'' \tag{5.9}$$

where F_N is the normal force required to just separate the spheres (i.e. adhesive force), γ_{ad} is the energy of adhesion of both surfaces and R is the relative radius of curvature (i.e. $R'' = R_1R_2/(R_1+R_2)$). The 3/2 constant appearing in the JKR model is for elastic contact but would change to 2 for the case of plastic contact [19].

Applying Rabinowicz's adhesion model to all contacting asperities, i.e. multiplying equation 5.8 by equation 5.4 and substituting equation 5.6 for the real area of contact, the total force of adhesion, F_{AD}, during sliding is given by:

$$F_{AD} = 2F_N \frac{W_{ab}\cot\theta}{p_Y r}\sqrt{1+12\mu^2} \tag{5.10}$$

The thermodynamic work of adhesion, W_{ab}, is expressed by [20]:

$$W_{ab} = \gamma_a + \gamma_b - \gamma_{ab} \tag{5.11}$$

where γ_a and γ_b are the surface energies of the two mating surfaces and γ_{ab} is the interface energy. Particularly for the case of metals, W_{ab} is strongly affected by contaminants, which tend to reduce it [4]. Since the interaction of asperities is also characterised by irreversible phenomena, such as plastic deformation, the thermodynamic work of adhesion should be substituted by the effective work of adhesion, G_c, such that $G_c > W_{ab}$, or simply $G_c = C_2 \cdot W_{ab}$ where Straffelini [5] estimates C_2 to be 4.

Unfortunately the thermodynamic work of adhesion term is poorly characterised since it relies on knowing the surface energy of the combined material, γ_{ab}. Two methods have been developed to estimate the thermodynamic work of adhesion. The first method, by Rabinowicz [7], utilises a compatibility parameter and has been applied to metal and non-metal systems. The second method was originally developed for calculating the interfacial tension of liquids by Girifalco and Good [21] but here it has been applied to metal and non-metal systems.

In the absence of detailed information for the γ_{ab} term, Rabinowicz [7] suggests that a compatibility parameter may be used to estimate the thermodynamic work of adhesion, i.e.:

$$W_{ab} = c_m (\gamma_a + \gamma_b) \tag{5.12}$$

where c_m is the compatibility parameter for the metals a and b and always lies in the range of zero to one. The value of c_m is assigned primarily by the metallurgical compatibility of the metals, as determined by their binary phase diagram. According to Rabinowicz [7] a metal pair is said to be compatible if their binary phase diagram shows liquid miscibility of at least 1% by volume, and at room temperature either complete solid solubility of the two metals or else 100% solid solubility of one metal in the other through a limited composition range; for example, the 100% solid solubility of cadmium in silver up to approximately 40 at% cadmium. Identical metal pairs are assumed to be perfectly compatible. Partially compatible metal pairs form one solution when they are melted together, and at room temperature have limited solubility between 0.1 at% and 1 at%. Partially incompatible metal pairs form one solution when molten but have very limited solid solubility (less than 0.1 at%) at room temperature. Incompatible metal pairs form two phases when molten and generally have very small solid solubility. A similar relationship exists for non-metals with the same procedure for obtaining the compatibility coefficient, given by:

$$W_{ab} = c_n (\gamma_a + \gamma_b) \tag{5.13}$$

where c_n is the non-metal compatibility parameter, determined in a similar manner to the metal compatibility parameter. The compatibility parameters are given in Table 5.1.

Table 5.1 – Summary of Rabinowicz's compatibility parameters [7].

Parameter	Identical	Compatible	Partially Compatible	Partially Incompatible	Incompatible
c_m	1.00	0.50	0.32	0.20	0.12
c_n	1.00	0.60	-	-	0.36

Part of the physical basis behind the choice of the compatibility parameters is that when the contacting materials are identical the formula reduces to the thermodynamic work of cohesion, W_{coh}, given by:

$$W_{coh} = 2 \cdot \gamma_a \tag{5.14}$$

The main shortcomings of this method are the relatively arbitrary nature of the compatibility parameters and the method's inability to estimate the thermodynamic work of adhesion for any pair of materials that falls outside these definitions.

By analogy to the Berthelot [22] relation for the attractive constants between like and unlike molecules, Girifalco and Good [21] estimate the thermodynamic work of adhesion to be:

$$W_{ab} = 2\Phi\sqrt{\gamma_a \gamma_b} \tag{5.15}$$

where Φ is a function of the molar volumes of the two liquids and γ is the surface energy of the respective liquid. The physical representation of this relationship is illustrated in Figure 5.4. Applying the geometric mean rule to solid systems, Φ becomes the ratio of molar volumes of the contacting materials, where Φ is less than one. As Φ represents a physical property, it is inherently temperature dependent, albeit weakly, since molar volume is the ratio of density to molecular mass. As with the Rabinowicz method for estimating the thermodynamic work of adhesion, the geometric mean rule also reduces to the thermodynamic work of cohesion formula for identical contacting materials.

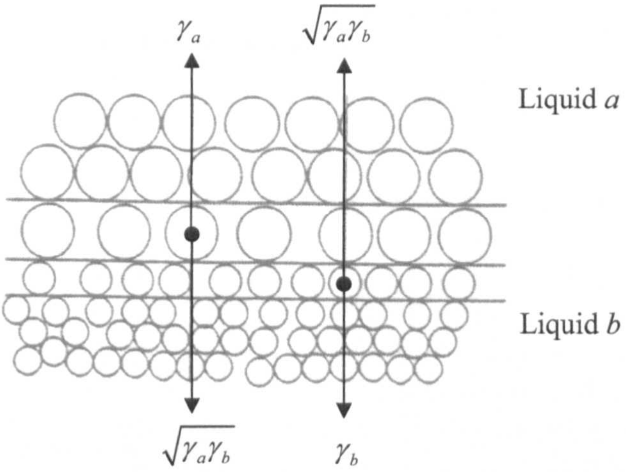

Figure 5.4 – The physical representation of the geometric mean rule applied to two liquids [23].

As has been seen earlier, in order to model friction force using the adhesion theory the junction shear strength must be estimated. It is considered in this formulation that the junction shear strength depends directly on the friction force during sliding. From equations 5.2, 5.6 and 5.10 and setting $F_T = \beta F_{AD}$, the junction shear strength can be estimated by:

$$\tau_m = 2\beta \frac{G_c \cot\theta}{r} \tag{5.16}$$

The value for the constant β is 0.5 [16], reflecting the irreversible nature of the shearing process and refers to the Tresca yield criterion [5]. This remains a relatively contentious point as there is usually significant scatter in friction testing experiments; however AFM experiments by Ando *et al.* [24] and Ando and Ino [25] support this supposition. A more useful relation can now be obtained between the friction coefficient, the effective work of adhesion and the roughness angle by combining equations 5.2, 5.6, 5.7 and 5.16 to give:

$$\frac{\mu}{\sqrt{1+12\mu^2}} = 5\times10^{-4} G_c \cot\theta \tag{5.17}$$

Based on experimental friction coefficient data of pin-on-disk dry sliding of copper on copper and aluminium on aluminium, shown in Figure 5.5, an equilibrium roughness angle of $\theta = 0.9°$ was determined.

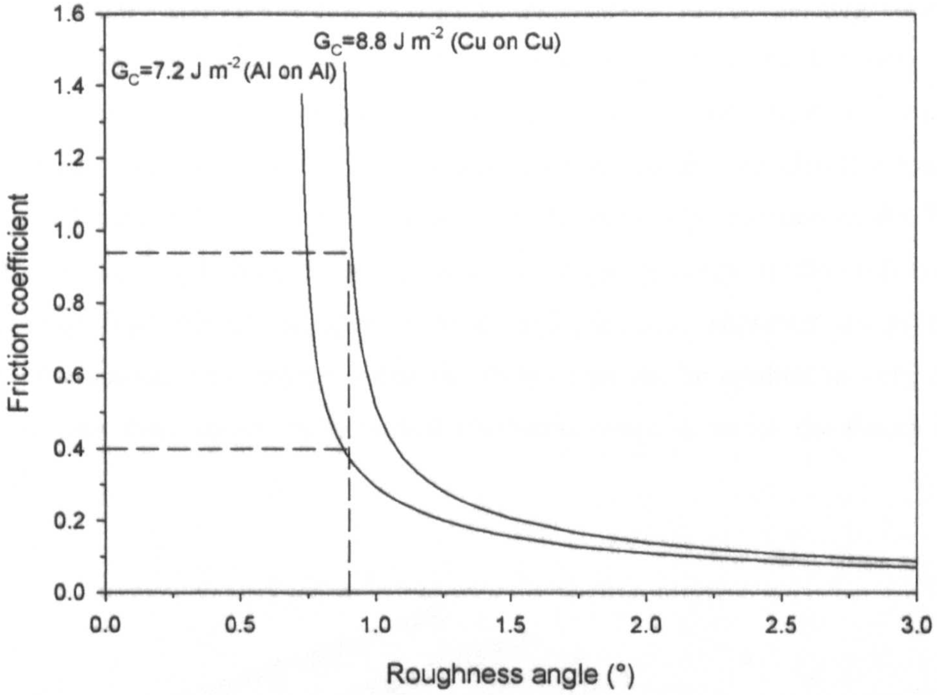

Figure 5.5 – The solid curves represent the effective work of adhesion for the copper-copper and aluminium-aluminium systems from equation 5.17. The horizontal dashed lines represent experimental friction coefficients for copper on copper ($\mu = 0.9$ [4]) and aluminium on aluminium ($\mu = 0.4$ [7]). The vertical dashed line indicates the intersection of the experimental data with the respective effective work of adhesion curves, both of which intersect at the roughness angle of 0.9°, defining the equilibrium roughness angle.

The fact that a single value for the roughness angle describes both the copper on copper system and the aluminium on aluminium system is due to both systems being fcc and having similar abilities for plastic deformation. Further evidence with respect to the development of an equilibrium roughness angle is given by Straffelini [5] who conducted dry sliding tests using a copper alloy disc and a tool steel block. The steel block was given an initial roughness value of 0.02 μm *Ra* for one test and 0.22 μm *Ra* for a second test; the recorded friction coefficient trace showed a consistent friction coefficient for the first two minutes of the test representing a "running-in" period. The constant friction coefficient is established almost immediately while observations after 40 seconds of sliding showed the steel block's new roughness was 0.01 μm *Ra*, although not stated it is implied that this was true for both blocks with the different initial roughness. The trace shows a transition region with a slight variation between the smooth and rough blocks' friction coefficient before another equilibrium friction coefficient is established. The blocks' surfaces at the end clearly show the presence of numerous copper particles firmly adhered to the blocks. Studies of single asperities have shown that under high loads there is a lateral displacement of surface material [26] whereas studies involving multiple asperities have shown plastic flow of the asperity tips resulted in partially filled valleys [27-30]. This implies that the effective roughness angle is established by the process rather than the surface preparation in the form of prior machining or grinding. In the literature the roughness angle is often referred to as the asperity slope, whose definition is shown in Figure 5.6. However, the asymptotic nature of equation 5.17 indicates that the theory can not be applied to very smooth surfaces, thus there should be a limited roughness range in which the theory can be applied.

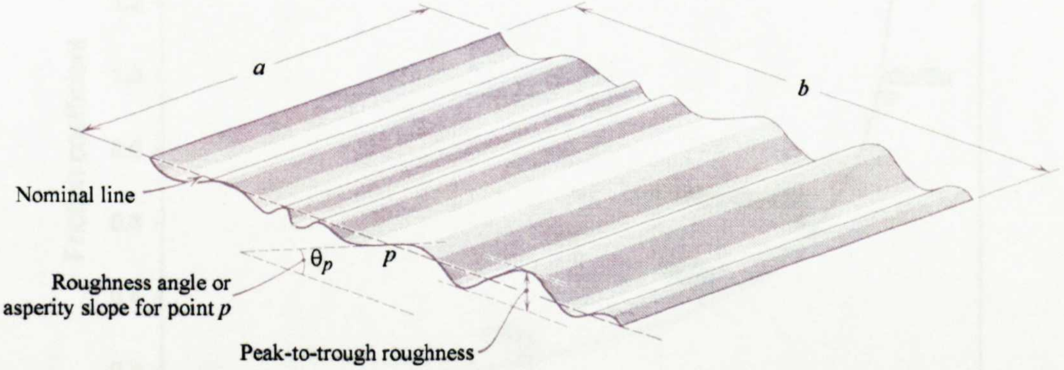

Figure 5.6 – Definitions of the roughness angle, or asperity slope, and peak-to-trough roughness [4].

The obtained equilibrium roughness of 0.9° is in line with post-sliding contact experiments by Tanaka *et al.* [31] who measured a mean peak slope of 0.70° for a carbon-carbon sliding contact of a computer hard drive simulation. In experiments involving polymethyl methacrylate (PMMA), Jain and Bahadur [32] report the variation of roughness angle is approximately proportional to the root mean square (RMS) roughness with minimal change in slope for the duration of a sliding test. Tallian [33] reports that a finely finished bearing surface can have an roughness angle of 0.81° whereas a relatively rough bearing surface can have an roughness angle of 3.44°. Hisakado and Suda [34] give the roughness angle of an abrasive grain, i.e. polishing paper grit, to be around 50°. Barwell *et al.* [30] measured the average roughness angle for a finely finished hardened steel piston, as used in aircraft practice, to be 0.16°, ranging to 3.1° and 7.35° for medium and rough finishes respectively.

The above analysis results in a single relationship for fcc metals between friction coefficient and thermodynamic work of adhesion by substituting $G_c = 4 \cdot W_{ab}$ into equation 5.17 with a roughness angle of 0.9° to give:

$$\frac{\mu}{\sqrt{1+12\mu^2}} = 0.127 \cdot W_{ab} \tag{5.18}$$

Equation 5.18 is compared with experimental sliding friction data in Figure 5.7.

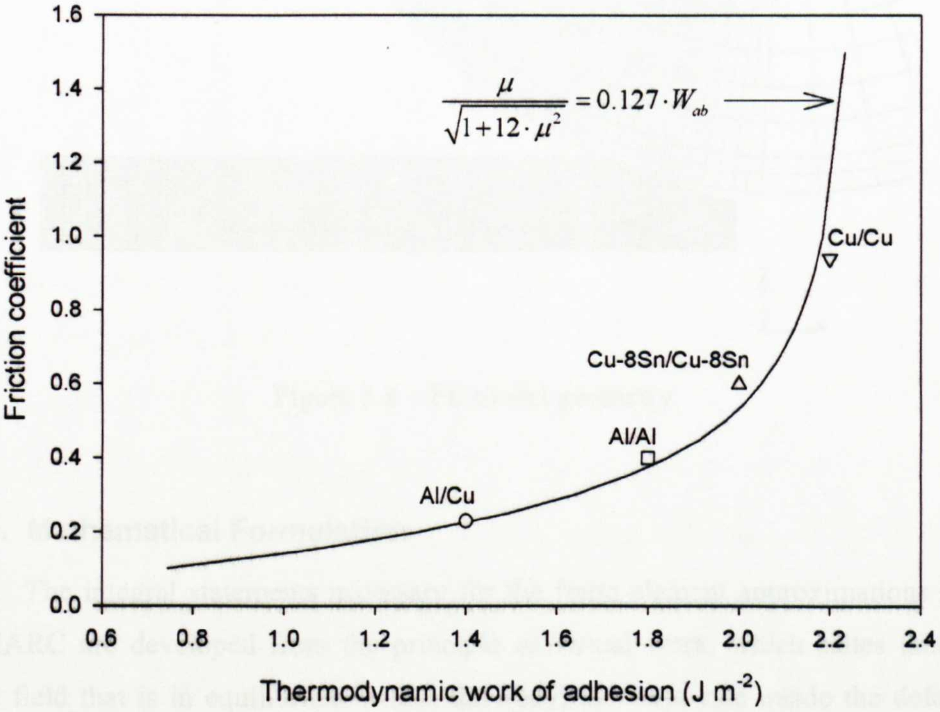

Figure 5.7 – Simplified adhesion theory compared to experimental data for fcc systems. Friction coefficient data obtained from [5,7,35,36]; thermodynamic work of adhesion calculated with surface energy data from [7].

5.3. Finite Element Modelling

The complex thermomechanical processing history during hot rolling means that modelling of the laboratory rolling experiment is necessary to correctly interpret the test. A powerful modelling technique is the finite element (FE) method, which enables the temperatures, stresses and strains to be predicted and validated against experimental data, typically temperature profiles. Furthermore, FE allows the inclusion of user-defined algorithms to calculate physical phenomena, such as microstructure or, as used in this research, friction. The rolling model used here was a 2-D, thermo-mechanically coupled model assuming a thin, adherent scale layer, the geometry of which is given in Figure 5.8, using the commercial finite element code MARC.

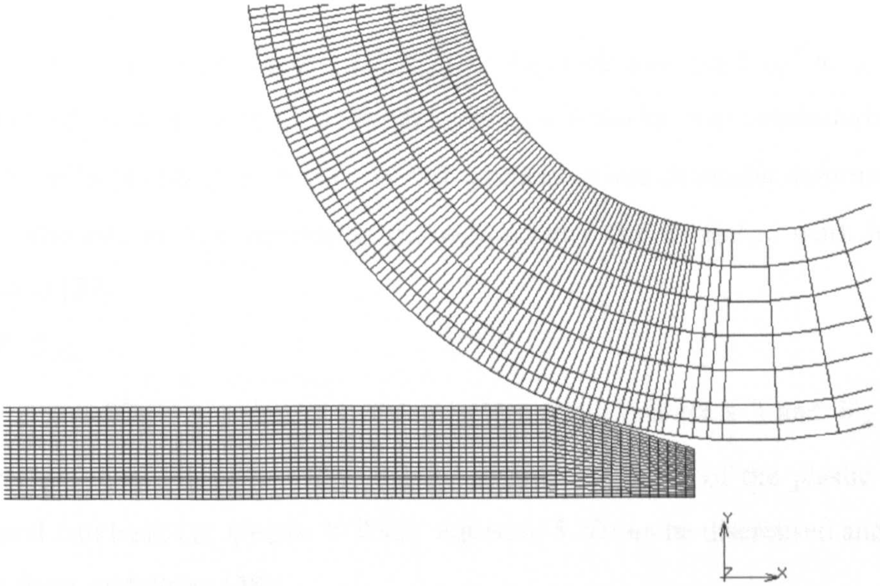

Figure 5.8 – FE model geometry.

5.3.1. Mathematical Formulation

The integral statements necessary for the finite element approximations solved by MARC are developed from the principle of virtual work, which states that for a stress field that is in equilibrium within the body, the work-rate inside the deforming body equals the work-rate done by the surface traction's for all velocity fields that are continuous and continuously differentiable.

Based on the principal of virtual work, the deformation process during hot rolling is modelled by:

$$\int_S [t]\cdot[\partial u]dS + \int_V [f]\cdot[\partial u]dV = \int \sum [\sigma]\cdot\left(\frac{\partial[\partial u]}{\partial[x]}\right)dV \qquad (5.19)$$

where $[t]$ is the traction force matrix per unit area, $[\partial u]$ is the displacement field, $[f]$ is the force matrix per unit volume, $[\sigma]$ is the true stress or Cauchy stress matrix and $[x]$ is the direction matrix (i.e. *x*, *y*, or *z* directions).

During the hot rolling process the temperature distribution within the strip is calculated using the unsteady-state heat conduction equation, according to:

$$\frac{\partial}{\partial x}\left(k\cdot\frac{\partial T}{\partial x}\right)+\frac{\partial}{\partial y}\left(k\cdot\frac{\partial T}{\partial y}\right)+\dot{Q}=\rho\cdot C_p\cdot\frac{\partial T}{\partial t} \tag{5.20}$$

where ρ is the strip density (in kg m^{-3}), C_p is the specific heat (in J kg^{-1} K^{-1}), T is the temperature of the strip (in °C), t is the time (in s), k is the thermal conductivity of the strip (in W m^{-1}K^{-1}) and $\dot{Q}$ is the rate of heat generation due to plastic deformation (in W m^{-3}). The rate of heat generation per unit volume due to plastic work has been quantified as [37]:

$$\dot{Q}=\eta\cdot\dot{\bar{\varepsilon}}\cdot\bar{\sigma}_{flow} \tag{5.21}$$

where η is an efficiency term, $\dot{\bar{\varepsilon}}$ is the effective strain rate (in s^{-1}) and $\bar{\sigma}_{flow}$ is the effective flow stress (in MPa). The model assumes that 95% of the plastic work is transformed into heat, i.e. η equal to 0.95. Equation 5.20 can be discretised and written in matrix form, as follows [38]:

$$[C_P]\{\dot{T}\}+[K_C]\{T\}=\{Q\} \tag{5.22}$$

where $[C_P]$ is the heat capacity matrix, $\{\dot{T}\}$ is the rate of temperature change vector, $[K_C]$ is the heat conduction matrix, $\{T\}$ is the temperature vector and $\{Q\}$ is the heat flux vector.

5.3.2. Boundary Conditions

Thermal boundary conditions for the rolling model were selected to describe the interface heat transfer conditions at the strip centreline, the inside radius of the work roll and at the interface between the strip and work roll.

Symmetry conditions have been assumed about the centreline of the strip for the rolling simulations. The thermal boundary condition for symmetry can be expressed as:

$$-k\cdot\frac{\partial T}{\partial y}=0 \quad @\ t>0;\ y=0 \tag{5.23}$$

where k is the thermal conductivity of the strip. A displacement boundary condition was also applied to prevent movement of the centreline in the y-direction.

The adiabatic thermal boundary condition at the inside radius of the work roll has been represented by:

$$-k \cdot \frac{\partial T}{\partial r} = 0 \quad @\ t>0, r = r_i \tag{5.24}$$

where k is the thermal conductivity of the work roll (in W m^{-1} K^{-1}). To ensure this condition is valid the model thickness of the work roll must be sufficient to avoid increases in temperature along the inner radius.

The thermal boundary condition between the strip and the work roll can be expressed as:

$$-k \cdot \frac{\partial T}{\partial y} = h \cdot \left(T_{strip} - T_{workroll}\right) \quad @\ t>0;\ y = \frac{Y(t)}{2} \tag{5.25}$$

where k is the thermal conductivity of the strip (in W m^{-1} K^{-1}) and h is the interface heat transfer coefficient at the interface (in W m^{-2} K^{-1}).

5.3.2.1. Friction Algorithm

The friction between the work roll and strip is a mechanical boundary condition that plays a role in determining the amount of shear deformation experienced by the strip. Typically a constant, average value is used in the FE calculations ranging from 0.3 for industrial rolling to as high as 0.5 under laboratory rolling conditions. For this study a friction algorithm has been developed, based on the theory above, that enables an instantaneous friction coefficient to be calculated throughout the roll bite.

The friction algorithm consists of passing the instantaneous surface temperature to the user-defined subroutine. Within the user-defined subroutine the effect of the temperature on the Young's modulus of the two materials, i.e. steel work roll and surface scale, is translated into energy values at that particular temperature. These surface energy values are used to calculate the work of adhesion term, which is then used to calculate the friction coefficient. Frictional heating is automatically incorporated in the solution by MARC but, in general, the heat generated as a result of friction, T_f, can be estimated using the following [39]:

$$T_f = \frac{\mu \cdot p \cdot v \cdot A \cdot \Delta t}{\rho \cdot C_p \cdot V} \tag{5.26}$$

where μ is the friction coefficient, p is the normal stress (in Pa), v is the sliding velocity (in m s^{-1}), A is the surface area at the material/tool interface (in m), Δt is the time interval (in s), ρ is the density of the material (in kg m^{-3}), C_p is the heat capacity of the material (in J kg^{-1} K^{-1}) and V is the volume subjected to the temperature rise (in m^3).

Once the rise in temperature due to friction does not change the friction coefficient beyond a given tolerance level the algorithm proceeds to the next step. This enables the algorithm to calculate an instantaneous friction coefficient throughout the roll bite and, using the FE model, the friction coefficient profile, the surface and contact forces throughout the roll bite are then known. The friction algorithm is graphically demonstrated in the flow diagram shown in Figure 5.9.

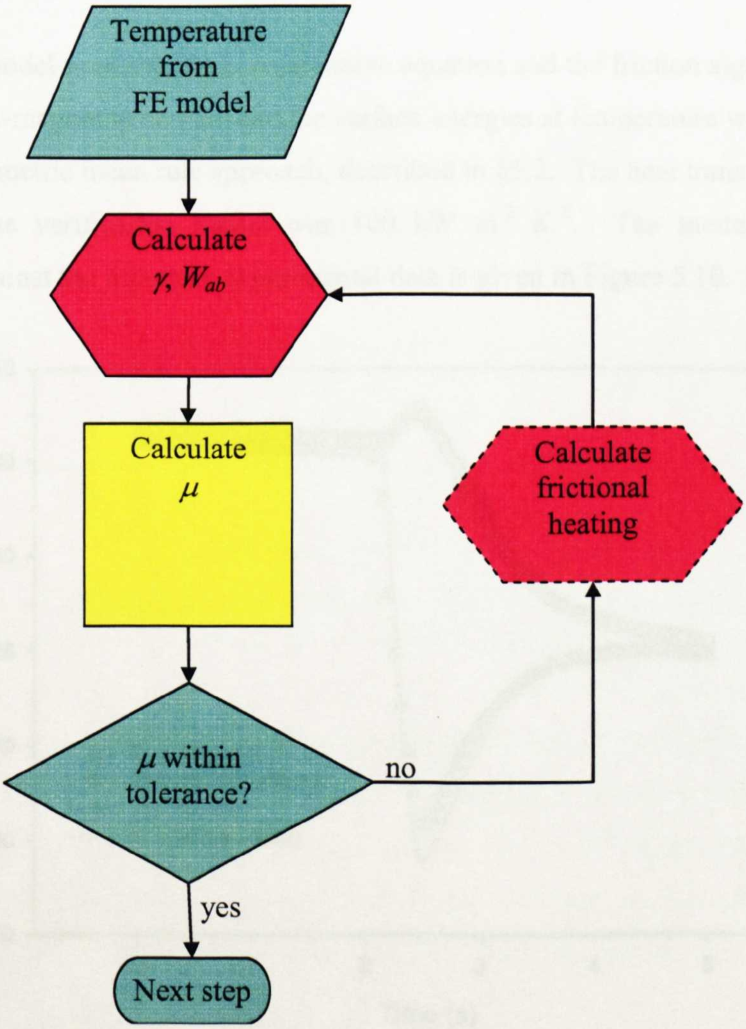

Figure 5.9 – Flow chart demonstrating the friction algorithm.

5.3.3. Model Results

To gain confidence in the model it has been validated against literature experimental temperature data under conditions similar to the experimental conditions used in this study [40]. The principal differences between the two experiments are the sample chemistry, the lack of a descaling pass for the literature data, literature sample thickness of 18 mm as compared to approximately 27 mm after a descaling pass and an initial rolling temperature of approximately 1025°C. The literature sample chemistry is given in Table 5.2.

Table 5.2 – Sample chemistry for the literature experimental data in wt%, rem. Fe [40].

C	S	P	Si	Mn	Cr	Ni	Mo
0.12	0.005	0.015	0.57	0.59	1.31	0.02	0.55

The model used the Shida constitutive equation and the friction algorithm, which assumed steel-magnetite contact and the surface energies at temperature were calculated using the geometric mean rule approach, described in §5.2. The heat transfer coefficient applied in the verification model was 100 kW m^{-2} K^{-1}. The model temperature prediction against the literature experimental data is given in Figure 5.10.

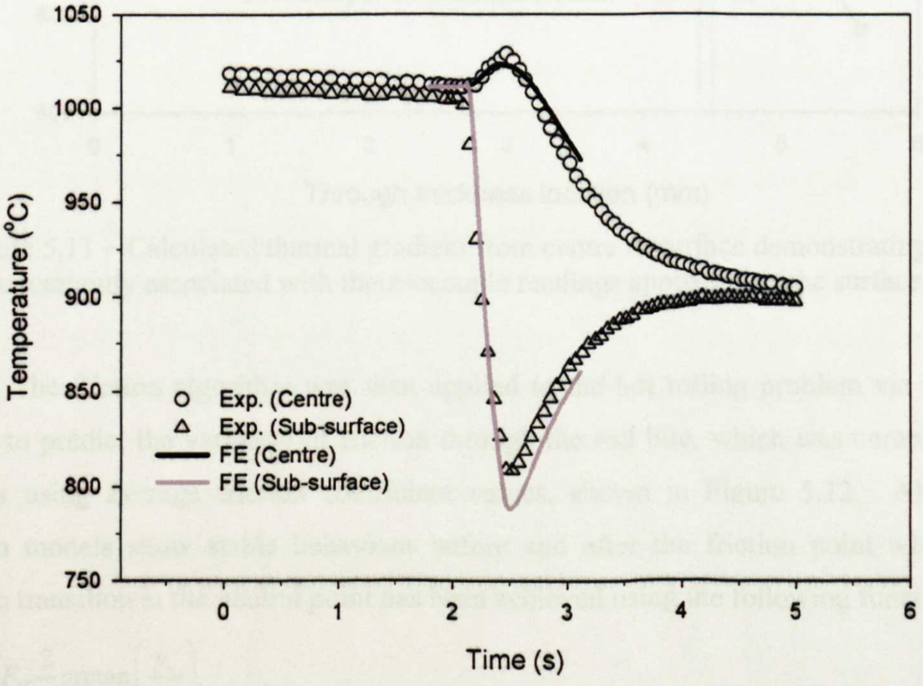

Figure 5.10 – Temperature comparison of literature of literature experimental data [40] and model predictions.

The fit of the model to the experimental data is quite good, particularly at the centreline, giving good confidence in applying the model results to the problem of friction during hot rolling. The comparison between the sub-surface model prediction and experimental temperature is also satisfactory despite the 20°C difference at the roll bite exit. This is a result of the steep temperature gradient that exists near the sample surface and the uncertainty of the exact location of the thermocouple weld bead, demonstrated in Figure 5.11, which is more than the 20°C by which the model prediction is out.

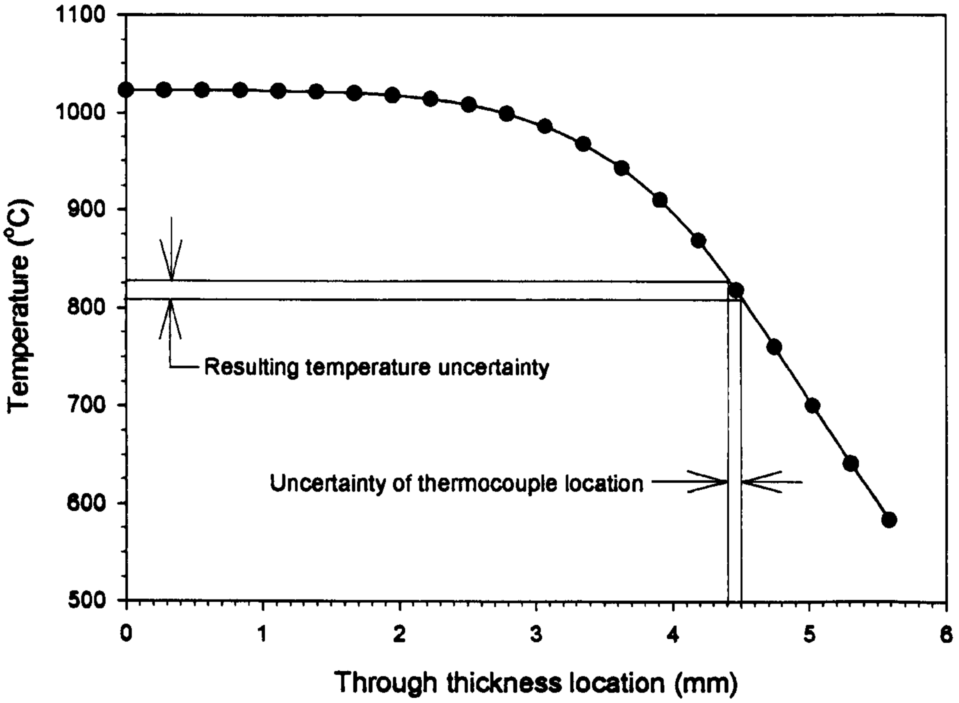

Figure 5.11 – Calculated thermal gradient from centre to surface demonstrating the uncertainty associated with thermocouple readings approaching the surface.

The friction algorithm was then applied to the hot rolling problem via the FE model to predict the variation of friction through the roll bite, which was compared to models using average friction coefficient values, shown in Figure 5.12. All three friction models show stable behaviour before and after the friction point while the smooth transition at the neutral point has been achieved using the following function:

$$F_T = \mu F_N \frac{2}{\pi} \arctan\left(\frac{v_r}{C_4}\right) \qquad (5.27)$$

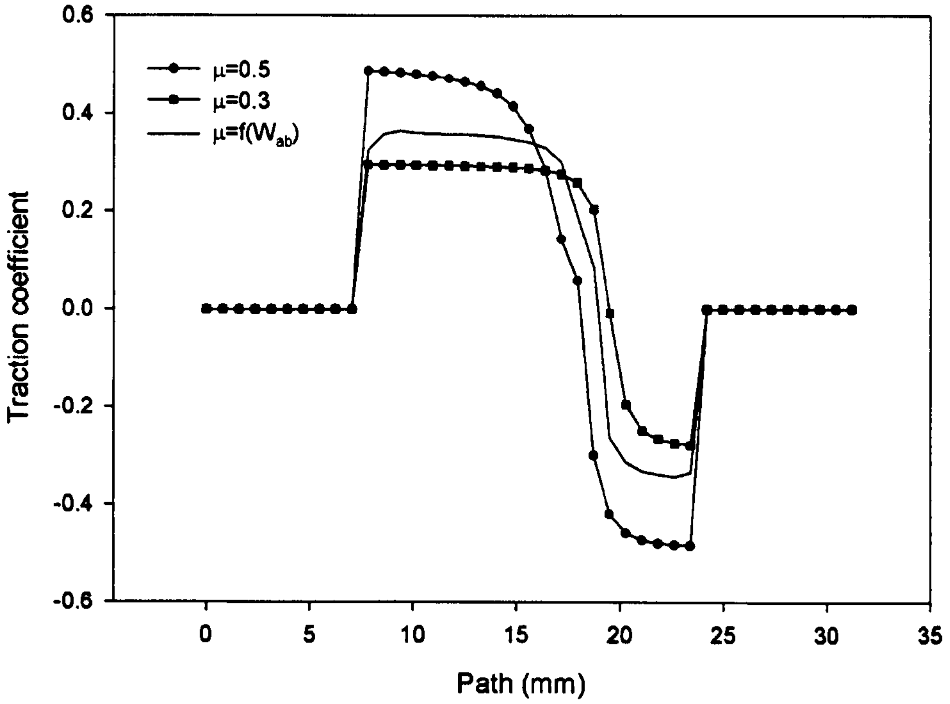

Figure 5.12 – Prediction of the variation of the friction coefficient through the roll bite.

where μ is the friction coefficient depending on the rolling condition, F_T is the tangential force, F_N is the normal reaction, v_r is the relative sliding velocity and C_4 is a constant that has a typical value of 10% of a mean sliding velocity. This formulation is necessary to prevent numerical instabilities at the neutral point within the FE model. The adhesion theory of friction, as described earlier, estimates that the friction coefficient at the entry to the roll bite is around 0.18. This is not shown in Figure 5.12 as a result of the resolution of the FE mesh combined with the rapid drop in surface temperature. The normal and shear stresses through the roll bite are given in Figure 5.13. The friction algorithm predicts intermediate values for both normal and shear stresses compared to the cases of constant friction coefficients. As the shear stress is a result of the friction coefficient it follows that the trends displayed by the normal and shear stresses are similar to that of the friction coefficient. Also, the lower shear stresses expected at the entry to the roll bite are lost in the mesh resolution.

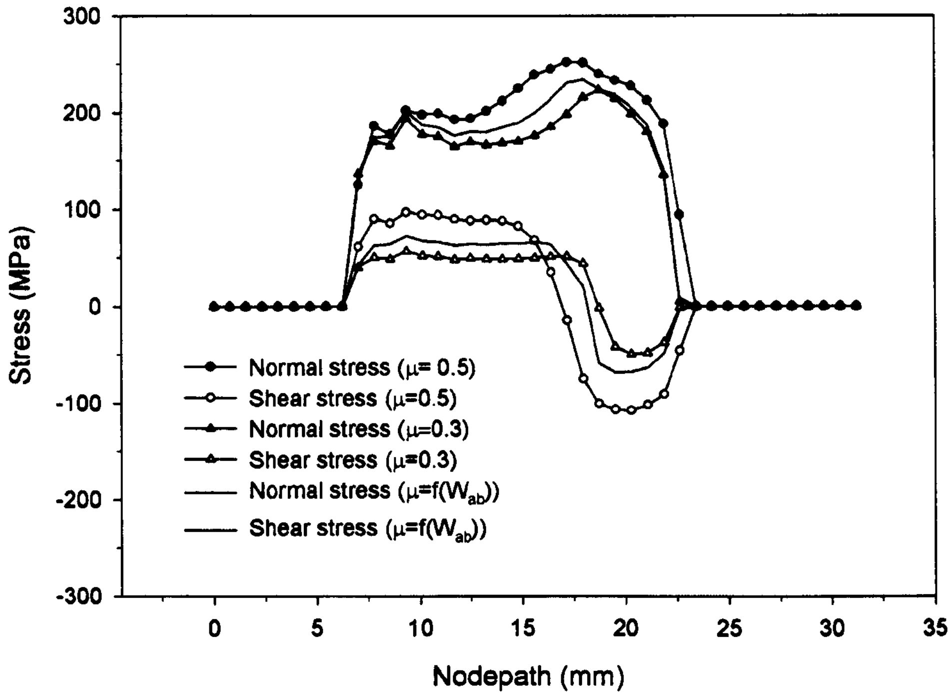

Figure 5.13 – Prediction of the variation of normal and shear stress through the roll bite.

From a practical viewpoint Figure 5.13 demonstrates that the variation in friction coefficient throughout the roll bite does not have a significant impact on the magnitude of the stresses experienced by the strip.

5.4. Contact Mechanics

The relative scale of the reciprocating friction testing is not conducive to FE modelling since the thickness of the elastic layer (i.e. oxide layer) is large compared to the surface features (i.e. asperities). Contact mechanics can be split into two distinct categories: with or without friction. If a single layer is assumed then Hertzian contact may be used. The calculations become significantly more difficult when multiple layers are considered, requiring the use of Non-Hertzian contact formulations.

The first concise analysis of the stresses resulting from the contact of two elastic solids was undertaken by Hertz [18] in 1882. The method employing Hertz's formulation but extended to include Amontons' Law for friction was developed by

McEwen [41] in 1949 for contacting cylinders in plane strain. McEwen determined the stresses at any point to be:

$$\sigma_x = \frac{-2F}{\pi a^2}\left[m - 2z + 2\mu(x-n) + m\frac{z^2+n^2}{m^2+n^2} + \mu n\frac{z^2-m^2}{m^2+n^2}\right] \tag{5.28}$$

$$\sigma_y = \frac{4F\nu}{\pi a^2}\left[m - z + \mu(x-n)\right] \tag{5.29}$$

$$\sigma_z = \frac{-2F}{\pi a^2}\left[m - m\frac{z^2+n^2}{m^2+n^2} - \mu n\frac{z^2-m^2}{m^2+n^2}\right] \tag{5.30}$$

$$\tau_{xz} = \frac{-2F}{\pi a^2}\left[\mu(m-2z) - n\frac{z^2-m^2}{m^2+n^2} + \mu n\frac{z^2+m^2}{m^2+n^2}\right] \tag{5.31}$$

where σ is the stress (in Pa), F is the load per unit length (in N m^{-1}), a is the half contact length (in m), μ is the friction coefficient, x, y, z are the coordinates, defined in Figure 5.14, and m, n are functions of a, x and z, given by:

$$m = \pm\sqrt{\frac{1}{2}\left\{\left(a^2 - x^2 + z^2\right) + \sqrt{\left(a^2 - x^2 + z^2\right)^2 + 4x^2z^2}\right\}} \tag{5.32}$$

$$n = \pm\sqrt{\frac{1}{2}\left\{-\left(a^2 - x^2 + z^2\right) + \sqrt{\left(a^2 - x^2 + z^2\right)^2 + 4x^2z^2}\right\}} \tag{5.33}$$

where the sign of m is always the same as that of z and the sign of n is always the same as x.

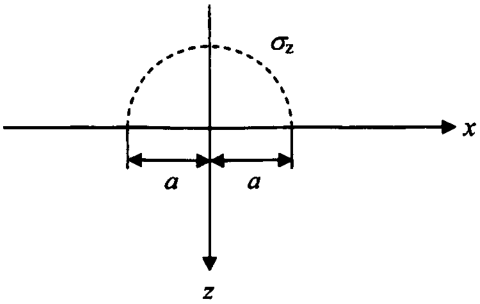

Figure 5.14 – Definition of the coordinate system used in equations 5.28 to 5.33. The y coordinate is into the paper.

A computer code was written by the author, using McEwen's equations, to predict the subsurface stresses. The maximum shear stress in the plane of deformation, τ_1, may then be calculated by:

$$\tau_1 = \frac{1}{2}\left[(\sigma_x - \sigma_z)^2 + 4\cdot\tau_{xz}^2\right]^{1/2} \tag{5.34}$$

where σ_x and σ_z are the stresses in the x and z direction respectively, and τ_{xz} is the shear stress in the xz direction.

Examples of the resulting maximum shear stress contours with different friction conditions are given in Figures 5.15 and 5.16. The maximum shear stress when the friction coefficient is zero occurs at $0.78a$ with a value of $0.3p_0$ (p_0 is the pressure under the centre of the indenter), shown in Figure 5.15. The friction coefficient causes the maximum shear stress to move towards the trailing edge and closer to the surface, as shown in Figure 5.16. In the case of the friction coefficient equal to 0.2 the location of the maximum shear stress moved to $0.6a$ in the z plane and $0.63a$ in the x plane and slightly increased in magnitude to $0.32p_0$.

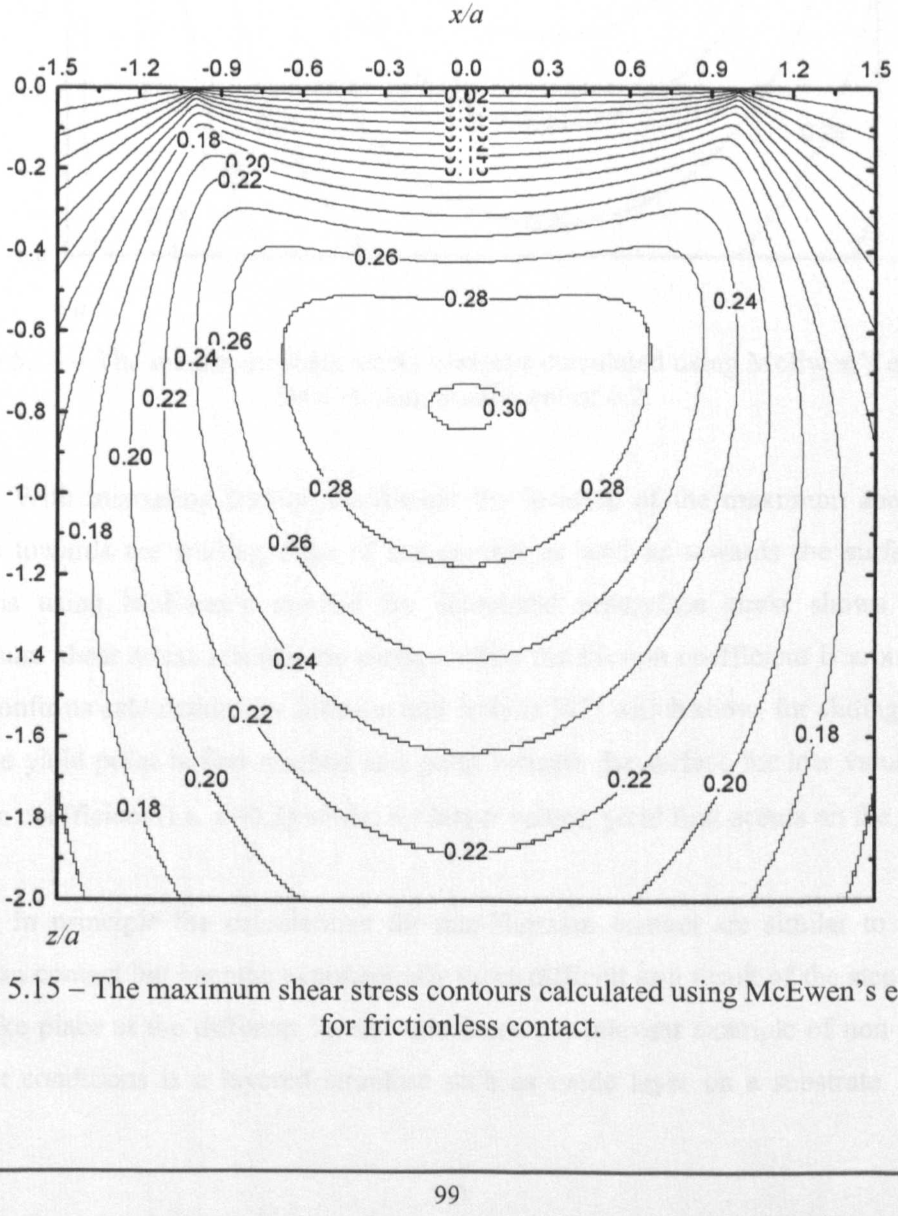

Figure 5.15 – The maximum shear stress contours calculated using McEwen's equations for frictionless contact.

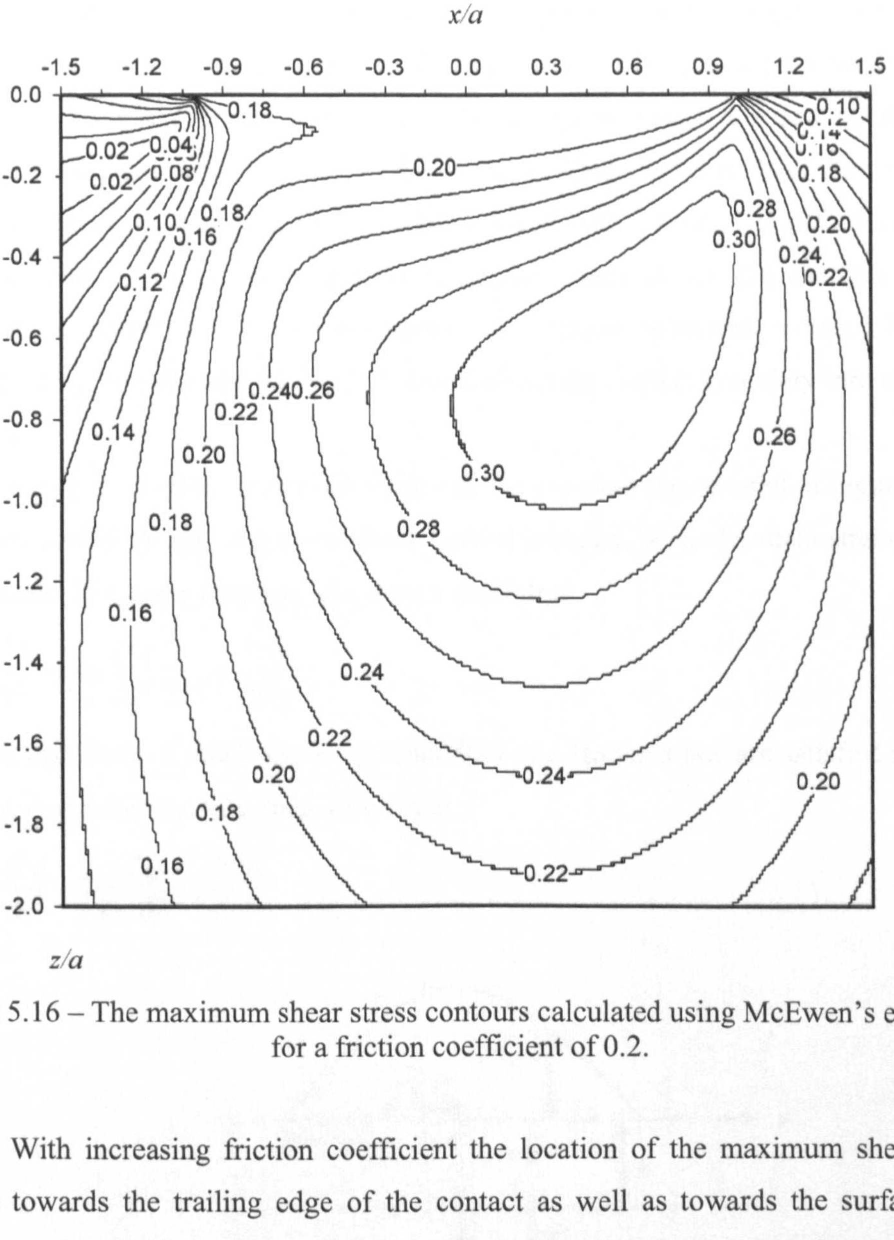

Figure 5.16 – The maximum shear stress contours calculated using McEwen's equations for a friction coefficient of 0.2.

With increasing friction coefficient the location of the maximum shear stress moves towards the trailing edge of the contact as well as towards the surface. An analysis using McEwan's method for calculated subsurface stress shows that the maximum shear stress reaches the surface when the friction coefficient is around 0.39. This confirms calculations by Johnson and Jefferis [42] which show, for sliding contact, that the yield point is first reached at a point beneath the surface for low values of the friction coefficient (i.e. μ<0.3) while, for larger values, yield first occurs on the surface.

In principle the calculations for non-Hertzian contact are similar to those of Hertzian contact but become exponentially more difficult as a result of the step changes that take place at the different layers' interfaces. A relevant example of non-Hertzian contact conditions is a layered structure such as oxide layer on a substrate. Strictly speaking, accounting for the effect of friction changes the conditions described above to non-Hertzian; fortunately, this effect is minimal and can be neglected without causing serious shortcomings in the solution. Different people have devised solutions for layered contact in different ways with the common theme between them the solution of the Airy stress function using Fourier transforms [43-49]. Fourier transforms enable a single solution for an otherwise piecewise function, such as the step changes in stress levels at the interface between two layers. A different numerical solution has been considered by Webster and Sayles [50] who divided the contact boundary into elements.

Using the Fourier transform technique the problem represented in Figure 5.17 is generally solved by applying an arbitrary normal pressure, $p(y)$, and shear stress, $q(y)$, to the surface. If a stress function, $\phi(x,y)$, is defined by:

$$\sigma_x = \frac{\partial^2\phi}{\partial y^2};\sigma_y = \frac{\partial^2\phi}{\partial x^2};\tau_{xy} = \frac{\partial^2\phi}{\partial x\partial y} \tag{5.35}$$

then the equations of equilibrium, compatibility and Hooke's law are satisfied provided that $\phi(x,y)$ satisfies the biharmonic equation:

$$\nabla^4\phi = \frac{\partial^4\phi}{\partial x^4} + 2\frac{\partial^4\phi}{\partial x^2\partial y^2} + \frac{\partial^4\phi}{\partial y^4} \tag{5.36}$$

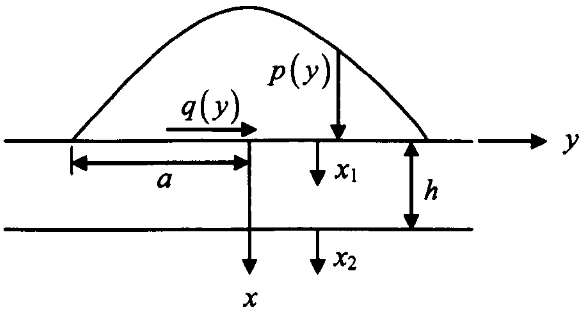

Figure 5.17 – Typical coordinate system for a layered contact solution where *p(y)* is the normal pressure distribution, *q(y)* is the tangential pressure distribution, *a* is the half-contact width and *h* is the thickness of the surface layer.

The general solution for a two-dimensional elastic solid has been expressed by Sneddon [51] in terms of Fourier integrals. The stresses and displacements, for the coordinate system shown in Figure 5.17, are given by:

$$\sigma_{x_i} = \frac{\partial^2\psi}{\partial y^2} = -\frac{1}{2\pi}\int_{-\infty}^{\infty}\omega^2 G_i e^{-j\omega y_i}d\omega \tag{5.37}$$

$$\sigma_{y_i} = \frac{\partial^2 \psi}{\partial x^2} = \frac{1}{2\pi}\int_{-\infty}^{\infty} \frac{d^2 G_i}{dx^2} e^{-j\omega y_i} d\omega \tag{5.38}$$

$$\tau_{xy_i} = -\frac{\partial^2 \psi}{\partial x \partial y} = \frac{1}{2\pi}\int_{-\infty}^{\infty} j\omega \frac{dG_i}{dx_i} e^{-j\omega y_i} d\omega \tag{5.39}$$

$$u_i = \frac{1-\nu_i^2}{2\pi E_i}\int_{-\infty}^{\infty}\left[\frac{d^3 G_i}{dx_i^3} - \left(\frac{2-\nu_i}{1-\nu_i}\right)\omega^2 \frac{dG_i}{dx_i}\right] e^{-j\omega y_i} \frac{d\omega}{\omega^2} \tag{5.40}$$

$$v_i = \frac{1-\nu_i^2}{2\pi E_i}\int_{-\infty}^{\infty}\left[\frac{d^2 G_i}{dx_i^2} + \left(\frac{\nu_i}{1-\nu_i}\right)\omega^2 G_i\right] j e^{-j\omega y_i} \frac{d\omega}{\omega} \tag{5.41}$$

where ψ is the Airy stress function that satisfies the biharmonic equation and G is the Fourier transform of ψ, given by:

$$\nabla^4 \psi = 0 \tag{5.42}$$

$$G = \int_{-\infty}^{\infty} \psi e^{j\omega y} dy \tag{5.43}$$

The solution for G is given in the form:

$$G = (A + Bx)e^{-|\omega|x} + (C + Dx)e^{+|\omega|x} \tag{5.44}$$

where the constants A, B, C and D are generally functions of the Fourier transform variable, ω. For a 2-layer contact eight simultaneous equations for A_1 to D_2 are obtained by taking inverse transforms of the relations for the stresses given above and substituting for G from equation 5.44 and are determined by matching the stresses and displacements at the layer interfaces, otherwise known as the boundary conditions, which are listed below. For any additional layers the boundary conditions are extended to match the interfaces of the layers. As a result of the last boundary condition C_2 and D_2 are zero, and

$$\begin{array}{ll}
\sigma_x^{(1)}(0,y) = -p(y); & \tau_{xy}^{(1)}(0,y) = -q(0,y) \\
\sigma_x^{(1)}(h,y) = \sigma_x^{(2)}(0,y); & \tau_{xy}^{(1)}(h,y) = \tau_{xy}^{(2)}(0,y) \\
u_1(h,y) = u_2(0,y); & v_1(h,0) = v_2(0,y) \\
\sigma_x^{(2)}(\infty,y) = \tau_{xy}^{(2)}(\infty,y) = 0 &
\end{array} \tag{5.45}$$

The simultaneous equations may then be solved using the following matrix:

$$[K]\begin{Bmatrix} A_1 \\ B_1 \\ C_1 \\ D_1 \\ A_1 \\ B_2 \end{Bmatrix} = \begin{Bmatrix} P(\omega) \\ Q(\omega) \\ 0 \\ 0 \\ 0 \\ 0 \end{Bmatrix} \tag{5.46}$$

where $P(\omega)$ and $Q(\omega)$ are the Fourier transforms of the normal pressure and shear traction on the surface, respectively, and the $[K]$ matrix is given by:

$$[K] = \begin{bmatrix} \omega^2 & 0 & \omega^2 & 0 & 0 & 0 \\ -|\omega| & 1 & |\omega| & 1 & 0 & 0 \\ 1 & h & q^2 & q^2 h & -q & 0 \\ -|\omega| & (1-|\omega|h) & |\omega|q^2 & (1+|\omega|h)q^2 & |\omega|q & -q \\ -f_1|\omega| & j_1-|\omega|hf_1 & f_1|\omega|q^2 & (j_1+|\omega|hf_1)q^2 & f_2|\omega|\gamma q & -j_2\gamma q \\ k_1|\omega| & (|\omega|hk_1-2) & k_1|\omega|q^2 & (|\omega|hk_1+2)q^2 & -k_2|\omega|\gamma q & 2\gamma q \end{bmatrix} \tag{5.47}$$

Although the above expressions are sufficient when including the effects of friction on the contact stresses, the usual procedure is to divide the solution into two steps [43,46,47]. The first step is to solve for the normal pressure at the surface and to set the tangential pressure at the surface to zero while the second step is to set the normal pressure to zero and solve for the effects of the tangential pressure since it is assumed for the case of fully-developed sliding contact that the pressure profile in the contact zone is unaltered by the shearing actions. This assumption is increasingly valid for higher values of Poisson's ratio and lower friction coefficients. The final stresses and displacements are then the summation of both of these components.

The effect of a thin layer on the subsurface stress distribution is strongly material property dependent. Results from King and O'Sullivan [43], shown in Figures 5.18 and 5.19, indicate that, when the Young's modulus of the surface layer is greater than the substrate, the stresses within the layer are increased significantly and the stresses at the interface are significant and relatively independent of friction. Whereas when the Young's modulus of the layer is less than the substrate, the stresses are dramatically reduced with minimal interface stresses. Mao *et al.* [46] suggest that these coatings can act as "stress barriers" and conclude that such coatings are beneficial in reducing contact stress.

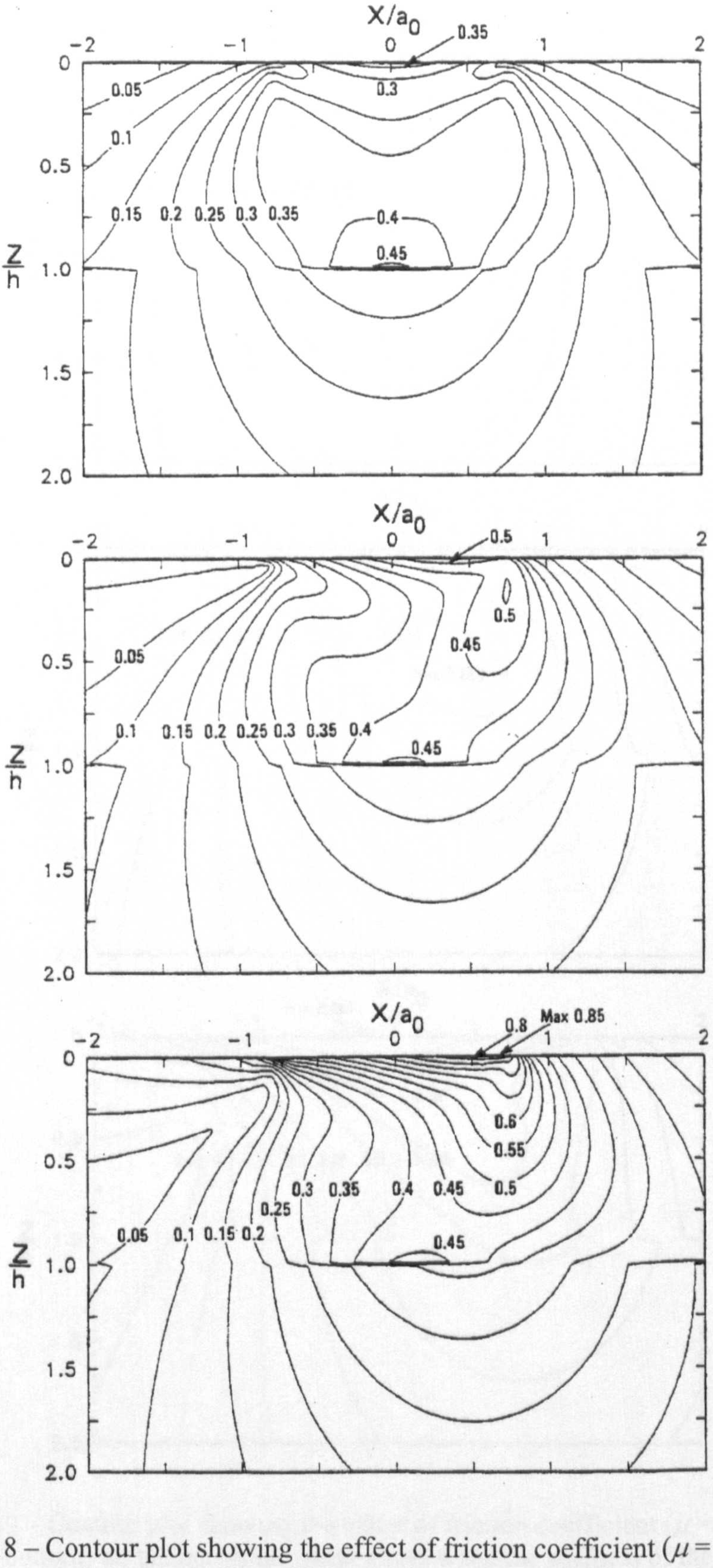

Figure 5.18 – Contour plot showing the effect of friction coefficient ($\mu = 0, 0.25, 0.5$ from top to bottom) on the maximum shear stress when the surface layer is twice that of the substrate (i.e. $E_1=2E_2$) [43].

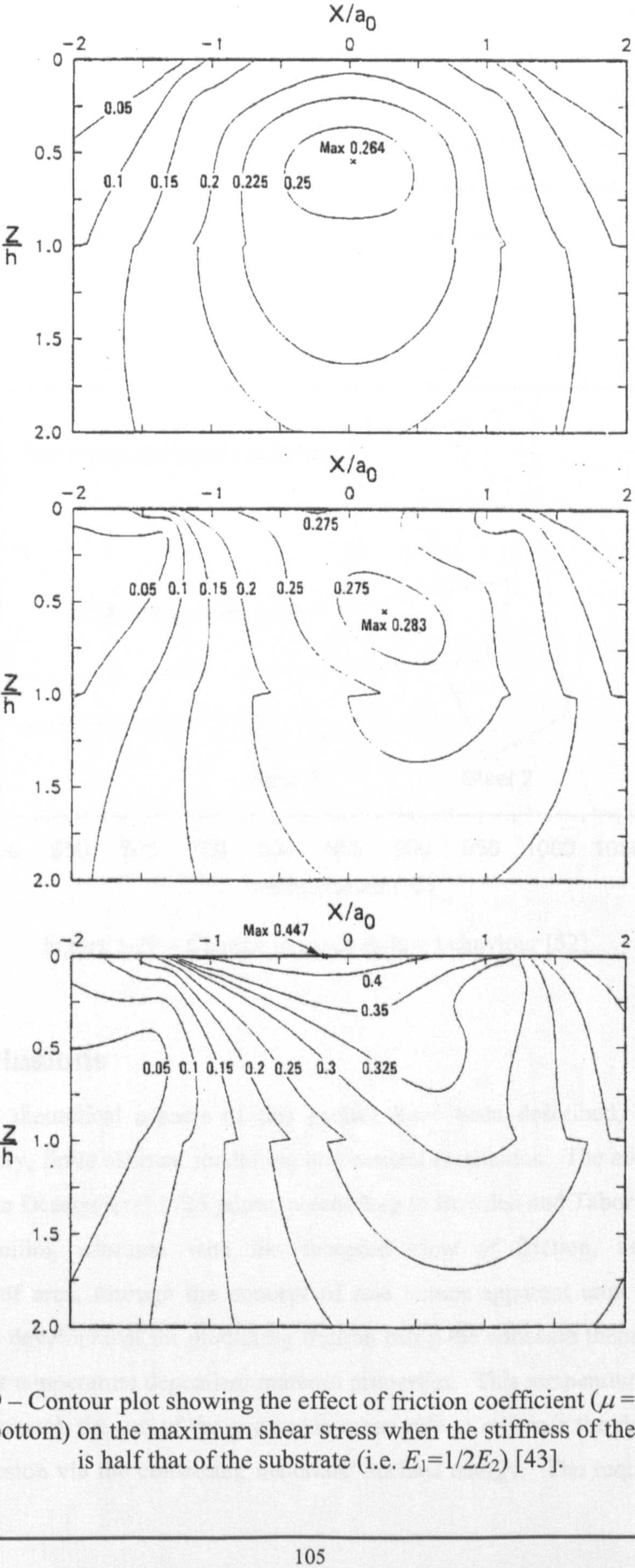

Figure 5.19 – Contour plot showing the effect of friction coefficient ($\mu = 0$, 0.25. 0.5 from top to bottom) on the maximum shear stress when the stiffness of the surface layer is half that of the substrate (i.e. $E_1=1/2E_2$) [43].

In terms of the hot rolling of steel, as the Young's modulus of iron oxide (magnetite) is less temperature dependent than the steel substrate, i.e. the oxide layer becomes stiffer than the steel substrate at higher temperatures, it follows that the shear stress at the oxide-steel interface will increase with temperature. This has been seen by Krzyzanowski and Beynon [52] who found that there was a temperature at which the failure behaviour of the oxide layer changed from cracking to raft sliding, shown in Figure 5.20.

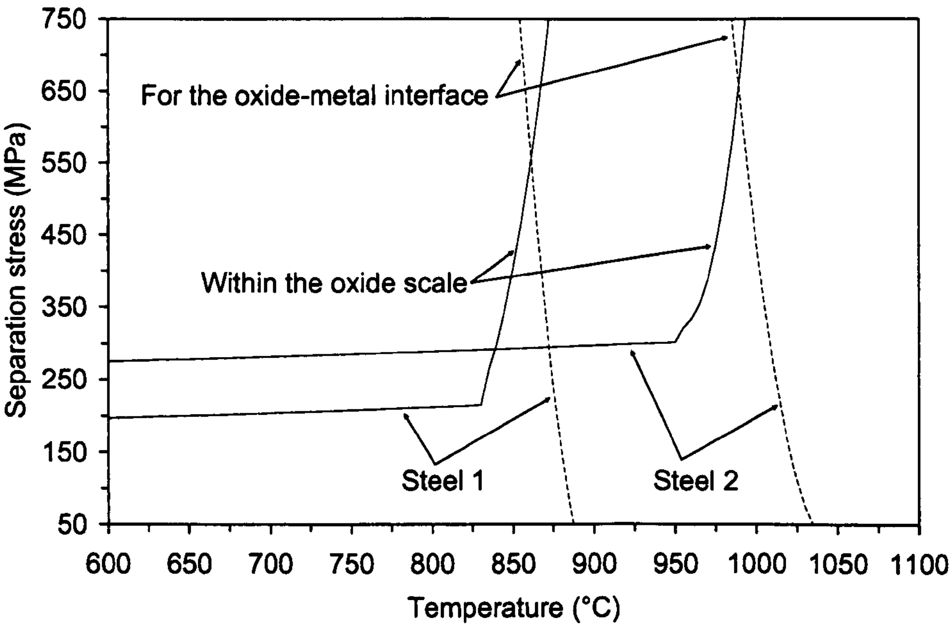

Figure 5.20 – Change in oxide failure behaviour [52].

5.5. Conclusions

Three theoretical aspects of this project have been described, namely: the adhesion theory, finite element modelling and contact mechanics. The adhesion theory has its roots in Desaguliers' 1725 paper, proceeding to Bowden and Tabor's work in the 1950s reconciling adhesion with the accepted view of friction, i.e. friction is independent of area, through the concept of real versus apparent area. Straffelini's mathematical development for predicting friction using the adhesion theory is extended to account for temperature dependent material properties. This temperature dependence is achieved through the use of the geometric mean rule to estimate the thermodynamic work of adhesion via the contacting materials' surface energy. The required factor in the geometric mean formulation, Φ, is the ratio of molar volumes for the contacting materials and should be less than one. As high temperature data for surface energy is generally unavailable, a method was devised in which the relative change in Young's modulus over temperature was applied to the room temperature surface energy value. The adhesion theory of friction was then applied to hot rolling of steel through finite element modelling. Within the finite element model, a user-defined subroutine was employed to calculate the instantaneous coefficient of friction based on the surface temperatures of the strip and work roll. The use of this subroutine also enables the coefficient of friction to change throughout the roll bite, rather than using an average value as is usually done. Lastly, contact mechanics theory has been reviewed with Hertzian theory showing that the effect of friction is to increase the subsurface maximum shear stresses and to move the point of maximum shear stress towards the surface and trailing edge of the moving contact, reaching the surface when the coefficient of friction is greater than or equal to 0.39. Non-Hertzian contact mechanics for a layered contact shows that the Young's modulus of the surface layer plays an important role in the subsurface maximum shear stress distribution. If the Young's modulus of the surface layer is greater than the substrate, the surface layer acts as a stress multiplier, increasing the magnitude of the maximum shear stress and increasing the shear stresses at the surface layer-substrate interface. If the Young's modulus of the surface layer is less than the substrate, the surface layer then acts as a stress barrier, reducing the magnitude of the maximum shear stress and minimal shear stresses at the surface layer-substrate interface.

5.6. References

1. J.T. Desaguliers "Some experiments concerning the cohesion of lead", Phil.Trans. R. Soc. Lond., 1725, 33, 345-347
2. F.P. Bowden and D. Tabor "The friction and lubrication of solids", 1st. ed., Oxford University Press, London, 1950,
3. F.P. Bowden and D. Tabor "Friction and lubrication", 1st ed., Methuen and Co. Ltd., London, 1956,
4. E. Rabinowicz "Friction and wear of materials", 1st ed., John Wiley and Sons, Inc., New York, 1965, Library of Congress # 65-12704
5. G. Straffelini "A simplified approach to the adhesive theory of friction", Wear, 2001, 249, 79-85
6. F.P. Bowden and D. Tabor "Friction and lubrication", 2nd ed., Methuen and Co. Ltd., London, 1967,

7. E. Rabinowicz "Friction and wear of materials", 2nd ed., John Wiley & Sons, Inc., New York, 1995, 0-471-83084-4
8. A. Molinari, Y. Estrin and S. Mercier "Dependence of the coefficient of friction on the sliding conditions in the high velocity range", Journal of Tribology (USA), 1999, 121, 35-41
9. J.S. McFarlane and D. Tabor "Relation between friction and adhesion", Proc. Roy. Soc., 1950, 202A, 244-253
10. F.P. Bowden and D. Tabor "Friction, lubrication and wear: a survey of work during the last decade", British Journal of Applied Physics, 1966, 17, 1521-1544
11. J.S. Courtney-Pratt and E. Eisner "The effect of a tangential force on the contact of metallic bodies", Proc. Roy. Soc. London, 1957, 238A, 529-550
12. D. Tabor "Junction growth in metallic friction: the role of combined stresses and surface contamination", Proc. Roy. Soc., 1959, 251A, 378-393
13. K.C. Ludema "Friction, wear, lubrication : a textbook in tribology", 1st ed., CRC Press, Boca Raton, 1996, 0849326850
14. K.L. Johnson "Deformation of a plastic wedge by a rigid flat die under the action of a tangential force", Journal of the Mechanics and Physics of Solids, 1968, 16, 395-402
15. S.C. Lim and M.F. Ashby "Wear mechanism maps", Acta Metallurgica, 1987, 35, 1-24
16. S. K. R. Chowdhury and H. M. Pollock "Adhesion Between Metal Surfaces: the Effect of Surface Roughness", Wear, 1981, 66, 307-321
17. K.L. Johnson, K. Kendall and A.D. Roberts "Surface energy and the contact of elastic solids", Proc. R. Soc. London, 1971, A324, 301-313
18. H. Hertz "Über die Berührung fester elastischer Körper", J. reine und angewandte Mathematik, 1882, 92, 156-171
19. D. Maugis and H. M. Pollock "Surface Forces, Deformation and Adherence at Metal Microcontacts", Acta Metall., 1984, 32, 1323-1334
20. V.K. Semenchenko "Surface phenomena in metals and alloys", 1st ed., Pergamon Press, Oxford, 1961, Library of Congress # 60-53072
21. L.A. Girifalco and R.J. Good "A theory for the estimation of surface and interfacial energies. I. Derivation and application to interfacial tension", Journal of Physical Chemistry, 1957, 61, 904-909
22. D. Berthelot "???" Compt. rend., 1898, 126, 1857-?
23. F.M. Fowkes "Dispersion forces contributions to surface and interfacial tensions, contact angles, and heats of immersion", Adv. Chem. Ser., 1964, 43, 99-111
24. Y. Ando, Y. Ishikawa and T. Kitahara "Friction characteristics and adhesion force under low normal load", Journal of Tribology (Transactions of the ASME) (USA), 1995, 117, 569-574
25. Y. Ando and J. Ino "Friction and pull-off forces on submicron-size asperities", Wear, 1998, 216, 115-122
26. A.H. Uppal and S.D. Probert "Deformation of single and multiple asperities on metal surfaces", Wear, 1972, 20, 381-400
27. A.H. Uppal and S.D. Probert "Topography changes resulting from surfaces being in contact under static and dynamic loads", Wear, 1970, 16, 261-271
28. A.H. Uppal, S.D. Probert and T.R. Thomas "The real area of contact between a rough and a flat surface", Wear, 1972, 22, 163-183
29. A.H. Uppal and S.D. Probert "Considerations governing the contact between a rough and a flat surface", Wear, 1972, 22, 215-234

30. F.T. Barwell, M.H. Jones and S.D. Probert "The interaction and lubrication of rough surfaces", Proceedings of the symposium of the International Union of Theoretical and Applied Mechanics (IUTAM), Enschede, Netherlands, ed. by de Pater and Kalker, Delft University Press, 20-23 August 1974, 304-329
31. K. Tanaka, J. Ishikawa and A. Shimamoto "Elastic contact and friction between sliders and circumferentially textured disks-Part III: Experiments", Journal of Tribology, 1998, 120, 800-807
32. V.K. Jain and S. Bahadur "Surface topography changes in polymer-metal sliding- I", Journal of Lubrication Technology, 1980, 102, 520-525
33. T.E. Tallian "Rolling bearing life modifying factors for film thickness, surface roughness, and friction", Journal of Lubrication Technology, 1981, 103, 509-520
34. T. Hisakado and H. Suda "Effect of asperity shape and summit height distributions on friction and wear characteristics", Wear, 1999, 225-229, 450-457
35. S.C. Lim, M.F. Ashby and J.H. Brunton "The effects of sliding conditions on the dry friction of metals", Acta Metallurgica, 1989, 37, 767-772
36. K. Lepper, M. James, J. Chashechkina and D.A. Ringley "Sliding behavior of selected aluminium alloys", Wear, 1997, 203-204, 46-56
37. B.K. Chen, S.K. Choi and P.F. Thomson "Simulation of evolution of microstructure in a thermo-mechanical analysis of the hot rolling of aluminium", Res. Mechanica, 1991, 31, 455-469
38. M.A. Wells "Mathematical modelling of the microstructure and texture changes during hot tandem rolling of AA5182 and AA5052 aluminum alloys", Ph.D. thesis, Metals and Materials Engineering, Vancouver, 1995
39. T. Altan, S.I. Oh and H.L. Gegel "Metal Forming", 1st ed., American Society for Metals, 1983, 0871701677
40. Y.H. Li and C.M. Sellars "Development of forward slip friction measurement method of rolling", DTI-NPL Project MMP6/M6, NPL, Oct. 1998
41. E. McEwan "Stresses in elastic cylinders in contact along a generatrix", Philosophical Magazine, 1949, 40, 454-459
42. K.L. Johnson and J.A. Jefferis "Plastic flow and residual stresses in rolling and sliding contact", Proc. Institution of Mechanical Engineers Symposium on Fatigue in Rolling Contact, London, UK, ed. by Johnson *et al.*, 1963, 54-65
43. R.B. King and T.C. O'Sullivan "Sliding contact stresses in two-dimensionally layered elastic half-space", International Journal of Solids and Structures (UK), 1987, 23, 581-597
44. P.K. Gupta and J.A. Walowit "Contact stresses between an elastic cylinder and a layered elastic solid", Journal of Lubrication Technology, 1974, 96, 250-257
45. W.T. Chen "Computation of stresses and displacements in a layered elastic medium", International Journal of Engineering Science, 1971, 9, 775-800
46. K. Mao, T. Bell and Y. Sun "Effect of sliding friction on contact stresses for multi-layered elastic bodies with rough surfaces", Journal of Tribology (Transactions of the ASME) (USA), 1997, 119, 476-480
47. K. Mao, Y. Sun and T. Bell "A numerical model for the dry sliding contact of layered elastic bodies with rough surfaces", Tribology Transactions (USA), 1996, 39, 416-424
48. S.J. Cole and R.S. Sayles "A numerical model for the contact of layered elastic bodies with real rough surfaces", Journal of Tribology (Transactions of the ASME) (USA), 1992, 114, 334-340

49. R.H. Bentall and K.L. Johnson "An elastic strip in plane rolling contact", Int. J. Mech. Sci., 1968, 10, 637-663
50. M.N. Webster and R.S. Sayles "A numerical model for the elastic frictionless contact of real rough surfaces", Journal of Tribology (Transactions of the ASME) (USA), 1986, 108, 314-320
51. I.N. Sneddon "The stress distribution due to a force in the interior of a semi-infinite elastic medium", Proceedings of the Cambridge Philosophical Society, 1944, 40, 229-238
52. M. Krzyzanowski and J.H. Beynon "Modelling the boundary conditions for thermo-mechanical processing - oxide scale behaviour and composition effects", Modelling Simul. Mater. Sci. Eng., 2000, 8, 927-945

Chapter 6 - Experimental Procedure

6.1. Introduction

As friction is affected by a number of different variables, it is important to choose an experiment that enables a desired variable to be isolated. However, according to the adhesion theory of friction there are effectively three variables that strongly influence friction: temperature, surface roughness and choice of material. This makes the frictional behaviour of materials at high temperature difficult to study as a result of oxidation, which may change the contact conditions over time. The experiments chosen to examine these variables were ring compression testing and reciprocating friction testing. The ring compression experiments of this study examined the effect of macro scale roughness and the reciprocating friction experiments examined the effect of temperature and choice of materials, as a result of the temperature range chosen. Finally, as this project is concerned with modelling friction during the hot rolling of steel, the adhesion theory developed is used to make predictions about the influence of friction on laboratory rolling experiments; thus laboratory rolling experiments were also conducted.

6.2. Ring Compression Testing

Ring compression tests have been employed in the literature [1-4] to ascertain an approximate level of friction, either in the form of a friction coefficient or friction factor, during the deformation of metal. The values associated with this test are largely empirical and the test is generally conducted under lubrication conditions; therefore it was decided to examine the influence of the oxide thickness as a lubricant in combination with directionally roughened platens. Due to the difficultly in controlling the oxide thickness a large variation in platen roughness was used to ascertain the effect of roughness interacting with the oxide layer. The following sections describe the experimental set-up, procedure and results.

6.2.1. Equipment Description

The equipment used in this experiment was: a 50 ton Marlco hydraulic press, tool steel platens with a specified roughness, a Surtronic 3+ roughness measuring device, a Banyard Inductoheat induction furnace and a National Instruments data acquisition system.

The 50 ton Marlco press has a single tool speed of approximately 4 mm s^{-1}, which did not vary significantly under load. A safety feature of the Marlco press was a guarding interlock such that the press could not be operated unless the guards were closed. The layout of the Marlco press in relation to the induction coil and the location of the interlock are shown in Figure 6.1.

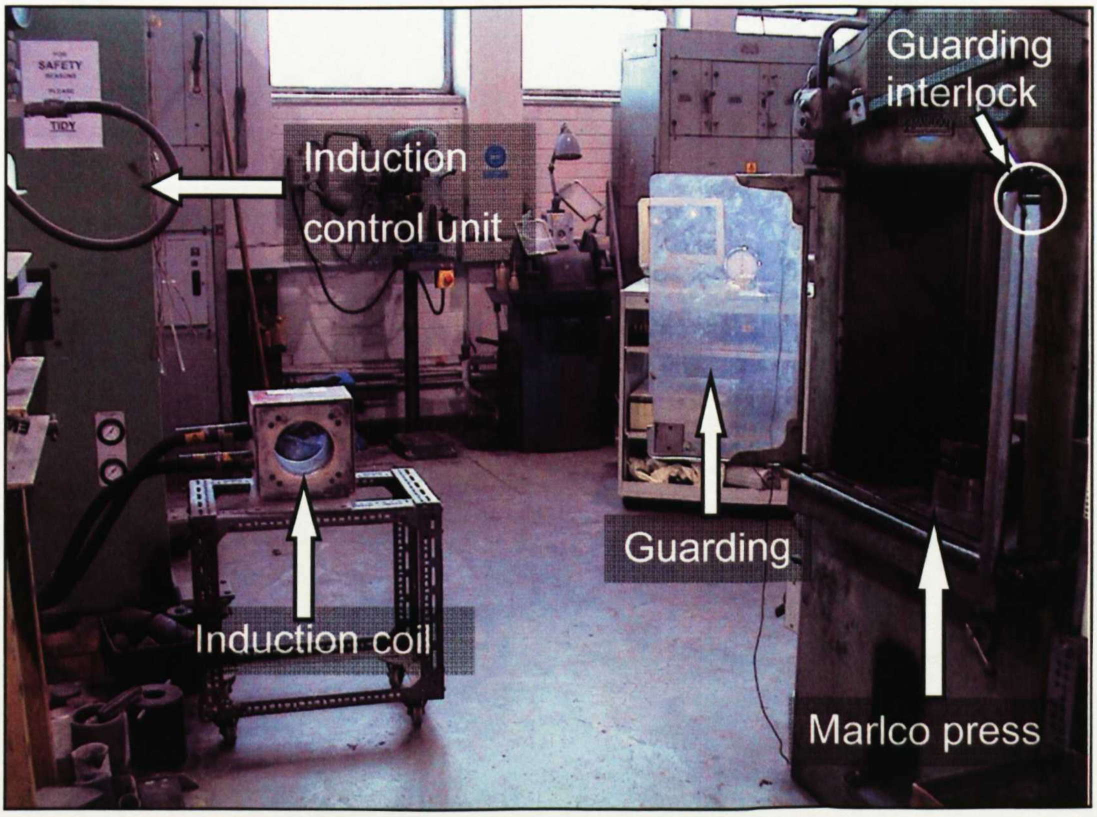

Figure 6.1 – The 50 ton Marlco press used in the ring compression experiments in relation to the induction furnace.

The platens with specified roughness were prepared using spark erosion in addition to a nominally smooth platen and a platen prepared earlier for a previous project. The surface profiles of the platens, shown in Figure 6.2, were obtained using the Surtronic 3+. It is important to note that the abscissa is in millimetres while the ordinate is in microns.

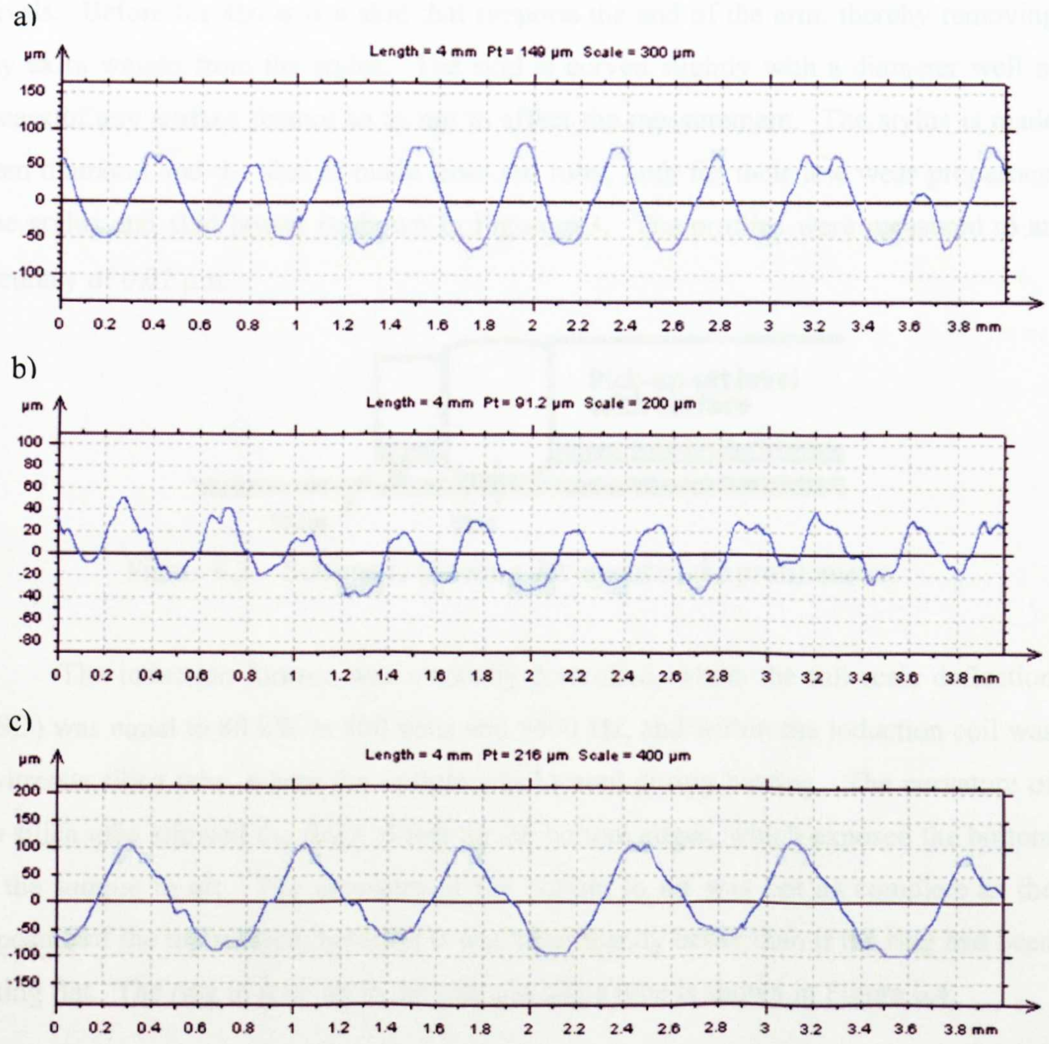

Figure 6.2 – Examples of platen surface profiles: a) platen 1; b) platen 2 and c) platen 4.

Not shown in Figure 6.2 are the surface profiles of the nominally smooth platen (Platen 0) and the third machined platen (Platen 3). The absence of the third platen was due to an inconsistent surface profile across the width and the results of the initial tests were considered to be inconclusive and no further tests were conducted with Platen 3.

The device used to measure the surface profiles was a Taylor Hobson Surtronic 3+. The output from this device is in terms of *Ra*, *Rq*, *Rz*(DIN), *Ry* and *Sm*, whose definitions and other roughness terminology are give in Appendix C. The device physically measures the profile using a stylus at the end of a movable arm. The stylus measures the height of the surface relative to a pre-set plane, along which the arm travels. Before the stylus is a skid that supports the end of the arm, thereby removing any extra weight from the stylus. The skid is curved slightly with a diameter well in excess of any surface feature so as not to affect the measurement. The stylus is made from diamond and the skid is made from red ruby, both for their low wear properties. The stylus and skid layout is shown in Figure 6.3. The profiles were measured to an accuracy of 0.02 μm.

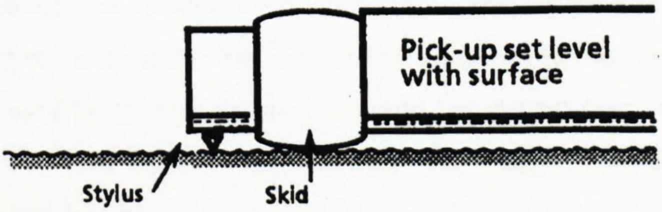

Figure 6.3 – Schematic showing the layout of the profilometer.

The induction furnace was manually controlled, where the full scale deflection (FSD) was equal to 80 kW at 800 volts and 9600 Hz, and within the induction coil was a vitreous silica tube, where the sample was located during heating. The curvature of the silica tube allowed the rings to rest on the bottom edges, which exposed the bottom of the sample to air. The exposure of the bottom to air was not as complete as the exposure of the top surface; however it was significantly better than if the ring had been sitting flat. The ring in relation to the vitreous silica tube is shown in Figure 6.4.

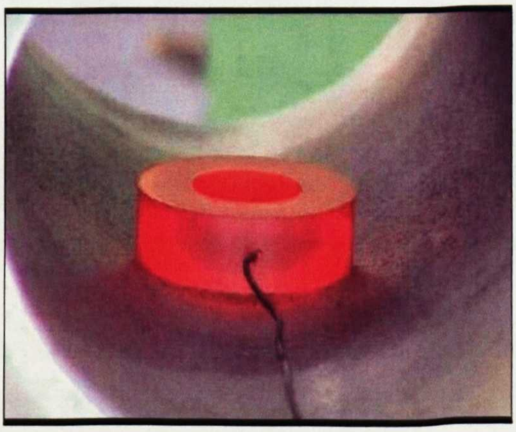

Figure 6.4 – Image showing the sample resting in the vitreous silica tube while being heated in air by the induction furnace.

The frequency of the induction furnace was sufficiently high so as to not affect the thermocouples readings, thus enabling the temperature of the samples to be continuously measured while heating in the induction furnace.

The National Instruments data acquisition system consisted of a PCI-6034E series data acquisition (DAQ) card, a SC-2345 signal conditioning unit, type K thermocouples and an LVDT. Solid state signal conditioning was applied to the thermocouple signals, i.e. the room temperature voltage was subtracted via a cold junction compensation (CJC) thermistor on the temperature signal processing board (TC-02) before passing the voltage to the DAQ card. The LVDT voltage signals were passed to the computer unconditioned. The experimental set-up showing the location of the LVDT device used to measure the displacement, the stopper ring, and the sample is shown in Figure 6.5. The stopper ring was required to ensure that the desired platen displacement was not exceeded.

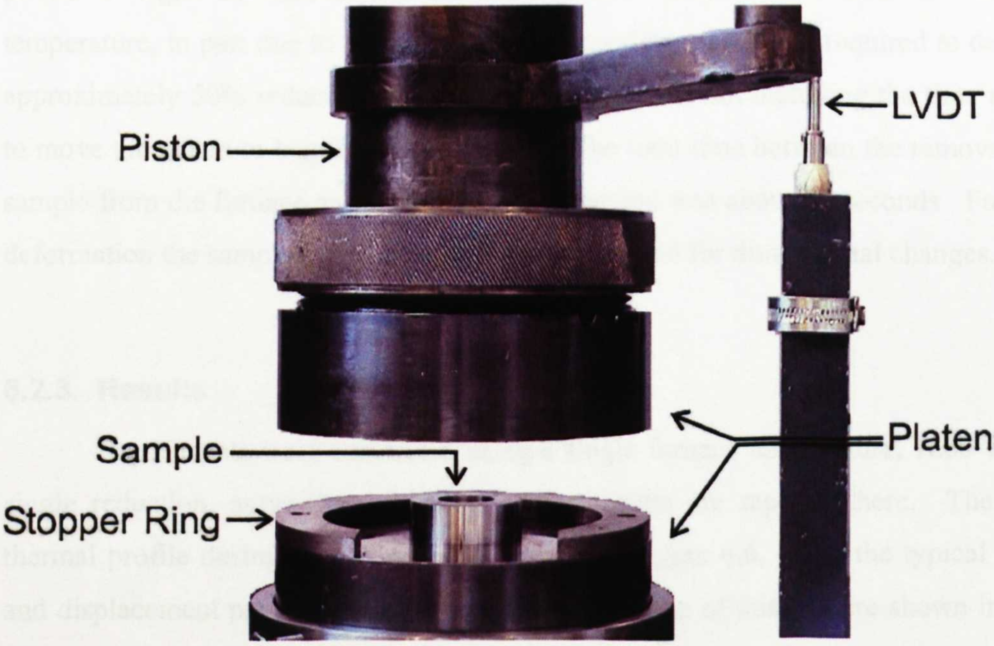

Figure 6.5 – Ring compression experimental set-up.

The ring compression tests were conducted using the "standard" ring geometry of 48 mm outside diameter, 24 mm inside diameter by 16 mm thick with the thermocouple located at the centreline. The samples were prepared from low carbon steel, whose composition is listed in Table 4.2.

Immediately prior to testing the top and bottom surfaces of the samples were polished to a 400-grit finish and cleaned using methanol to remove any grease (including fingerprints). Once the surfaces had been cleaned the samples were only handled with latex gloves to prevent contamination. The platens were also cleaned with methanol just prior to the each test to remove as much oil and grease as possible.

6.2.2. Experimental Procedure

With a thermocouple attached, the samples were placed in the induction furnace coil and heated in air to 1200°C using a consistent heating profile of 30% full scale deflection (FSD) to 1050°C followed by 40% FSD to 1200°C. Once the desired temperature was reached the furnace was turned off and the sample removed from the furnace using tongs, gripping the sides to minimize the damage to the top and bottom oxides. The samples were placed in approximately (speed being important) the centre of the bottom platen and the press activated. During the time required to move the top platen to begin the deformation the samples lost around 100°C from the centreline temperature, in part due to the closing of the guarding. The time required to deform to approximately 50% reduction was around two seconds, not including the time required to move the platen to begin the deformation. The total time between the removal of the sample from the furnace and the start of deformation was about 15 seconds. Following deformation the samples were air cooled and examined for dimensional changes.

6.2.3. Results

Experiments were conducted using a single furnace temperature, 1200°C, and a single reduction, approximately 50%, whose results are reported here. The typical thermal profile during the entire test is shown in Figure 6.6, while the typical thermal and displacement profiles during the deformation stage of this test are shown in Figure 6.7.

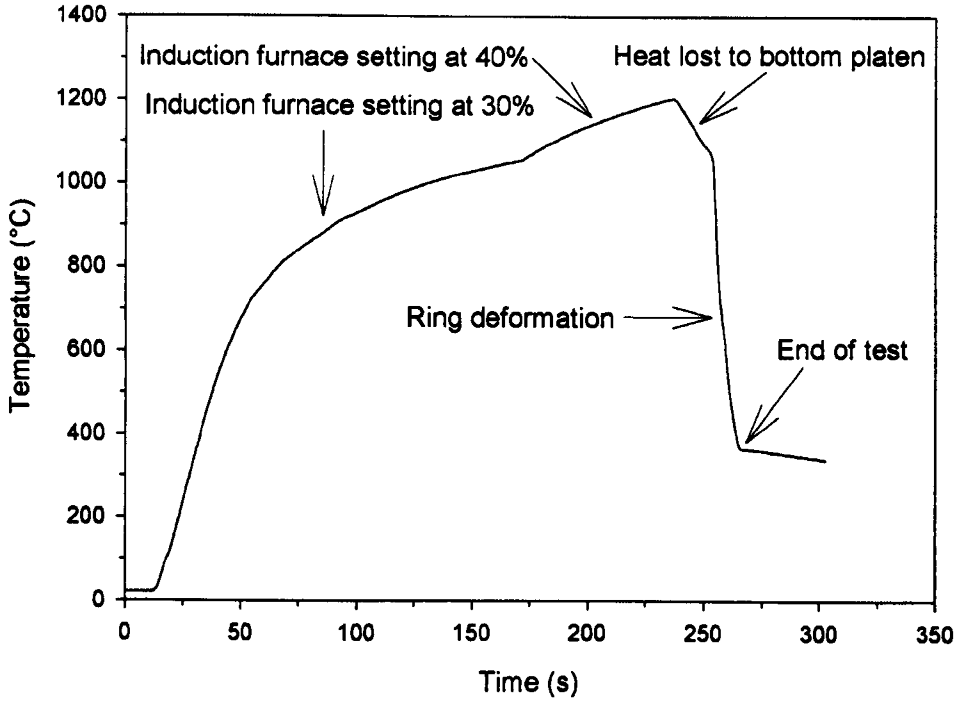

Figure 6.6 – Typical thermal profile during ring compression testing.

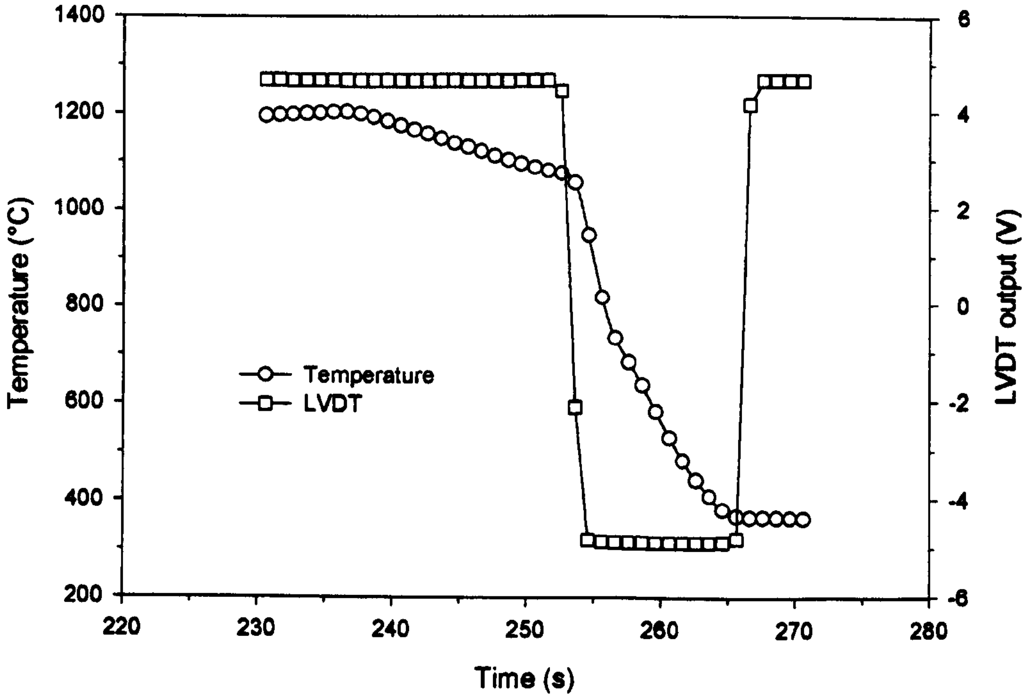

Figure 6.7 – Typical thermal and displacement profile during deformation.

As can be seen in Figure 6.7, the available data acquisition rate of 1 Hz was sufficient to measure an average deformation time.

A comparison of the final dimensions of the deformed rings is given in Figure 6.8, showing the long axis, short axis and final thickness. The samples are labeled *x.y.z*, where *x* is the sample temperature out of the furnace, *y* identifies the platen used and *z* indicates the sample number.

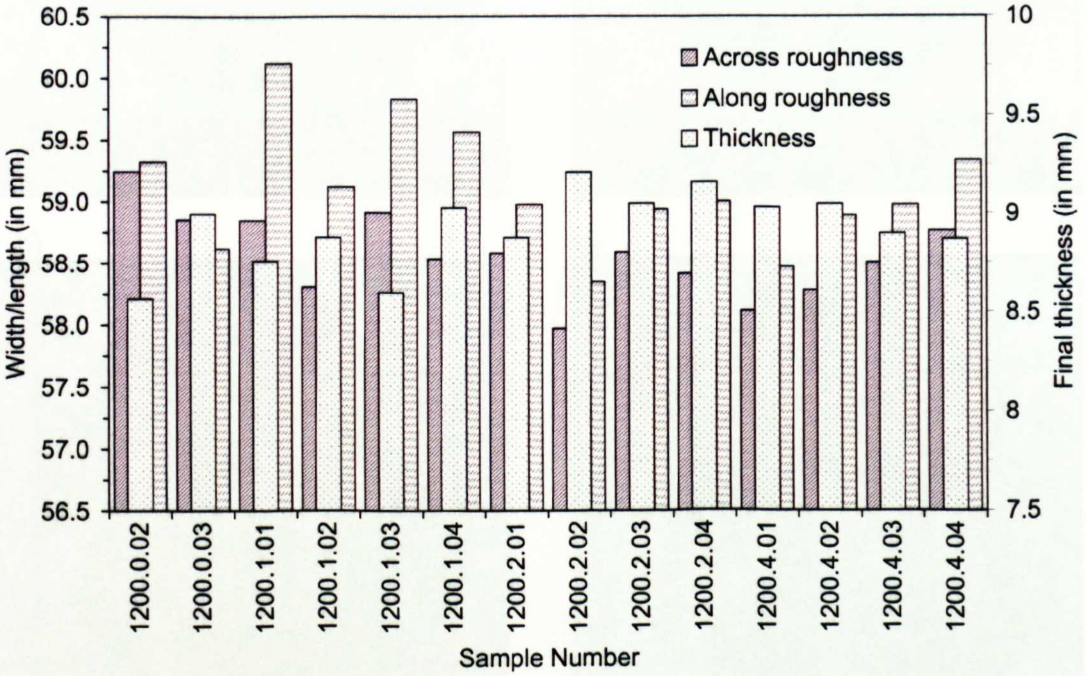

Figure 6.8 – Comparison of the final dimension across the roughness (i.e. the short axis) to the final dimension along the roughness (i.e. the long axis) and the final thickness.

These results show a relatively consistent final thickness around 9 mm, measured with the majority of the oxide still in place, indicating consistency between experiments, as expected due to the presence of the stopper ring. Platen 1 samples show the greatest degree of preferred deformation, albeit very small and, as expected, Platen 0 samples showed virtually no preferred direction of deformation.

Examples of the post-deformation rings for each platen are shown in Figure 6.9. Within the deformed ring there are some features that require further comment. The patchy appearance of the samples is the result of the oxide adhering more strongly in

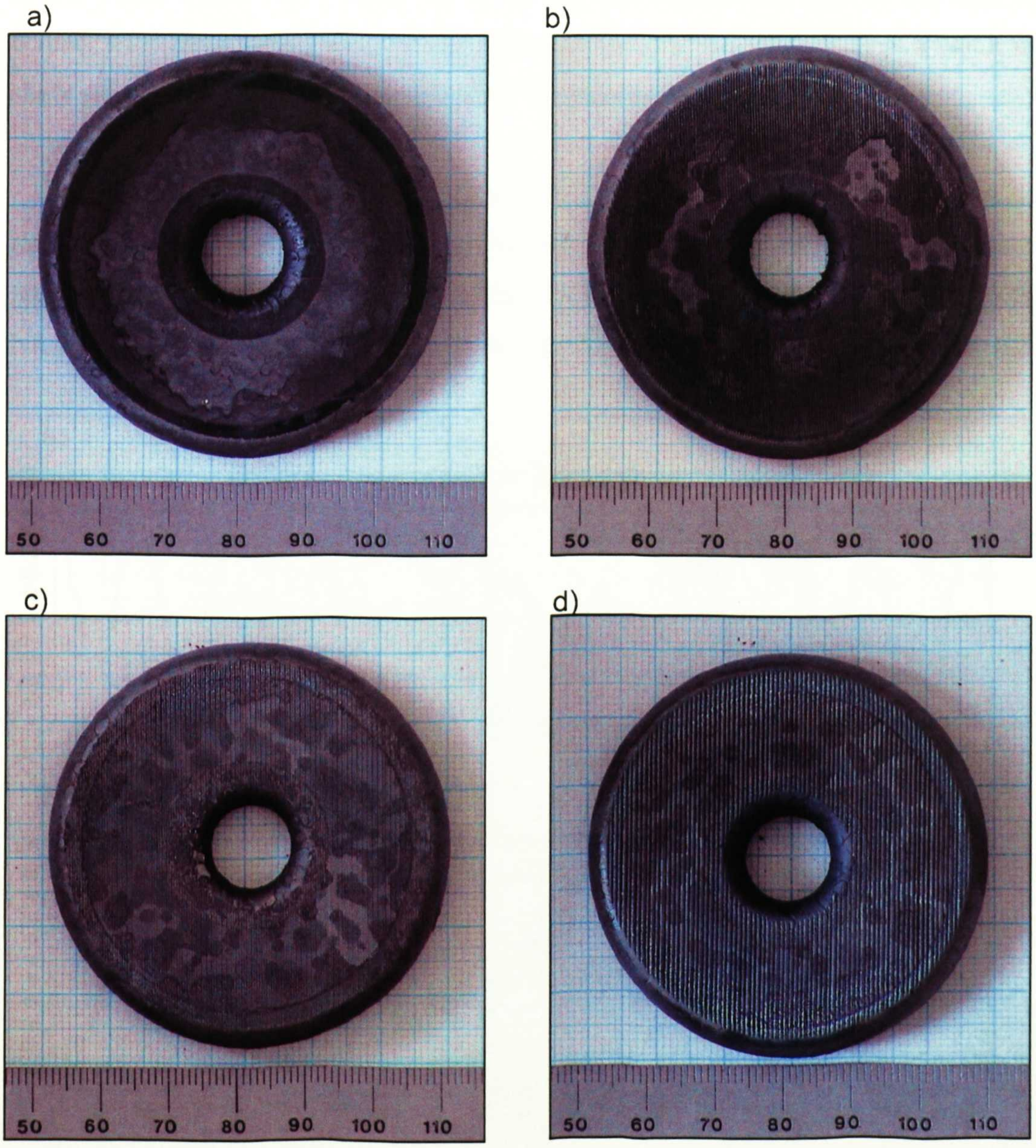

Figure 6.9 – Post deformation ring samples: a) 1200.0.02, b) 1200.1.01, c) 1200.2.01 and d) 1200.4.01.

some areas than others. The lighter colour indicates where the oxide was removed, either as a result of the deformation or thermal shock. There is a trend for the shape of the removed oxide area to be longer in the direction of the roughness, i.e. in the direction of greater strain. This feature is most visible on sample 1200.1.01. A second feature is the circle of slightly different colour on the inside and outside, most obvious on sample 1200.0.02, which indicates areas of fold-over. Fold-over occurs when the top and bottom surfaces of the ring cannot stretch enough to match the expanding diameter of the walls, which then causes the uppermost and bottommost area of the wall to contact with the platens. The uneven nature of the folded-over regions is a result of slight misalignments between the "floating" top platen and the piston.

Using the Surtronic 3+ surface profiles were taken from the areas of oxide removal for the samples deformed using the roughened platens. Typical surface profiles, shown in Figure 6.10, confirm that the impressed surface on the ring reflects, but does not mirror, the surface of the platen, profiles for which are shown in Figure 6.2.

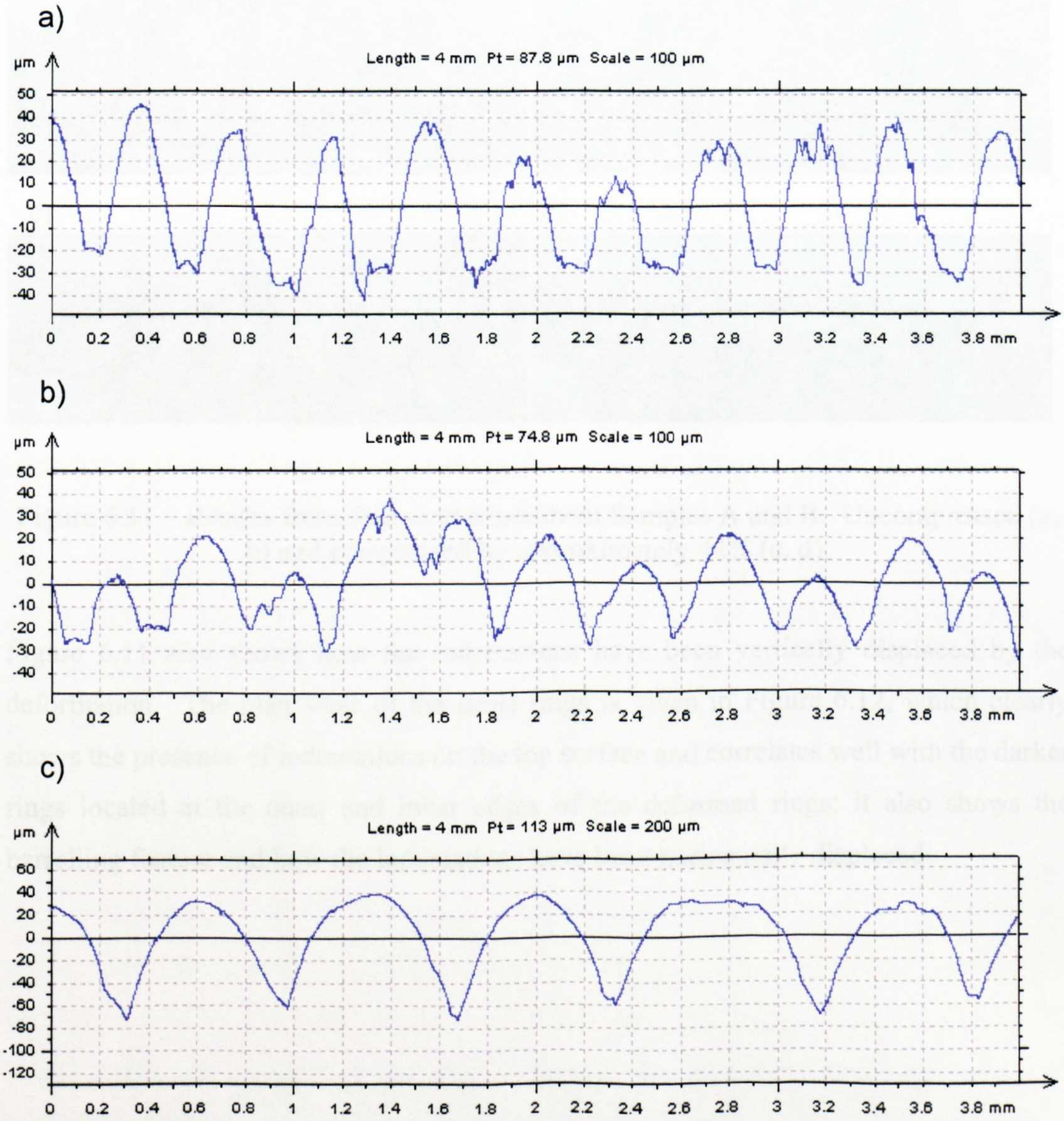

Figure 6.10 – Surface profiles taken from locations with a minimum amount of oxidation: a) 1200.1.01, b) 1200.2.01 and c) 1200.4.01.

The process of fold-over was further investigated by marking the sides of the undeformed ring with indentations, i.e. punch marks. The rings were then tested in the same manner as previously with the smooth platen chosen to reduce the number of variables affecting the outcome. The presence of fold-over can be clearly seen in Figure 6.11, which shows the side view of the stamped rings, since the number of indentations visible on the undeformed rings is more than those visible on the deformed rings.

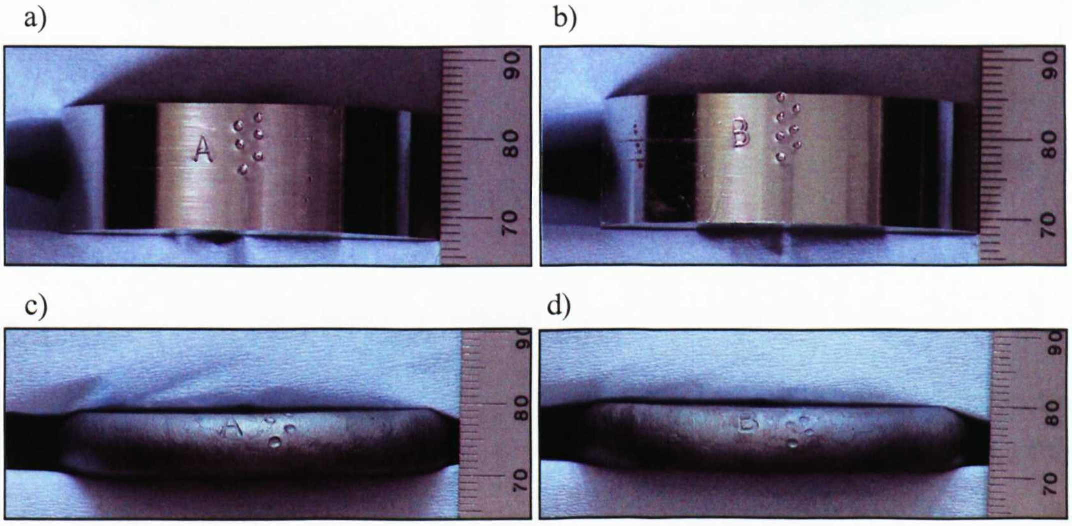

Figure 6.11 – Results from fold-over experiment Samples A and B. Uncompressed (a, b) and compressed by approximately 44% (c, d).

Figure 6.11 also shows how the indentations have been vertically displaced by the deformation. The plan view of the same rings is given in Figure 6.12, which clearly shows the presence of indentations on the top surface and correlates well with the darker rings located at the outer and inner edges of the deformed rings; it also shows the barrelling feature and how the indentations have been horizontally displaced.

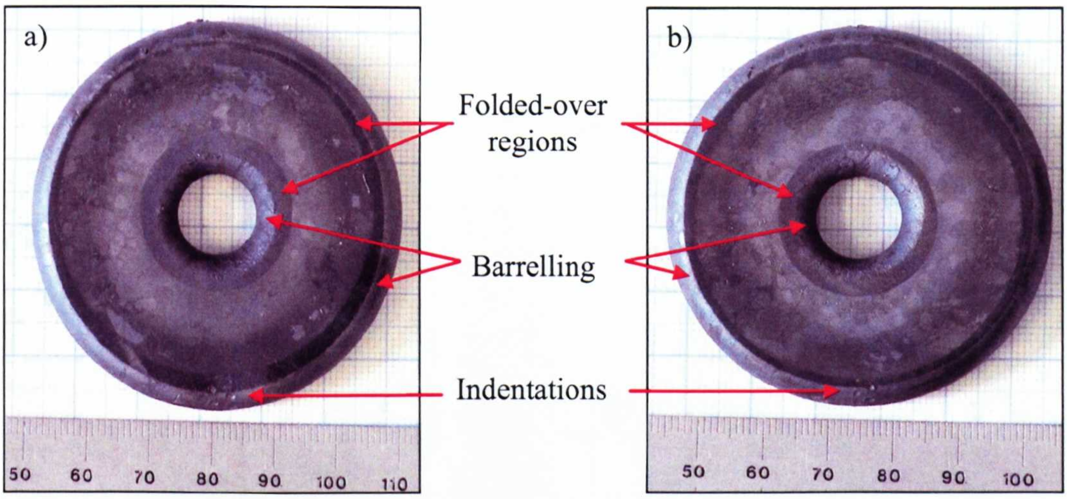

Figure 6.12 – Plan view from Samples A and B, identified as a) and b), showing indentations on the tool-work piece interface.

6.3. Reciprocating Friction Testing

In partnership with Corus' IJmuiden Technology Centre (IJTC) the reciprocating friction tester that was used by the author for this series of experiments was the Plint TE-77 High Temperature (HT) High Frequency Friction Tester (HFFT). The high temperature option allows a maximum operating temperature of 800°C, compared to the normal maximum operating temperature of 600°C. This is an important distinction as the kit is generally used to assess the durability of lubricants at temperatures up to only about 200°C. Although the maximum temperature possible was not tested, the high temperature option enabled the desired temperatures to be reached more quickly. The following sections describe the experimental set-up, procedure and results.

6.3.1. Equipment Description

The Plint TE-77 HT had three main elements, shown in Figure 6.13, comprising of the motor assembly, the loading assembly and the sample testing assembly. The oscillating motion was achieved using an offset cam mounted on the motor shaft. The stroke length may be adjusted by changing the cam configuration to achieve a minimum length of nominally zero and a standard length of 15 mm. The oscillation frequency may be set between 0 and 50 Hz, using a thyristor-controlled variable speed motor with

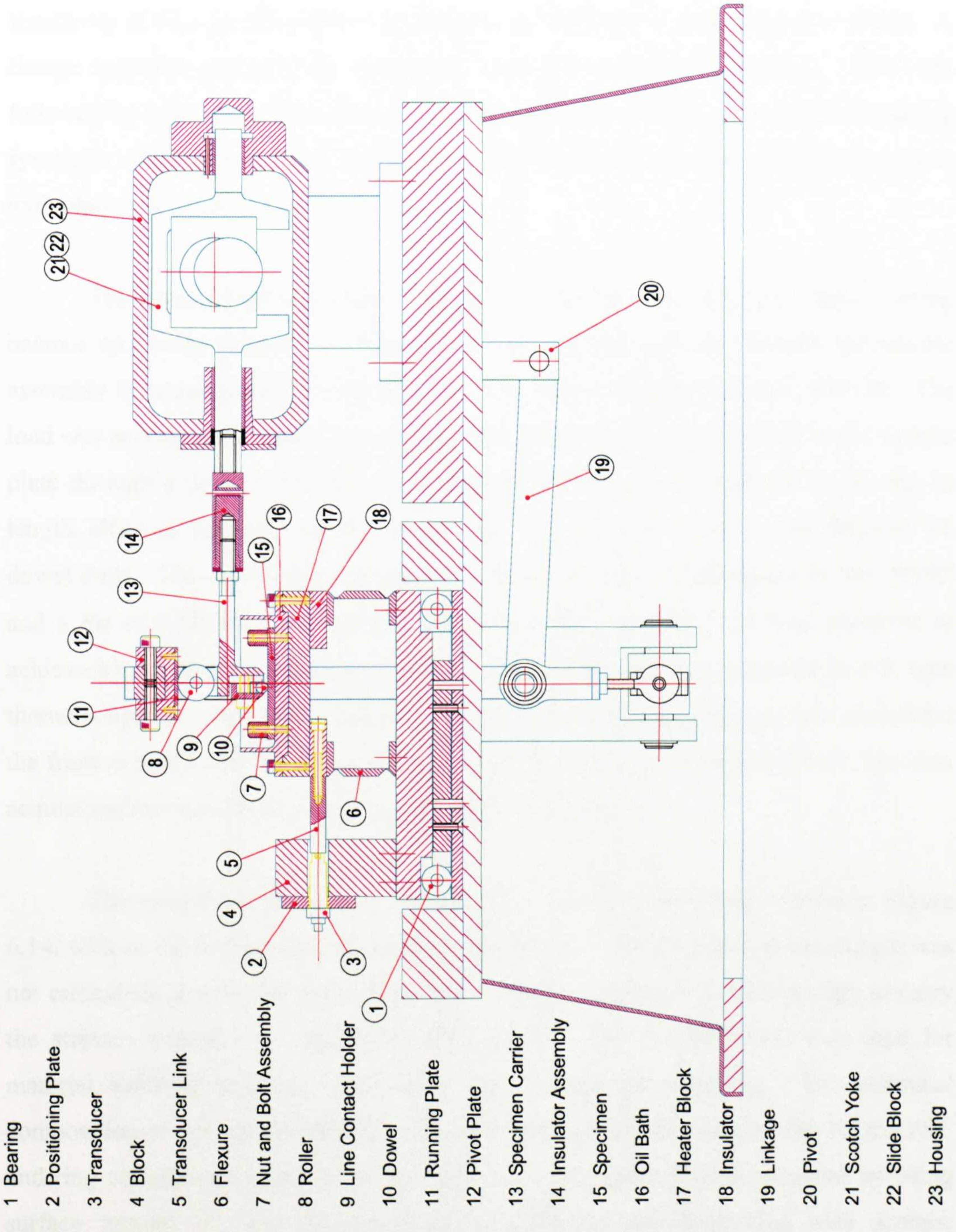

Figure 6.13 – Side view of Plint TE-77 showing oscillating mechanism and friction force measurement arrangement [5].

tacho generator feedback to ensure that a stable oscillating frequency is maintained. However, the maximum stroke distance can only be used when the frequency is below 30 Hz. The sample assembly was mounted on a flexure, which enabled the friction force to be measured using a Kistler Piezo-electric force transducer with a typical sensitivity of 43.5 picoColoumbs per Newton (pC N^{-1}) and a range from 0 to 500 N. A charge amplifier converts the measured force to a proportional voltage. This was followed by a low-pass filter, which fixed the upper cut off frequency of the measuring system to suppress transducer resonance. Final scaling of the signal for voltage output took place in a second stage amplifier.

The normal load was applied through the combination of a servo-motor, spring balance and beam linkage. A Kistler load cell mounted directly beneath the sample assembly then measured the normal load. The load cell range was 0 to 1000 N. The load was applied to the specimen using a yoke, which transmitted the load to the sample plate through a dowel. The dowel dimensions were 6 mm in diameter by 16 mm in length, although the actual contact length was 12.8 mm due to the conical shape of the dowel ends. The dowel material was 100Cr6 tool steel with a hardness of 841 HV05 and a *Ra* of 0.18 μm. The sample was heated by four 200 W heating elements to achieve a maximum temperature of 800°C. The temperature was measured by a K-type thermocouple attached to the sample surface. The accompanying software calculated the friction coefficient according to the ratio of friction force to normal force. The data acquisition rate used in this set of experiments was 1 Hz.

The sample geometry was 58 mm by 37 mm by 4 mm thick, shown in Figure 6.14, with an oxide layer grown *in-situ* on the test rig. The thickness of the sample was not critical since only the surface was tested and the sample was thick enough to carry the stresses without any significant deformation. The threaded hole was used for material handling purposes and proved very useful for polishing. The chemical composition of the reciprocating friction steel samples was the same as that for the PSC and ring compression tests, given in Table 4.2. The samples were prepared by being surface ground followed by polishing to 1000-grit and degreasing with acetone immediately prior to testing. From tests that were conducted with an overnight delay between polishing and testing it was found that a thin oxide layer formed despite the sample being dried using acetone and stored in a fume cupboard. This oxide formation was attributed to the increase surface energy as a result of the deformation caused by polishing. The sample relative to the line contact holder is shown in Figure 6.15.

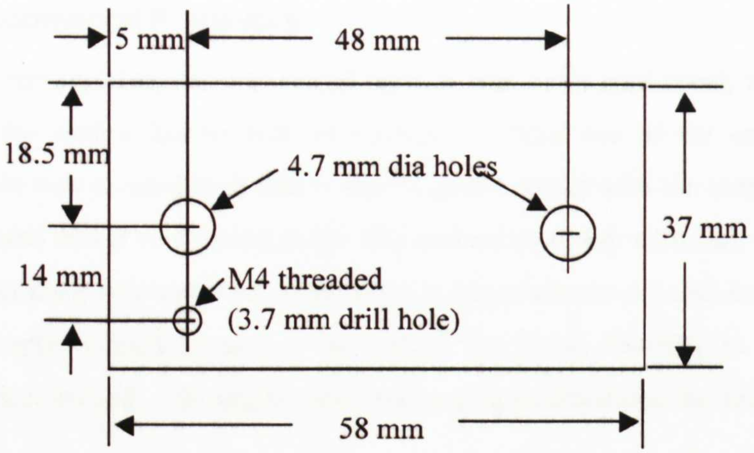

Figure 6.14 – Reciprocating friction test sample geometry.

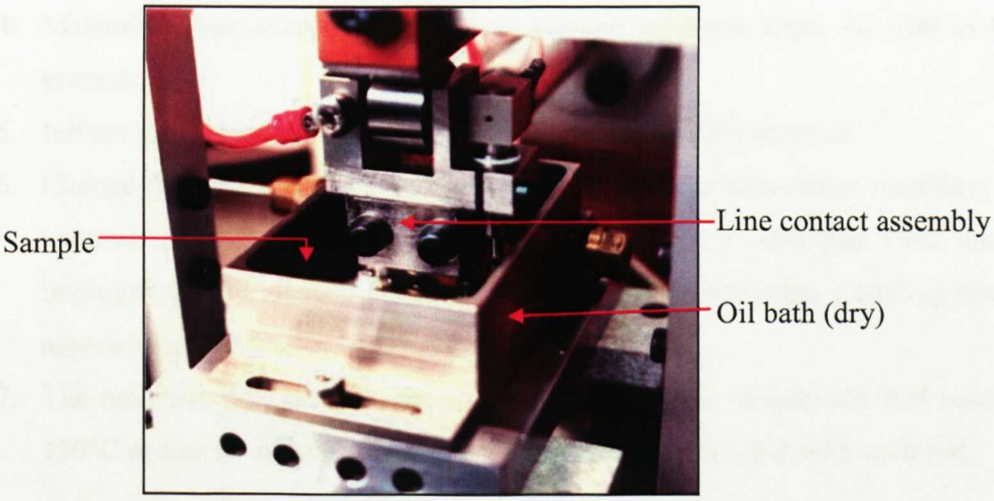

Figure 6.15 – Reciprocating friction test experimental set-up showing the line contact assembly in relation to the sample.

The remaining piece of equipment employed in these experiments was the Surtronic 3+, described in more detail in §6.2.1. The Surtronic 3+ was used to measure post reciprocating experiment roughness from both damaged and undamaged areas of the samples. The post experiment roughness was chosen since the oxide layer will obscure any surface features of the steel prior to oxidation [6].

6.3.2. Experimental Procedure

The reciprocating friction test procedure was not complicated; the sample was secured in the sample holder with two screws. Under one of the screws a type K thermocouple was secured such that it was in good contact with the sample surface. A new, degreased dowel was placed in the line contact assembly with care taken to ensure that a level contact was achieved. This point is important since a non-level contact will cause unacceptably high stresses at the end of the dowel resulting in abrasive wear, making the test invalid. The sequence of events programmed into the friction tester was as follows:

1. Apply small load, i.e. 1 N, to stabilise the yoke.
2. Set heating power to maximum, achieving a heating rate of approximately 1.1 K s^{-1}, until desired temperature is reached.
3. Increase normal load to desired level, i.e. 25, 50 or 100 N.
4. Maintain temperature for duration of desired oxidation time, i.e. 300 to 900 seconds.
5. Initiate the reciprocating cycle, set at 2 Hz, to run for 600 seconds.
6. Change the temperature set point to room temperature to continue recording the temperature upon cooling. Turn on compressed air, arranged such that it impinges directly against the bottom of the oil bath, achieving a cooling rate of approximately 0.6 K s^{-1}.
7. The next test may then started once the heater block temperature had reached 150°C or less to ensure the formation of a similar oxide layer with each test.

6.3.3. Results

The reciprocating friction experiments were conducted in two stages. The initial experiments were designed to investigate the usefulness of the Plint TE-77 reciprocating friction tester under dry conditions at elevated temperatures and to assess the applicability of this apparatus for studying dry friction. To this end the preliminary experiments were conducted at a single temperature, 450°C, a single oscillating frequency, 2 Hz, and a fixed running time of 10 minutes. The thickness of the oxide layer was varied through longer or shorter holding times at temperature and the normal load was varied between 25, 50 and 100 N. The second stage was to compare the extended, temperature dependent adhesion theory to experimental friction results by conducting experiments at various temperatures. The initial experiments showed that variations in the experimental parameters of oxide thickness, normal load and running time did not have a large effect on the outcome, as such the running time and hold times were set to 600 seconds and 120 seconds respectively to ensure a constant temperature during the test and the normal load was set at 100 N so as to be able to compare these results with the initial experimental results.

6.3.3.1. Initial Experimental Results

The results from the initial experiments, conducted in November 2002, are given here. The sample identification and corresponding test conditions are summarised in Table 6.1.

Table 6.1 – Summary of sample identification, test conditions and average friction coefficients.

	Oxidation time (s)		
Load (N)	300	600	900
25	air-i2b-07 $\bar{\mu}$=0.56	air-i2b-10 $\bar{\mu}$=0.51	air-i2b-12 $\bar{\mu}$=0.57
	air-i2b-08 $\bar{\mu}$=0.52	air-i2b-11 $\bar{\mu}$=0.58	air-i2b-13 $\bar{\mu}$=0.55
	air-i2b-09 $\bar{\mu}$=0.55		air-i2b-14 $\bar{\mu}$=0.53
50	air-i2b-15 $\bar{\mu}$=0.49	air-i2b-17 $\bar{\mu}$=0.49	air-i2b-18 $\bar{\mu}$=0.49
	air-i2b-16 $\bar{\mu}$=0.50	air-i2b-19 $\bar{\mu}$=0.50	air-i2b-20 $\bar{\mu}$=0.50
100	air-i2b-21 $\bar{\mu}$=0.50	air-i2b-23 $\bar{\mu}$=0.49	air-i2b-25 $\bar{\mu}$=0.49
	air-i2b-22 $\bar{\mu}$=0.47	air-i2b-24 $\bar{\mu}$=0.48	air-i2b-26 $\bar{\mu}$=0.48

The oxide thickness was expected to increase with time in accordance with parabolic behaviour. The average friction coefficients measured for the 300 second, 600 second and 900 second experiments were reasonably consistent for the normal loads of 50 and 100 N, regardless of the oxide thickness. The results for the 25 N experiments were inconsistent independent of the oxide thickness. Thus it was considered that the friction coefficient was independent of both load and oxide thickness when the load was greater than 50 N.

Typical friction coefficients measured during a test are shown in Figure 6.16. The spike at the beginning of the trace was caused by the force necessary to begin the movement since the dowel was in contact with the sample and the load was applied during the oxidation stage. Further friction coefficient traces are given in Appendix D.

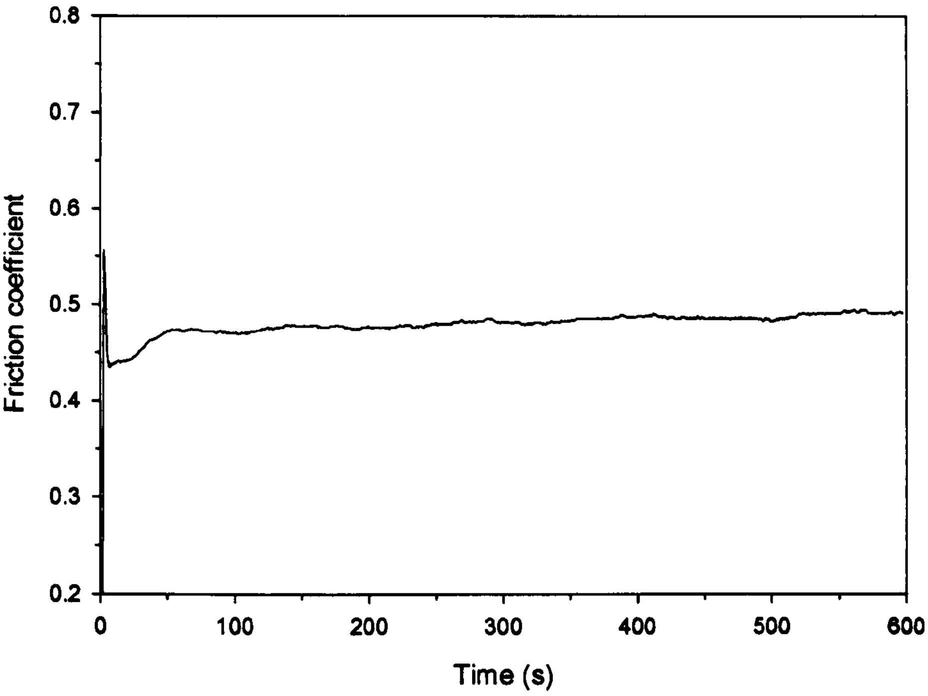

Figure 6.16 – The friction coefficient trace for sample air-i2b-25; oxidised at 450°C for 900 seconds and tested with a normal load of 100 N.

6.3.3.2. Validation Experimental Results

The results from the experiments, conducted in August 2003, designed to test the temperature dependence of friction, as predicted by the extended adhesion theory, are given here. The temperature range investigated was 200°C to 600°C; however, in experiments outside the 450° to 500°C range the experimental conditions changed as a result of the formation of particles removed from the oxide surface. In experiments conducted at 400°C and below the oxide layer was aggressively removed within the first few strokes of the reciprocating arm while in experiments conducted at 550°C and above a fine powder was formed shortly after the tests began but the oxide layer remained otherwise intact. In the range 450°C to 500°C the oxide layer remained intact with no particle formation, satisfying the desired test conditions. There was some minor variation in friction coefficient for the tests conducted at 450°C with an average of 0.48, compared with an average of 0.49 achieved in the first set of experiments. There were differences between the test conditions that could explain these results. First, the initial experiments were conducted in November 2002 when the weather was damp while the validation experiments were conducted in August 2003 when the weather was unseasonably warm and dry, which is important as humidity has been shown to affect friction coefficient results [7]. Second, the temperature control was significantly better in the initial experiments as all the tests were run at a single temperature whereas the validation experiments were conducted at a variety of temperatures. Since the equipment is typically used to test lubricants at temperatures around 200°C the equipment's heating capacity had not yet been optimised. The combined results for the reciprocating friction test are given in Table 6.2. Friction coefficient traces at 450°C, 475°C and 500°C are shown in Figure 6.17, showing the consistency between the initial experiments and validation experiments conducted at 450°C and the differences in friction coefficient observed between the experiments at 475°C and 500°C.

Table 6.2 – Combined test results using the Plint TE-77 reciprocating friction test device.

Temperature (°C)	Number of tests	Average μ	Standard Deviation	Comments
200	2	-	-	Debris formed
300	2	-	-	Debris formed
400	2	-	-	Debris (slightly less than above)
450	14	0.49	0.008	Suitable test conditions
475	1	0.46	-	Suitable test conditions
500	5	0.45	0.017	Suitable test conditions
550	2	-	-	Powder formed
600	4	-	-	Powder formed

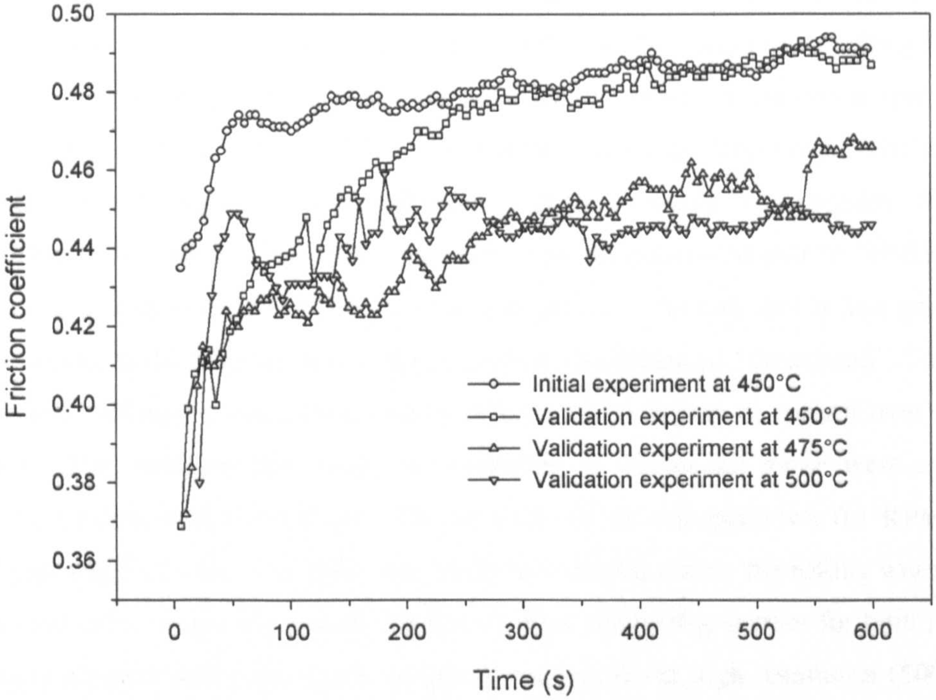

Figure 6.17 – Traces showing the variation of friction coefficient with temperature for samples oxidised at temperature for 600 seconds and a normal load of 100 N.

6.4. Laboratory Rolling

The use of laboratory rolling experiments to examine friction is not uncommon; however, the results of these experiments are typically not applicable to the industrial scale since the rolling conditions are significantly different. The main advantage of laboratory rolling is the control of the variables and the ability to measure the necessary parameters for a detailed study. As the extended adhesion theory is based on fundamentals it may be used to make predictions on both the laboratory and industrial scales. This supports the use of laboratory rolling experiments for validation purposes.

6.4.1. Mill Description

The equipment employed for this series of experiments consisted of a 2-high Hille Rolling Mill, a protective atmosphere furnace and a National Instruments DAQ system.

The 50 ton Hille mill, shown in Figure 6.18, has a 4 pole, 18.5 kW induction motor coupled with a 50:1 reduction gear and an AC motor controller, and a 3 kW 2000 RPM servo motor for roll gap control. The mill could be controlled by either a Control Techniques Interface Unit (CTIU) system in either manual or automatic modes, or in combination with a National Instruments system for user flexibility. The system is capable of multi-pass operations independent of the user with the exception of material handling. The material handling was directed by an automated pair of "traffic lights", shown in Figure 6.18, one for each rolling direction. The red, amber and green lights were linked to the programmed rolling schedule and indicated "do not roll", "prepare to roll" and "rolling" respectively; thus enabling a large degree of control over interpass times. The variables that could be controlled in automated mode were roll speed (including direction) and roll gap. The accuracy of the roll speed was 0.1 RPM and the roll gap was 0.01 mm. Variables that could be recorded during the rolling were load via two load cells, torque via a shaft clamp-on torque measuring system for both rolls with induction power and radio signal coupling, roll speed via high resolution (5000 points per revolution) optical encoders and temperature.

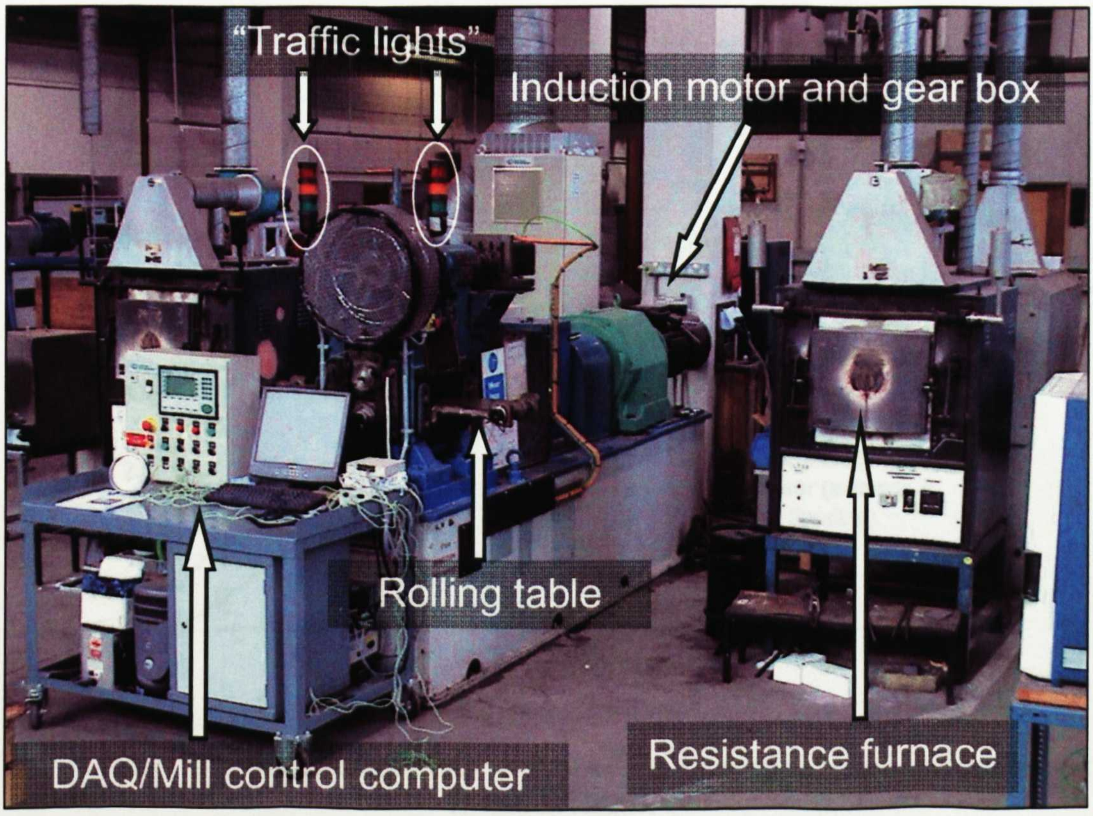

Figure 6.18 – General layout of the 50 ton Hille mill.

The torque sensors of the top and bottom drive shafts were calibrated by applying a known static torque and comparing it against the measured torque, as shown in Figure 6.19. At torques above approximately 150 Nm both sensors gave linear loading curves, which were used for the calibration equations given by:

$$M^{bottom}_{applied} = 1.014\left(M_{measured} - 34.594\right) \tag{6.1}$$

$$M^{top}_{applied} = 1.018\left(M_{measured} + 35.009\right) \tag{6.2}$$

The resistance furnace used silicon carbide spiral elements and is capable of a maximum temperature of 1400°C with a protective atmosphere. The protective atmosphere consisted of 85.6% by volume nitrogen, 10.6% by volume carbon dioxide, 2.0% by volume carbon monoxide and 1.8% by volume hydrogen supplied by an Atmo-Gen XCFGC30 exothermic gas generator. The National Instruments DAQ system consisted of a PCI-6040E Multifunction I/O board and a PCI-6602 Counter/Timer board.

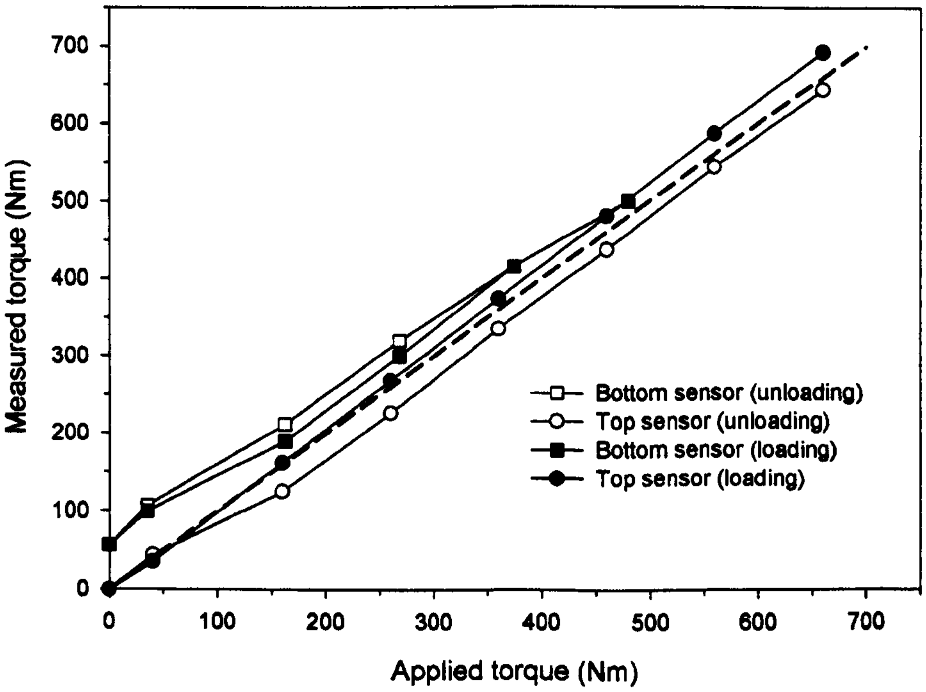

Figure 6.19 – Torque calibration curves showing the applied torque against the measured torque.

The rolling samples were 30 mm wide by 25 mm tall by 200 mm long, chosen so that the samples become close to square after the descaling pass. As the sample was to be rotated by 90° it was necessary for the thermocouple holes to be drilled from the end of the sample rather than is usual from the side, as shown in Figure 6.20. Due to the difficulty of drilling a 1.6 mm diameter hole to the centre of the sample the majority of the length was drilled as an oversized hole of 2.5 mm in diameter with the last 10 mm at 1.6 mm diameter. To secure the thermocouples steel split pins were inserted in the opening to reduce the size of the hole sufficiently to centre punch the material to pinch the thermocouple in place. The chemical composition of the rolling samples is given in Table 6.3.

Table 6.3 – Rolling samples chemical composition in weight%, remainder iron.

C	Mn	Si	S	P
0.18	0.82	0.27	0.015	0.037

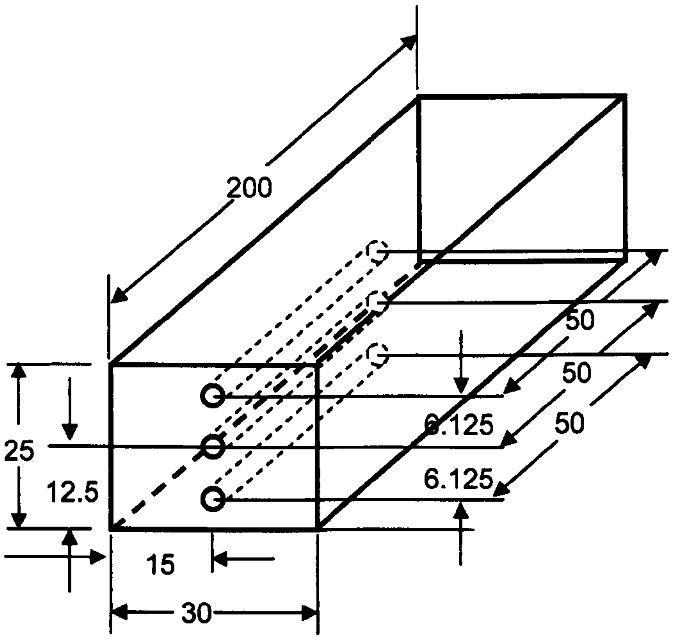

Figure 6.20 – Schematic of rolling sample with dimensions in mm. Note: not to scale.

The roll diameter was measured to be 139.4 mm with an average transverse *Ra* of 0.88 μm and 0.78 μm for the top roll and bottom rolls respectively, measured using a Surtronic 3+ profilometer.

6.4.2. Experimental Procedure

The procedure followed for the laboratory rolling experiments was the following: The thermocouple extension leads were fed through the roll gap and attached to the sample, which were then heated in a protective atmosphere to the desired temperature. Upon removal of the sample from the furnace the automatic control of the mill was started and the sample fed into the mill, thermocouple leads first, such that the thermocouples were oriented horizontally rather than vertically, when told to do so by the "traffic lights". The sample was then manually rotated by 90° while the mill automatically reversed the direction of the work rolls and set the second pass roll gap. The sample was then fed back into the mill, again when told to do so by the "traffic lights".

The mill control system has five parameters: Pass time, mill set-up time, number of passes, roll speed and gap size. The pass time indicates the amount of time available for rolling per pass, set to 10 seconds for these trials. The number of passes is indicated by the number of mill set-up times required, for these trials the mill set-up time was 10 seconds. The roll speed for the first pass was +10 RPM and -10 RPM for the second pass, where the negative sign indicates the reversing direction of the work rolls. The roll gap was 27 mm for the first pass and 20 mm for the second pass.

6.4.3. Results

There were two objectives for the laboratory rolling experiments: 1) to obtain a thin adherent scale layer and 2) to obtain process data for comparison to the FE model. The results of the laboratory rolling tests are summarised in Table 6.4.

Table 6.4 – Summary of laboratory rolling parameters and results.

Sample ID	Furnace exit T (°C)	Interpass time (s)	1st pass entry T (°C)	2nd pass entry T (°C)	Average torque (Nm)*	Average load (kN)
13-09	1065	11	1025	966	772	82.0
06-10a	1100	45	1040	830	1159	89.7
06-10b	1056	12	1008	933**	946	86.6
06-10c	1070	13	1020	947**	959	84.6
01-11a	1080	9	1005	940	943	87.7
01-11b	1080	13	1025	943	933	83.4
01-11c	1090	13	1041	943	859	76.6
03-11a	1050	12	995	916	987	92.5
03-11b	1046	13	985	907	1042	92.0
03-11c	1057	12	1010	930	935	87.1
03-11d	1048	13	988	913	1009	90.8

* includes bearing torque

** estimated

From Table 6.4 it can be seen that the two-pass rolling schedule achieved consistent interpass roll times, with the exception of sample 06-10a where there was a material handling error causing the increased interpass time. As a result of the consistent interpass time there was a correlation between the 1st pass entry temperature and the 2nd pass entry temperature for samples with consistent interpass times, thus sample 06-10a was not included, given in Figure 6.21. A regression analysis gave a linear equation of the following form:

$$T_{2nd\_pass}^{entry} = 1.14 \cdot T_{1st\_pass}^{entry} - 216 \qquad (6.3)$$

Equation 6.3 was used to estimate the 2nd pass entry temperature of samples 06-10b and 06-10c, which was necessary due to the breakage of the centreline thermocouple.

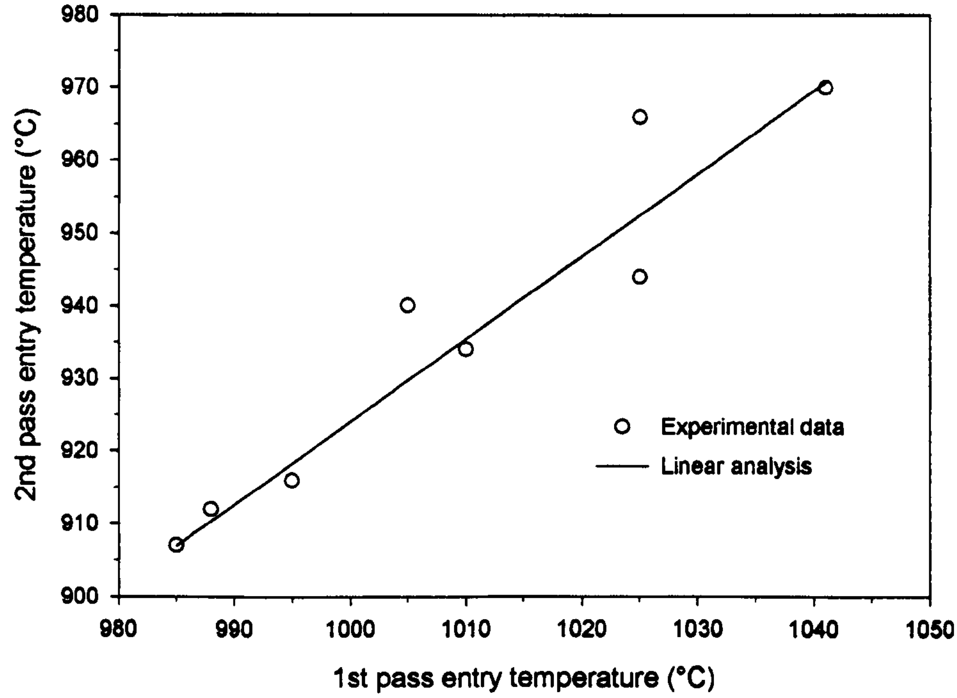

Figure 6.21 – Correlation between the 1st pass entry temperature and the 2nd pass temperature for samples with between an interpass time between 11 and 13 seconds.

6.4.3.1. Scale Layer during Rolling

One of the major assumptions of the FE model is the presence of a thin, adherent scale layer. To achieve a thin scale layer a two-pass rolling schedule was designed; unfortunately quantitative assessment of the scale layer entering the roll gap was unrealistic. Qualitatively the scale removal was deemed successful by visually comparing the extent of the scale removal from the sides of the sample. Images taken from video footage showing the roll bite for each of the descaling and principal rolling passes for sample 03-11a are given in Figure 6.22. In a similar fashion images showing the roll bite entry/exit are shown in Figure 6.23 and 6.25 for samples 03-11b and 03-11c

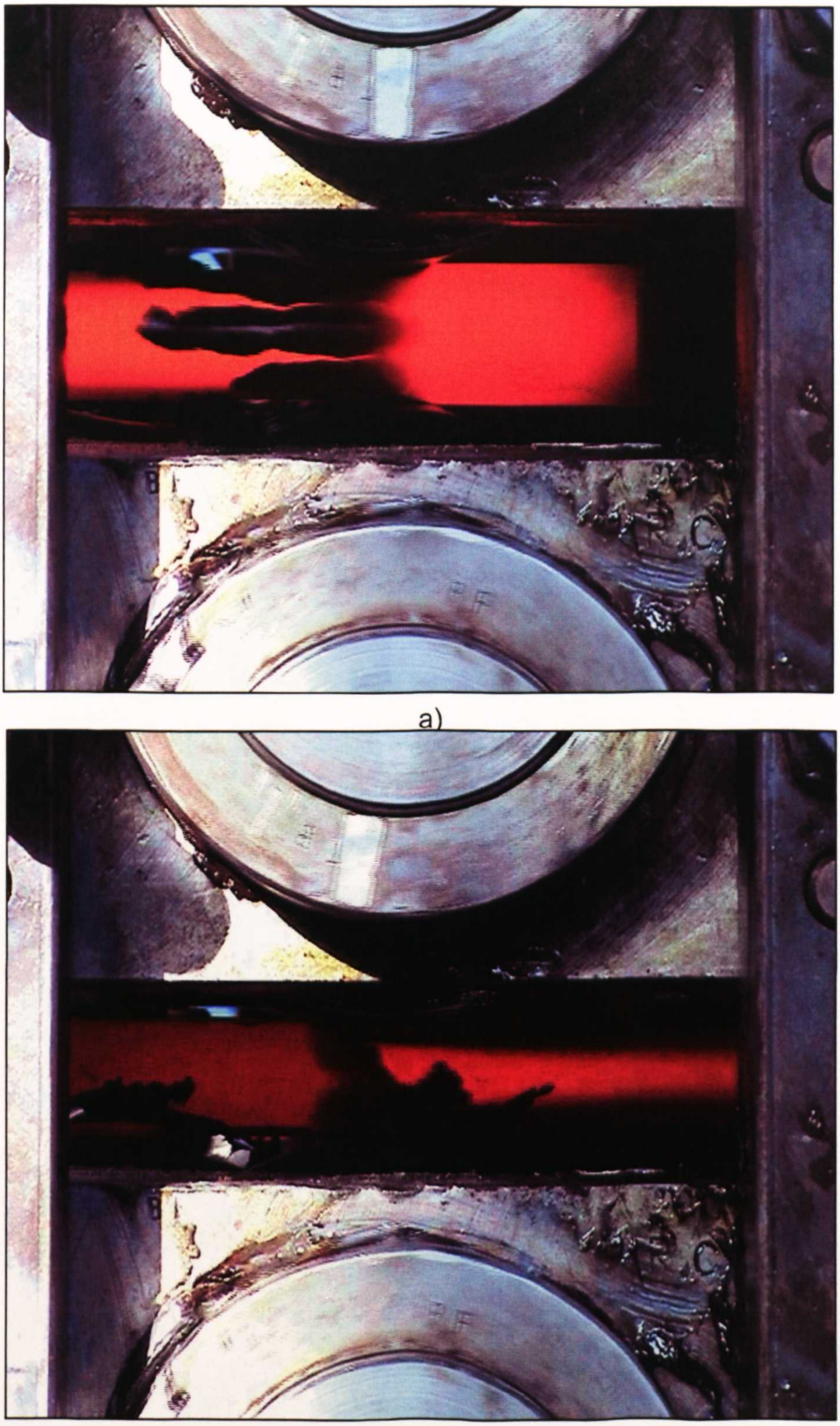

a)

b)

Figure 6.22 – Effect of the different rolling passes on the scale layer removal as seen looking at the roll gap for sample 03-11a; where a) is the descale pass (10% reduction) travelling from right to left, and b) is the principal rolling pass (20% reduction) travelling from left to right.

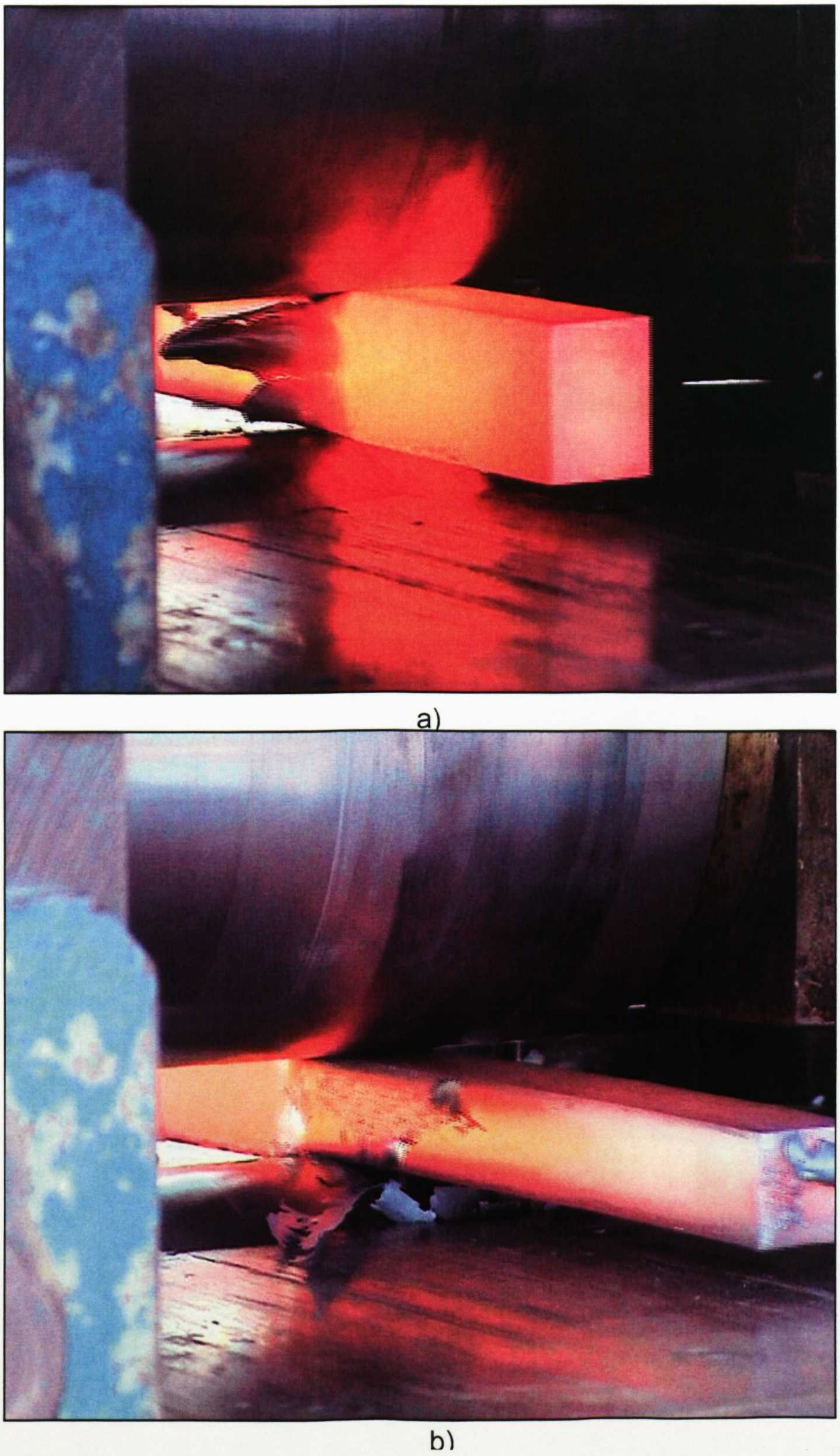

Figure 6.23 – Effect of the different rolling passes on the scale layer removal for sample 03-11b; where a) is looking at the roll bite entry for the descale pass (10% reduction), and b) is the looking at the roll bite exit for the principal rolling pass (20% reduction).

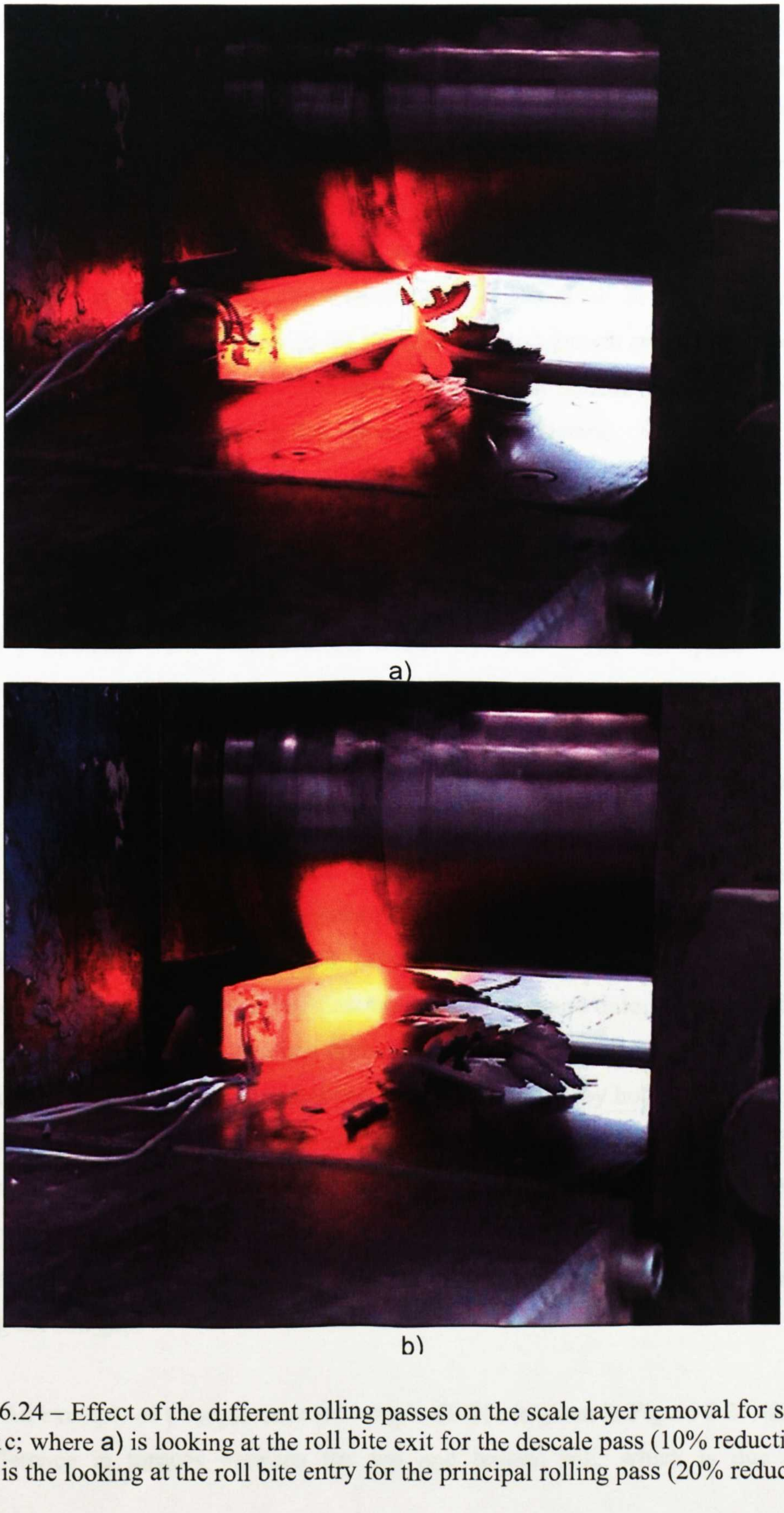

a)

b)

Figure 6.24 – Effect of the different rolling passes on the scale layer removal for sample 03-11c; where a) is looking at the roll bite exit for the descale pass (10% reduction), and b) is the looking at the roll bite entry for the principal rolling pass (20% reduction).

respectively. The descaling pass was deemed effective by the reduced amounts of scale peeling from the sides of the sample during the 20% reduction rolling pass compared with the 10% reduction descaling pass. This effect was not as obvious in Figure 6.24 as there appears to be significant amounts of scale peeling from the sides during the 20% reduction, especially compared with the amounts visible in Figure 6.23. This could be explained by the differences in temperature at both the furnace exit and the entry of the 2nd pass, since at high temperatures a small increase can result in substantially more scale growth if the scale growth is in the linear and mixed growth regions, as discussed in §3.4.3. Furthermore Figure 6.24b shows the sample surface to have a uniform colour, i.e. temperature, indicating that the scale layer is adherent.

6.4.3.2. Rolling Process Parameters

The rolling process parameters recorded for comparison of experimental results and FE predictions were: temperature, torque and load. The roll speed was also recorded, for checking consistency rather than for comparative purposes.

The temperature traces for sample 03-11d during the 20% reduction pass are given in Figure 6.25. Heat generated by plastic deformation can be seen at the centreline and quarter positions where the temperature has increased once the sample has entered the roll gap. The temperature traces for the quarter positions and the centreline position are not identical because the quarter position thermocouples measured the heat lost to the environment during the interstand time, 13 seconds for this sample, showing the thermal gradient through the sample when it entered the pass. The similarity between these thermocouple readings was achieved by holding the sample off the rolling table during the interpass time. The location of the thermocouples, 50 mm from the end of the sample, was the maximum depth that could be achieved without excessive time and cost for each thermocouple hole and were chosen to record the temperatures during steady-state deformation, avoiding the end effects of the sample entering the roll gap.

An example of a torque trace for sample 06-10c is given in Figure 6.26, showing the difference in torques between the top and bottom roll, which is due to the

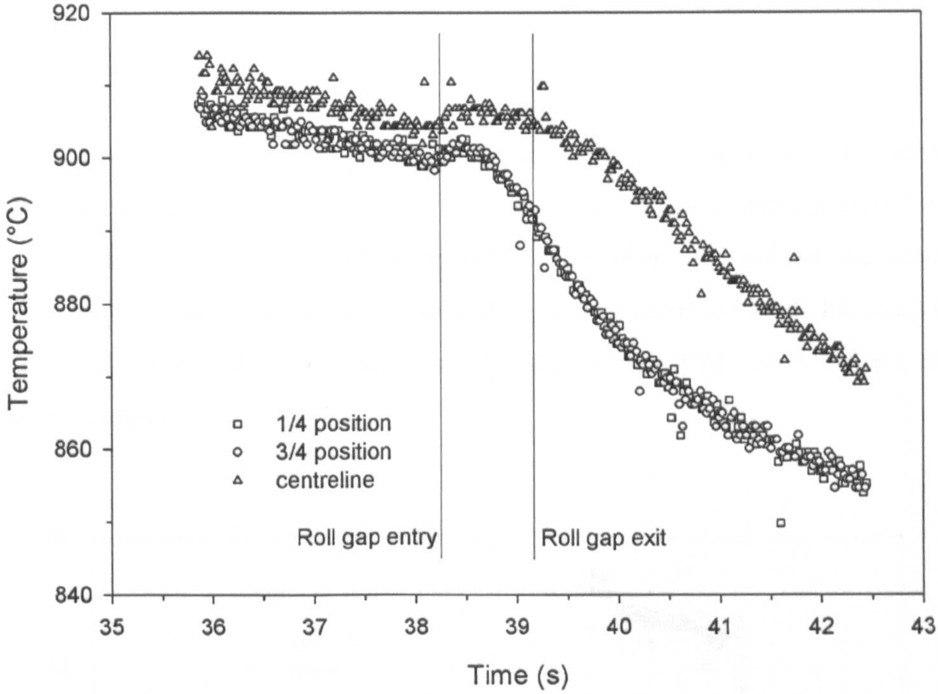

Figure 6.25 – An example of the temperature trace through the roll gap for sample 03-11d with 20% reduction at a roll speed of 10 RPM.

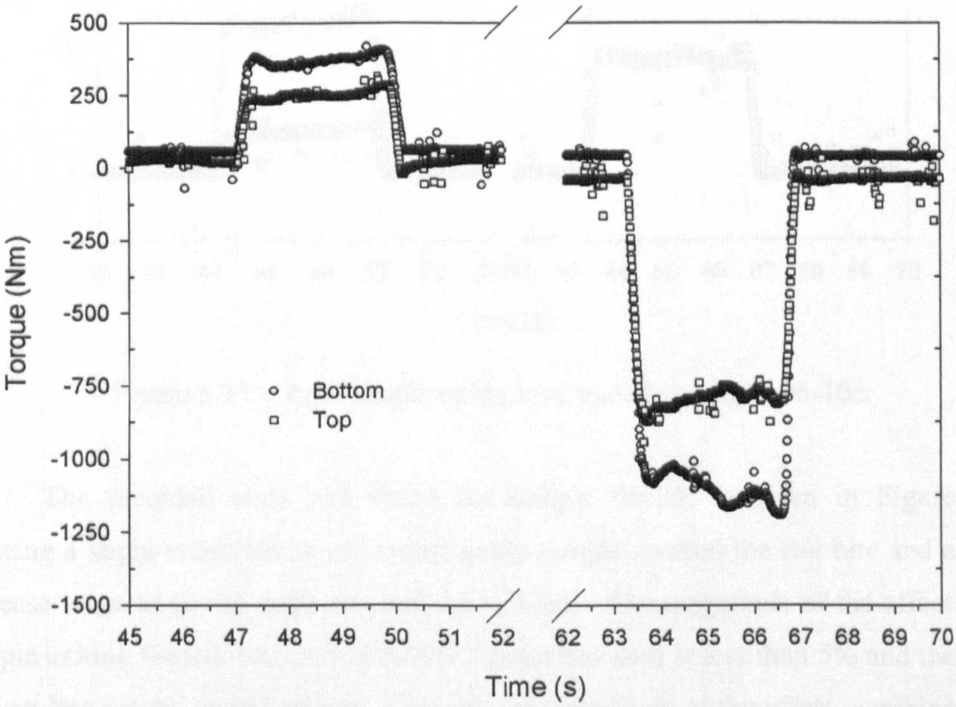

Figure 6.26 – An example of the torque trace for sample 06-10c.

nature of laboratory rolling. Also shown was an offset in the recorded torque for the top work roll. It should be noted that the measured torques includes the torques from the drive bearings.

An example of the recorded rolling load is given in Figure 6.27 for sample 06-10c showing the difference between the load cell on the drive side compared with the operator's side due to the sample being fed on the drive side half of the work rolls, which can be seen in Figure 6.24, by the differences in recorded loads between the two load cells, which was done to keep the other side of the rolls unused for a different rolling experiment.

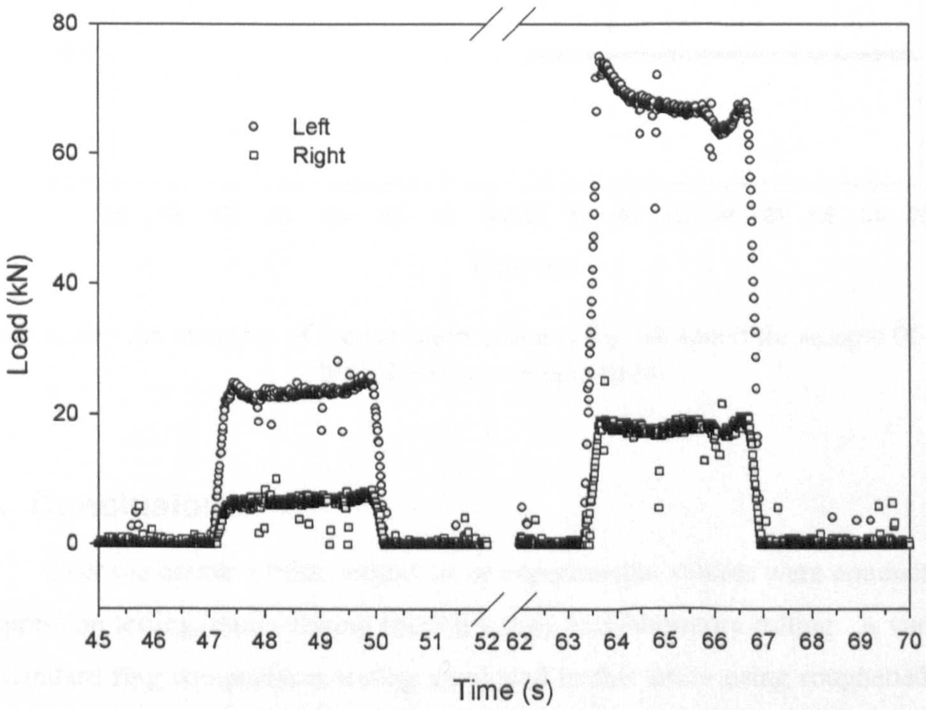

Figure 6.27 – An example of the load trace for sample 06-10c.

The recorded work roll speed for sample 06-10c is given in Figure 6.28, showing a slight reduction in roll speed as the sample entered the roll bite and a slight increase in speed as the sample exited the roll bite. The magnitude of the effect of the sample exiting the roll bite during the 20% reduction pass is less than 5% and the effect is even less for the descaling pass. The minute magnitude of the effect, combined with the rapid return to the desired roll speed, means that this can be neglected in the analysis but highlights that there are effects due to the equipment, in addition to the material.

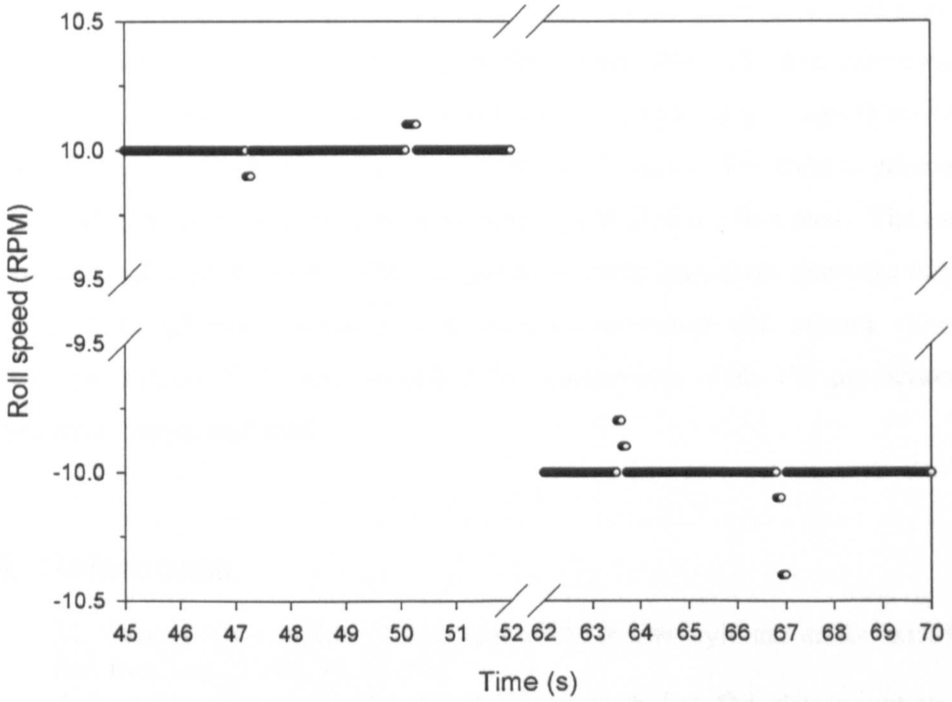

Figure 6.28 – An example of the variation of the work roll speed for sample 06-10c, for both directions of operation.

6.5. Conclusions

Over the course of this project three experimental studies were conducted: ring compression testing, reciprocating friction testing and laboratory rolling. A variation on the standard ring compression testing employed in this study using roughened platens; however the technique was not found to be sufficiently sensitive for further use towards a fundamental study of friction.

The reciprocating friction test gave consistent results between tests of nominally identical conditions and tests were conducted over a temperature range of 200°C to 600°C. The only suitable experimental conditions were in the temperature range of 450°C to 500°C; during experiments at temperatures below this range there was an aggressive removal of the oxide layer and at temperatures above this range the formation of a powder at the surface occurred. Within this 50 K temperature range the measured friction coefficients were sufficiently consistent at the applied normal loads and oxide thickness.

The laboratory rolling experiments were conducted with a two-pass rolling schedule to obtain a scale layer that was as thin as possible. The first pass used a 10% reduction to remove the scale from the side of the sample, which was then rotated so that the descaled sides became the top and bottom surfaces. The sample geometry was chosen such that the sample became relatively square after the first pass. The use of the automatic capability of the mill control system enabled consistent interpass times to be achieved, although some variation from human intervention still existed. The rolling process parameters that were recorded for comparison with FE predictions were temperature, torque and load.

6.6. References

1. M. Kunogi "On the plastic behaviour of the hollow cylinder under axial load", J. Sci. Res. Inst., 1954, 30, 63-92
2. A.T. Male and M.G. Cockcroft "A method for the determination of the coefficient of friction of metals under conditions of bulk plastic deformation", J. Inst. Metals, 1964, 93, 38-46
3. N.T. Rudkins, P. Hartley, I. Pillinger and D. Petty "Friction modelling and experimental observations in hot ring compression tests", Journal of Materials Processing Technology, 1996, 60, 349-353
4. J.D. Fletcher, Y.H. Li, J.H. Beynon and C.M. Sellars "The influence of surface conditions in hot forming determined by ring upsetting: a numerical and experimental investigation", Proc Instn Mech Engrs Part J, Journal of Engineering Tribology, 1998, 212, 453-465
5. Phoenix Tribology Ltd, "Plint TE-77 Operator's Manual"
6. Y. Yu and J.G. Lenard "Estimating the resistance to deformation of the layer of scale during hot rolling of carbon steel strips", Journal of Materials Processing Technology, 2002, 121, 60-68
7. K. Tanaka, J. Ishikawa and A. Shimamoto "Elastic contact and friction between sliders and circumferentially textured disks-Part III: Experiments", Journal of Tribology, 1998, 120, 800-807

Chapter 7 - Discussion

7.1. Introduction

The most elegant theory in the world is of limited practical value unless it has been demonstrated to be grounded in reality. To this end the developed friction theory, via the friction algorithm, is compared to laboratory rolling experiments in order to be validated. The validation procedure is necessary to gain confidence in the theory before applying it to other systems, such as industrial rolling. The following discussion is centred on aspects of validating the developed theory but also considers how the theory may be applied in other circumstances.

Before a validation of the theory is accepted the experiments used, in this case reciprocating friction tests and laboratory rolling tests, should be examined. Since the theory predicts a phenomenon that is difficult to measure experimentally a sensitivity analysis has been conducted to show which parameters used in the theory have the biggest effect on the friction coefficient. One of the assumptions of the theory is particularly contentious, namely the role of roughness angle. Therefore this parameter is discussed in detail to support the assumptions required by the theory.

The friction theory developed in this work was an extension of the existing adhesion theory of friction. There have been some criticisms levelled against the original adhesion theory; these criticisms, as well as potential criticisms, and their rebuttals are also discussed.

There are two principal types of friction models, i.e. Coulomb and friction factor. A Coulomb type model is preferable in some situations while a friction factor is more suited to others. Therefore the theory has been re-derived in terms of a friction factor model.

Lastly, some blue sky engineering is indulged in to speculate on material pairings that should reduce the friction coefficient during the hot rolling of steel.

7.2. Experimental Considerations

In order to justify the soundness of the theory it is necessary to examine the experiments that were used to identify and verify the theory. In this case, the reciprocating friction test provided data used to confirm applicability of the theory for different temperatures and materials than those quoted in the original derivation; and laboratory rolling tests were used to show the theory could be applied to the hot rolling of steel.

7.2.1. Reciprocating Friction Test

Given the narrow band of experimental conditions available to test the modified adhesion theory two questions should be considered, namely:

1) Does the oxide layer on the sample surface remain intact?

The surface profiles were measured across the sample, i.e. perpendicular to the direction of travel, using a Surtronic 3+ profilometer. The average roughness of the scuffed surface is compared to the average roughness of the smooth surface in Figure 7.1, using the *Ra* measure, showing that the load has not affected the average roughness of the samples which suggested that the test was independent of the oxide thickness.

The *Ry* method indicates the maximum peak-to-valley height across a sample, shown in Figure 7.2. The maximum *Ry* value was seen in Sample 7, with a value of 20 μm; however, from the surface profile the actual penetration depth is closer to 10 μm since it is likely that there had been a build-up of material that makes the penetration depth appear greater than it actually was. With later samples, the penetration depths were reduced and became more consistent. The deeper penetration may have been caused by abrasive wear since the load did not have an obvious effect on the overall surface roughness.

Thus, the independence of the friction coefficient with respect to the thickness of the oxide layer, along with the absence of any trend in the *Ra* and *Ry* measurements suggests that the dowel is not interacting with the steel substrate.

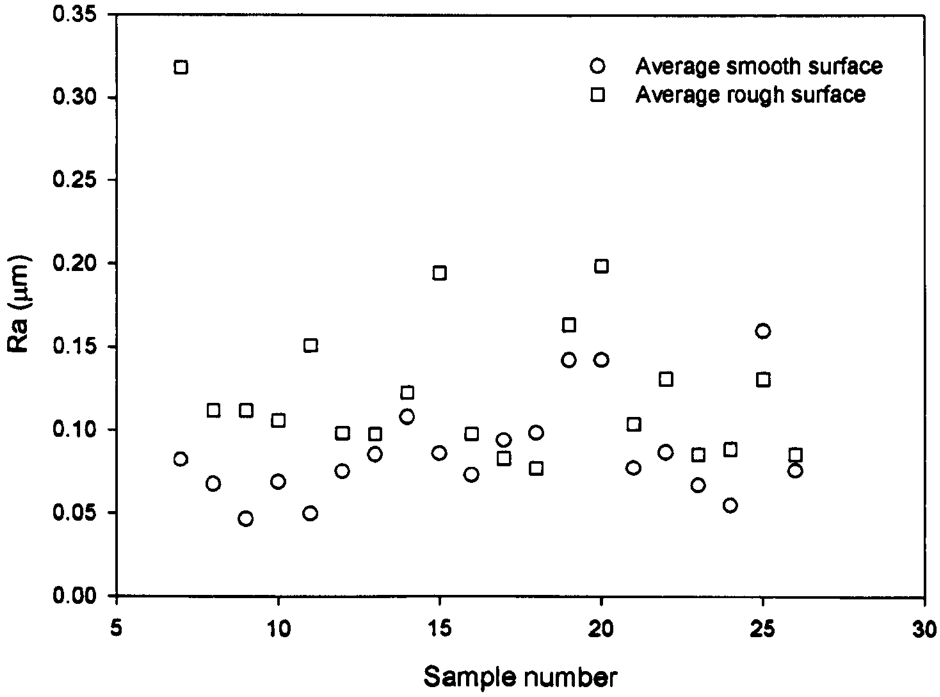

Figure 7.1 – Average surface roughness (*Ra* in μm) versus sample number.

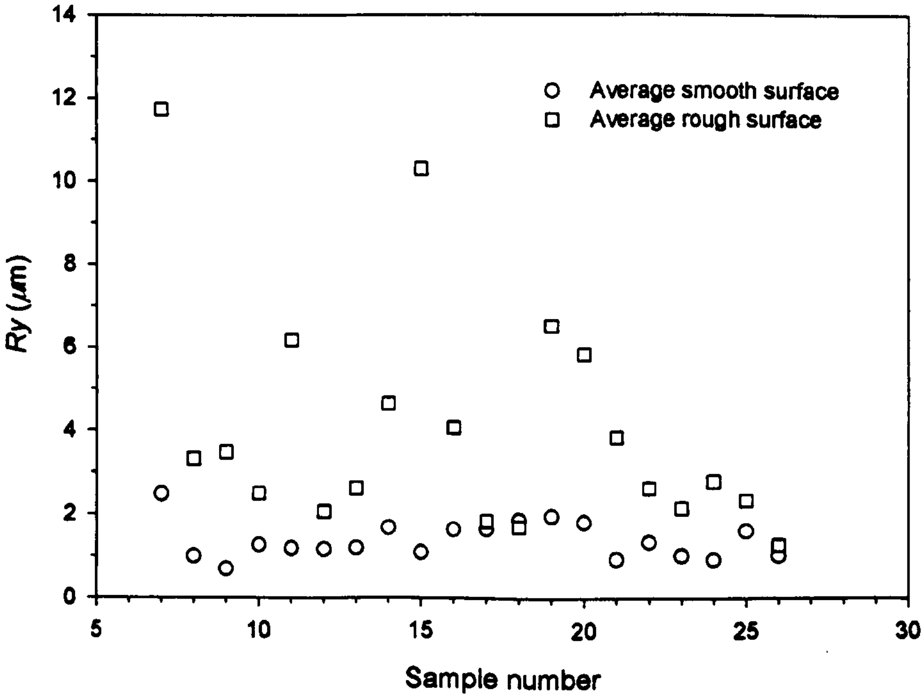

Figure 7.2 – Average peak-to-valley heights (*Ry* in μm) versus sample number.

The samples subjected to a normal force of 50 N or 100 N showed a consistent friction coefficient of approximately 0.49, independent of the oxide thickness. The samples subjected to a normal load of 25 N showed a slight increase in friction coefficient over time as well as a variation of friction coefficient from test to test for nominally the same conditions. The results for the 25 N normal load experiments are in line with those expected for a contacting surface with a thin, stiff surface layer, i.e. an oxide layer, since the deformation of the asperities may not necessarily be plastic or the junctions formed may not have a constant specific shear strength; thus violating the conditions required for Coulomb friction [1]. Also, the range of the friction coefficients at the end of the test was relatively consistent between oxide thicknesses.

Furthermore, in the tests that were used to develop the theory as applied to high temperature friction conditions, namely the tests between 450°C and 500°C, virtually no debris was observed, especially compared to the sub-450°C tests, where there was wholesale removal of the oxide layer, or above 500°C, where an obvious powder was formed. Thus it was considered that the friction coefficient for the tribo-pair of tool steel and magnetite was measured.

2) Is the consistency of the results real?

A total of fourteen tests were conducted at 450°C with two load levels over a period of ten days. The overall average and standard deviation of these tests were 0.491 and 0.008 respectively, while the average and standard deviation from the initial experiments, of which there were twelve results, were 0.492 and 0.008 respectively. For the second set of experiments two tests were conducted at 450°C for comparison with the previous results, recording an average and standard deviation of 0.483 and 0.007 respectively. In addition to this, five tests were conducted at 500°C with an average of 0.449 and a standard deviation of 0.017. The repeatability of these experiments is in line with those quoted by Gee and Lay [2] for reciprocating friction testers. Furthermore, Blau [3] compared the behaviour of the Plint TE-77 using various contact geometries, including ring/liner-contact, in an international round-robin testing program led by the Oak Ridge National Laboratory leading to approval for ASTM Standard G-133 testing. Therefore it was concluded that the Plint TE-77 reciprocating tester was able to accurately and consistently measure the friction coefficient for the experimental conditions employed in this study.

7.2.2. Laboratory Rolling

Laboratory rolling is well described in the literature [4,5] but cannot be directly applied to the industrial case largely as a result of the strain rate sensitivity of steel [6]. The friction model described in §5.2 relies upon the parameters of temperature and contacting materials, both of which can be taken from either the laboratory or industrial cases. This leads to the following two questions:

1) How does the scale layer in the laboratory relate to industrial rolling?

The thickness of the oxide layer entering the second pass is determined by the sample temperature and the interpass time, assuming that the majority of the scale layer is removed by the first descaling pass. With industrial rolling the interpass time represents the distance (or time) between the post roughing descalers and the first stand; measured thicknesses of the tertiary scale on strips from various hot rolling mills range between 2 and 30 μm [7-9]. Laboratory scale thicknesses, including a descaling pass, have been reported to vary between 20 and 60 μm, depending on the oxidation start temperature [10]. The oxide thickness was most strongly affected by temperature followed by time; although humidity also has a strong influence. Generally the experimental interpass time was around 12 or 13 seconds, longer than the time of a typical rolling mill of around 5 seconds, but the rolling temperatures were lower and the humidity was much lower than in an industrial rolling mill. All of which gives credence to the assumption that the experimental scale layer during the second pass was of a similar order of magnitude as the industrial system, thus the laboratory rolling procedure employed in this study provided a relevant scale layer.

2) Is the surface of the scale layer magnetite?

As noted above, the time available for oxidation of the sample surface was around 13 seconds at a temperature above 900°C. Various oxidation studies [11-14] have disagreed over the levels of wüstite, magnetite and hæmatite at hot rolling temperatures. Differences in the results of these oxidation studies have been attributed to the degree of scale adherence and ferrous ion supply [8]. One of these studies of scale formed on steel was conducted by Blazevic [14], using mild steel samples and non-isothermal conditions to estimate the scale composition with temperature, shown in Figure 7.3.

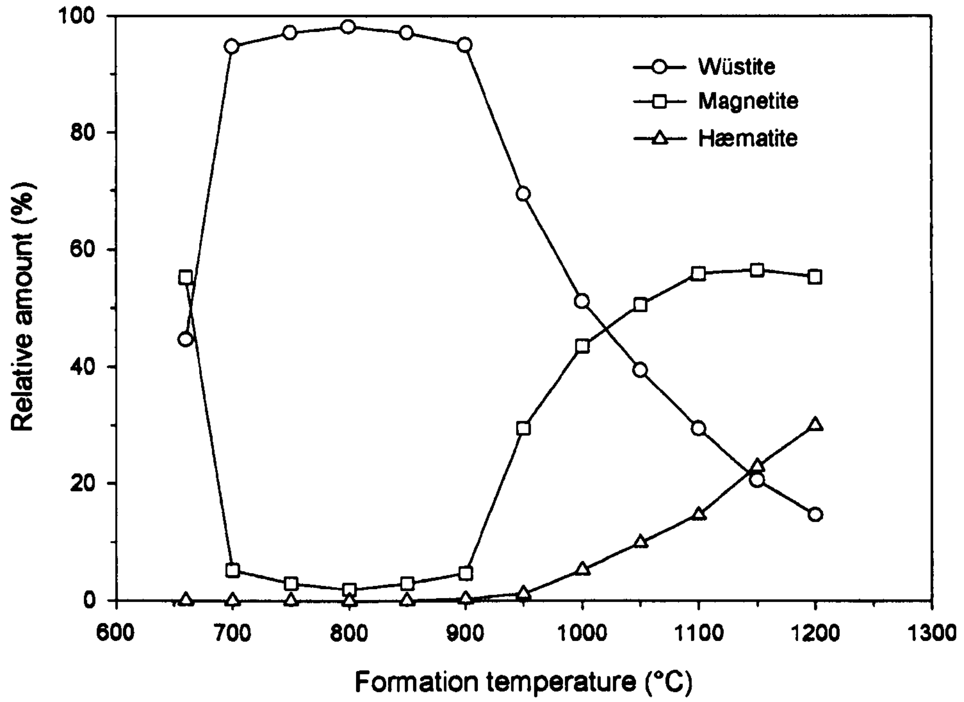

Figure 7.3 – Scale composition during oxidation [14].

Below 570°C, the scale composition will be primarily of magnetite with small amounts of hæmatite depending on the oxidising conditions. Between 700°C and 900°C the scale consists primarily of wüstite with a small amount of magnetite and virtually no hæmatite. Above 900°C the relative amount of wüstite rapidly drops with a corresponding rapid increase in magnetite and increases in hæmatite. The second pass rolling temperatures for this study were all above 900°C, which suggests that significant amounts of magnetite would be formed. Since magnetite is oxygen rich compared to wüstite it will always form at the oxygen-solid interface, i.e. at the surface, rather than the solid-solid interface. Thus it is a reasonable assumption that the surface of the sample contacting the work rolls consisted primarily of magnetite. The difficulty in determining this assumption experimentally is that any characterisation of a sample by x-ray diffraction would include a quantity of transformed magnetite (since wüstite is not stable below 570°C) and possibly any magnetite that reacts with oxygen to form hæmatite.

7.3. Model Comparison

The development and verification against literature data of the rolling model, including the friction algorithm, has been discussed in §5.3. Assumptions specific to the rolling models to be compared with the laboratory rolling results were as follows: the Shida equations were used to calculate the steel flow stress for a 0.18 wt% carbon steel, the oxide surface was assumed to be magnetite contacting the clean steel surface of the work roll, the sample was reduced from 26 mm in thickness to a final thickness of 20 mm, the geometric mean rule has been used to estimate the thermodynamic work of adhesion and the heat transfer coefficient employed was 25 kW m^{-2} K^{-1}. The model was then compared with experimental data for the parameters of temperature, rolling load and rolling torque. The effect of the friction algorithm is further demonstrated with a comparison of the predicted friction coefficient through the roll bite with average values.

7.3.1. Temperature Comparison

One means used to validate finite element (FE) models is a temperature comparison. The temperature comparison for sample 03-11d is shown in Figure 7.4, showing a good fit between the model predictions and experimental results for a heat transfer coefficient of 25 kW m^{-2} K^{-1}, which is in line with the heat transfer coefficients reported by Li and Sellars [4]. The fit is considered good, despite the obvious differences between the experimental temperatures and the predicted temperatures, since the model predicts the same thermal recovery rate approximately 1 second after entering the roll gap. The maximum temperature rise recorded at the centreline was approximately 3°C and does not match the expected temperature rise of 12°C based on adiabatic heat generation due to plastic deformation, T_d, given by [15]:

$$T_d = \frac{U_p}{\rho C_p} = \frac{\bar{\sigma} \cdot \bar{\varepsilon} \cdot \mathrm{B}}{\rho C_p} \qquad (7.1)$$

where U_p is the work of plastic deformation per unit volume, ρ is the density (in kg m^{-3}), C_p is the specific heat capacity of the material (in J kg^{-1} K^{-1}), $\bar{\sigma}$ is the mean flow stress (in MPa), $\bar{\varepsilon}$ is the mean strain and B is the fraction of deformation work converted into heat, which is conservatively 0.95 with the remainder of the deformation work stored in the material as energy associated with the defect structure. The probable reason for the reduced measured temperature rise is a slight time delay in recording the temperature during the 20% reduction pass as a result of the 10% deformation being insufficient for the thermocouples to achieve an intimate contact with the surrounding metal, shown schematically in Figure 7.5; thus the recorded temperature profile during rolling cannot be directly used for comparison with FE predictions.

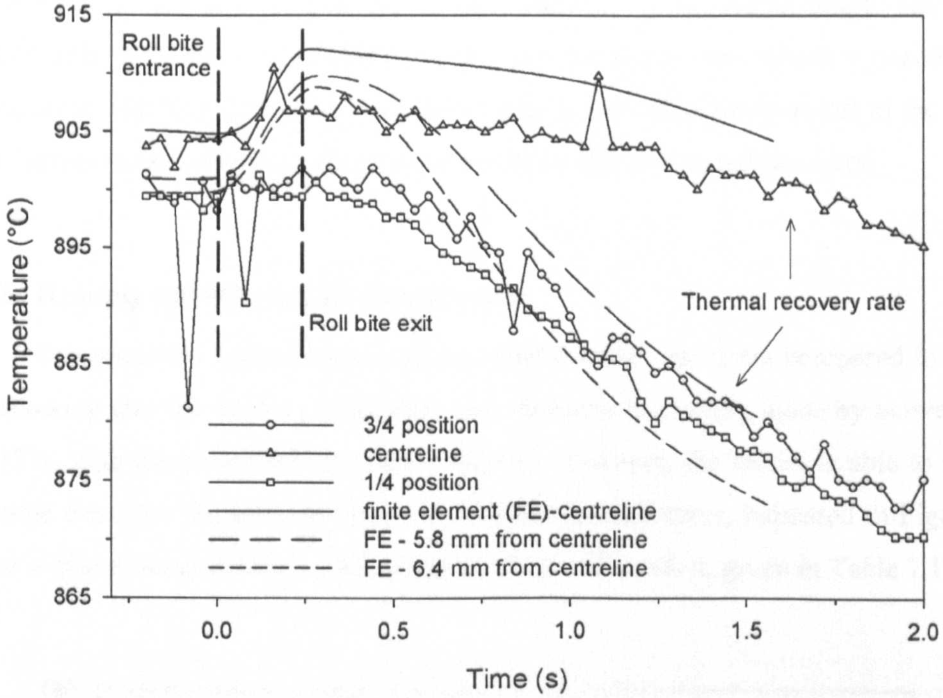

Figure 7.4 – Comparison of experimental results with finite element predictions for sample 03-11d for a heat transfer coefficient of 25 kW m^{-2} K^{-1}.

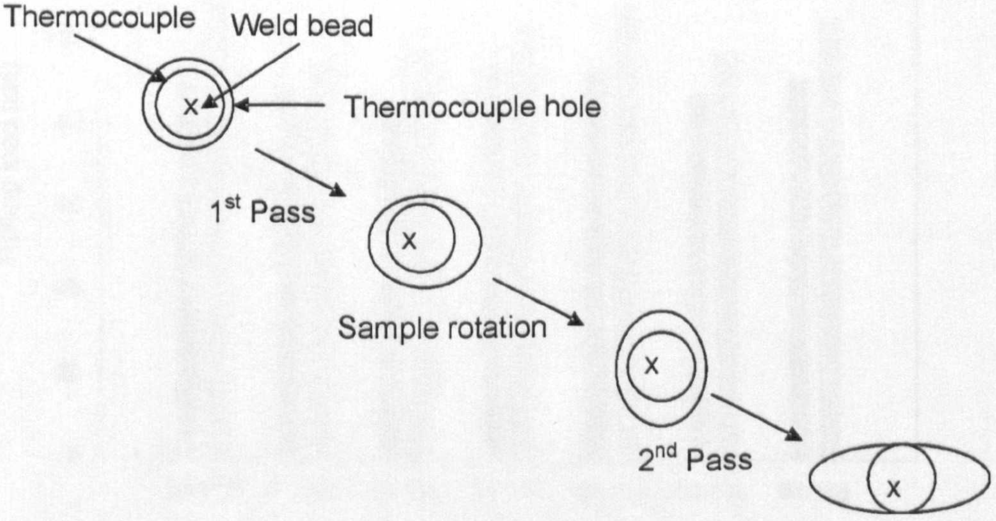

Figure 7.5 – Schematic showing the deformation of the thermocouple hole that results in a slight time delay in recording the 2nd pass temperature.

Also shown in Figure 7.4 is the variation that can exist in the actual thermocouple location; the designed thermocouple location was 6.1 mm from the centreline, which would not be significantly affected by the first pass since the thermocouples were arranged horizontally, but the FE predictions suggest that the two thermocouples were between 5.8 mm and 6.4 mm from the centreline. This is a reasonable difference given the depth of a drilled hole of a small diameter, i.e. 50 mm, where the drill bit can drift, and the 1.6 mm diameter of the thermocouple hole itself. Furthermore, there are small differences between the ¼ position, which is nearer to the rolling table, and ¾ position due to their location as a result of the heat lost to the rolling table; however, both thermocouples show a similar rate of thermal recovery.

7.3.2. Rolling Load/Torque Comparison

The predicted rolling loads and the experimental results are compared in Figure 7.6, showing that the model consistently over-predicts the rolling loads by between 8% and 17%, with the exception of sample 06-10a. However, the model is able to predict the same trend for the samples rolled at different temperatures, indicated in Figure 7.6 by the different temperatures at which the samples were rolled, given in Table 7.1.

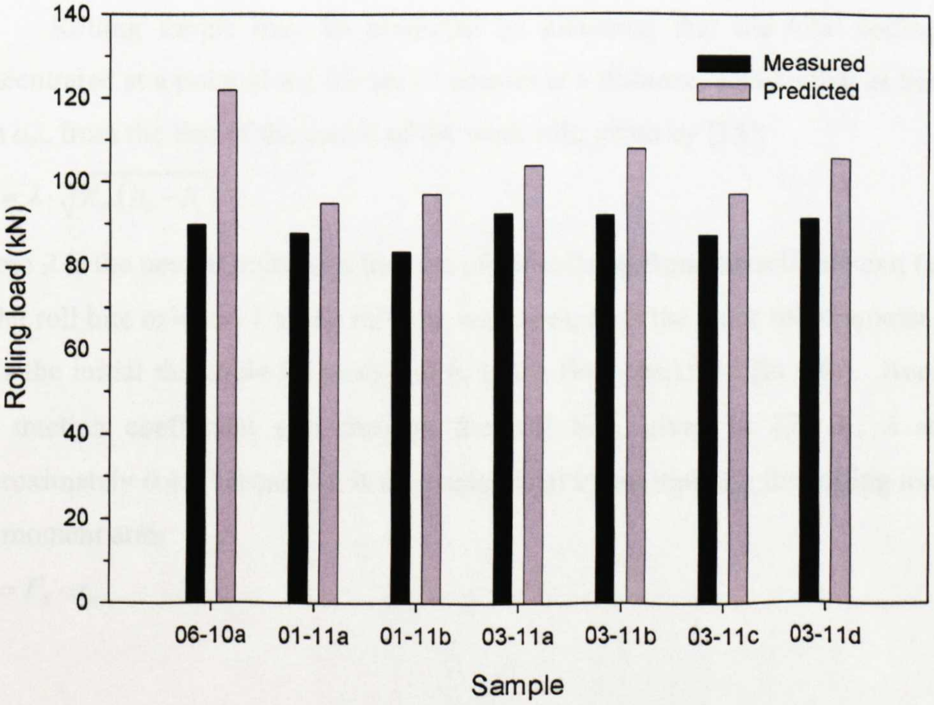

Figure 7.6 – Rolling load comparisons of model predictions and experimental results.

Table 7.1 – Summary of rolling temperatures.

Sample	Rolling Temperature (°C)
06-10a	830
01-11a	940
01-11b	943
03-11a	916
03-11b	907
03-11c	930
03-11d	913

The significant differences between the predicted rolling load and the measured rolling load for sample 06-10a, shown in Figure 7.6, could be the result of poor thermocouple contact with the steel, which would result in a lower recorded temperature than the level of the rolling load would indicate. The predictions of models using average friction coefficients of 0.25 and 0.35 for sample 03-11d were 104 kN and 107 kN respectively, thus showing that the friction algorithm predictions were physically reasonable. The principal source of the difference between the measured and predicted rolling loads was likely to be the constitutive equation used to describe the flow stress behaviour of the material, but there will also be some differences due to the model being 2-D plane strain, which did not take any edge effects into consideration.

Rolling torque may be predicted by assuming that the total rolling load is concentrated at a point along the arc of contact at a distance, also known as the moment arm a_m, from the line of the centre of the work roll, given by [15]:

$$a_m = \lambda \cdot \sqrt{R_f \left(h_0 - h_1\right)} \tag{7.2}$$

where λ is the neutral point as a fraction of the roll gap from the roll bite exit (equal to 0 at the roll bite exit and 1 at the roll bite entrance), R_r is the work roll diameter (in mm), h_0 is the initial thickness (in mm) and h_1 is the final thickness (in mm). According to the traction coefficient plot through the roll bite, given in §7.3.3., λ should be approximately 0.4. Torque, M, is then calculated by multiplying the rolling load, F_R, by the moment arm:

$$M = F_R \cdot a_m \tag{7.3}$$

The predicted torques, using the rolling loads predicted by the model, shown in Figure 7.6, and the moment arm calculated using equation 7.2, are compared with the experimental results in Figure 7.7.

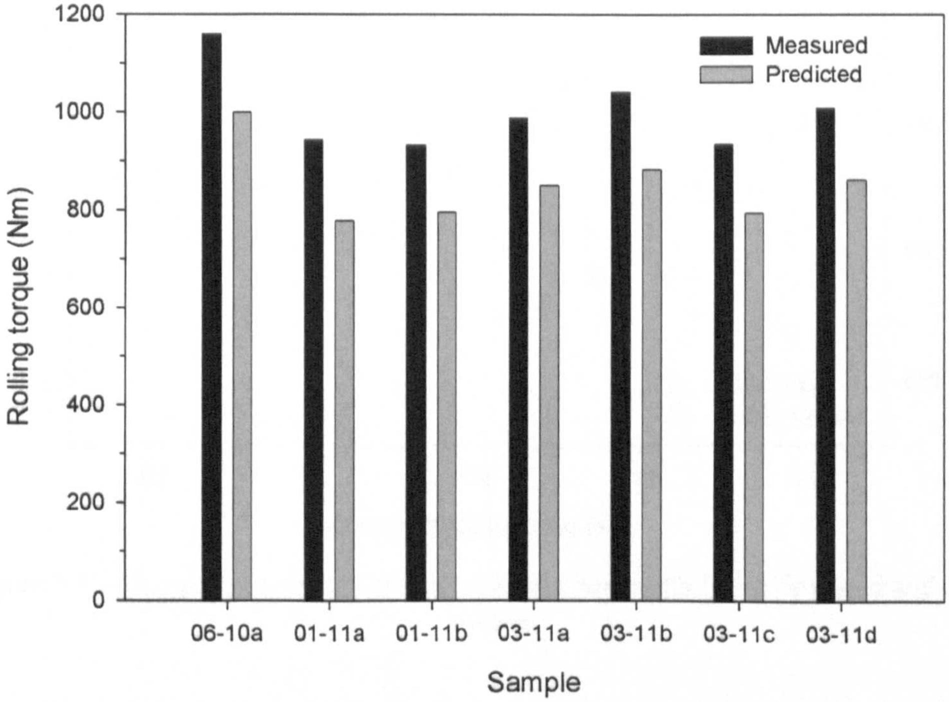

Figure 7.7 – Rolling torque comparisons of model predictions and experimental results using equations 7.2 and 7.3 with $\lambda = 0.4$, $R = 70$ mm, $h_0 = 26$ mm and $h_f = 20$ mm.

Unlike the rolling load predictions, Figure 7.7 shows that the model using the friction algorithm under-predicts the experimental torque, in this case by between 13% and 17%. This level of accuracy for predicting torque is generally considered acceptable [16]. In general the torque measurements were more sensitive to the sample temperature than the rolling loads, shown in Figure 7.8 and 7.8. Bearing torque is difficult to determine but Duan and Sheppard [16] suggest that the bearing torque in industrial aluminium hot rolling is around 5%; unfortunately the basis of the bearing torque determination was not disclosed. Once the estimated bearing torque had been taken into account the accuracy of the model was increased to between 8% and 13%. However, it should be recognised that there is a difference between unloaded and loaded bearing torques, which is important as the torque sensors were calibrated under different conditions than those that would be experienced during the experiments.

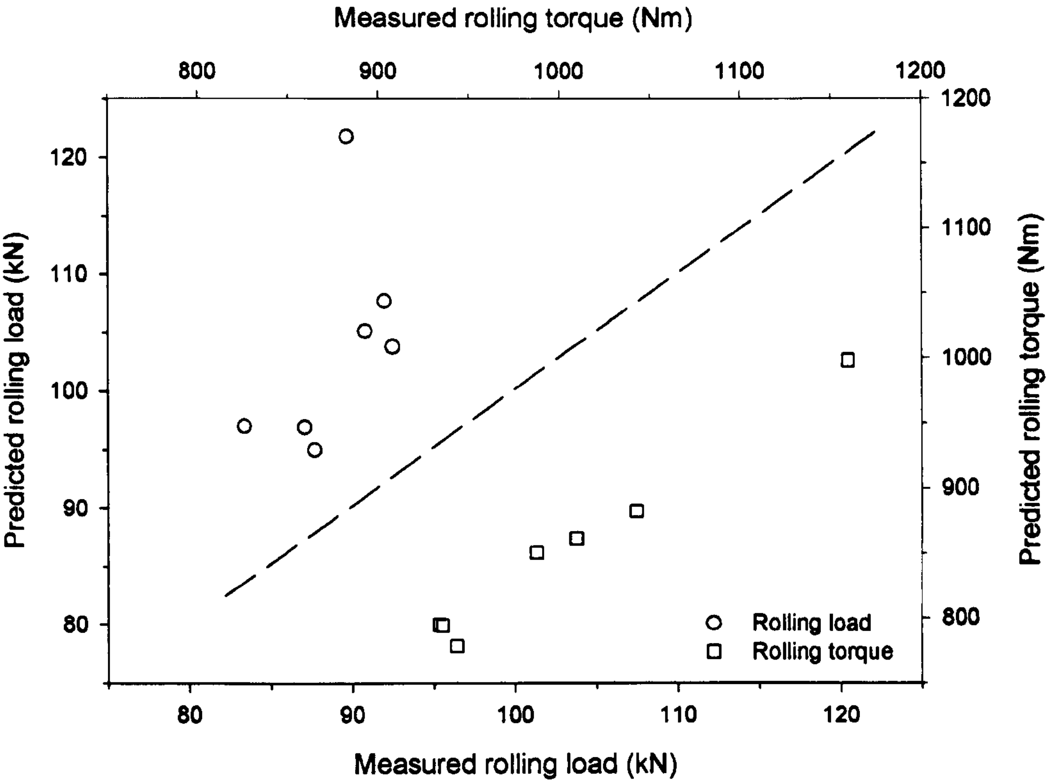

Figure 7.8 – Comparison of predictions with measurements for rolling load and rolling torque.

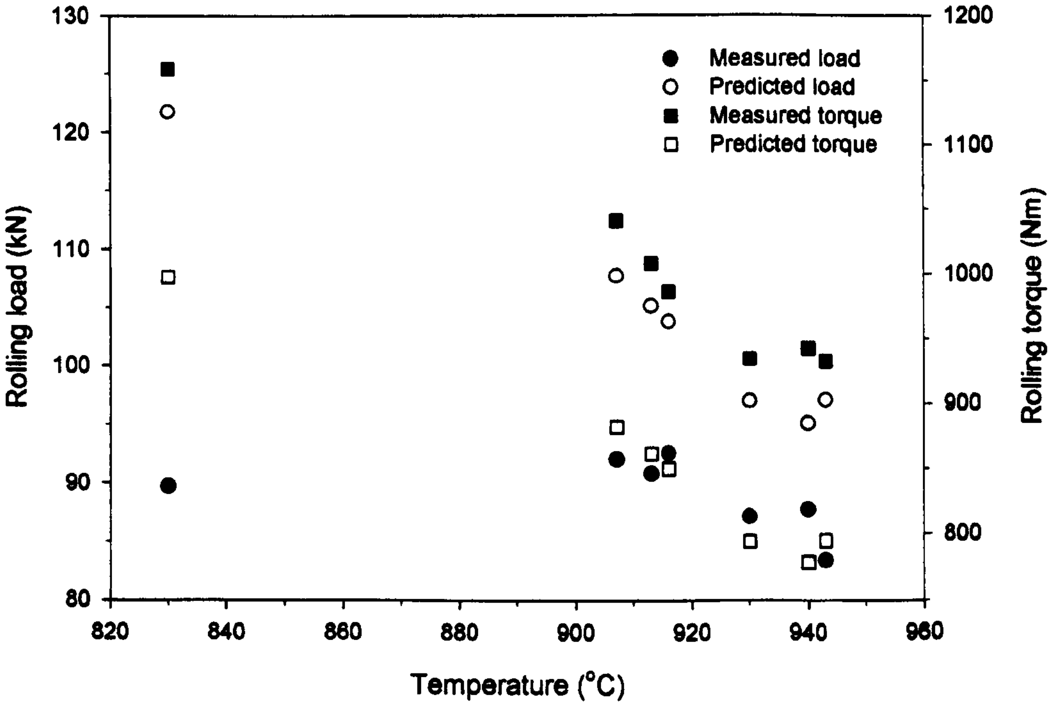

Figure 7.9 – Comparison of predictions with measurements for rolling load and rolling torque with regards to temperature.

When the friction algorithm predictions were compared with constant friction coefficient predictions it was found that the models varied by approximately 1% when μ=0.25 and by approximately 2% when μ=0.35, which is not significant. However, it must be reiterated that the friction algorithm does not require any preconceptions regarding the level of friction.

7.3.3. Friction Coefficient Prediction through the Roll Bite

One of the advantages of calculating friction as a function is the ability to continuously estimate the friction coefficient through the roll bite. The traction coefficient through the roll bite, given in Figure 7.10, shows that the friction coefficient predicted by the algorithm was not a constant value, even accounting for the smoothing function used to avoid the mathematical singularity at the neutral point as discussed in §5.3.3. A minor point is that the apparent inconsistency of the roll bite entrances; the delayed roll bite entrance for the μ=0.25 curve is simply a function of the mesh density, which was relatively coarse in this analysis. It can also be seen in Figure 7.10 that the

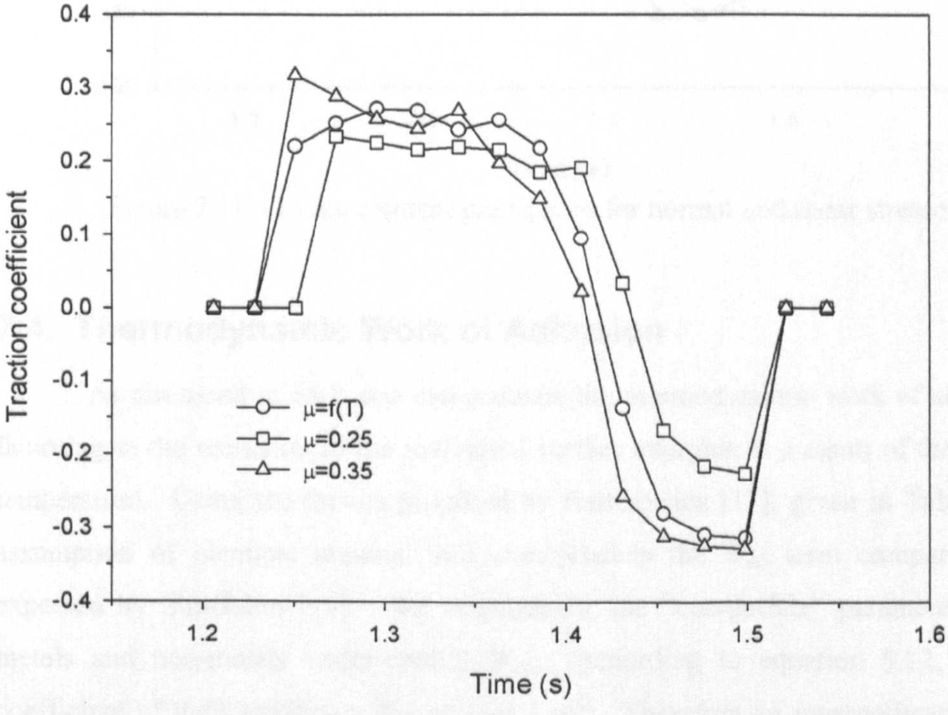

Figure 7.10 – Finite element predictions of the traction coefficient through the roll bite for sample 03-11d showing the friction coefficient calculated as a function of temperature compared to assumed average values.

neutral points of the three curves were moving closer to the roll gap entrance with increasing friction coefficients. The normal and shear stresses for the three cases considered, shown in Figure 7.11, follow the same trends as the friction coefficient curves. Furthermore, the normal stress curves do not display a significant variation in magnitude throughout the roll bite, i.e. are relatively flat, indicating that a constant heat transfer coefficient was a reasonable assumption for this model.

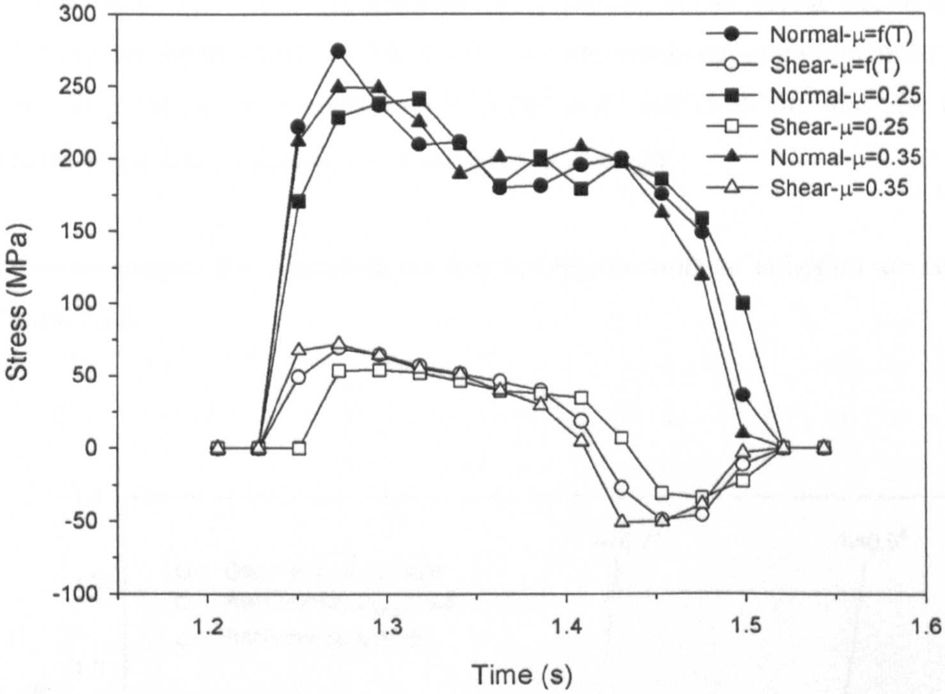

Figure 7.11 – Finite element predictions for normal and shear stresses.

7.4. Thermodynamic Work of Adhesion

As discussed in §5.2, one can estimate the thermodynamic work of adhesion by factoring in the reduction of the individual surface energies as a result of the increased temperature. Using the factors proposed by Rabinowicz [17], given in Table 5.1, the assumption of identical material still over-predicts the W_{ab} term compared to that expected by Straffelini [18]. Not surprisingly, the "compatible" parameters of both metals and non-metals under-predict W_{ab}. According to equation 5.12, a friction coefficient of 0.49 predicts a W_{ab} of 1.94 J m^{-2}. Therefore an intermediate parameter specific to metals contacting their oxides, $c_{Me\text{-}ox}$, was proposed. The $c_{Me\text{-}ox}$ term needed to obtain a value of 1.94 J m^{-2} is 0.79. Given the experimental uncertainties a value of

$c_{Me-ox} = 0.8$ was suggested, which estimated the W_{ab} at 450°C to be 1.97 J m^{-2}. Furthermore, since both a metal and a non-metal were involved in the contact either compatibility parameters could reasonably be used, although it would appear that the roughness angle is determined by the harder material, which suggests that the non-metal compatibility parameter could be more appropriate.

Also discussed in §5.2, the thermodynamic work of adhesion can be estimated using the geometric mean rule. For the situation of a 100Cr6 dowel contacting magnetite a simplifying assumption that the dowel will have approximately the same molar volume as iron. Thus the molar volumes were 7.08 cm^3 mol^{-1} and 11.30 cm^3 mol^{-1} for iron and magnetite respectively, resulting in a value for Φ of 0.626.

The two techniques for estimating the thermodynamic work of adhesion are compared in Figure 7.12.

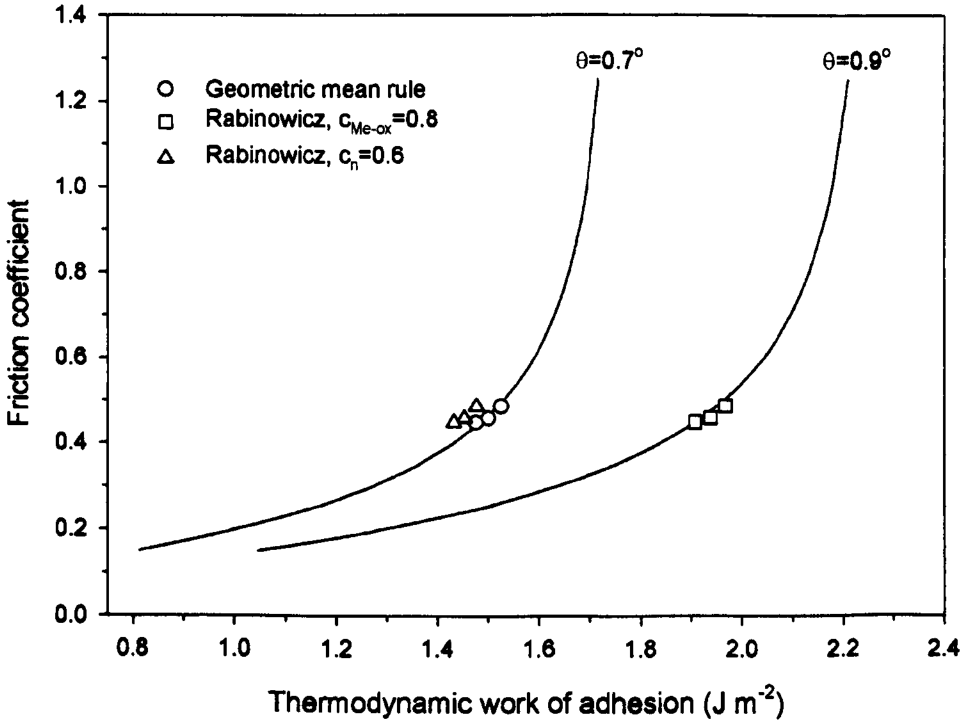

Figure 7.12 – Calculations for the thermodynamic work of adhesion made using the Rabinowicz method and the geometric mean rule compared with experimental results.

Figure 7.12 shows that both methods for calculating the thermodynamic work of adhesion give satisfactory results. The principal difference between the approaches is that the Rabinowicz method requires the equilibrium roughness angle to be 0.9°, based on experiments using fcc metals. The equilibrium roughness angle is then used to "tune" the compatibility parameter used in the Rabinowicz equations. Alternatively, the use of the non-metal compatibility parameter does not require this assumption and, as can be seen in Figure 7.12, suggest that the equilibrium roughness angle is close to 0.7°, which is similar to that suggested by the geometric mean rule. The geometric mean rule also does not make any assumptions regarding the equilibrium roughness angle, which results in the prediction of an equilibrium roughness angle of 0.7°. In the absence of experimental friction coefficient data similar to that used to determine the roughness angle for the fcc metals, this technique provides a physically reasonable value without requiring any further simplifying assumptions. Also shown are the estimated thermodynamic work of adhesions as calculated using Rabinowicz's method and the compatible non-oxide parameter, which largely agrees with the GMR results. However, this appears to be more by good fortune than good planning since the Φ ratios are 0.78 and 0.57 for aluminium-aluminium oxide pairs and copper-copper oxide pairs respectively, which do not result in similar estimates of the thermodynamic work of adhesion between the two methods.

7.5. Sensitivity Analysis

Within the developed friction model there are a number of parameters that can affect the predicted coefficient of friction, some of which are poorly defined. Most of these variables will have little effect on the overall prediction because they are accounted for in the formulation via other relationships. An example of this is the shear strength of the contacting junctions. However, there are a number of assumptions built into the model that may, or may not, have a large effect on the friction coefficient predictions, namely: the average asperity junction radius (r), the constant α, the constant β, the equilibrium roughness angle (θ) and the thermodynamic work of adhesion (W_{ab}). There is also the sensitivity of the thermodynamic work of adhesion to temperature.

Further to the discussion of § 5.2 the average asperity junction radius has been defined as:

$$r = \frac{C_1}{p_y} \tag{7.4}$$

where C_1 is a constant (in MN m^{-1}). Literature values for this constant vary from 0.1 MN m^{-1} to 0.0012 MN m^{-1}. Lim and Ashby [19] suggest that C_1 should be equal to 0.1 MN m^{-1}, which they have used in their calculations for flash heating of pin-on-disc, while Rabinowicz [17] also used sliding tests for flash heating calculations resulting in a value for C_1 of 0.0012; the major difference between the experiments appears to be the experimental sliding velocities .

The value for α varies in the literature between 3 and 25. The value of 3 obtained by McFarlane and Tabor [20] resulted from experimental data for indium while the value of 25 is a result of the assumption that the uniaxial yield strength of metals is approximately 5 times their shear strength [21].

The β term results from the following relationship:

$$F_T = \beta \cdot F_{AD} \tag{7.5}$$

where F_T is the friction force and F_{AD} is the adhesive force. Straffelini [18] uses the β term to represent the shearing process at the junctions, reflecting the irreversibility of the process. The destructive nature of this process leads to considerations of the Tresca failure criterion, which inevitably leads to the possibility of applying the von Mises failure criterion instead. Straffelini [18] suggests that published experimental data [20,22,23] supports the use of 0.5 as the value for β.

The roughness angles that have been published vary between 0.7° [24] and 3.44° [25]. The roughness angle of 0.7° is from post carbon-carbon sliding contact [24] whereas Tallian [25] has shown that a finely finished bearing can have a roughness angle of 0.81° and a relatively rough bearing can have a roughness angle of 3.44°.

The friction model with C_1, α, β and θ as variables is given as:

$$\frac{\mu}{\sqrt{1+\alpha \cdot \mu^2}} = \frac{8\times10^{-6} \cdot \beta}{C_1 \tan\theta} \cdot W_{ab} \tag{7.6}$$

The effect of these variables, in addition to the thermodynamic work of adhesion, on the friction coefficient is given in Table 7.2.

Table 7.2 – Sensitivity of the friction coefficient to the variables C_l, α, β, θ and W_{ab}.

	C_l (MN m^{-1})	α	β	θ(°)	W_{ab} (J m^{-2})	μ	% change
Base	0.002	12	0.5	0.9	1.5	0.255	0.0
+10%	0.0022	12	0.5	0.9	1.5	0.217	-14.7
	0.002	12	0.55	0.9	1.5	0.306	20.3
	0.002	13.2	0.5	0.9	1.5	0.265	4.1
	0.002	12	0.5	0.99	1.5	0.217	-14.7
	0.002	12	0.5	0.9	1.65	0.306	20.3
-10%	0.0018	12	0.5	0.9	1.5	0.313	22.9
	0.002	12	0.45	0.9	1.5	0.214	-16.0
	0.002	10.8	0.5	0.9	1.5	0.245	-3.7
	0.002	12	0.5	0.81	1.5	0.313	22.9
	0.002	12	0.5	0.9	1.35	0.214	-16.0

From Table 7.2 it can be seen that the thermodynamic work of adhesion and β parameters have the strongest influence on the friction coefficient when the values are +10%, but the C_l parameter and the roughness angle have the strongest influence when the values are -10%. In both cases the α parameter has the weakest influence on the friction coefficient. However, with the exception of the α parameter the remaining variables have a similar influence on the friction coefficient; therefore the definition of all these terms is important.

The sensitivity of the thermodynamic work of adhesion to temperature depends on the materials involved and the method used to estimate it. The reciprocating friction experiments involved steel-on-magnetite contact. Young's modulus for steel shows a strong dependence on temperature while magnetite shows a weak dependence on temperature, discussed in §4.2.1. The effect of temperature on the molar volume ratio, Φ, required by the geometric mean rule is negligible and will be ignored in this analysis, whereas the compatibility parameters employed by Rabinowicz do not have any temperature dependence. As type K thermocouples were used for these experiments the thermocouple accuracy given by International Electrotechnical Commission (IEC) 584-

2 (1989) are assumed. The temperature dependent accuracy of the thermocouple according to IEC 584-2 (1989) is given in Table 7.3.

Table 7.3 – Temperature dependence of Type K thermocouple accuracy according to IEC 584-2 (1989).

Class 1		Class 2	
Temperature (°C)	Accuracy (°C)	Temperature (°C)	Accuracy (°C)
$-40 < T \leq 375$	±1.5	$-40 < T \leq 333$	±2.5
$375 < T \leq 1000$	$\pm 0.004 \cdot T$	$333 < T \leq 1200$	$7.6 \pm 0.0075 \cdot T$

The class of the thermocouples used in the experiments was unknown, so it was assumed that the worse accuracy of the Class 2 thermocouples applies. At 450°C, a Class 2 thermocouple should have an accuracy of ±3.4°C, similarly at 1000°C an accuracy of ±7.5°C. This was the inherent error in the thermocouples; the overall data acquisition system also had some inaccuracies built in. The effect of temperature on the thermodynamic work of adhesion, calculated by both the geometric mean rule and Rabinowicz's method, is given in Table 7.4.

Table 7.4 – Effect of temperature on the thermodynamic work of adhesion as calculated by the geometric mean rule (GMR) and Rabinowicz's method (RM).

Temperature (°C)	Materials	W_{ab} (GMR)	W_{ab} (RM)
440-440	$Fe\text{-}Fe_3O_4$	1.534	1.979
450-450	$Fe\text{-}Fe_3O_4$	1.525	1.967
460-460	$Fe\text{-}Fe_3O_4$	1.515	1.817
325-840	$Fe\text{-}Fe_3O_4$	1.406	1.799
325-850	$Fe\text{-}Fe_3O_4$	1.397	1.788
325-860	$Fe\text{-}Fe_3O_4$	1.387	1.776

The temperatures chosen in Table 7.4 reflect the experimental conditions against which the theory was developed and tested. In both situations the temperature does not have a large effect on the thermodynamic work of adhesion; for instance, at the temperatures the reciprocating friction tests were conducted, ±7.5°C results in a variation of friction coefficient of ±0.012 using the geometric mean rule formulation. The variation in the thermodynamic work of adhesion for the approximate laboratory rolling temperatures, i.e. 325°C for the work roll and approximately 850°C for the sample surface, is similar in magnitude to the variation seen with the reciprocating friction test temperatures, but the resulting variation in friction coefficient is only ±0.007, again using the geometric mean rule. The influence of temperature on the friction coefficient is more acute with higher thermodynamic work of adhesion as a result of the approaching asymptote. Overall, the reason for the seemingly small differences in thermodynamic work of adhesion is that the magnitude of the surface energies is small compared with the Young's modulus, thus when the change in Young's modulus with temperature is taken as a percentage and applied to the surface energy it results in a relatively small number.

7.6. Effect of Roughness Angle

An important aspect of the extended theory is the link between the friction coefficient and both physical and material parameters. The material parameter of the theory, work of adhesion, is reasonably well established, while the physical parameter, roughness angle, requires further discussion given the lack of agreement on the best method of characterising surface roughness and the debate with regards to whether or not an equilibrium surface structure is established. The potential impact of the establishment of an equilibrium surface roughness is also considered.

7.6.1. Roughness Angle versus *Ra*

One of the most common definitions used for surface roughness is the *Ra* parameter, primarily for its simplicity and ease of measurement. Unfortunately, the *Ra* parameter is not very explicit and a large variety in surface profiles can exist for a given *Ra* value. However, consistent grinding practices can be expected to give consistent surface profiles that may be differentiated between using the *Ra* parameter. Furthermore, the *Ra* measure is widely used in industry. Thus it would be useful to have a relationship between roughness angle and *Ra*. The definition of *Ra* is given as [26]:

$$Ra = \frac{1}{L}\int_0^L |y(x)|dx \tag{7.7}$$

where L is the measured length, y is the relative elevation compared to a given datum. Assuming that the asperities are uniformly distributed and there is complete penetration of the surface, with the definition of roughness angle, θ, given by Rabinowicz [17], the relationship between roughness and *Ra* is given by:

$$Ra = \frac{1}{2} r \tan\theta \tag{7.8}$$

As the junction radius, r, has been related to the yield strength of the weaker material, Ra can be described in terms of yield stress, σ_y (in MPa) and roughness angle:

$$Ra = \frac{1}{2}\left(\frac{C_1}{2.8 \cdot \sigma_y}\right)\tan\theta \tag{7.9}$$

where C_1=0.002 MN m^{-1}. Assuming that it is the strength of the oxide layer that governs the depth of penetration, rather than the steel substrate, which has an approximate strength of between 5 and 10 MPa at 1000°C [27] (this calculation assumed 5 MPa) and a roughness angle of 0.7° is established the resulting Ra would be 0.9 μm. This is close to the measured transverse Ra of ground laboratory work rolls with an average value of 0.83 μm, as reported in §6.4.1, or a transverse roughness of 1.4 µm and a longitudinal roughness of 1.0 μm for sand blasted laboratory work rolls reported by Lenard and Barbulovic-Nad [28].

7.6.2. Evolution of Roughness Angle

As the extended adhesion theory assumes an equilibrium roughness angle, there must be a physical mechanism to enable this surface to be established. Straffelini [18], in part, attributes this angle to the crystal structure of the contacting materials with the reported experimental data for fcc metals. This may be the result of the ability of the fcc crystal to deform but does not suggest a mechanism. At the high temperatures and the highly stressed environment of hot rolling the situation is further complicated by oxidation and wear. A study by Burdek [29] has tracked the evolution of temper work roll surfaces over a rolling campaign, lending credence to the idea of an equilibrium roughness angle. However, as the theory was derived by Straffelini with room temperature data, a mechanism must exist to explain the evolution of the surface. This mechanism has been examined, albeit in different contexts, by Meine *et al.* [30] and Packham [31].

Burdek [29] used a Rank Taylor Hobson Talyscan and TalyMap software to measure the change in surface topography during temper rolling. The variations in two top work rolls, A and B, were tracked over two different campaigns (since it was not stated, the campaigns were assumed to be of a similar nature) with starting *Ra* values of 2.82 μm and 2.47 μm respectively. At the end of the campaigns with approximately 70 km rolled, the measured *Ra* values had reduced to 1.88 μm and 1.23 μm for rolls A and B respectively. A second parameter, MVR, was used to describe roughness, defined as the total volume of void of the surface obtained by measuring the space between the points of the surface and an imaginary horizontal plane at the maximum elevation of the surface, which effectively measures the average void volume. The initial MVRs for the two rolls were 15.31×10^{-3} mm^3 mm^{-2} and 13.33×10^{-3} mm^3 mm^{-2} for A and B respectively, which were representative of the different initial *Ra* values. Most interesting, however, is that this parameter rapidly converged to a similar value, irrespective of the different *Ra* measurements at the first measurement during the campaign. The final value for the MVR parameter for both rolls was almost identical at $A=4.16 \times 10^{-3}$ mm^3 mm^{-2} and $B=3.86 \times 10^{-3}$ mm^3 mm^{-2}. What this may indicate is the redistribution of the asperity peaks into the valleys, which would not be identified by the *Ra* parameter because it simply measures the average relative height and does not differentiate with respect to the profile of the surface. Furthermore, after the initial drop in the MVR value the measurements are relatively consistent through the bulk of the rolling campaign until a small drop at the end, shown in Figure 7.13. Thus, according to the MVR parameter, the roll surfaces may be considered to have an equilibrium surface roughness over the bulk of a temper rolling campaign.

Meine *et al.* [30] conducted experiments on micro grooves measuring the friction force of a hard sphere on a silica layer over a silicon substrate. The micro groove was prepared by lithography techniques in the silica layer such that the silicon was not exposed; the hard sphere was loaded and traversed back and forth across the length of the sample with the friction force continuously recorded, shown schematically in Figure 7.14. This experiment was conducted for a variety of sphere materials showing the friction force increasing over a short distance rather than a virtually instantaneous step, an example of which is given in Figure 7.15. The conclusion drawn by Meine *et al.* was that the change of the deformed sample volume in sliding direction is considered the most likely reason for the change of friction force at a step. The result of elastic deformation of the groove is reasonable given that the sharp edge of the groove would be required to carry very high pressures as the area of contact is reduced, thus elastically deforming. As the experiments were conducted at low loads, slow speeds and relatively low temperatures the elastic deformation described by Meine *et al.* is likely to incur increasing plastic deformation with increasing loads, speed, frequency and temperature.

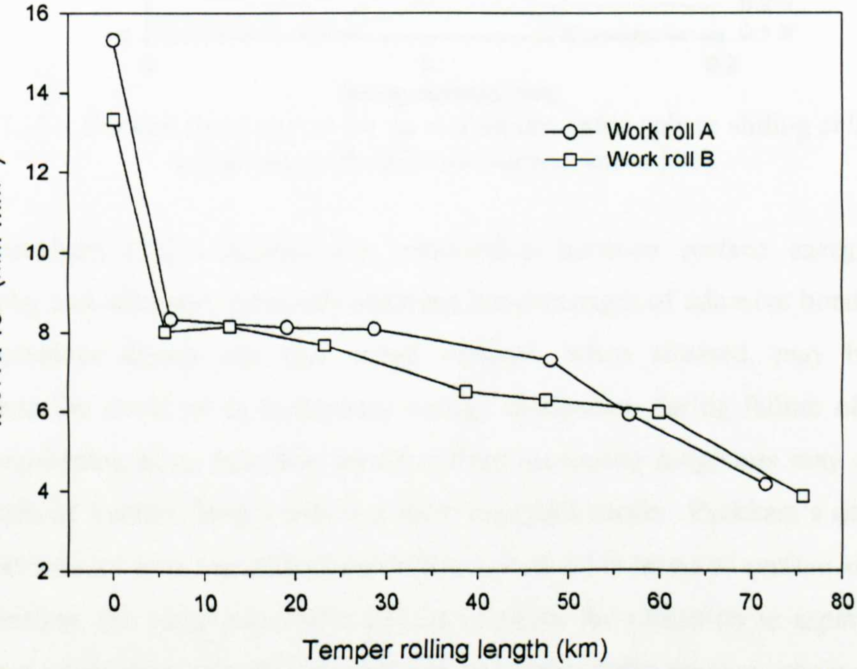

Figure 7.13 – The evolution of the roughness parameter MVR for two work rolls over a rolling campaign [29].

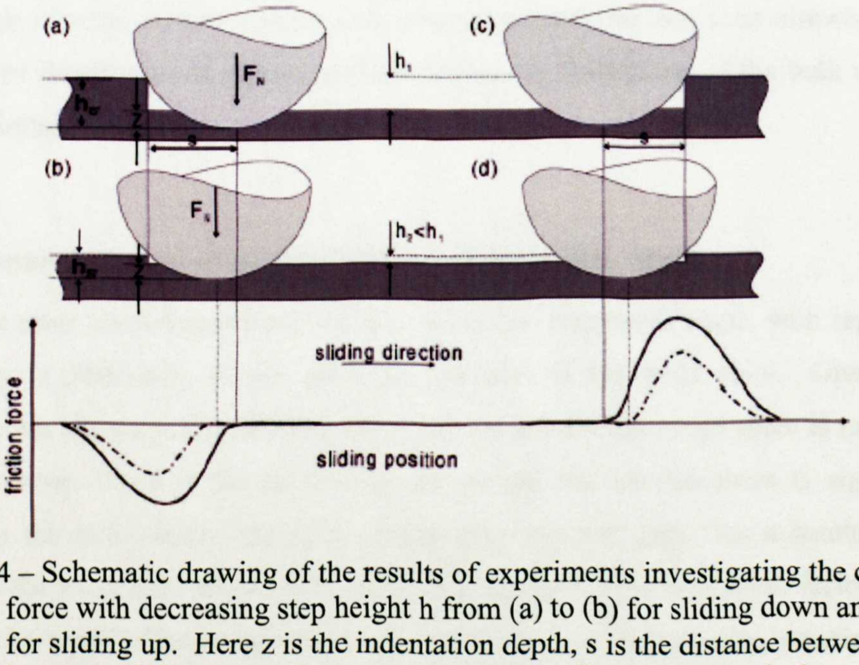

Figure 7.14 – Schematic drawing of the results of experiments investigating the changes in friction force with decreasing step height h from (a) to (b) for sliding down and from (c) to (d) for sliding up. Here z is the indentation depth, s is the distance between the edge of the step and the centre of the contact area on a flat surface, F_N is the normal force and h_S is equal to h + z [30].

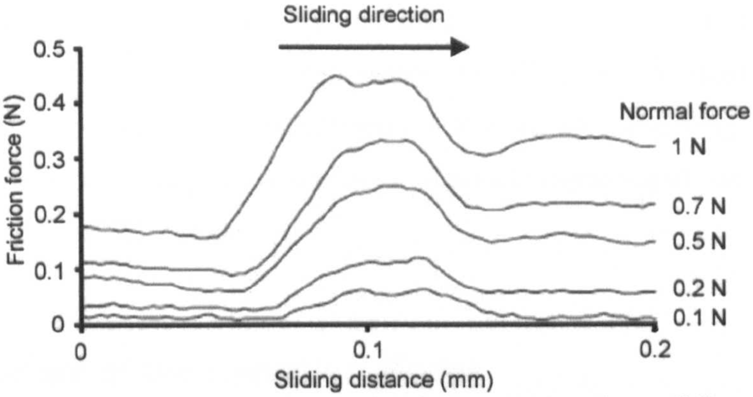

Figure 7.15 – Friction force curves for an aluminium oxide sphere sliding at 0.7 mm s^{-1} up the step with different normal forces [30].

Packham [31] examined the relationship between surface energy, surface topography and adhesion, primarily studying bond strength of adhesive bonds. One of the conclusions drawn was that rough surfaces, when stressed, may be able to redistribute the stress so as to increase energy dissipation during failure of the joint. The strengthening of an interface resulting from increasing roughness may change the mechanism of fracture from a less to a more energetic mode. Packham's definition of roughness was not in terms of *Ra*, instead it was defined in terms of surface area. Using this definition, the roughening of a surface involves the reduction in asperity height; although a mechanism was not suggested for the stress redistribution, one possibility is plastic flow of the asperity tips. This finding is physically reasonable since asperity tips have a high relative surface energy and similar mechanisms are seen elsewhere; for example, the dissolution of sharp asperities before the dissolution of the bulk metal in electro-refining.

7.6.3. Consequences of an Equilibrium Roughness Angle

The most immediate impact of an equilibrium roughness angle, with regards to hot rolling, is potentially on the grinding practices of the work rolls. Operational experience has shown that with work rolls that are ground too rough there is rapid and significant wear, while if the work rolls are ground too smooth there is significant slippage to the point where the strip cannot enter the roll gap. As a result of this experience the work rolls are given a finish that attempts to balance these factors. The effect that an equilibrium roughness angle would have on the grinding practice is the optimisation of the required surface finish, assuming that the transition point between friction mechanisms can be accurately identified, which is discussed in §7.7. Other consequences could involve the implementation of online surface measurement, data from which could be used to optimise rolling schedules by identifying when the roll surfaces are beginning to degrade and allow traditional techniques of roll scheduling to attempt to restore the roll surfaces.

7.7. Criticisms of the Adhesion Model

Although the original adhesion theory of friction has reached mainstream engineering circles, there have been criticisms of the original adhesion theory and there are some parameters that have been observed to affect the friction coefficient that are not explicitly identified in the extended adhesion theory, such as: pressure sensitivity, real contact area, contact time and relative velocity.

7.7.1. Original Criticisms of the Adhesion Theory

There are a number of criticisms of the original adhesion theory that Rabinowicz [26] addresses; however, in light of the extended adhesion theory some of the points raised need to be readdressed:

1. "It is not readily apparent how the strong junctions between the contacting materials, as strong as actual welds, are produced since in many cases the temperature at the contacts is quite low, interdiffusion of the surface atoms is unlikely to occur, and the alignment of the surface atoms is likely to be poor."

Rabinowicz's reply: "Modern work in adhesion has shown that clean metals adhere very strongly when pressed together in such a way as to extend and break up oxide and other surface films."

Current theory: In addition to the breaking up of surface films the geometric mean rule suggests that the alignment of the atoms at the contacting interface is a function of the molar volumes. Thus, when there is a large difference in molar volumes the work of adhesion is reduced and the friction coefficient is subsequently reduced. Therefore the physical alignment of the atoms is likely only to be crucial on the atomic scale.

2. “A more important criticism is that although strong adhesion between contacting materials is postulated in this theory, it is a fact that if the normal force pressing the surfaces together is removed, this adhesion cannot be detected.”

Rabinowicz's reply: “The junctions are deformed elastically as well as plastically and that removal of the load breaks off most of the junctions, as a result of the elastic spring back.”

Current theory: Although, strictly speaking not a part of this theory, adhesion experiments were conducted by Desaguliers [32] in 1725 with lead spheres to measure an adhesion force, albeit in an irreproducible manner. This suggests that adhesion should be experimentally measurable at either higher temperatures or using materials with low yield stresses.

3. “Objection is made on the ground that the brittle non-metals, with which plastic deformation does not occur, show frictional properties similar to those of metals.”

Rabinowicz's reply: “The material at the interface is under high compressive stress and that brittle materials deform plastically under these high compressive stresses.”

Current theory: The degree of deformation required for brittle materials, under the high compressive stresses at the asperities, is less than that of metals since there is an assumed equilibrium or average roughness of the weaker contacting surface. In brittle materials, such as alumina, the extended theory suggests that it will have a smaller roughness angle but otherwise the friction coefficient is still primarily a function of surface energies via the thermodynamic work of adhesion term.

4. “There are objections based on the magnitude of the friction force. It is known that for most metals the shear strength s is about 1/2 of σ_y, the plastic yield strength in tension, and the penetration hardness p is about 3 σ_y. Hence the ratio s/p has a value of about 1/6, whereas actual friction values, which should equal s/p, are about 0.4, or about two or three times as great as s/p.

"Furthermore the adhesion theory treats the normal stress p and the shear stress s as independent variables. Yet they are related by some yield criterion in that, when a high normal stress p is applied to an interface, the shear stress required to initiate sliding must be diminished. Accordingly the derivation of [$f=s/p$] is in error, and we should in practice expect friction coefficients smaller than s/p.

"We would also expect friction phenomenon to be affected by contaminants at the interface. Experiments carried out in air may agree poorly with [$f=s/p$] but the agreement can become progressively better when the contaminants were removed by carrying out tests in dry air, then in vacuum, and finally after outgassing at elevated temperatures, in a high vacuum. In fact tests carried out with clean metal surfaces in a good vacuum (e.g. copper) do not agree at all with [$f = s/p$], and the friction is found to be very high (order of magnitude 100) and to depend critically on the surface geometry (Bowden and Hughes [33]; Gwathmey [34]; Bowden and Young [35])."

Rabinowicz's reply: "The real area of contact tends to be larger than the value L/p that is assigned to it in [$A_r = L/p$]. Since the actual value of A_r, once displacement starts, is larger than it should be by a factor of two or three, the shear strength has a substantial value, and the friction coefficient is correspondingly larger than the theoretical value of 1/6. The very high values of friction coefficient observed with very clean metals are due to a further increase in A_r, above the value just considered because of the coming into play of surface energy effects. If we combine [$L = \pi r^2 p - 2\pi r W_{ab} \cot\theta$] with an expression for the shear force at a circular junction of radius r,

$$\Delta F = s \cdot \pi r^2 \qquad [7.10]$$

we find that

$$\frac{\Delta F}{\Delta L} = \frac{s}{p} \cdot \frac{1}{1 - 2 \cdot W_{ab} \cdot \cot\theta / rp} \qquad [7.11]$$

"[Equation 7.11] becomes the relation for the friction coefficient if we regard θ as an average surface roughness angle and r as an average junction radius. We see that very high values of friction coefficient can occur when the ratio of surface energy of adhesion W_{ab} to hardness p is high and the surface roughness angle θ is very small. These are the conditions that produce very high friction coefficients [Figure 7.16]."

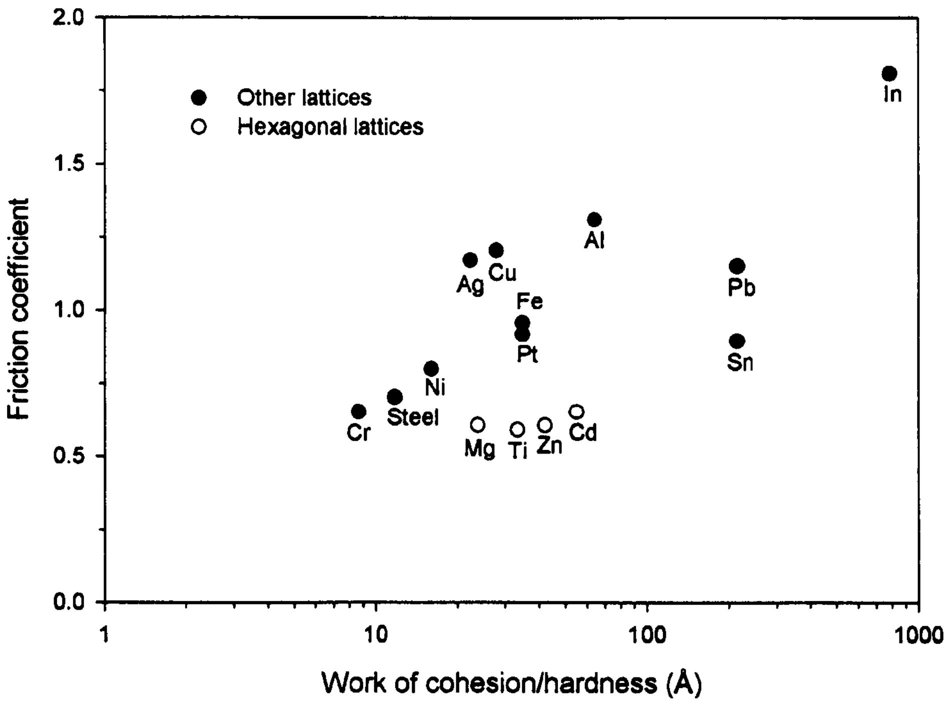

Figure 7.16 – Friction coefficients for clean similar metals [26]. Experimental conditions: like metals, unlubricated, load~1000 g, speed < 10 mm s^{-1} [26].

Current theory: One of the initial assumptions of the extended theory is that the real area of contact scales in proportion to the normal force and inversely proportional to the yield strength of the material involved. This changes the basis upon which the remaining theory is derived compared to the original adhesion theory, thus the argument about the relationship between shear strength and yield strength and the resulting friction coefficient prediction is not applicable. Referring to Rabinowicz's modified adhesion theory, given by equation 7.11, the main differences between that and the extended theory are: the extended theory considers the energy consumed by the deformation process to be negligible and takes into account N junctions, rather than a single asperity, as assumed by Rabinowicz. Furthermore, the extended theory uses an experimental relationship between real area of contact and friction coefficient. The relationship between friction coefficient and work of adhesion shown in Figure 7.16 is different from the relationship predicted by the extended theory as a result of different experimental conditions, thus representing a different operating window.

7.7.2. Pressure and Real Area of Contact Dependence

In the original definition of Coulomb's friction model the friction coefficient is defined by the ratio between the shear stress and the normal pressure. The extended adhesion theory relies on the relationship between the adhesive force and the normal force, which in turn is related to the rolling pressure. The definition of the friction coefficient is the ratio of normal and tangential forces, thus a pressure dependency for the friction model is implied.

However, friction models available in the literature suggest that friction also displays a pressure dependency [36,37]. The majority of these models are empirically or laboratory rolling based and, as such, tend to incorporate the effects of a large number of variables. Although the extended adhesion theory of friction is material and temperature dependent, the concept of a friction coefficient must be taken in the context of hot rolling, thus the other phenomena that exist must also be considered; one of these phenomena is heat transfer between the strip and work roll. Typically the heat transfer is modelled through a heat transfer coefficient representing the resistance to heat flow between the contacting materials and is taken as a constant value throughout the roll bite. However, Samarasekara *et al.* [38-40] have modelled the heat transfer coefficient, h (in kW $m^{-2}K^{-1}$), as a function of roll pressure, P_R (in MPa), given as [38]:

$$h = 0.695 \cdot P_R - 34.4 \tag{7.12}$$

This model was the result of analysing industrial data for a number of different rolling stands and different rolling conditions [39]. Applying this model gives the temperature dependent friction model an additional pressure dependency. From a phenomenological viewpoint an increase in heat transfer coefficient with pressure would result in a reduction in strip surface temperature and an increase in work roll surface temperature. As a result of the relationship between Young's modulus and temperature the effect of temperature on the friction coefficient is more prevalent at high temperature than low temperature, thus the friction coefficient should increase with increasing pressure for a given set of rolling conditions.

Similar to pressure dependency the real area of contact is one of the underlying assumptions in the derivation of the extended adhesion theory. The theory relies on the relationship between shear force, junction shear strength and real area of contact to develop the relationship between the (effective) work of adhesion, roughness angle and friction coefficient. Confidence in this relationship was established by the fit achieved with experimental results compared to the derived model, given in §5.2; one of the results of this set of assumptions is that an equilibrium roughness for the harder surface develops. However, the simplified approach to the adhesion theory proposed by Straffelini [18] was developed under room temperature conditions, which means that the behaviour of the softer material at higher pressures may not be sufficiently addressed since plastic contacts are only accounted for as a constant applied to the force of adhesion term, i.e. 2 instead of 3/2. At the temperatures at which hot rolling occurs the softer material will fill the serrations, for lack of a better word, of the surface roughness of the harder material. As the work roll serrations are filled the real area of contact will increase, giving a corresponding increase in the friction coefficient, which may be accounted for in the same fashion as the pressure dependency by taking the holistic approach towards modelling the surface behaviour in the roll gap and including the pressure dependency of the heat transfer coefficient.

Ultimately the contact phenomena during the hot rolling of steel should not be seen to exist independently. The extended theory identifies the friction component, which by its definition is independent of pressure, while industrial observations have shown that the heat transfer between the strip and the work roll are pressure dependent. The concept of real area of contact is present in both of these phenomena, affecting both the area available for adhesion and the area available for heat transfer.

7.7.3. Effect of Contact Time

There are models in the literature [41] that show the friction coefficient with a dependency on variables such as roll velocity, roll radius and draught. These variables will affect the friction coefficient as a result of their effect on the rolling contact time. The principal manner in which the rolling contact time will affect the friction coefficient is through the resulting temperature profile; in general an increase in rolling contact time means a reduced temperature of the stock surface, which results in an increased friction coefficient.

Roll velocity should influence the friction coefficient since with increasing roll speed the strain rate will increase; steel exhibits strain rate sensitivity resulting in increased flow stress, as a result of the increased strain rate, and increased heat of deformation, which in turn increases the temperature of the scale. This generalisation is true over the entire temperature range but the friction coefficient becomes more sensitive to roll velocity at lower rolling temperatures, which may be explained in terms of the extended theory that lower temperatures result in higher work of adhesion terms, resulting in a steeper curve as the asymptote of the friction coefficient-work of adhesion relationship is approached. This scenario is further complicated by the changing oxide states at the contacting surfaces with temperature. Thus the overall effect of roll velocity may be blurred as a result of the formation of an oxide layer with a higher surface energy, for instance the formation of hæmatite.

Roll radius and draught will both affect the rolling pressure and contact time. According to the roll force model of Ford and Alexander [42] combined with industrial data from Siciliano *et al.* [43], an increase in roll radius will increase the rolling pressure, for a given reduction, while decreasing the contact time (see Appendix E). Hence there are the competing factors of increased heat lost to the work roll, but less time is available for the heat to transfer to the work roll. However, the magnitude of the increase in heat transfer coefficient with increased rolling load is likely to have less of an impact than the decreased time for heat to be lost, thus an increase in roll radius for a given reduction should result in a decrease in friction coefficient. Whereas the effects of an increase in draught are additive, i.e. an increase in draught results in an increase of pressure, for a given roll radius, and an increase in contact time leading to lower strip surface temperatures and an increase in friction coefficient.

7.7.4. Effect of Relative Velocity

The relative velocity between the strip and the work roll will vary from the roll gap entry to the neutral point and then again to the roll bite exit. Lundberg [44] suggests that continuous rolling at 3 m s^{-1} will give a maximum relative speed of 0.6 m s^{-1} at the roll gap entry and 0.15 m s^{-1} at the roll gap exit; to obtain a relative velocity of 3 m s^{-1} a roll speed of 15 m s^{-1} is required. In the finishing rolling stands, the strip will speed up continuously from the first stand, with a typical strip speed of around 0.5 m s^{-1}, and can exit the seventh stand with the strip speed exceeding 20 m s^{-1}, depending on the mill set-up and rolling parameters. Lundberg has taken data published by Wusatowski [45], giving the friction coefficient as a function of temperature and rolling speed to show that decreasing rolling speed will increase the friction coefficient. Unfortunately, as noted by Lundberg [44], the method used to determine the friction coefficient was not disclosed; however, the trend is in line with the adjustment parameter for Ekelund's friction model [46] given by Lundberg [44] indicating that rolling speeds below 2 m s^{-1} do not have an effect on the friction coefficient whereas speeds greater than 2 m s^{-1} will reduce the overall friction coefficient according to:

$$Q2 = 0.4 + 0.6\exp\left[-0.2(v-2)\right] \tag{7.13}$$

where $Q2$ is a multiplication factor and v is the rolling speed (in m s^{-1}). This relationship suggests that the effect of the rolling speed will saturate with a maximum reduction in the friction coefficient of 60%. This effect can be seen using the extended adhesion theory as a result of frictional heating, where the increase in rolling speeds results in an increase in relative velocities between the strip and the work roll, ultimately causing the surface to increase in temperature with the associated reduction in the friction coefficient.

7.8. Other Contributions to Friction

There are two factors that can affect friction that remain unaccounted for in this theory, namely ploughing and electrical contact. Ploughing, with respect to friction, can be defined as a hard surface with a "sharp" asperity sliding over a softer surface that will dig into the surface and produce a groove. As noted by Rabinowicz [26], the energy of deformation represented by the groove must be supplied by the friction force, which in turn must be larger than if no such groove had been produced. The additional friction force as a result of ploughing has been estimated by Rabinowicz [26] as a result of a circular cone (i.e. an asperity) with a roughness angle θ pressed into a softer surface. The area of the groove that is created during sliding, A_g, may be estimated by:

$$A_g = 2\left(\tfrac{1}{2}\cdot r\cdot r\tan\theta\right) = r^2\tan\theta \tag{7.14}$$

where r is the asperity radius and θ is the roughness angle. Assuming that the additional resistance of sliding is equal to the normal pressure multiplied by the area of the groove, the ploughing component, in terms of the original adhesion theory, becomes:

$$\mu = \frac{F_T}{F_N} = \frac{\pi r^2 s + r^2 p \tan\theta}{\pi r^2 p} = \frac{s}{p} + \frac{\tan\theta}{\pi} \tag{7.15}$$

where F_T is the friction force, F_N is the normal force, s is the shear strength and p is the yield strength. The extended adhesion theory has been derived under the assumption that adhesion is the dominant friction mechanism and the contacting surfaces are sufficiently smooth that any ploughing that takes place is in the form of asperities deforming. Applying this approximation to the extended adhesion theory gives:

$$\mu = \frac{\dfrac{8\times10^{-6}\beta}{C_1\tan\theta}W_{ab}}{\sqrt{1-\alpha\left(\dfrac{8\times10^{-6}\beta}{C_1\tan\theta}W_{ab}\right)^2}} + \frac{\tan\theta}{\pi} \tag{7.16}$$

where α, β and C_1 are constants and W_{ab} is the thermodynamic work of adhesion term. This equation has been applied to a copper on copper system, shown in Figure 7.17.

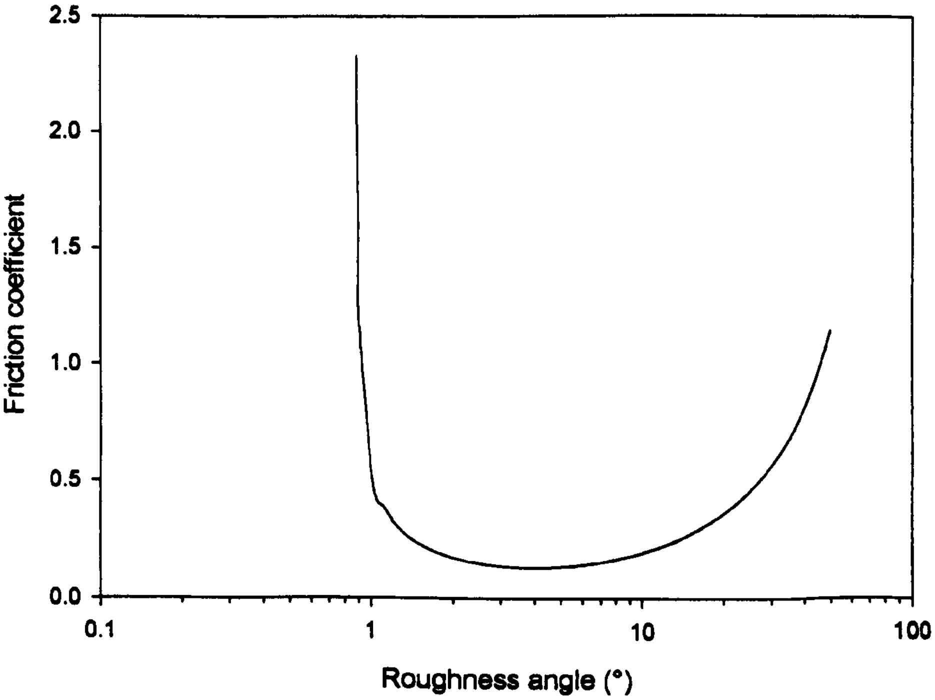

Figure 7.17 – The results of equation 7.16 for a copper on copper system where: W_{ab}=2.2 J m^{-2}, α=12, C_1=0.002 MN m^{-1} and β=0.5.

Figure 7.17 shows that equation 7.16 qualitatively predicts what has been experimentally observed by Rabinowicz [26] with high friction coefficients for smooth surfaces, a transition region with constant friction coefficient and an increasing friction coefficient for rough surfaces. The predictions are reasonable for smooth surfaces, where adhesion is the dominant friction mechanism, and rough surfaces, where friction is caused by interlocking asperities, but equation 7.16 does not give a reasonable prediction for the transition from adhesion to interlocking asperities as the dominant friction mechanism. Despite this inability to predict the transition region, Figure 7.17 may indicate the roughness range for which the equilibrium roughness angle will develop as the local minimum of the curve, in this case around 4°; above this roughness angle the surface should roughen while below this angle the equilibrium roughness angle should be obtained. The transition roughness angle will depend on the denominator of the $\tan\theta/\pi$ term, which is likely to be a function of roughness angle since the friction coefficient should equal $\tan\theta$ for the situation of asperities sliding over one another. Figure 7.17 also suggests that the smoothest contacting surface that is feasible for copper is around 0.88°.

The electrical component of friction will occur when unlike materials are contacting each other, which is a result of the electrical double layer that forms at the junctions. The breaking of these junctions must be accompanied by the separation of unlike electrical charges, which leads to an increase in the friction force as a result of the separation [47]. In metals this appears to be extremely small in comparison with other factors affecting friction but this effect has been used to explain the increase in friction force observed during fretting tests of glass fibre-epoxy composites [48]. Furthermore, the electrical component of friction is dominant in micro-mechanisms [49].

7.9. Coulomb Friction versus Friction Factor

Coulomb friction models are not applicable in situations where the normal pressure greatly exceeds the shear strength of the contacting materials. Although the simplified adhesion theory has been derived with the assumption that the pressure is less than $0.577 \cdot \sigma_0$, following Straffelini [18] the theory was re-derived as a relationship for friction factor instead of friction coefficient.

The friction coefficient, μ, is given here in terms of shear stress, τ, and yield pressure, p_Y, and recognising that friction factor is related to the friction coefficient by a factor of $\sqrt{3}$ gives:

$$\mu = \frac{\tau_m}{p_Y} = \frac{m}{\sqrt{3}} \tag{7.17}$$

Using equation 5.16 as starting point, given here:

$$\tau_m = 2\beta \frac{G_c}{r \tan\theta} \tag{7.18}$$

and, following §5.2, assuming $r = \frac{C_1}{p_Y}$, equation 7.18 becomes:

$$\frac{\tau_m}{p_Y} = \frac{2 \cdot \beta \cdot G_c}{C_1 \tan\theta} = \frac{m}{\sqrt{3}} \tag{7.19}$$

However, the shear strength of the junction cannot exceed the shear strength of the weaker material, which is the definition of sticking where m=1, results in the following relationship:

$$1 = \frac{2\sqrt{3} \cdot \beta \cdot G_c}{C_1 \tan\theta} \tag{7.20}$$

In other words, the smoothest a surface can be during sliding before adhesion is suggested by:

$$\tan\theta = \frac{2\sqrt{3} \cdot \beta \cdot G_c}{C_1} \tag{7.21}$$

Although this is the logical extension of the theory, the applicability of this equation for very smooth surfaces remains in question as a result of its asymptotic nature. If the friction force is assumed to be only the result of the adhesion force, i.e. β=1, equation 7.21 correctly predicts the asymptotes for the roughness angle from equation 5.17, examples of which are given in Table 7.5 when C_1 is equal to 2000 N m^{-1}. This assumption is reasonable since the β term represents the shearing process at the junctions; if the shear strength is equal to the junction shear strength then the material may fail either in the material or at the junction.

Table 7.5 – Comparison of asymptotic roughness angles predicted by equation 7.21 with roughness angles calculated by equation 5.17.

Effective work of adhesion (J m^{-2})	Predicted $\theta_{asymptote}$ (°)	Observed $\theta_{asymptote}$ (°)
0.5	0.050	0.050
2.0	0.199	0.199
4.0	0.397	0.397
8.0	0.794	0.794
12.0	1.191	1.191

Substituting equation 7.17 into equation 5.17 gives:

$$\frac{m}{\sqrt{1+\alpha'\cdot m^2}}=\frac{2\cdot\beta\cdot G_c}{C_1\cdot\tan\theta} \tag{7.22}$$

where α' is a constant equal to 2. The lower friction limit of m=0, gives the result that G_c=0, which is physically representative as there must be adhesion to create a friction force. For the upper limit of m=1, equation 7.22 reduces to equation 7.21. Although, as mentioned earlier, the upper limit of friction factor this equation may not be valid and some experimental validation should be conducted.

The question of which friction model, Coulomb or friction factor, is more applicable now arises. This can be determined by comparing the von Mises equivalent stress multiplied by 0.577 (the shear yield stress) to the shear stress at the sample surface for an assumed friction coefficient of 0.5, shown in Figure 7.18. Since the shear yield stress is always greater than the shear stress at the sample surface in the roll bite for a friction coefficient of 0.5, which is the maximum friction coefficient that is likely to be experienced in hot rolling, the Coulomb friction model is always valid in the roll bite. A situation in which friction factor is more appropriate than a Coulomb friction coefficient is forging, thus it may be able to validate the developed friction factor equation from the adhesion theory against controlled forging tests.

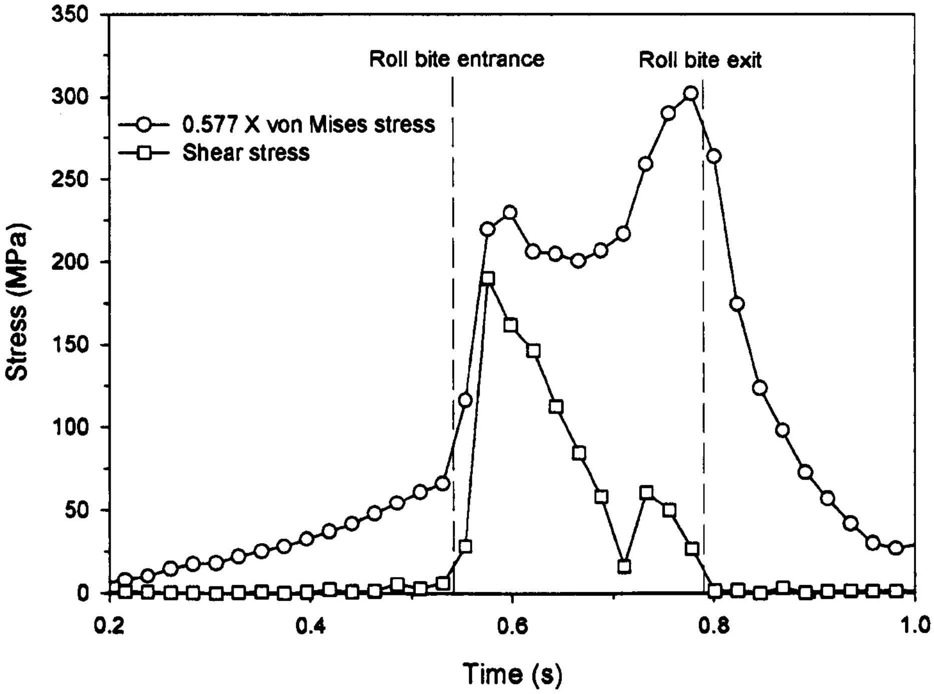

Figure 7.18 – Comparison of the von Mises equivalent shear stress and the shear stress at the sample surface from finite element calculations.

7.10. Speculative Material Pairings

In the hot rolling of steel there are two contacting materials: the strip and the work roll. The steel strip surface is limited to iron, wüstite, magnetite or hæmatite. As noted by numerous sources hæmatite has a deleterious effect on both strip surface quality and work roll wear, thus it is advisable to avoid its formation. Magnetite or a combination of magnetite and wüstite is the current typical surface of the oxide layer, which has a surface energy value of 1.5 J m^{-2} but is not dramatically affected by temperature. Wüstite has a lower surface energy than magnetite at 0.94 J m^{-2}; in the context of the adhesion theory makes it preferable to a magnetite surface for one of the rolling contact surfaces. At room temperature iron (or steel) has a surface energy equal to magnetite but at hot rolling temperatures it may be as little as ¼ this value. Thus, according to this theory, preventing or reducing the oxidation of the strip should result in lower friction coefficients, assuming that the work roll material remains the same.

There is considerably more freedom in the selection of the work roll material, if financial and other physical restraints are neglected. The only restraint that should not be overlooked is the assumption that oxidation will take place; therefore the material should be an oxide. The only problem with this approach is finding the surface energy data for a given material. Two examples of alternative roll materials, for which surface energy data are available, are CrAlN and TiO_2. A study involving the coating of tool steels [50] suggests that coating with CrAlN can stabilise the surface energy of the coated tool as oxidation takes place, resulting in a reduction in surface energy of approximately 15% after 20 hours at 550°C, compared with uncoated tool steel. From the biomedical industry a study on the surface properties of silver doped titanium oxide films found that the surface energy of the TiO_2 ranging from 0.35 J m^{-2} to 0.45 J m^{-2} for silver concentrations from 1.4 at% to 11.2 at% respectively [51]. The low surface energy at room temperature, compared with the iron oxides, suggests that the friction coefficient would be dramatically reduced if surface energy were the only requirement for a work roll material, bearing in mind that some friction is required to perform rolling.

7.11. References

1. F.P. Bowden and D. Tabor "Friction and lubrication", 2nd ed., Methuen and Co. Ltd., London, 1967, 0416406300
2. M.G. Gee and L.A. Lay "Results of the second round robin exercise carried out by the UK wear test methods group on the sliding wear of alumina ceramic", NPL DMA(D) 751, November 1989
3. P. J. Blau "A review of sub-scale test methods to evaluate the friction and wear of ring and liner materials for spark- and compression ignition engines", ORNL/TM-2001/184, Oak Ridge National Laboratory, November 2001
4. Y.H. Li and C.M. Sellars "Comparative investigations of interfacial heat transfer behaviour during hot forging and rolling of steel with oxide scale formation", Journal of Materials Processing Technology (Netherlands), 1998, 80-81, 282-286
5. M. Krzyzanowski and J.H. Beynon "Modelling the behaviour of oxide scale in hot rolling", CAMP-ISIJ, 2001, 14, 315-318
6. I. Schindler, E. Hadasik and R. Kawalla "Strain-Rate Sensitivity in Hot Forming of Steels- Influence of Microstructure, Temperature and Chemical Composition", Steel Research International, 2003, 74, 617-623
7. F. Friedel, H. Pircher, P.H. Bolt, X. Cornet, S. Ehlers and F. Steinert "Investigation of the formation, constitution and properties of scale formed during the finishing rolling, cooling and coiling of thin hot strips", Technical Report No. 2, ECSC steel RTD project 7210.PR/153, September 2000

8. P.H. Bolt, F. Friedel, H. Pircher, X. Cornet, S. Ehlers and F. Steinert "Investigation of the formation, constitution and properties of scale formed during the finishing rolling, cooling and coiling of thin hot strips", Technical Report No. 3, ECSC steel RTD project 7210.PR/153, March 2001
9. H. Pircher, P.H. Bolt, X. Cornet, S. Ehlers, F. Friedel and F. Steinert "Investigation of the formation, constitution and properties of scale formed during the finishing rolling, cooling and coiling of thin hot strips", Technical Report No. 1, ECSC steel RTD project 7210.PR/153, March 2000
10. H. Okada, T. Fukugawa, H. Ishihara, A. Okamoto, M. Azuma and Y. Matsuda "Prevention of red scale formation during hot rolling of steels", ISIJ International, 1995, 35, 886-891
11. J. Paidassi "Contribution a l'etude de l'oxydatin du fer dans l'air dans l'intervale 700-1250°C", Les Mémoires scientifiques de la Revue de métallurgie, 1957, 54, 569-585
12. K. Sachs and C.W. Tuck "Surface oxidation of steel in industrial furnaces", Proceedings of the Conference on Reheating for Hot Working, London, UK, ed. by The Iron and Steel Institute, 1967, 1-17
13. J. Bernard and O. Coquelle "Nouvelle recherches sur l'oxydation du fer aux temperatures elevees par la methode micrographique", Compte Rendus, 1946, 22, 796
14. D.T. Blazevic "Tertiary rolled in scale - The hot strip mill surface problem of the 1990s", 37th Mechanical Working and Steel Processing, Hamilton, Canada, ed. by Iron and Steel Society, 1996, 33-38
15. G.E. Dieter "Mechanical metallurgy", SI Metric ed., McGraw-Hill Book Company, London, 1988, 0-07-084187-X
16. X. Duan and T. Sheppard "Three dimensional thermal mechanical coupled simulation during hot rolling of aluminium alloy 3003", International Journal of Mechanical Sciences, 2002, 44, 2155-2172
17. E. Rabinowicz "Friction and wear of materials", 1st ed., John Wiley and Sons, Inc., New York, 1965, Library of Congress # 65-12704
18. G. Straffelini "A simplified approach to the adhesive theory of friction", Wear, 2001, 249, 79-85
19. S.C. Lim and M.F. Ashby "Wear mechanism maps", Acta Metallurgica, 1987, 35, 1-24
20. J.S. McFarlane and D. Tabor "Relation between friction and adhesion", Proc. Roy. Soc., 1950, 202A, 244-253
21. K.C. Ludema "Friction, wear, lubrication : a textbook in tribology", 1st ed., CRC Press, Boca Raton, 1996, 0849326850
22. Y Ando and J Ino "The effect of asperity array geometry on friction and pull-off force", Journal of Tribology, 1997, 119, 781-787
23. Y. Ando, Y. Ishikawa and T. Kitahara "Friction characteristics and adhesion force under low normal load", Journal of Tribology (Transactions of the ASME) (USA), 1995, 117, 569-574
24. K. Tanaka, J. Ishikawa and A. Shimamoto "Elastic contact and friction between sliders and circumferentially textured disks-Part III: Experiments", Journal of Tribology, 1998, 120, 800-807
25. T.E. Tallian "Rolling bearing life modifying factors for film thickness, surface roughness, and friction", Journal of Lubrication Technology, 1981, 103, 509-520
26. E. Rabinowicz "Friction and wear of materials", 2nd ed., John Wiley & Sons, Inc., New York, 1995, 0-471-83084-4

27. Y. Hidaka, T. Anraku and N. Ostuka "Deformation of iron oxides upon tensile tests at 600-1250°C", Oxid. Met., 2003, 59, 97-113
28. J. G. Lenard and L. Barbulovic-Nad "The coefficient of friction during hot rolling of low carbon steel strips", Journal of Tribology, 2002, 124, 840-845
29. M. Burdek "A roll surface topography change during temper rolling", Metal Forming 2004, Krakow, Poland, ed. by Kusiak *et al.*, 351-354
30. K. Meine, T. Schneider, D. Spaltmann and E. Santer "The influence of roughness on friction. Part I: The influence of a single step", Wear, 2002, 253, 725-732
31. D. E. Packham "Surface energy, surface topography and adhesion", International Journal of Adhesion and Adhesives (UK), 2003, 23, 437-448
32. J.T. Desaguliers "Some experiments concerning the cohesion of lead", Phil.Trans. R. Soc. Lond., 1725, 33, 345-347
33. F.P. Bowden and T.P. Hughes "Friction of clean metals and influence of adsorbed gases", Proc. Roy. Soc., 1939, A172, 263-279
34. A.T. Gwathmey "The study of the fundamentals of lubrication with the aid of large metal crystals", Ann. New York Acad. Sci., 1951, 53, 987-994
35. F.P. Bowden and J.E. Young "Friction of clean metals and the influence of adsorbed films", Proc. Roy. Soc., 1951, A208, 311-325
36. X. Tan "Comparisons of friction models in bulk metal forming", Tribology International, 2002, 35, 385-393
37. T Wanheim and N Bay "A model for friction in metal forming processes", Annals of CIRP, 1978, 27, 189-194
38. U. Wankhede and I.V. Samarasekera "Thermal behaviour of high speed steel work rolls in the finishing train of a hot strip mill", Iron and Steelmaker (USA), 1997, 24, 55-60
39. W.C. Chen, I.V. Samarasekera and E.B. Hawbolt "Fundamental phenomena governing heat transfer during rolling", Metall. Trans. A, 1993, 24A, 1307-1320
40. C. Devadas and I.V. Samarasekera "Heat transfer during hot rolling of steel strip", Ironmaking and Steelmaking, 1986, 13, 311-321
41. C. Fedorciuc-Onisa and D.C.J. Farrugia "Through process characterisation of frictional conditions for long product hot rolling", Metal Forming 2004, Kraków, Poland, ed. by Kusiak *et al.*, 19-22 September 2004, 331-336
42. H. Ford and J.M. Alexander "Rolling hard materials in thin gauges", J. Inst. Metals, 1963, 92, 397
43. F. Siciliano Jr., K. Minami, T.M. Maccagno and J.J. Jonas "Mathematical modeling of the mean flow stress, fractional softening and grain size during the hot strip rolling of C-Mn steels", ISIJ Int., 1996, 36, 1500-1506
44. S. E. Lundberg "Evaluation of friction in the hot rolling of steel bars by means of on line forward slip measurements", Scand. J. Metall., 2004, 33, 129-145
45. Z. Wusatowski "Fundamentals of rolling", 1st ed., Pergamon Press, 1969, 0080122760
46. S. Ekelund "Nagra dynamiska forhallanden vid valsing", Jernkontorets Annaler, 1927, 2, 39
47. R. Schnurmann and E. Wardlow-Davies "The electrostatic component of the force of sliding friction", Proc. Phys. Soc. (London), 1942, 54, 14-27
48. C. Turki, B. Kechaou, D. Treheux, Z. Fakhfakh and M. Salvia "Fretting behaviour of unidirectional glass fibre–epoxy composites, influence of electric charge effects", Wear, 2004, 257, 531-538

49. C. Guerret-Piecourt, J. Vallayer and D. Treheux "Limitation induced by electrical charges effects on micromechanisms", Wear, 2003, 254, 950-958

50. E. Lugscheider, K. Bobzin, St. Baerwulf and Th. Hornig "Oxidation characteristics and surface energy of chromium-based hardcoatings for use in semisolid forming tools", Surface and Coatings Technology (Switzerland), 2000, 133-134, 540-547

51. F. Zhang, G.K. Wolf, X. Wang and X. Liu "Surface properties of silver doped titanium oxide films", Surface and Coatings Technology (Switzerland), 2001, 148, 65-70

Chapter 8 - Conclusions and Further Work

8.1. Conclusions

The objectives of this project were: to investigate friction in a fundamental way, to develop a fundamental model of friction based on the physics of the process, and to apply the friction model to the hot rolling of steel. In the course of this work the following observations were made:

- The modified ring compression testing technique using pre-roughened platens was not suitable for investigating stick-slip friction conditions.
- Reciprocating friction testing provided consistent and applicable results for stick-slip friction conditions between 450°C and 500°C using samples with oxide layers grown *in situ*.
- Below this temperature range the oxide layer was aggressively removed as a result of the friction force exceeding the shear strength of the oxide; above 500°C a fine powder material was removed/formed changing the friction conditions to 3rd body lubrication.
- Two-pass laboratory hot rolling experiments were conducted to investigate the effect of temperature on friction, via load and torque measurements. The first pass successfully used a 10% reduction, combined with the sample geometry, to remove the secondary scale formed in the furnace and immediately prior to rolling. The sample was rotated by 90° before the second pass of 20% reduction, of which the torque and load were measured. In terms of scale removal, the sample geometry of the initial height being greater than the initial width played an important role.
- The rolling model incorporating the friction algorithm was validated in terms of temperature (using a constant heat transfer coefficient of 25 kW m^{-2} K^{-1}).
- The algorithm to predict the friction coefficient for the rolling experiments was found to be physically reasonable; based on comparisons with predictions using constant friction coefficients to predict rolling load and torque. The advantages of the friction algorithm are that no initial assumption regarding the magnitude of the friction coefficient is required and it can predict the friction coefficient throughout the roll bite.

- The predicted rolling loads were between 8% and 17% greater than the experimental loads while the rolling torques were between 13% and 17% less than the experimental torques before accounting for bearing torque. The accuracy of the rolling torques improved to between 8% and 12% when a 5% allowance was made for bearing torque.
- The thermocouples were unable to accurately record the heat generated by plastic deformation. The short delay in the thermocouple weld bead making intimate contact with the steel was a result of the initial 10% reduction and the rotation of the sample.
- The mill control system was used to automatically change the roll gap and direction of rolling to obtain consistent interpass times, thereby producing consistent results.

Advances in friction theory as a result of this work are as follows:

- The adhesive friction theory was further developed to include temperature dependence of the work of adhesion term via the contacting materials' surface energies.
- The adhesive friction theory was re-derived in terms of a friction factor, rather than a Coulomb-type friction coefficient, but it was shown that a Coulomb-type friction coefficient was still applicable to the rolling experiments that were conducted.
- The geometric mean rule for estimating the thermodynamic work of adhesion was applied to solids using the ratio of molar volumes.
- The relative change in surface energy of a material at any temperature was estimated by the relative change in Young's modulus.
- A single equation was used to estimate the Young's modulus for magnetite over the temperature range of 25°C to 850°C.
- The application of the adhesive friction theory over a range of temperatures was verified with experimental data from reciprocating friction tests.
- Criticisms of the adhesive friction model, past and present, have been considered and explained in terms of the current model.
- Other contributions to friction were considered with the effect of ploughing on the friction coefficient shown to be minimal with smooth surfaces and dominant with rough surfaces. The electrical component of friction was considered to be negligible at the macro scale.

Advances in rolling theory as a result of this work are as follows:

- The reciprocating friction test and laboratory rolling were deemed suitable and reproducible for the development and validation of the friction theory.
- A friction algorithm using the modified adhesion friction theory for calculation of the friction coefficient was developed as a user-defined subroutine for finite element analysis to predict the friction coefficient throughout the roll bite.
- The application of the friction algorithm in a rolling model compared favourably against laboratory rolling experiments using torque and load comparisons.
- The friction algorithm predicted that the friction coefficient would continuously vary between 0.25 and 0.35 from the roll gap entrance to exit.
- The sensitivity analysis of the friction coefficient equation, i.e. equation 7.6, showed that all the variables, with the exception of the constant α (defined in §5.2), had similar influence on the friction coefficient prediction.
- The roughness angle employed in the theory was considered and it was found that the roughness angle of 0.7° can be related to a *Ra* of 0.9 μm, which is similar to the work roll roughness used in the rolling experiments. Furthermore the roughness of a surface has been shown to evolve and approach an equilibrium level.
- The work of adhesion term in the friction algorithm allows industrial work roll surfaces to be estimated; thereby enabling the effect of changing the scale layer composition has on the friction coefficient to be examined.
- It was speculated that changing the oxide scale at the strip surface to wüstite would reduce the friction coefficient while work roll coatings of CrAlN or TiO_2 would also reduce the friction coefficient.

Lastly, while the friction algorithm within the rolling model did not have a significant impact on the model results in terms of rolling load and torque compared with assumed constant friction coefficients the advantage this method has over constant friction coefficients is that no preconceptions regarding the level of friction is required prior to modelling a rolling pass.

8.2. Further Work

The developed friction model is a generic model as it relies only upon the contacting materials, the contacting temperature and roughness of the contacting surface. Furthermore, as the modified adhesive friction theory has also been derived as a friction factor, rather than a Coulomb-type friction coefficient, the model may be applied to many other metal forming operations. However, in the literature there is a lack of data regarding the properties of oxides, particularly stress-strain curves, and a lack of surface energy data for many materials, including metals and oxides.

From a material properties viewpoint, further work may involve:

- Determining the mechanical properties of the different iron oxides, i.e. stress-strain curves at various temperatures and strain rates.
- Determining the surface energy of contacting materials over a range of temperatures; specifically for hot rolling, tool steels and their oxides and the surface energy of iron oxides with temperature.
- Studying the interface between the oxide layer and the steel substrate using a layered contact mechanics approach.

With respect to hot rolling, further work may involve:

- Using the model to study the development of the work roll oxide layer, i.e. tracking the changes in the surface energy necessary to give the evolving friction coefficient seen in industry.
- Examining the influence of the roughness angle on the friction coefficient.
- More accurately modelling the surface energy of the work roll oxide layer, perhaps in terms of weighted averages of the oxide components, for example chromium oxide and iron oxides.
- Investigating the sticking zone around the neutral point in laboratory rolling.
- Applying the modified adhesive friction theory to other systems, such as the cold rolling of steel or aluminium rolling.

For metal forming operations other than rolling, further work may involve:

- Applying the modified adhesive friction theory to forging operations, such as plane strain compression or ring compression, using the developed friction factor model.

Appendix A – Self-Consistent Units Used in Finite Element Analysis

Quantity	SI	Multiplier	mm/tonne/s/K (or SI-mm)
Length	m	1000	mm
Time	s	1	s
Mass	kg	$\frac{1}{1000}$	tonne Mg
Force	kg m s^{-2} N	1	tonne mm s^{-2} N
Density	kg m^{-3}	$\frac{1}{1000^4}$	tonne mm^{-3} Mg mm^{-3}
Stress	kg m^{-1} s^{-2} N m^{-2}	$\frac{1}{1000^2}$	tonne mm^{-1} s^{-2} MPa or N mm^{-2}
Energy	kg m^2 s^{-2} J	1000	tonne mm^2 s^{-2} mJ or N mm
Temperature	K	1	°C
Specific Heat Capacity	m^2 s^{-2} K^{-1} J kg^{-1} $°C^{-1}$	1000^2	mm^2 s^{-2} $°C^{-1}$
Heat Convection	kg s^{-3} K^{-1} W m^{-2} $°C^{-1}$	$\frac{1}{1000}$	tonne s^{-3} $°C^{-1}$ N s^{-1} K^{-1} mm^{-1}
Thermal Conductivity	kg m s^{-3} K^{-1} W m^{-1} $°C^{-1}$	1	tonne mm s^{-3} $°C^{-1}$ N s^{-1} K^{-1}
Thermal Expansion	m m^{-1} K^{-1}	1	mm mm^{-1} $°C^{-1}$

Appendix B – Derivation of Stress Function Coefficients in Layered Contact Analysis

The stress function coefficient matrix required for the analysis of the contact stresses between an elastic cylinder and a single layered elastic solid with friction is derived. Assumption and substitutions by Mao *et al.* [1,2] have been used.

B.1. Assumptions

1. Perfect adherence between the layer and the substrate as well as frictionless contact with the cylinder is assumed.
2. The system is taken as being in contact with another elastic body, which may be an elastic half-space or another multi-layered body.
3. The stresses as a result of the contact are assumed to be plane strain.
4. The strains are assumed to be small; therefore all the usual assumptions with regards to linear elastic theory are also applicable.
5. The contact is considered to be dry.
6. The coordinate system used in this analysis is described in Figure B.1.

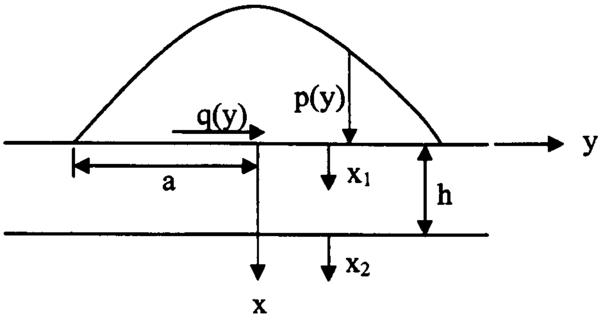

Figure B.1 – Coordinate system and sample geometry.

B.2. Substitutions

$$q = e^{|\omega|h}$$

$$\gamma = \frac{\left(1-\nu_2^2\right)E_1}{\left(1-\nu_1^2\right)E_2}$$

$$\nu' = \frac{2-\nu}{1-\nu}$$

$$\nu'' = \frac{\nu}{1-\nu}$$

$$p(\omega) = \int_{-\infty}^{\infty} p(y)e^{j\omega y_1}\,dy$$

$$q(\omega)=\frac{1}{\omega}\int_{-\infty}^{\infty}q(y)e^{j\omega y_i}dy$$

B.3. Surface Deflection Due to Unit Line Load

The general solution for a two-dimensional elastic solid has been expressed by Sneddon [3] in terms of Fourier integrals. The stresses and displacements are given by:

$$\sigma_{x_i}=\frac{\partial^2\psi}{\partial y^2}=-\frac{1}{2\pi}\int_{-\infty}^{\infty}\omega^2 G_i e^{-j\omega y_i}d\omega \tag{B.1}$$

$$\sigma_{y_i}=\frac{\partial^2\psi}{\partial x^2}=\frac{1}{2\pi}\int_{-\infty}^{\infty}\frac{d^2G_i}{dx^2}e^{-j\omega y_i}d\omega \tag{B.2}$$

$$\tau_{xy_i}=-\frac{\partial^2\psi}{\partial x\partial y}=\frac{1}{2\pi}\int_{-\infty}^{\infty}j\omega\frac{dG_i}{dx_i}e^{-j\omega y_i}d\omega \tag{B.3}$$

$$u_i=\frac{1-\nu_i^2}{2\pi E_i}\int_{-\infty}^{\infty}\left[\frac{d^3G_i}{dx_i^3}-\left(\frac{2-\nu_i}{1-\nu_i}\right)\omega^2\frac{dG_i}{dx_i}\right]e^{-j\omega y_i}\frac{d\omega}{\omega^2} \tag{B.4}$$

$$v_i=\frac{1-\nu_i^2}{2\pi E_i}\int_{-\infty}^{\infty}\left[\frac{d^2G_i}{dx_i^2}+\left(\frac{\nu_i}{1-\nu_i}\right)\omega^2 G_i\right]e^{-j\omega y_i}\frac{d\omega}{\omega} \tag{B.5}$$

where ψ is the Airy stress function that satisfies the biharmonic equation and G is the Fourier transform of ψ, given by:

$$\nabla^4\psi=0 \tag{B.6}$$

$$G=\int_{-\infty}^{\infty}\psi e^{i\omega y}dy \tag{B.7}$$

The solution for G is given in the form:

$$G=(A+Bx)e^{-|\omega|x}+(C+Dx)e^{+|\omega|x} \tag{B.8}$$

where the constants A, B, C and D are generally functions of ω and are determined by the boundary conditions.

B.4. Derivatives of G With Respect to X

$$G=Ae^{-|\omega|x}+Bxe^{-|\omega|x}+Ce^{|\omega|x}+Dxe^{|\omega|x} \tag{B.9}$$

$$G'=-|\omega|Ae^{-|\omega|x}+Be^{-|\omega|x}-|\omega|Bxe^{-|\omega|x}+|\omega|Ce^{|\omega|x}+De^{|\omega|x}+|\omega|Dxe^{|\omega|x} \tag{B.10}$$

$$G'' = |\omega|^2 Ae^{-|\omega|x} - 2|\omega|Be^{-|\omega|x} + |\omega|^2 Bxe^{-|\omega|x} + |\omega|^2 Ce^{|\omega|x} + 2|\omega|De^{|\omega|x} + |\omega|^2 Dxe^{|\omega|x} \tag{B.11}$$

$$G''' = -|\varpi|^3 Ae^{-|\omega|x} + 3|\omega|^2 Be^{-|\omega|x} - |\omega|^3 Bxe^{-|\omega|x} + |\omega|^3 Ce^{|\omega|x} + 3|\omega|^2 De^{|\omega|x} + |\omega|^3 Dxe^{|\omega|x} \tag{B.12}$$

B.5. Boundary Conditions

$$\begin{array}{ll}
\sigma_x^{(1)}(0,y) = -p(y); & \tau_{XY}^{(1)}(0,y) = -q(0,y) \\
\sigma_x^{(1)}(h,y) = \sigma_x^{(2)}(0,y); & \tau_{XY}^{(1)}(h,y) = \tau_{XY}^{(2)}(0,y) \\
u_1(h,y) = u_2(0,y); & v_1(h,0) = v_2(0,y) \\
\sigma_x^{(2)}(\infty,y) = \tau_{xy}^{(2)}(\infty,y) = 0 &
\end{array} \tag{B.13}$$

Eight simultaneous equations for A_1 to D_2 are obtained by taking inverse transforms of the relations for the stresses given above and substituting for G from Equation 8. As a result of the last boundary condition C_2 and D_2 are zero.

B.6. Solving for the stress function coefficients (aka the A matrix)

B.6.1. Matching normal stresses at the surface

Substituting the first boundary condition into Equation B.1 gives:

$$-p(y_1) = -\frac{1}{2\pi}\int_{-\infty}^{\infty} \omega^2 G_1 e^{-j\omega y_1} d\omega \tag{B.14}$$

Using the inverse Fourier transform, this equation reduces to [3]:

$$\omega^2 G_1 = \int_{-\infty}^{\infty} p(y) e^{j\omega y_1} dy = p(\omega) \tag{B.15}$$

$$\omega^2 (A_1 + C_1) = p(\omega) \tag{B.16}$$

For constant unit pressures applied over the interval $-a/2 \le y \le a/2$, this formula becomes:

$$P = \int_{-\infty}^{\infty} p(y) e^{j\omega y_1} dy = \int_{-a/2}^{a/2} \cos(\omega y) dy = \frac{2}{\omega}\sin\frac{\omega a}{2} \tag{B.17}$$

Substituting Equation B.17 into Equation B.15, and setting $x_1 = 0$ gives:

$$\omega^2 (A_1 + C_1) = P \tag{B.18}$$

B.6.2. Matching shear stresses at the surface

Substituting the shear stress boundary condition into Equation B.3 gives:

$$-q(y_i) = \frac{1}{2\pi}\int_{-\infty}^{\infty} j\omega \frac{dG_i}{dx_i} e^{-j\omega y_i} d\omega \qquad \text{(B.19)}$$

Again, using the inverse Fourier transform this equation reduces to:

$$\frac{dG_1}{dx_1} = \frac{1}{\omega}\int_{-\infty}^{\infty} q(y) e^{j\omega y_1} dy = q(\omega) \qquad \text{(B.20)}$$

In this example, the shear stress at the surface is zero therefore the integral is equal to zero. Differentiating Equation B.8 with respect to x_1 and solving for $x_1 = 0$, gives:

$$-|\omega| A_1 e^{-|\omega| x_1} + B_1 e^{-|\omega| x_1} - |\omega| B_1 x_1 e^{-|\omega| x_1} + |\omega| C_1 e^{|\omega| x_1} + D_1 e^{|\omega| x_1} + |\omega| D_1 x_1 e^{|\omega| x_1} = q(\omega)$$

(B.21)

$$-|\omega| A_1 + B_1 + |\omega| C_1 + D_1 = q(\omega) \qquad \text{(B.22)}$$

For constant unit pressures applied over the interval $-a/2 \le y \le a/2$, $q(\omega)$ becomes:

$$Q = \frac{1}{\omega}\int_{-\infty}^{\infty} q(y) e^{j\omega y_1} dy = \frac{\mu}{\omega}\int_{-a/2}^{a/2} \cos(\omega y) dy = \frac{2\mu}{\omega^2}\sin\frac{\omega a}{2} \qquad \text{(B.23)}$$

Thus:

$$-|\omega| A_1 + B_1 + |\omega| C_1 + D_1 = Q \qquad \text{(B.24)}$$

B.6.3. Matching the normal stresses at the interface

G_1 at $x_1 = h$ is equal to G_2 at $x_2 = 0$:

$$(A_1 + B_1 h) e^{-|\omega| h} + (C_1 + D_1 h) e^{+|\omega| h} = A_2 \qquad \text{(B.25)}$$

$$e^{-|\omega| h} A_1 + h \cdot e^{-|\omega| h} B_1 + e^{|\omega| h} C_1 + h \cdot e^{|\omega| h} D_1 - A_2 = 0 \qquad \text{(B.26)}$$

$$A_1 + h \cdot B_1 + \left(e^{|\omega| h}\right)^2 C_1 + h \cdot \left(e^{|\omega| h}\right)^2 D_1 - e^{|\omega| h} A_2 = 0 \qquad \text{(B.27)}$$

$$A_1 + h \cdot B_1 + q^2 C_1 + h \cdot q^2 D_1 - q \cdot A_2 = 0 \qquad \text{(B.28)}$$

B.6.4. Matching the shear stresses at the interface

dG_1/dx_1 at $x_1 = h$ is equal to dG_2/dx_2 at $x_2 = 0$.

$$\left.\frac{dG_1}{dx_1}\right|_{x_1=h} = -|\omega|A_1e^{-|\omega|h} + B_1e^{-|\omega|h} - |\omega|B_1he^{-|\omega|h} + |\omega|C_1e^{|\omega|h} + D_1e^{|\omega|h} + |\omega|D_1he^{|\omega|h} \qquad \text{(B.29)}$$

$$\left.\frac{dG_2}{dx_2}\right|_{x_2=0} = -|\omega|A_2e^{-|\omega|(0)} + B_2e^{-|\omega|(0)} - |\omega|B_2(0)e^{-|\omega|(0)} \qquad \text{(B.30)}$$

$$-|\omega|A_1 + \left(1-|\omega|h\right)B_1 + |\omega|\cdot q^2\cdot C_1 + \left(1+|\omega|h\right)\cdot q^2\cdot D_1 + |\omega|\cdot q\cdot A_2 - q\cdot B_2 = 0 \qquad \text{(B.31)}$$

B.6.5. Matching the vertical displacement at the interface

$$\frac{1-\nu_1^2}{2\pi E_1}\int_{-\infty}^{\infty}\left[\frac{d^3G_1}{dx_1^3} - \frac{2-\nu_1}{1-\nu_1}\omega^2\frac{dG_1}{dx_1}\right]e^{-i\omega y}\frac{d\omega}{\omega^2} = \frac{1-\nu_2^2}{2\pi E_2}\int_{-\infty}^{\infty}\left[\frac{d^3G_2}{dx_2^3} - \frac{2-\nu_2}{1-\nu_2}\omega^2\frac{dG_2}{dx_2}\right]e^{-i\omega y}\frac{d\omega}{\omega^2}$$

$$\frac{1-\nu_1^2}{E_1}\left.\left[\frac{d^3G_1}{dx_1^3} - \frac{2-\nu_1}{1-\nu_1}\omega^2\frac{dG_1}{dx_1}\right]\right|_{x_1=h} = \frac{1-\nu_2^2}{E_2}\left.\left[\frac{d^3G_2}{dx_2^3} - \frac{2-\nu_2}{1-\nu_2}\omega^2\frac{dG_2}{dx_2}\right]\right|_{x_2=0} \qquad \text{(B.32)}$$

$$\frac{1-\nu_1^2}{E_1}\Big\{\left[-|\omega|^3t^{-1}A_1 + \left(3|\omega|^2 - |\omega|^3h\right)t^{-1}B_1 + |\omega|^3t\cdot C_1 + \left(3|\omega|^2 + |\omega|^3h\right)tD_1\right] - \frac{2-\nu_1}{1-\nu_1}\omega^2$$
$$\left[-|\omega|\cdot t^{-1}A_1 + \left(1-|\omega|h\right)\cdot t^{-1}B_1 + |\omega|\cdot t\cdot C_1 + \left(1+|\omega|h\right)\cdot t\cdot D_1\right]\Big\} = \frac{1-\nu_2^2}{E_2}\Big\{\left[-|\omega|^3A_2 + 3|\omega|^2B_2\right] -$$
$$\frac{2-\nu_2}{1-\nu_2}\omega^2\left[-|\omega|A_2 + B_2\right]\Big\} \qquad \text{(B.33)}$$

Collecting the terms:

$$\frac{1-\nu_1^2}{E_1}\left\{\left(-1+\frac{2-\nu_1}{1-\nu_1}\right)|\omega|^3e^{-|\omega|h}A_1 + \left[\left(3-|\omega|h\right) - \frac{2-\nu_1}{1-\nu_1}\left(1-|\omega|h\right)\right]|\omega|^2e^{-|\omega|h}B_1 + \right.$$
$$\left.\left(1-\frac{2-\nu_1}{1-\nu_1}\right)|\omega|^3e^{|\omega|h}C_1 + \left[\left(3+|\omega|h\right) - \frac{2-\nu_1}{1-\nu_1}\left(1+|\omega|h\right)\right]|\omega|^2e^{|\omega|h}D_1\right\} - \frac{1-\nu_2^2}{E_2}\cdot$$
$$\left\{\left(-1+\frac{2-\nu_2}{1-\nu_2}\right)|\omega|^3A_2 + \left(3-\frac{2-\nu_2}{1-\nu_2}\right)|\omega|^2B_2\right\} = 0 \qquad \text{(B.34)}$$

Dividing through by $|\omega|^2$ and simplifying:

$$\left(\nu_1'-1\right)|\omega|A_1 + \left[3-|\omega|h - \nu_1'\left(1-|\omega|h\right)\right]B_1 + \left(1-\nu_1'\right)|\omega|\cdot q^2C_1 + \left[2+\left(1+|\omega|h\right)\left(1-\nu_1'\right)\right]\cdot q^2D_1 +$$
$$\left(1-\nu_2'\right)|\omega|\gamma\cdot q\cdot A_2 + \left(\nu_2'-3\right)\gamma\cdot q\cdot B_2 = 0 \qquad \text{(B.35)}$$

B.6.6. Matching the horizontal displacement at the interface

$$\frac{1-\nu_1^2}{2\pi E_1}\int_{-\infty}^{\infty}\left[\frac{d^2G_1}{dx_1^2}+\left(\frac{\nu_1}{1-\nu_1}\right)\omega^2G_1\right]e^{-i\omega y}\frac{d\omega}{\omega}=\frac{1-\nu_1^2}{2\pi E_2}\int_{-\infty}^{\infty}\left[\frac{d^2G_2}{dx_2^2}+\left(\frac{\nu_2}{1-\nu_2}\right)\omega^2G_2\right]e^{-i\omega y}\frac{d\omega}{\omega} \tag{B.36}$$

$$\frac{1-\nu_1^2}{E_1}\left[\frac{d^2G_1}{dx_1^2}+\frac{\nu_1}{1-\nu_1}\varpi^2G_1\right]\Bigg|_{x_1=h}=\frac{1-\nu_2^2}{E_2}\left[\frac{d^2G_2}{dx_2^2}+\frac{\nu_2}{1-\nu_2}\varpi^2G_2\right]\Bigg|_{x_2=0} \tag{B.37}$$

$$\begin{aligned}&|\omega|^2A_1-2|\omega|B_1+|\omega|^2hB_1+|\omega|^2t^2C_1+2|\omega|t^2D_1+|\omega|^2ht^2D_1+\nu_1''\omega^2A_1+\nu_1''\omega^2hB_1+\\&\nu_1''\omega^2t^2C_1+\nu_1''\omega^2ht^2D_1-\gamma|\omega|^2t\cdot A_2+2\gamma|\omega|\cdot t\cdot B_2-\gamma\nu_2''\omega^2t\cdot A_2=0\end{aligned} \tag{B.38}$$

Collecting terms:

$$\begin{aligned}&(1+\nu'')|\omega|^2A_1+(-2+|\omega|h+\nu_1''|\omega|h)|\omega|B_1+(1+\nu'')|\omega|^2\cdot t^2C_1+(2+|\omega|h+\nu''|\omega|h)|\omega|\cdot t^2D_1\\&-(1+\nu_2'')|\omega|^2\cdot\gamma\cdot t\cdot A_2+2\gamma|\omega|\cdot t\cdot B_2=0\end{aligned} \tag{B.39}$$

Dividing by $|\omega|$ and simplifying gives:

$$\begin{aligned}&(1+\nu_1'')\cdot|\omega|\cdot A_1+\left[|\omega|h(1+\nu_1'')-2\right]B_1+(1+\nu_1'')\cdot|\omega|\cdot q^2C_1+\left[|\omega|h(1+\nu_1'')+2\right]\cdot q^2D_1\\&-(1+\nu_2'')\cdot\gamma\cdot|\omega|\cdot q\cdot A_2+2\gamma\cdot q\cdot B_2=0\end{aligned} \tag{B.40}$$

B.7. References

1. K. Mao, T. Bell and Y. Sun "Effect of sliding friction on contact stresses for multi-layered elastic bodies with rough surfaces", Journal of Tribology, 1997, 119, 476-480
2. K. Mao, Y. Sun and T. Bell "A numerical model for the dry sliding contact of layered elastic bodies with rough surfaces", Tribology Transactions, 1996, 39, 416-424
3. I.N. Sneddon "Fourier Transforms", 1st ed., McGraw-Hill Book Company, Inc., London, 1951

Appendix C - Glossary of Roughness Measurement Terminology

Mean line	The Mean Line is commonly used in surface texture measurement and it is based on a least squares method. Basically it is a line that bisects the profile such that the areas above and below the Mean Line are equal. For example: 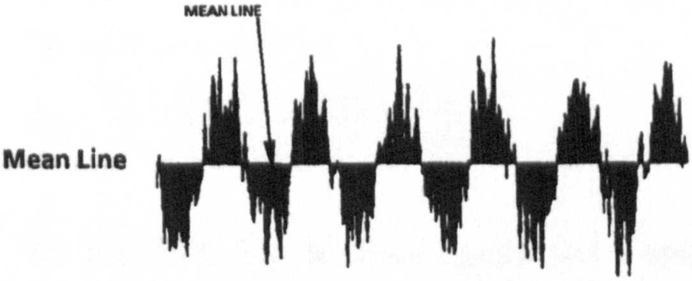
Ra	Ra is the arithmetic mean of the departures of the profile from the mean line, given by: $Ra = \frac{1}{L}\int_0^L \lvert y(x)\rvert dx$
Rq	Rq is the rms parameter corresponding to Ra, given by: $Rq = \sqrt{\frac{1}{L}\int_0^L y^2(x)dx}$
Ry	The largest peak to valley heights within each cut-off length (known as Rti values) are determined. The Ry value is the largest Rti values of the assessment. For example: 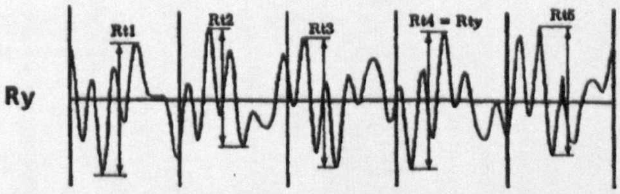
Rz(DIN)	The Rz(DIN) parameter, also known as Rtm, is the average of all the Rti values in the assessment length, given by: $Rz(DIN) = \frac{(Rt_1 + Rt_2 + Rt_3 + ... + Rt_n)}{n} = \frac{1}{n}\sum_{n=1}^{n} Rt_i$

Sm

Sm is the mean spacing between profile peaks at the mean line, measured over the assessment length. For example:

The equation is given by:

$$Sm = \frac{(S_1 + S_2 + S_3 + \ldots + S_n)}{n} = \frac{1}{n}\sum_{i=1}^{n} S_i$$

2CR

The 2CR (ISO) filters have been standardised to have a transmission of 75% at the selected cut-off, i.e. the amplitudes of the irregularities having a spacing equal to the cut-off length are reduced to 75% of their true value. The amplitudes of the shorter wavelength irregularities will be virtually unchanged while the amplitudes of the longer wavelength irregularities are progressively reduced. The amplitude transmission ratio for a sinusoidal waveform is given as:

$$ratio = \frac{output}{input} = \frac{3}{3+\alpha^2} \quad \text{where:} \quad \alpha = \frac{\lambda(input)}{\lambda(cut-off)}$$

The filter transmission characteristics with cut-off roughness spacings of A=0.25 mm, B=0.80 mm and C=2.5 mm are summarised by:

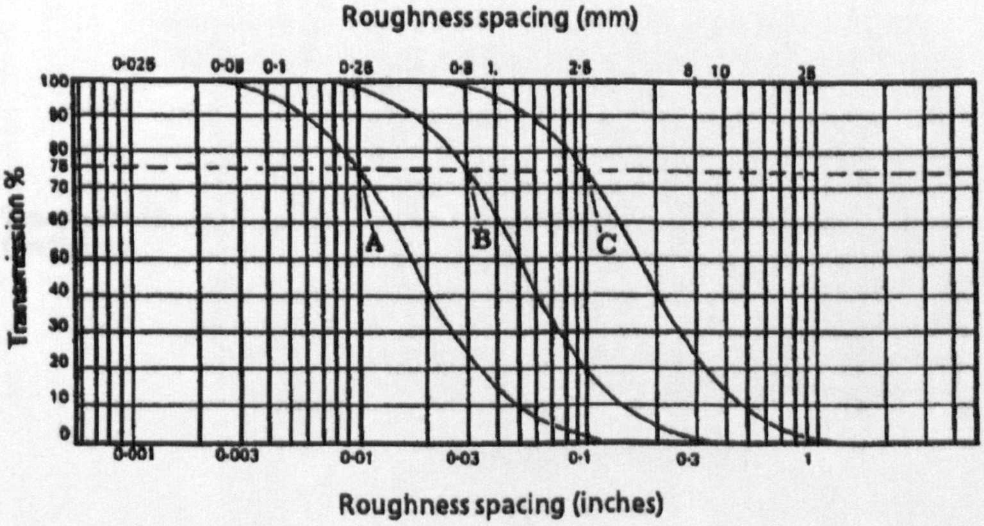

Gaussian

Gaussian filtering does not simulate a specific electronic filter but is a mathematical function applied to the profile data. The filter is a weighted mean of the profile where the weights have a gaussian shape. Since the shape is symmetrical the resulting filter is phase corrected.

A property of a Gaussian filter is the ability to take account of data before and after the effective stylus position. The response at the cut-off value is 50% of the maximum transmission within the band. The weighting function for the Gaussian filter is given by the following:

$f(x) = \frac{1}{\sqrt{2\pi\sigma^2}} \exp\left(-\frac{(x-m)^2}{2\sigma^2}\right)$ where m is the mean and σ^2 is the variance. The transmission characteristics are made up of two components: (a) the transmission characteristics of the mean line and (b) the wavelength characteristics of the roughness profile. The filter characteristic is determined from the weighting function, by means of the Fourier transformation. The roughness profile is the difference between the actual profile and the mean line. The filter characteristic is, therefore, the difference between the wavelength characterisation of the roughness profile. The filter characteristics with cut-off roughness spacing of A=0.25 mm, B=0.80 mm and C=2.5 mm are summarised by:

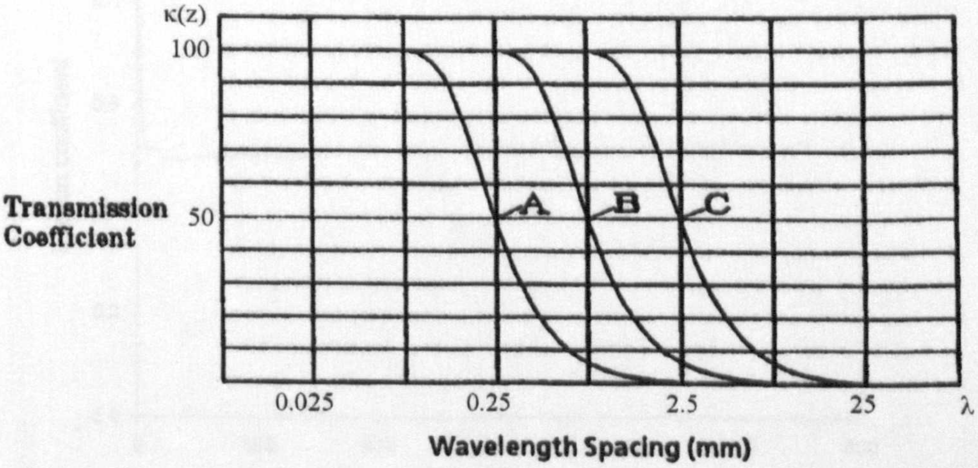

Appendix D – Experimental Friction Coefficient Traces

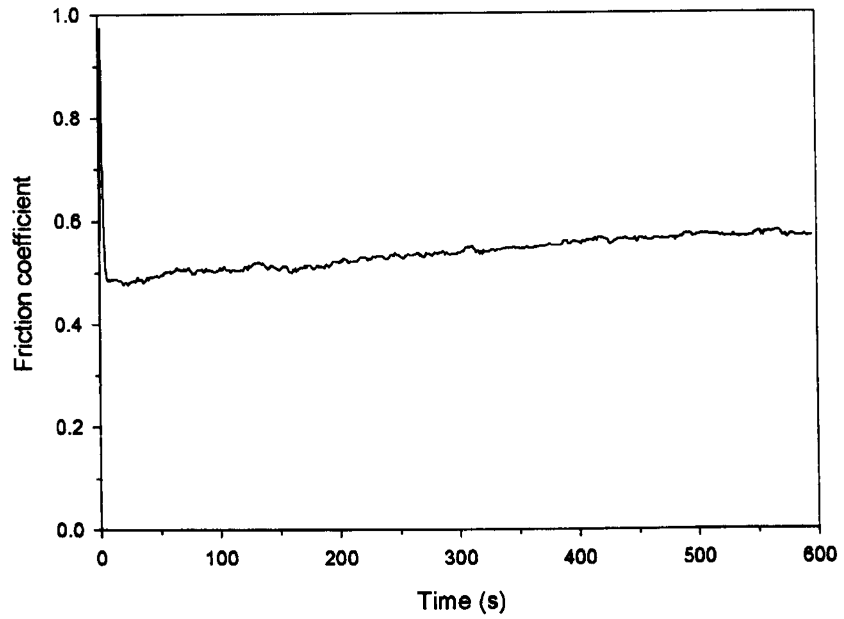

Figure D.1 – Sample air-i2b-07. Normal load=25 N, oxidation time=300 s.

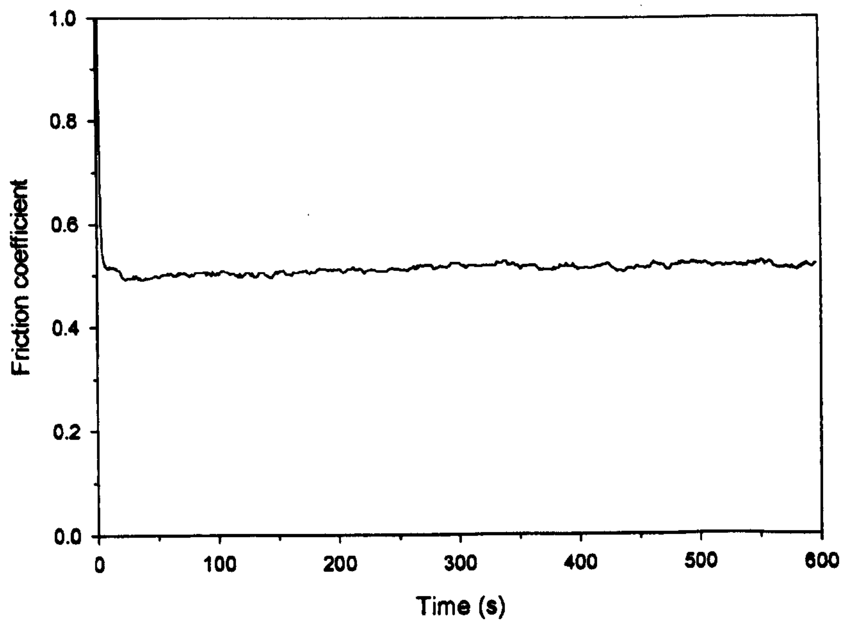

Figure D.2 – Sample air-i2b-08. Normal load=25 N, oxidation time=300 s.

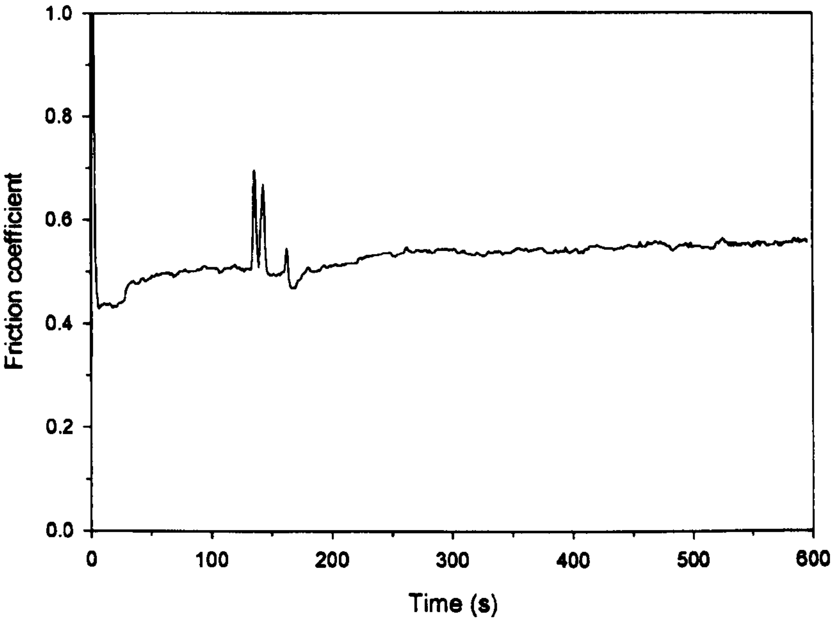

Figure D.3 – Sample air-i2b-09. Normal load=25 N, oxidation time=300 s.

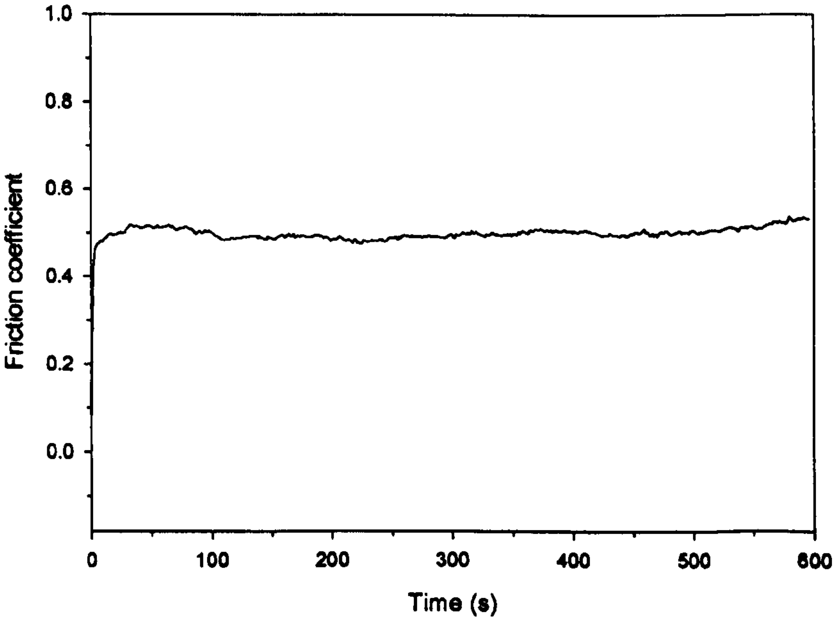

Figure D.4 – Sample air-i2b-10. Normal load=25N, oxidation time=600 s.

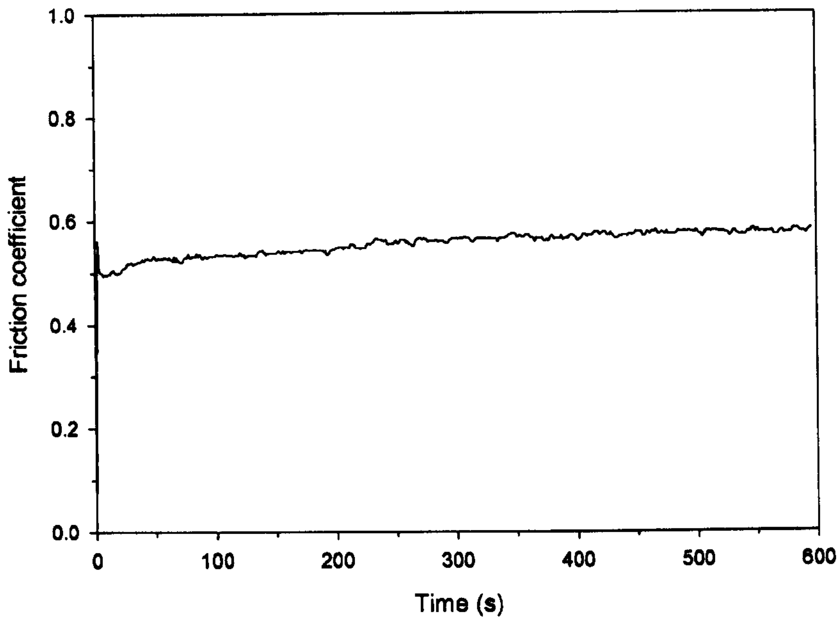

Figure D.5 – Sample air-i2b-11. Normal load=25 N, oxidation time=600 s.

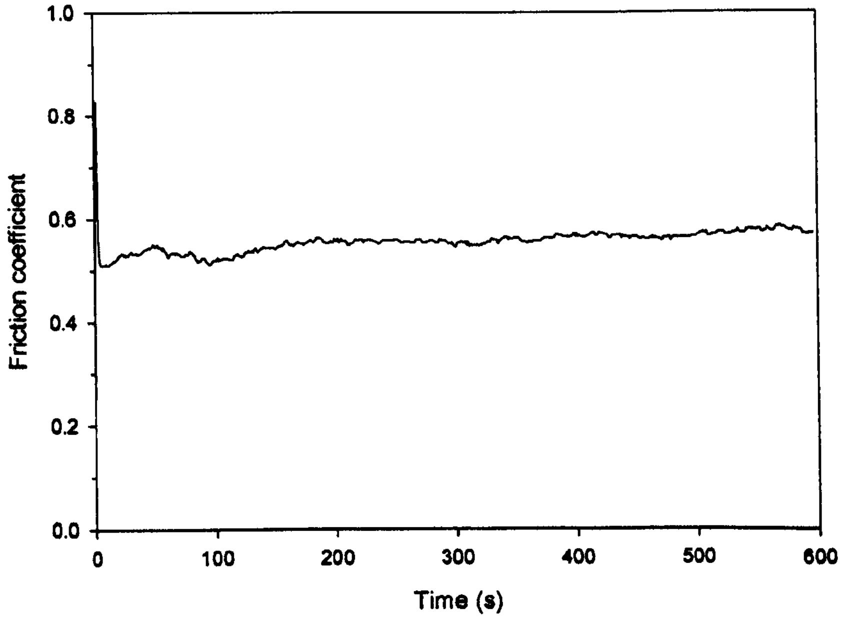

Figure D.6 – Sample air-i2b-12. Normal load=25N, oxidation time=900 s.

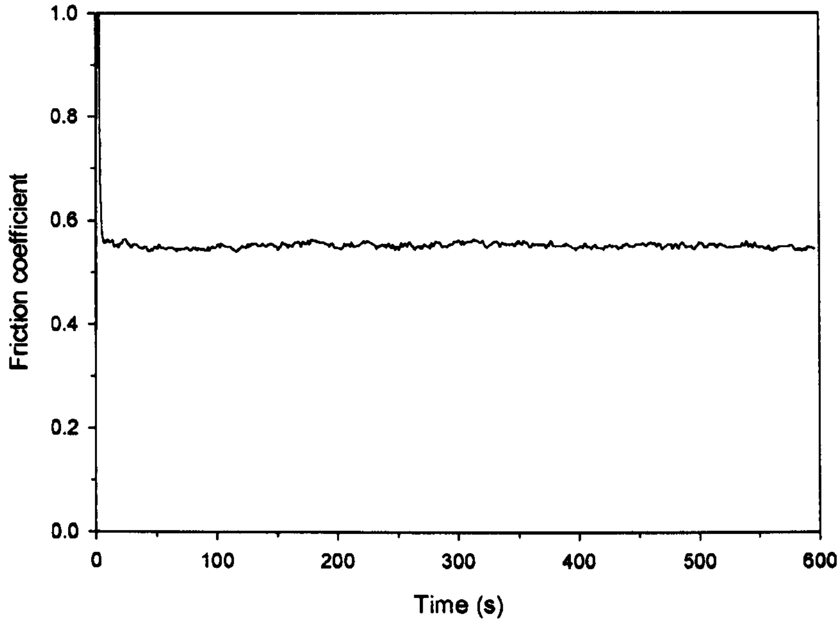

Figure D.7 – Sample air-i2b-13. Normal load=25 N, oxidation time=900 s.

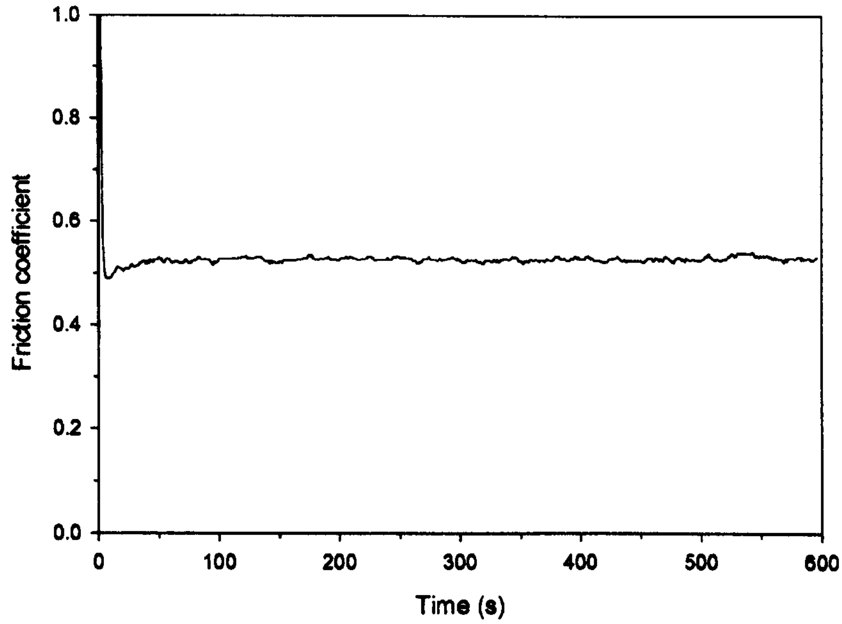

Figure D.8 – Sample air-i2b-14. Normal load=25 N, oxidation time=900 s.

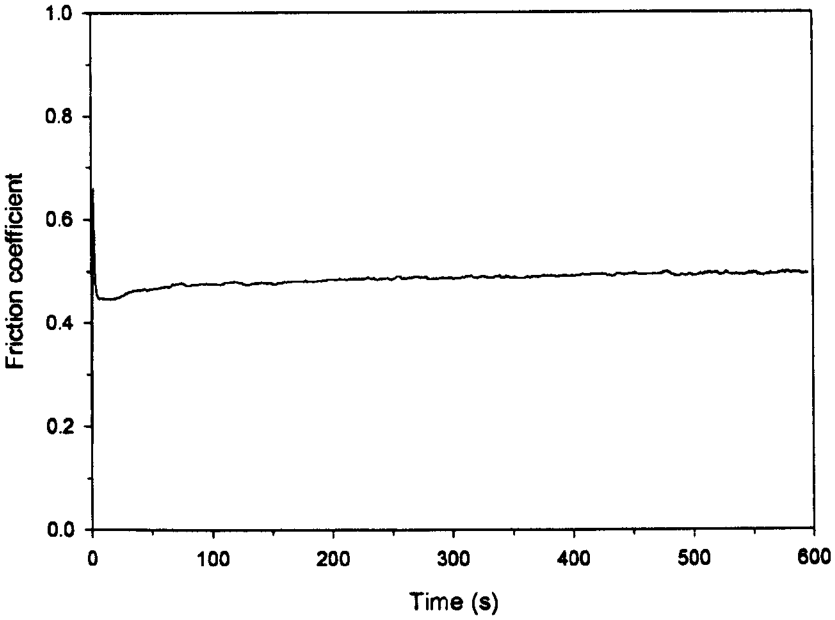

Figure D.9 – Sample air-i2b-15. Normal load=50 N, oxidation time=300 s.

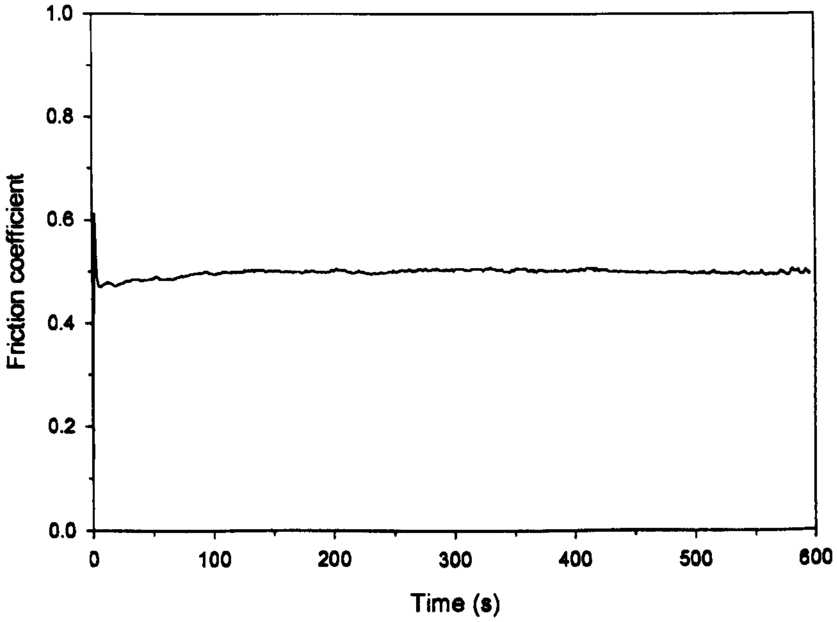

Figure D.10 – Sample air-i2b-16. Normal load=50 N, oxidation time=300 s.

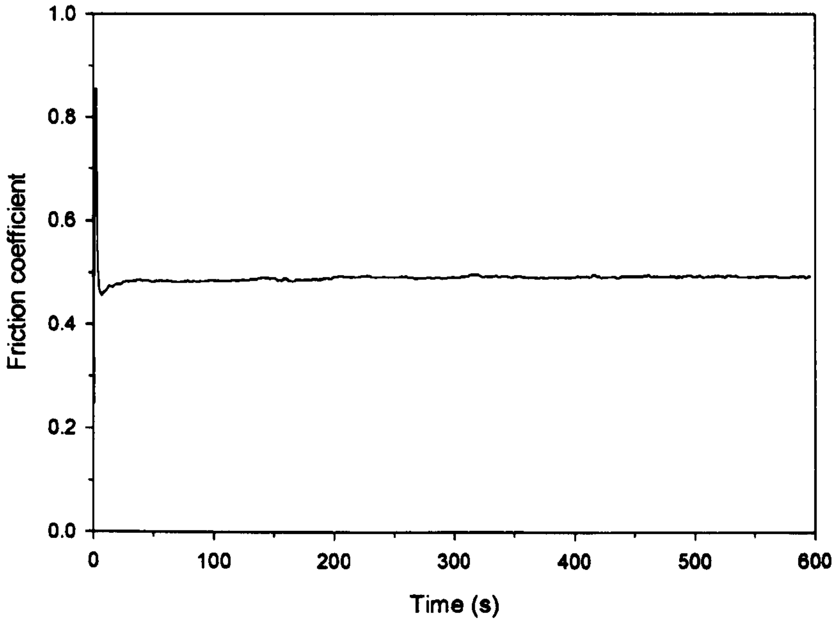

Figure D.11 – Sample air-i2b-17. Normal load=50 N, oxidation time=600 s.

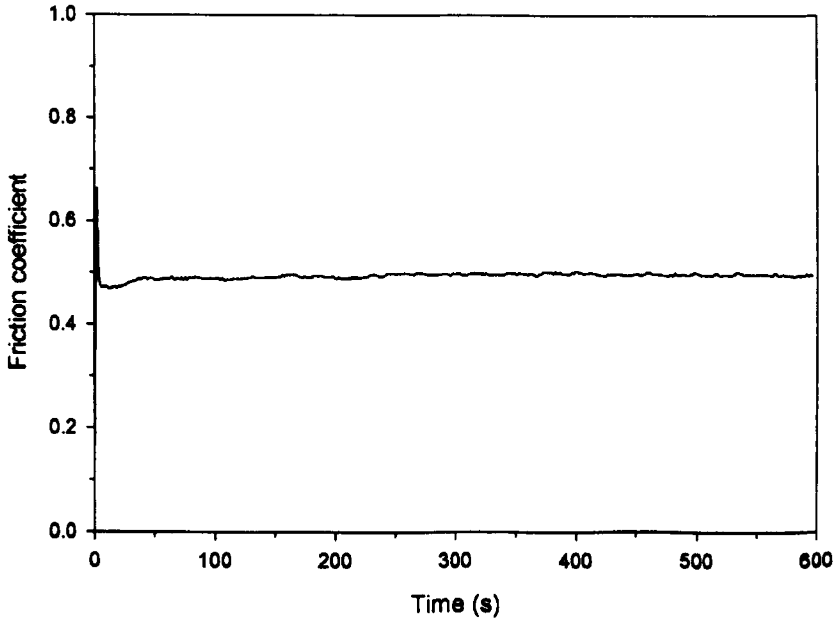

Figure D.12 – Sample air-i2b-19. Normal load=50 N, oxidation time=600 s.

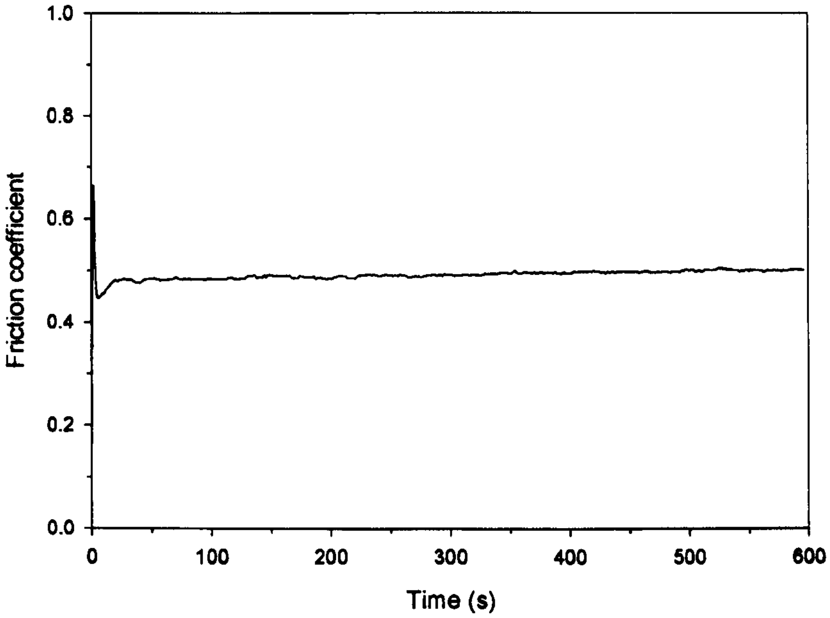

Figure D.13 – Sample air-i2b-18. Normal load=50 N, oxidation time=900 s.

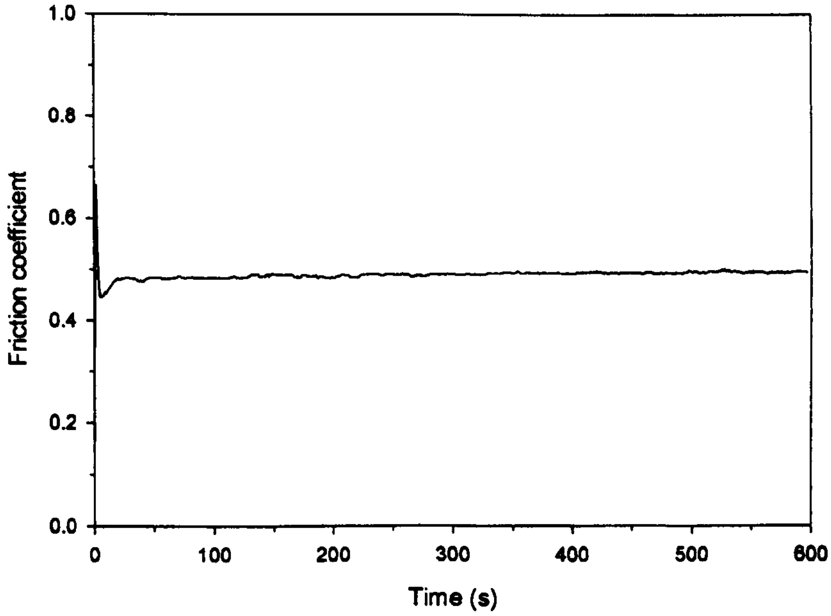

Figure D.14 – Sample air-i2b-20. Normal load=50 N, oxidation time=900 s.

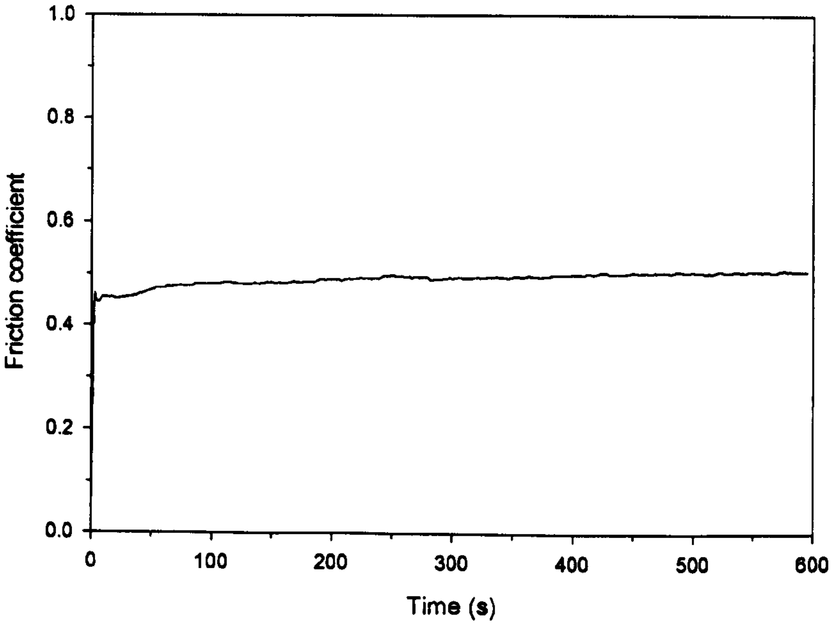

Figure D.15 – Sample air-i2b-21. Normal load=100 N, oxidation time=300 s.

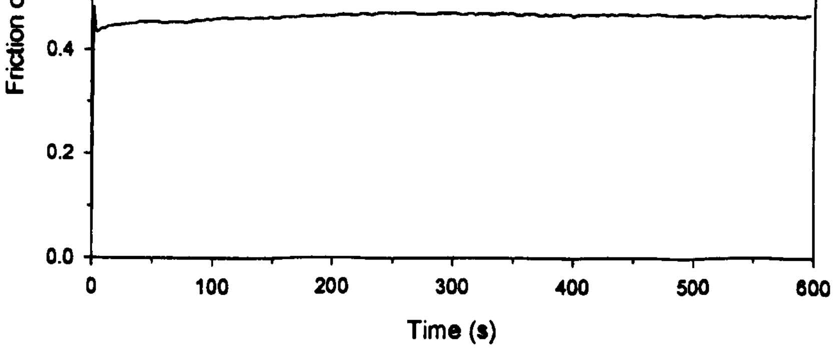

Figure D.16 – Sample air-i2b-22. Normal load=100 N, oxidation time=300 s.

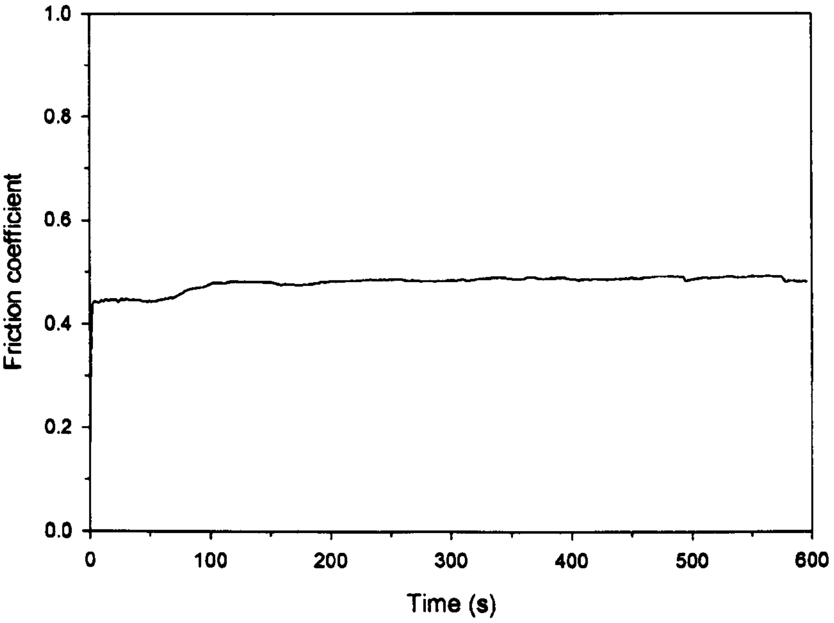

Figure D.17 – Sample air-i2b-23. Normal load=100 N, oxidation time=600 s.

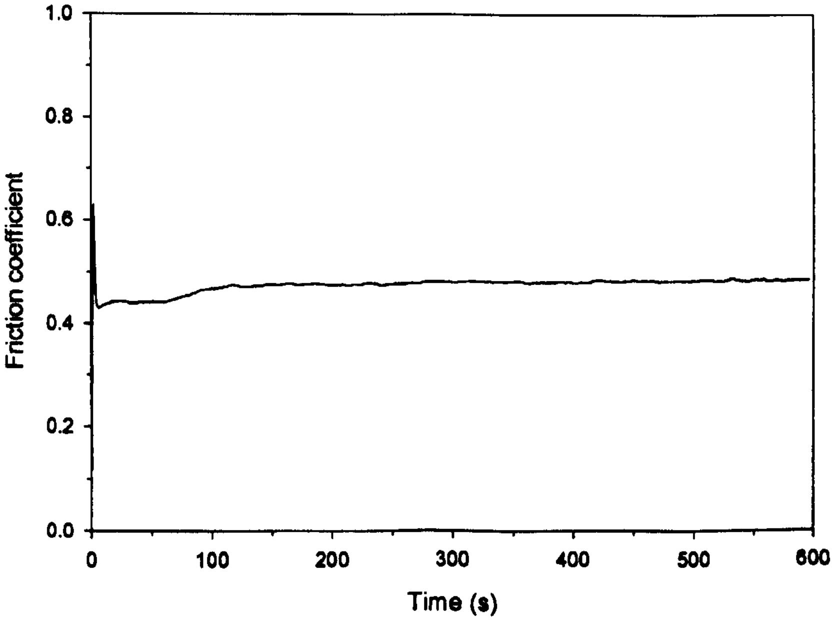

Figure D.18 – Sample air-i2b-24. Normal load=100 N, oxidation time=600 s.

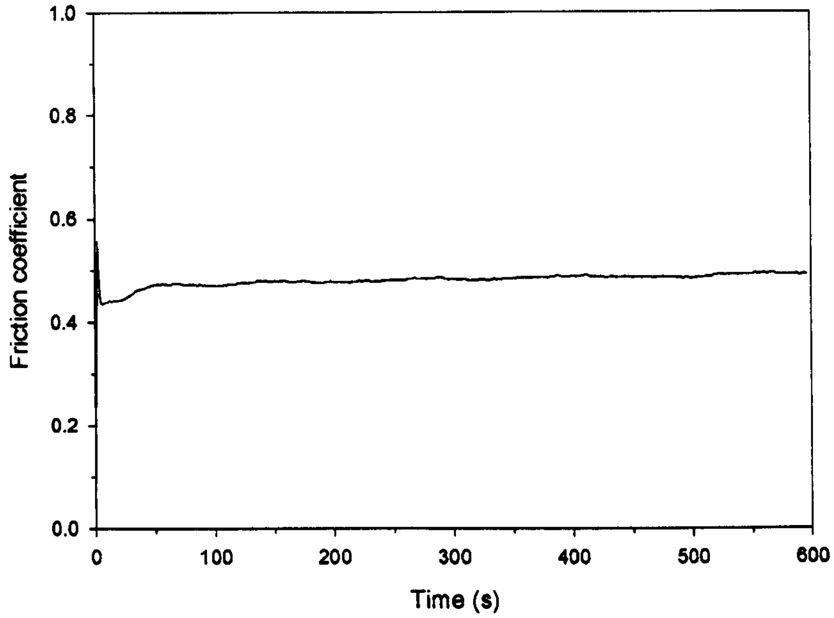

Figure D.19 – Sample air-i2b-25. Normal load=100 N, oxidation time=900 s.

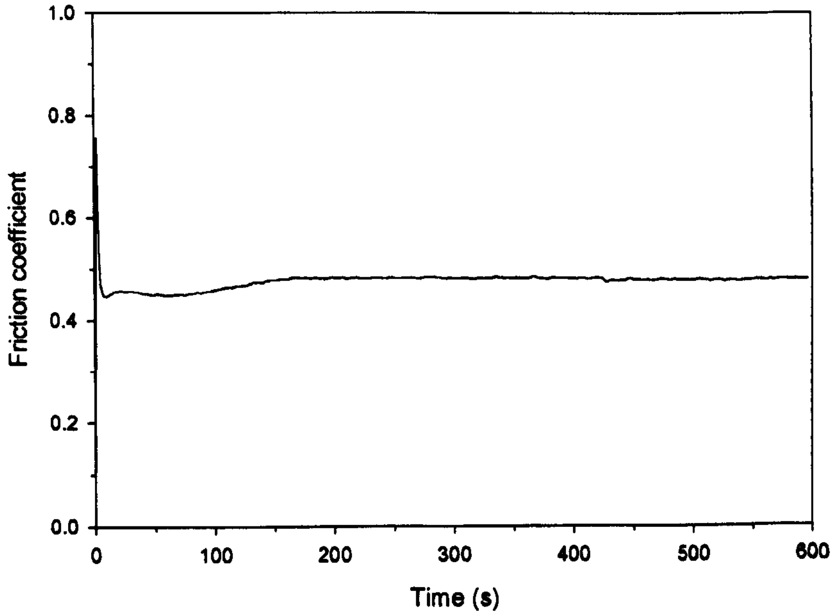

Figure D.20 – Sample air-i2b-26. Normal load=100 N, oxidation time=900 s.

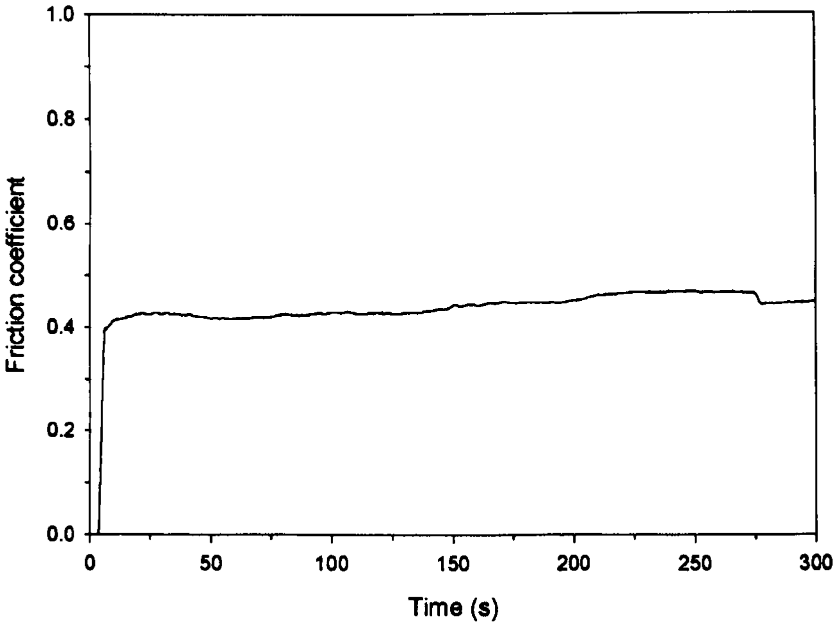

Figure D.21 – Sample air-450-07. Normal load=100 N, oxidation time=600 s.

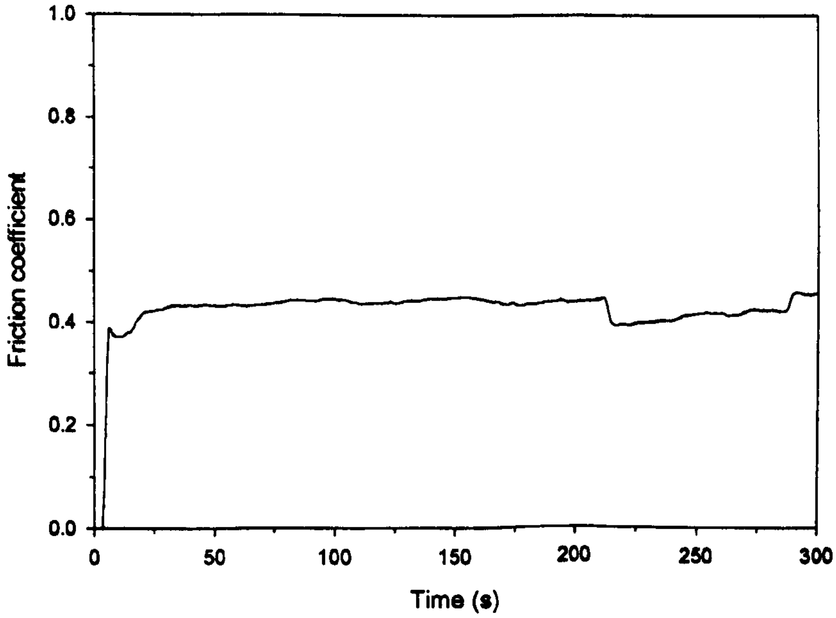

Figure D.22 – Sample air-450-08. Normal load=100 N, oxidation time=600 s.

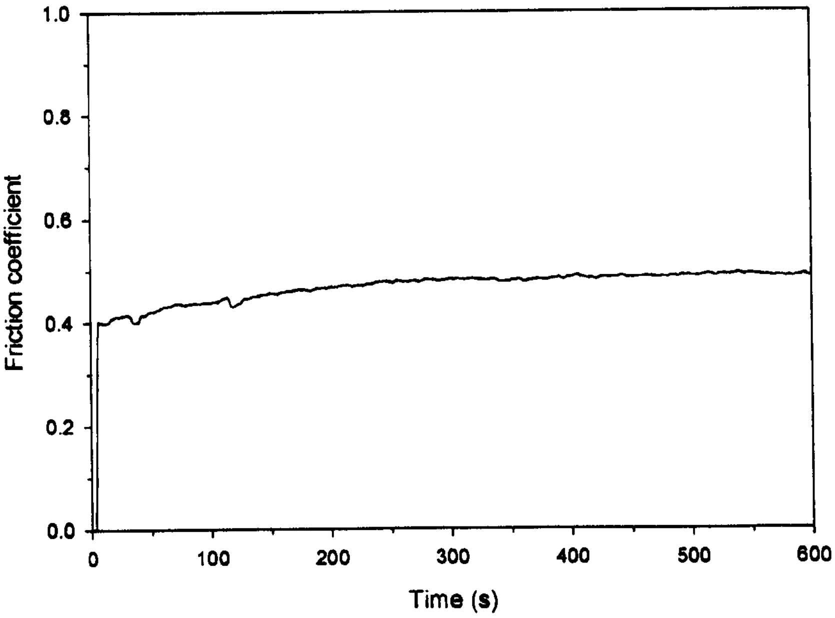

Figure D.23 – Sample air-450-09. Normal load=100 N, oxidation time=600 s.

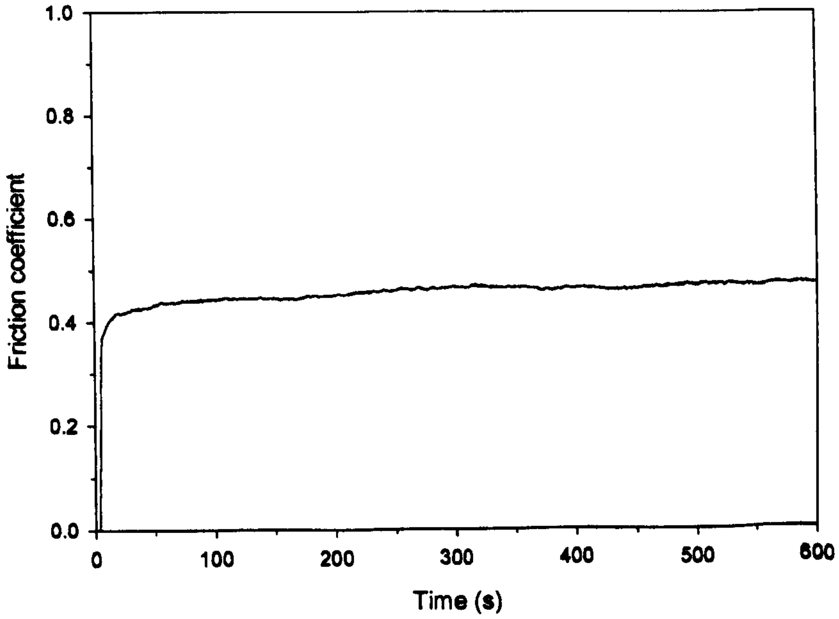

Figure D.24 – Sample air-450-10. Normal load=100 N, oxidation time=600 s.

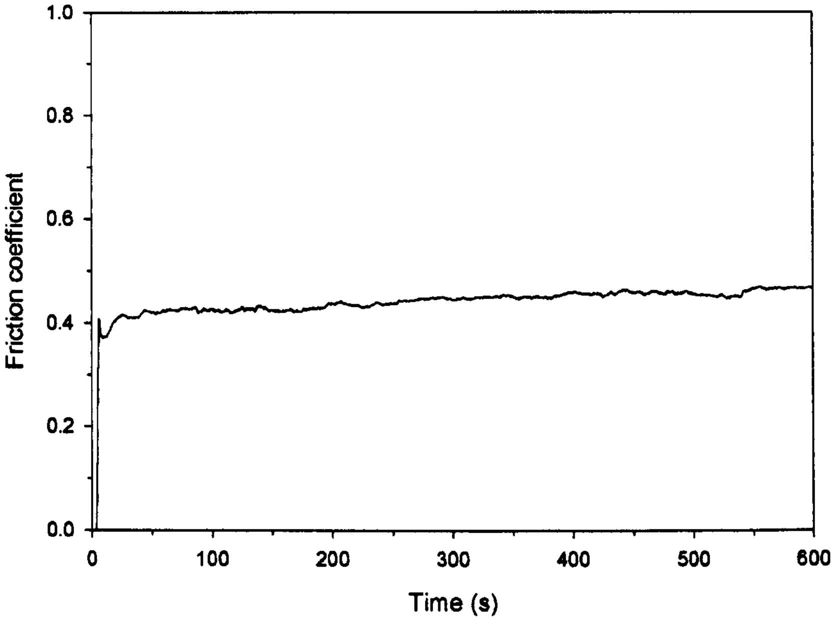

Figure D.25 – Sample air-475-01. Normal load=100 N, oxidation time=600 s.

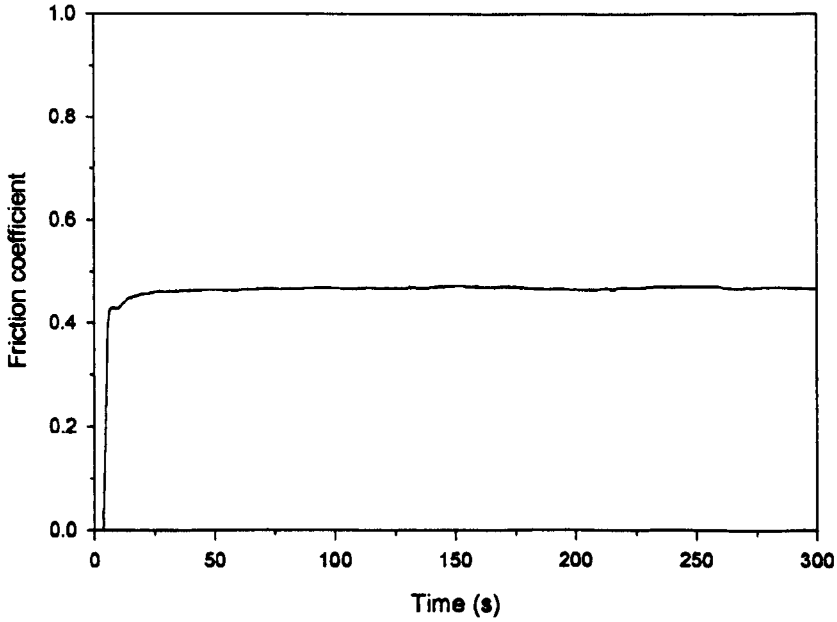

Figure D.26 – Sample air-500-01. Normal load=100 N, oxidation time=600 s.

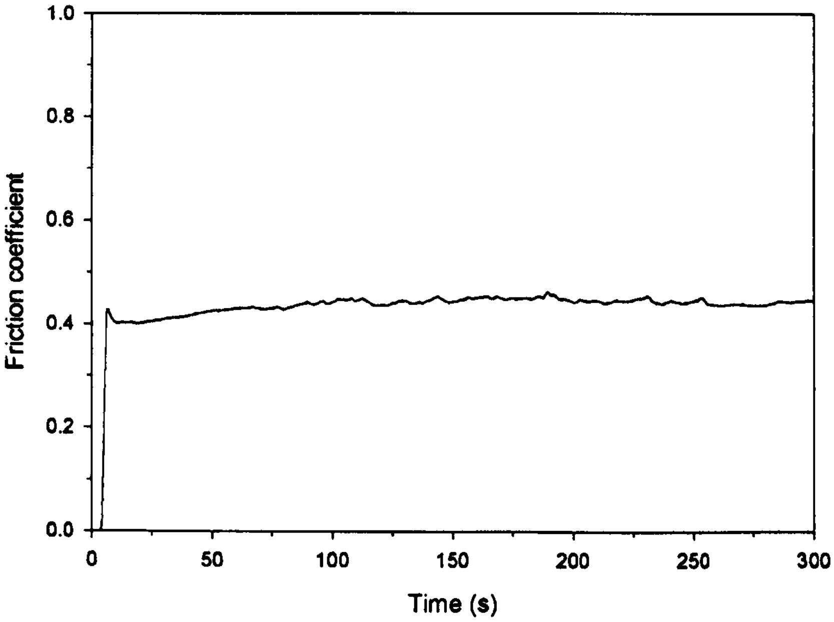

Figure D.27 – Sample air-500-02. Normal load=100 N, oxidation time=600 s.

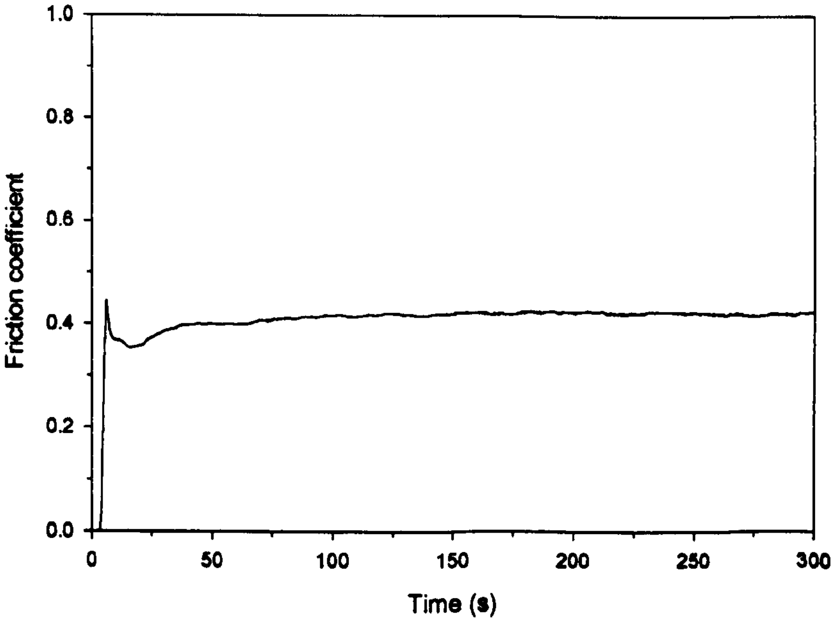

Figure D.28 – Sample air-500-03. Normal load=100 N, oxidation time=600 s.

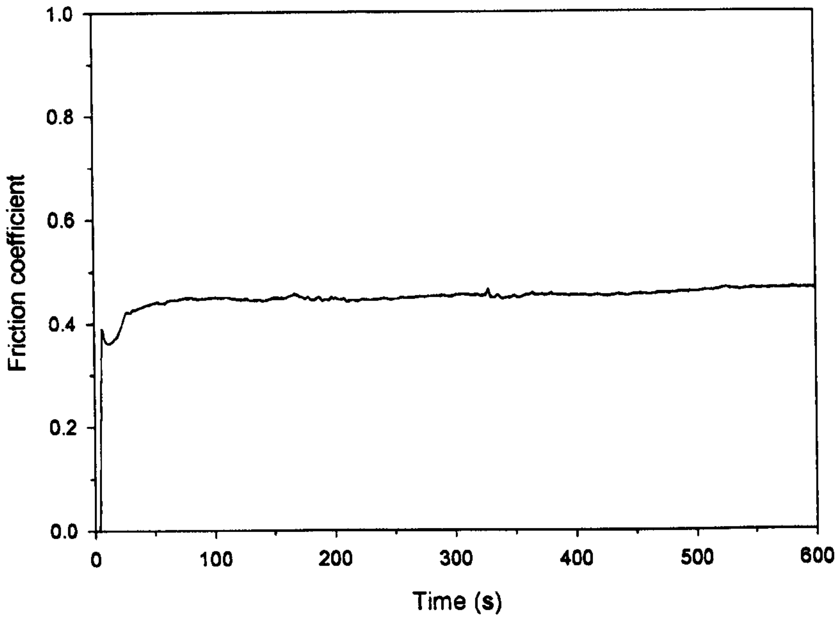

Figure D.29 – Sample air-500-04. Normal load=100 N, oxidation time=600 s.

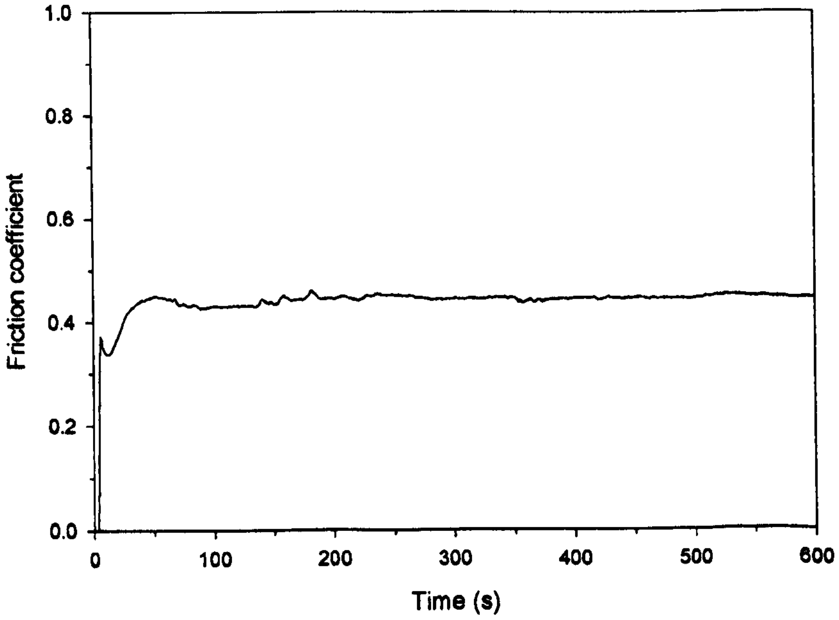

Figure D.30 – Sample air-500-05. Normal load=100 N, oxidation time=600 s.

Appendix E - Approximate Effect of Roll Radius and Draught on Contact Time

To determine the approximate effect of the work roll radius and draught on the contact time of the strip with the work roll the roll force model by Ford and Alexander (*J. Inst. Met.*, 1963, 92) is combined with the industrial data from Siciliano *et al.* (*ISIJ Int.*, 1996, 36) and the pressure dependent heat transfer coefficient model by Devadas and Samarasekera (Ironmaking and Steelmaking, 1986, 13) in the following way:

The roll force model is given as:

$$F = MFS \cdot Q_p \cdot l_d \cdot w \qquad (.1)$$

where F is the roll force (in N), MFS is the mean flow stress (in N mm^{-2}), l_d is the contact length (in mm), w is the strip width (in mm) and Q_p is given by:

$$Q_p = 0.25(\pi + Q) \qquad (.2)$$

$$Q = \frac{2 \cdot l_d}{(h_i + h_f)} \qquad (.3)$$

$$l_d \approx \sqrt{R\Delta h} \qquad (.4)$$

where h_i and h_f are the entry and exit thicknesses respectively (in mm), R is the work roll radius (in mm) and Δh is the difference in entry and exit thickness or draught (in mm). Using the mill data for the mean flow stress the pressure, P, can be calculated using:

$$P = \frac{F}{l_d \cdot w} \qquad (.5)$$

The pressure dependent heat transfer coefficient, HTC, is given as:

$$HTC = 0.695 \cdot P - 34.3 \qquad (.6)$$

where the units of the HTC and pressure are kW m^{-2} K^{-1} and MPa respectively.

The contact time is then determined by dividing the contact length by the work roll surface speed.

The effect of changing the work roll radius and draught on the heat transfer coefficient and contact time is given in Table E.1.

Table E.1 – Calculations from equations E.1 to E.6 showing the effect of roll radius, *R*, and draught, Δh, on the contact time, *t*, and heat transfer coefficient, *HTC*.

R (mm)	Δh (mm)	*P* (MPa)	Roll velocity (mm s^{-1})	*t* (s)	Δt	*HTC* (kW m^{-2} K^{-1})	ΔHTC
393.50	13.27	228.07	1396.92	0.052	1.000	124.11	1.000
354.15	13.27	221.04	1257.23	0.055	1.054	119.23	0.961
432.85	13.27	234.76	1536.62	0.049	0.953	128.76	1.037
393.50	13.27	228.07	1257.23	0.057	1.111	124.11	1.000
393.50	13.27	228.07	1536.62	0.047	0.909	124.11	1.000
393.50	10.21	224.60	1396.92	0.045	0.877	121.69	0.981
393.50	16.33	229.23	1396.92	0.057	1.109	124.92	1.006